A Computational Screening of Supported Metal Films

Jane Laura Ruth Yates

Thesis submitted for the Degree of Doctor of Philosophy

of the University College London

Department of Chemistry

UNIVERSITY COLLEGE LONDON

2016

I, Jane Laura Ruth Yates, confirm that the work presented in this thesis is my own. Where information has been derived from other sources, I confirm that this has been indicated in the thesis.

Acknowledgements

I would like to take this opportunity to thank my supervisor Dr Glenn Jones for his considerable patience, guidance and advice throughout the whole project and especially for teaching me how to compute. At Johnson Matthey, Drs Geoff Spikes and Misbah Sarwar (and earlier Alice Xia) have been ever-present and willing sources of scientific advice and constructive feedback, thank you for the hours of conversation and all the proof reading at every stage. At UCL thanks go to Prof. Nora De Leeuw for giving me the opportunity to study in collaboration with the M3S and Dr Zhimei Du for her continued kindness and organisational help. My time here at UCL would not have been half so fun nor productive without the help and friendship of Liam Bennett, the residents of room 230 past and present, Ya Hu, Saeedeh Tafreshi, Ashley Shields and Hellen Chuma. Without the technical expertise of Dr Jörg Sassmanshausen, David Ladd and Charles Willoughby, and the Legion@UCL and ARCHER support groups, significantly less of this thesis would have been completed. The UK's HEC Materials Chemistry Consortium is acknowledged for access to HECToR and later ARCHER UK National Supercomputing Service (EPSRC EP/L000202) without which the majority of these calculations would have been impossible. Finally, I would like to thank Jonathan Sharman and David Thompsett at JMTC and the EPSRC for funding this project.

Special thanks go to my husband Ed, parents Peter and Nina and my wider family who have supported and encouraged me from day one of this project. Thank you for the patient reassurance, hugs and for reminding me that my identity is in Jesus.

Abstract

This thesis presents the results of first-principles Density Functional Theory (DFT) calculations of Pt-carbide and tie-layered carbide systems in an effort to produce computational screening methods for industrial application. The agglomeration of Pt and PGM catalytic materials on supports leads to loss of surface area and diminished activity towards the industrial processes being targeted. In this work, we have explored the possibility of using carbides as cores for core-shell nanoparticles as a means to thrift Pt loading, promote Pt availability and increase catalyst activity towards the Oxygen Reduction Reaction (ORR) present in hydrogen fuel cells.

For our initial dataset 6 carbides were selected for theoretical investigation; TiC, SiC-β, NbC, TaC and hexagonal and cubic WC. Pt overlayers were then adsorbed on to the carbides and detailed analysis of the resultant electronic structures made in order to identify carbide characteristics which predict good Pt adsorption. WC and SiC were calculated to allow full Pt encapsulation whilst the fcc carbides experienced limited Pt adsorption.

Since full encapsulation of the catalyst core is crucial for Pt availability and both core and shell stability, other metallic layers were also trialled in an effort to promote Pt adsorption. These metals were observed to offer different levels of stability with respect to the Pt forming the outer surface layer although Pt introduction on to previously unfavourable carbide facets is theoretically possible using this method.

The activity of the Pt overlayers towards ORR was then assessed via the study of O adsorption energies, revealing that several of the Pt/carbide structures are indeed predicted to produce ‘Pt-like’ or weakened O adsorption strengths which should maintain or promote ORR activity with the use of much less Pt.

Finally, the stability of the Pt overlayers towards agglomeration was considered. Pt cluster calculations were carried out in order to investigate the effect on electronic structure of cluster size and geometry. These results were then used to assess the strength of Pt hemispheres interactions at the carbide surface. A thermodynamic model was also developed to enable the prediction of Pt overlayer structures under differing conditions and form the basis for entropic corrections to be made in overlayer-cluster comparisons.

Contents

Table of Figures

Table of Tables

1. Introduction

Interest in the field of renewable energy has grown significantly as the environmental and economic effects of a fossil-fuel based economy have become better understood.[1,2] Whilst appropriate green solutions will be dependent on a country's natural resources, fuel cells have been cited as part of the answer in a wide range of cases as they are efficient and clean energy converters.[3,4,5] Fuel cells are also suitable power sources for a wide range of applications from stationary power units to portable toys.[6] In the UK, as of 2012 77% of the power produced was from combustion of fossil fuels. Whilst the proportion of energy from renewable sources has steadily increased to 6% of production, much more needs to be done in order to achieve the EU's 2020 target of 15% of total energy consumed originating from renewable sources.[7,8] Transportation as a proportion of the UK's gross energy consumption has risen from 19 to 37% between 1970-2011[9] and the use of hydrogen fuel cells to power vehicles has been targeted as an area in which emissions and oil consumption may be reduced.[10,11] The Proton Exchange Membrane Fuel Cell (PEMFC), which works at relatively low temperatures (typically 60-80°C) and yet can yield power in the range of 250kW[6] is often advanced as a solution for this application. The PEMFC provides the application backdrop for the research included in this thesis.

At the simplest level, PEMFCs consist of two electrodes and a conducting polymer membrane which acts as the electrolyte (Fig. 1).[12] Hydrogen is introduced at the anode where it undergoes oxidation and the resultant protons move through the membrane to combine with oxygen in the Oxygen Reduction Reaction (ORR) at the cathode.

Reaction at the anode:

$H_2 \rightarrow 2H^+ + 2e^-$

Reaction at cathode:

$O_2 + 4H^+ + 4e^- \rightarrow 2H_2O$

Overall reaction:

$2H_2 + O_2 \rightarrow 2H_2O$

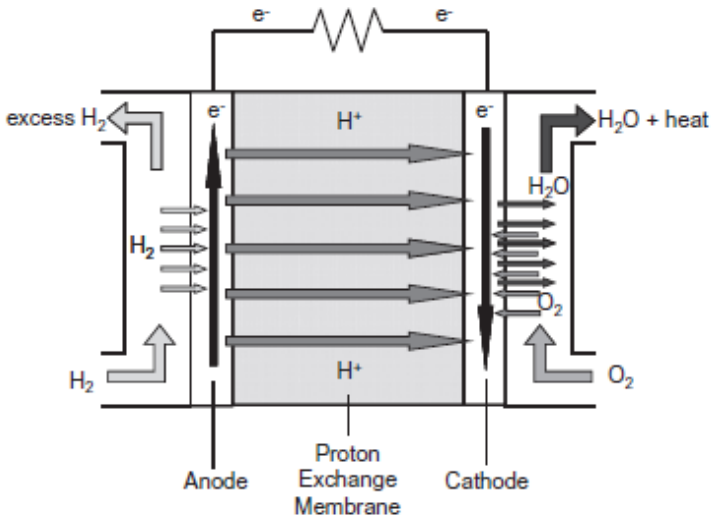

Figure 1 Schematic diagram of a PEMFC, reproduced from Dupuis[12]

The core section of this set-up, the Membrane Electrode Assembly (MEA), consists of gas diffusion layers, the catalyst coated electrodes and the membrane. The membrane is an acidic polymer, often a Perfluorosulfonic acid (PFSA) derivative such as Nafion®(E.I du Pont de Nemours & Co.) containing water filled channels which are used for the proton transfer itself. Both electrodes are treated with a catalytic Pt layer most commonly Pt/C_{black} or 2-5nm Pt nanoparticles on a high surface area carbon support. Platinum is used as the principle catalyst due to its intrinsic activity and comparative corrosion-resistance in the acidic operational environment of the cell. The theoretical maximum cell voltage for the system outlined above is 1.23 V as governed by standard reduction potentials,[13] however it is well known that a significant overpotential is observed resulting in a reduction of the efficiency of the cell. This and other challenges posed in the implementation of fuel cells are highlighted in the following section.

1.1 Fuel Cell Challenges

A major concern for the use of fuel cells in mobile applications is the reduction of power produced by the cell over time. These losses in PEMFCs can be attributed to 3 main sources: mass transport limitations resulting in a lack of oxygen when operating at high current densities, Ohmic losses as a result of fuel cell component and interface resistances and activation losses caused by the kinetics of the ORR at the cathode. The most substantial contributor is the last as the ORR is six orders of magnitude slower than the reaction occurring at the anode.[14] The origin of this overpotential was reported by Nørskov *et al.* to be due to the high stability of adsorbed O and OH on the catalyst surface at high potentials inhibiting the necessary proton and electron transfer.[15] Efforts to minimise the kinetic energy losses have centred around the use of bimetallic or Pt alloy materials to weaken the O binding energy. This approach, utilising computational screening, will be further described in section 1.4 of this introduction. Ohmic losses and mass transport limitations have already been significantly minimised through optimised design of MEA components.

The durability of the catalyst itself is also a crucial factor for fuel cell development. The agglomeration of Pt nanoparticles on conventional carbon supports and the precipitation of Pt into the electrolytic layer are well known phenomena that can significantly reduce cell efficiency. The loss of Pt surface area at higher voltages (>0.8V), is believed to be driven by a dissolution and precipitation method analogous to Ostwald Ripening.[16,17] Higher voltages present in start-up and shut-down cycles around breaking events for example are known to accelerate catalyst

degradation.[18] Pt agglomeration reduces the number of active surface sites for catalysis, thereby lessening the turn over frequency of the cell.

The precipitation of Pt and corrosion products from other fuel cell components into the PEM also causes the degradation of the electrolytic membrane. Some contaminants simply mechanically block pores whiles others have a more serious impact on the integrity of the membrane itself. Metallic cations such as Fe^{3+} and Ni^{2+} enter the porous channels and bind to the sulphonate side chains. Their presence not only promotes the formation of peroxide radicals, which go on to attack the polymer structure, but also reduces the conductivity of the membrane as the sulfonic sites bind the metallic cations preferentially over the H^{+}. The metallic ions also exhibit lower mobility due to their size, further compounding the problem.[19,20] Other sources of contamination include the air and the hydrogen feedstock used to fuel the cell. The introduction of NO_X and SO_X through the oxygen inlet leads to rapid poisoning of the cathode as the molecules bind to the Pt surface preventing subsequent oxygen adsorption. CO and related contaminants from the steam reformation process[20] likewise poison the anode. Thus, significant investment in the improvement of fuel processing is necessary to extend the working life of the fuel cells.[21]

The membrane electrolyte must also meet exacting requirements in order to promote the efficiency of the cell. Water management, both in the necessary hydration of the membrane to allow proton conductivity and in the prevention of flooding of the cell is crucial.[18] The prevention of fuel cross-over and limitation of solvent drag whilst maintaining excellent proton exchange is also complex. Membranes must also be thermally, mechanically and chemically stable under operation conditions.[12] The combination of multiple polymers and the inclusion of a wide range of inorganic components into the polymer membrane have been investigated for the improvement of performance.[22] For PEMFC applications it has been observed that the inclusion of proton conductors such as heteropolyacids (HPA) in the Nafion can improve the proton conductivity of the membrane and beneficially retain water under dry gas operating conditions.[23]

Whilst the fuel cell electric vehicle, FCEV, market has seen tremendous advance in recent years, including Hyundai's small scale production of the ix35 fuel cell vehicle from February 2013 [24] and the release of the Toyota Mirai on the UK market in 2015, arguably the most crucial continuing barrier to large scale commercialization of the technology is the cost. Seven leading automotive manufacturers have committed to introduce FCEV from 2015-17 at prices competitive with diesel-hybrid vehicles,[24] but for these aims to be met significant reductions to the price of the fuel cell

stack must be made. Whilst manufacturing savings would be made with production scale-up,[25] the baseline cost of Pt has been identified as the lower limit to the cost of production.[10]The US Department of Energy has identified its 2017 targets for automotive fuel cells as a reduction of platinum group metal (PGM) loading to 0.125 $mgcm^{-2}$, an increase of specific activity to 0.44 A mg_{Pt}^{-1} and durability exceeding 5000 hours.[26]

1.2 Historical and Current Catalytic Approaches

In the literature many suggestions for lowering the Pt loading of PEMFC catalysts have been made. These approaches may be categorised as Pt-free[27,28], Pt-support[29,30] and modified Pt solutions.[31,32] The relative success and merits of these approaches will be discussed giving a broad overview of the field as it stands before considering the use of computational resources to aid further catalyst optimisation in the modified Pt field.

1.2.1 Platinum Free Catalysts

Initial ORR catalyst research involved other PGMs being employed as Pt replacements, however the reduced activity of these metals resulted in increased loadings being necessary to achieve comparable output ruling them out under the DOE targets. Although markedly less active, the transition metals (TMs) were subsequently investigated as non-precious alternatives. Inclusion of TMs such as Co with organic macrocycles similar to Porphyrin[33,34] led to the development of M-N/C materials which, following calcination, had sufficient stability to be considered for ORR applications. Conductive polymers such as polypyrrole and polyaniline (PPy and PANI respectively) have been used as N/C precursors for pyrolized M-N/C systems as well as base materials for TM complex insertion.[35] Transition metal chalcogenides ($M_zM'_{3-z}X_4$ where X=S,Se, Te)[36] as well as oxides, carbides and nitrides have each been considered as principal catalysts, though varied activity toward ORR and stability in acidic media place them with consistently lower activity than conventional Pt/C.[35] Lefèvre's 2009 report of a Fe/N/C catalyst with a current density akin to that of $0.4mg_{Pt}/cm^2$ loaded conventional Pt cathode at a voltage of 0.9V was the first example of a competitive non-precious metal catalyst. However, it must be noted that the inclusion of an organic framework in the system resulted in limited stability under operation conditions, the current density produced dropped from 0.75 A/cm^2 to 0.33 A/cm^2 over 100 hours.[37] Whilst Pt-free catalysts are attractive from a cost perspective, stability is a limiting factor in their utility. According to the 2013 US DRIVE Report, non-PGM catalyst activities would also need to increase 5-fold to reach the DOE activity targets at 0.8 V.[26]

1.2.2 Pt nanoparticles on novel supports

A second approach to reducing Pt loading for MEAs catalysts is the maximisation of active Pt surface area. This is achieved by depositing small Pt nanoparticles and maintaining the dispersion of nanoparticles on the support surface. A number of techniques have been used to assess the presence of a particle-size versus activity relationship for the ORR. Rotating Disk Electrode (RDE) experiments on catalyst samples with surface areas in the range 0-120 m^2/g_{Pt} (d_{Pt} ≈15-2 nm) shown in figure 2 revealed a significant particle size effect between 0-80 m^2/g_{Pt} after which a shallow maximum was reached at 90 m^2/g_{Pt} suggesting no benefit from finer separation.[38]

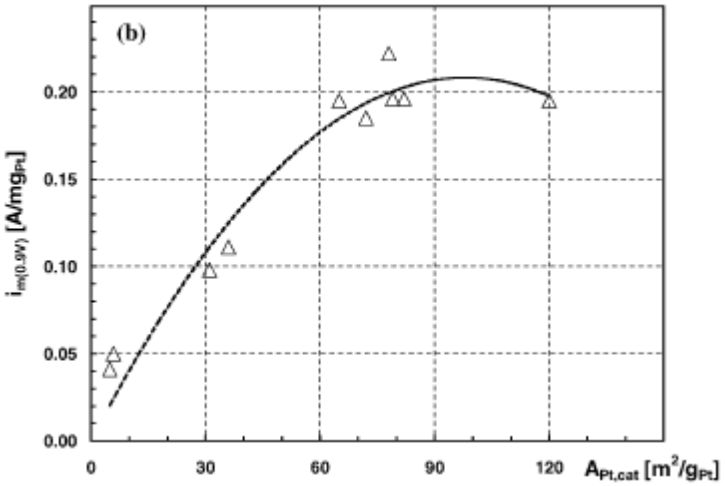

Figure 2 ORR mass activities of polycrystalline Pt catalysts reproduced from Gasteiger[38]

An absence of the particle size effect between diameters of 1-5 nm for ORR was also reported by Yano following 'channel flow double electrode' cell measurements. Electrochemical nuclear magnetic resonance (EC-NMR) carried out concurrently with the cell measurements elucidated no significant changes in Pt peak position or relaxation rate, indicating that no size dependent alteration of the Fermi level local DOS (E_f LDOS).[39] It should also be noted that small particles (~2 nm) have been observed to lack stability in PEMFC operational environments.[40] In summary, a lack of activity enhancement for small diameter nanoparticles suggests that attention should be focused on maintaining the dispersion of the Pt and maximising the availability of surface Pt atoms to act as a catalyst.

The requirements for catalyst supports have been summarized by Shao *et al.* as: 1) high specific surface area, 2) low combustive reactivity, 3) high electrochemical stability under fuel cell operating conditions, 4) high conductivity and 5) facile recovery of Pt post decommissioning.[41] A large selection of materials have been investigated for this role including conductive

diamonds,[42]transition metal oxides,[43] nitrides and carbides,[44] SiC and mesoporous and structured nanocarbons.[41]

Whilst conductive diamonds have been found to exhibit excellent morphological stability with and without Pt in excess of 1.4 V, [45] low surface areas, low conductivity and the poor dispersion of catalytic Pt make them poor candidates as PEMFC supports. Although the prevention of Pt agglomeration on the support is possible by further deposition of diamond, the initial Pt particle diameters of 50-350nm[46] are too large for fuel cell applications. Transition metal nitrides (TMNs) and carbides (TMCs) offer improved conductivity and are known to exhibit some innate catalytic ability. However their chemical stability under fuel cell conditions varies as does the commercial availability of high surface area powders.[47] It has been noted that deposition of monolayers of Pt on to TMC surfaces has resulted in altered Pt performance and so these carbide materials will be further considered in this review in the context of Pt modifying systems where the limiting stability of the carbide may be overcome via its inclusion as a core rather than a support.[48,49]

Carbon Nanotubes (CNTs) have attracted much interest as they have great potential to meet all of Shao's requirements. Once functionalised with carboxyl, hydroxyl and carbonyl groups, CNTs allow for excellent dispersion of nanoparticles on the support with particle sizes of 5-8nm.[50] CNTs also exhibit enhanced electron transfer characteristics leading to improved catalytic activity for the Pt.[30] Their ability to form porous networks also suggests that CNT architectures could be used to aid gas diffusion. Whilst the presence of defect sites is known to contribute to the catalytic enhancement, they are also locations of Pt sintering and CNT corrosion. CNT durability and the prevention of nanoparticulate agglomeration or detachment may be improved with the addition of a SiO_2 coating without harming the system's activity towards the ORR.[51] The stability of bridged CNTs and other CNT architectures developed to optimise activity may also be ameliorated by the addition of dopants such as nitrogen which act as electron donors, stabilising the CNT π bonding. Heteroatom addition was also shown to enhance the ORR on CNTs without any metal being present.[52]

An alternative approach to the use of supports was shown in the development of 3M's nanostructured thin film catalyst (NSTF) where organic pigment whiskers were completely covered by a thin Pt layer.[53] The encapsulation of the support reduced the risk of corrosion and Pt dissolution considerably enhancing the system durability. The NSTF also exhibited a 5-fold increase in specific activity over conventional high surface area Pt/C, this compensated for the

support's smaller surface area, producing equivalent ORR performance at a greatly reduced Pt loading. However operational short comings such as poor electron conduction under dry conditions and flooding at the cathode have been noted. In order to expand the usefulness of the catalysts under fuel cell conditions extra system components such as silica nanoparticles have been tested and provide some amelioration of the problems.[54]

Whilst the strength of the metal-support interaction (MSI) determines the adhesion and stability of the metal on the surface,[16] supports may also influence the activity of the metal by modulating its electronic structure. Bimetallic systems and Pt alloys were developed to exploit the fact that the combination of materials often results in properties differing from those of the components.

1.2.3 Modified Pt : Bimetallics and Alloys

The causes of the differing electronic and chemical properties exhibited by bimetallic monolayer systems (BMSs) are twofold. Firstly, the addition of a layer of heteroatoms to a pure metal results in the formation of heteroatomic bonds, shifting the surface metal electronic states due to the ligand effect. Secondly, dependent on the difference in lattice parameters between the components, geometric strain is introduced into the system. The alteration of orbital overlap in turn effects the surface density of states (DOS) altering adsorbate binding energies and hence the activity of the material.[55,56]

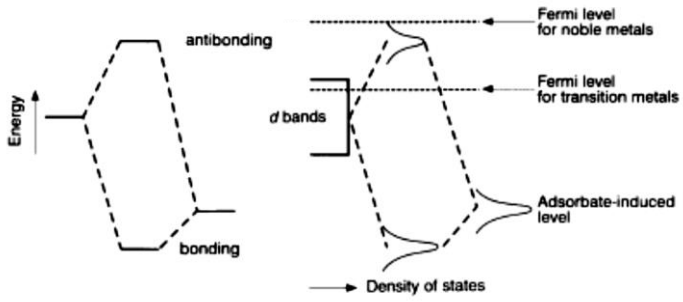

Figure 3 Schematic of metal and reagent interaction reproduced from Hammer[57]

Since the adsorption trends of reagent molecules on TM and PGM surfaces can be well rationalized in terms of the hybridization of the metal d-band and the reagent valence bands shown in figure 3,[57] the centre of the d-band (E_d) can be used to correlate the electronic structure to reagent binding energies. Adsorption on to a metal with E_d near E_f would result in high lying, unfilled antibonding orbitals and so a stronger bond whereas adsorption on a metal with a very negative E_d would result in weaker bonding. For example, upon surface expansion the M-M orbital overlap decreases and the d-band width is reduced, in order to maintain the same d-band filling the energy

of the band must be increased, moving E_d towards E_f. In addition to the ligand and strain effects there is also charge transfer between elements in bimetallic systems, however this was observed to be less than 2% so it is assumed that this does not account for the chemical changes observed.[58]

Both the ligand and strain effect are dependent on the metal overlayer thickness. In the case of a Pd nanoparticle on Au, the reactivity of the system towards proton reduction increased by two orders of magnitude as the thickness of the Pd decreased from 10 to 2 monolayers.[59] The 4.8% lattice mismatch between Pd and Au 'healed' as the Pd thickness increased, resulting in surface electronic properties similar to those of bulk Pd and loss of the activity enhancement. This implies that activity enhancement of the surface metal is only applicable in systems with a very thin overlayer.

Zhang *et al.* showed that alteration of the d-band centre of monolayer (ML) Pt was observed following deposition on Au(111), Rh(111), Pd(111), Ru(0001) and Ir (111). The resulting trend of experimental activity for ORR shown in figure 4 was 'volcano-like', placing Pt/Pd at the maximum above pure Pt. The volcano plot displays the activities of the compounds in 2 essential ORR steps: O-O dissociation (favoured by strong bonding and less negative E_d) and O-H bond formation (favoured by materials with a lower bonding strength and more negative E_d). In accordance with the Sabatier principle,[60] optimal ORR catalysts would be expected to have intermediate E_d values to allow both reactions to progress at a favourable rate.[61]

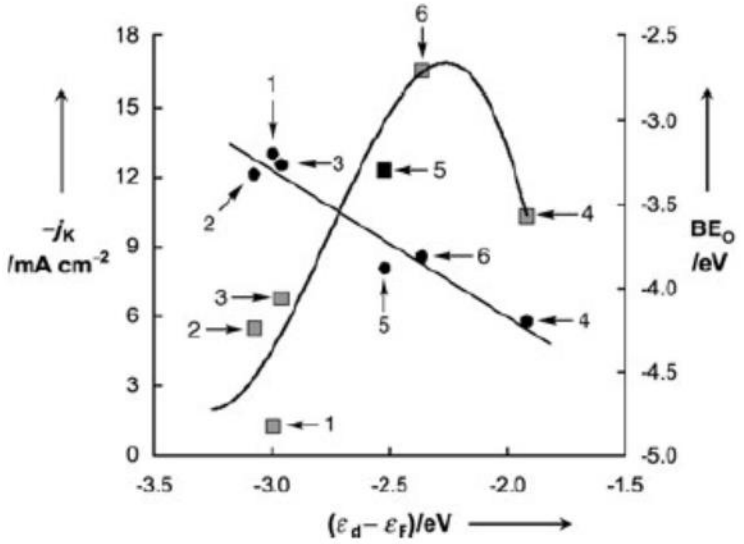

Figure 4 Kinetic currents, squares, at 0.8V for ORR of ML Pt on 1. Ru(0001) 2. Ir(111) 3. Rh(111) 4. Au(111) 5. Pt(111) 6. Pd(111), Solid circles represent binding energies of atomic oxygen. Reproduced from Zhang[61]

The use of Pd as a support resulted in a 33% overall efficiency increase for ORR whilst Pt loading was reduced by a factor of 10. Sasaki *et al.* observed significant Pd leaching from Pd/Pt core-shell

particles and have suggested that this loss actually protected the Pt shell via sacrificial oxidation and dissolution. Pd loss was postulated to occur via imperfections in the Pt ML.[62] Although alteration of the E_d and improved ORR kinetics proved that low Pt content catalysts could exceed the activity of pure Pt, the use of expensive PGMs as supports was unsuitable for large scale PEMFC applications. BMSs utilizing less expensive TMs such as Ti, Ni and Fe have also been observed to lower E_d resulting in weaker O_2 and H_2 binding.[63]

Whilst variation in the bimetallic surfaces was limited to surface and subsurface integration of the Pt layer, alloying the metals in the bulk gave scope for much greater variation in both composition and nanoparticle structure.[64] It must be noted that this variation makes comparison of alloyed structures more complex. 'The intrinsic activity of nanoparticles depends on size, shape and composition', meaning simple comparisons normalised by mass or surface area are not reliable for elucidating trends concerning components.[31]

Pt/TM alloys were observed to cause variation in the position of the Pt d-band and to improve electrocatalytic activity: Cr, Mn, Fe, Co and Ni alloys all produced a 2 to 4-fold increase for the ORR.[65] Variation of the bulk alloy composition using 30-50% 5d TMs was later used to produce volcano plots of composition versus activity for Ni, Fe and Co.[66] Comparison of ORR kinetics at different potentials allowed activity-component relationships to be elucidated, including Pt<PtNi<PtCo where Pt_3X<PtX.[67] The stability of alloyed surfaces was also found to be composition dependent, with 1:1 systems being significantly more likely to lose base metal than 3:1 systems.[68] A significant milestone for binary alloys was Stamenkovic *et al.*'s discovery of $Pt_3Ni(111)$, possessing 10 times the ORR activity of Pt(111) and 90 times that of conventional Pt/C .[69] Unfortunately the stability of this compound when in the presence of oxygen was shown to be minimal. Following a small number of cycles the Ni leached from the system due to the very strong Ni-O affinity leaving a Pt catalyst.[70]

Whilst loss of base metal leading to contamination of the membrane is highlighted by many as a potential problem with alloyed systems,[71] the removal of TM and subsequent exposure of Pt may actually contribute to enhanced catalytic capabilities.[68] TM loss, limited to only the first few ML of the surface, results in Pt-rich surface regions. The loss of base metal is linked to the nature of the synthesis of the initial alloy as well pre-treatments such as annealing and the tendency of the bulk toward order or disorder.

The trend for Pt_3X systems to develop Pt rich surface structures was noted by Stamenkovic *et al.*[31] and Pt skeleton and Pt-skin motifs were identified for samples which had undergone dissolution and annealing respectively. Annealed samples exhibited negligible TM loss upon acidic immersion whilst surfaces resembling the bulk alloy configuration experienced a TM rinsing, leaving a Pt surface. The Pt-rich surfaces exhibited a lower d-band centre than pure Pt, shifting Pt_3Co and Pt_3Ni toward the catalytic peak of the volcano plot, whilst the structural trend $Pt<Pt_{skeleton}<Pt_{skin}$ was defined for activity toward ORR. Electrochemical TM dissolution has also been used to produce 'dealloyed' PtCu nanoparticles with 4-6 fold improved ORR activity.[72] It is noted that as Pt skin thickness increases, there is a clearly correlated loss in ORR enhancement.[73] Although the alloy core is better protected from dissolution improving the materials' durability, the presence of the TM was shielded and so any E_d alteration lost.

The propensity of alloyed materials to form core-shell arrangements benefits both catalyst stability and ORR activity, however post processing such as annealing is often required and results in nanoparticles significantly larger than those conventionally used (>9 nm).[71] The physical origins of surface segregation can be discussed in terms of surface energy and strain. If there is a difference in surface energies between the pure constituents of the alloy, the element with the lower surface energy will form the shell.[74] For TMs where an appreciable atomic size mismatch is present, the component which will relieve strain at the surface will segregate there i.e. the smaller atom will be segregated to the core. Following a comprehensive computational investigation by Wang and Johnson the following principle was put forward; in the case of alloys constructed from elements in different groups surface energy will dominant segregation whereas alloys constructed from the same group will experience segregation dominated by strain.[75] Some deviations from the simple surface energy model were noted for early transition metals and attributed to structural contributions to the segregation energy.[76] These trends have been observed for extended surfaces[76] and 55 atom clusters[75] and use of DFT tight-binding has proven that d-band centres can describe the segregations as the cohesive energy and atomic radii are taken into account by the E_d and d-band width.[75]

The combination of the modified embedded atom method (MEAM) with Monte Carlo statistical mechanics enabled the segregation behaviour of nanoparticles with over a hundred atoms to be considered. $Pt_{75}Ni_{25}$, $Pt_{75}Re_{25}$ and $Pt_{80}Mo_{20}$ cubo-octahedra were investigated and nearly pure Pt outermost layers were created during the simulations. These calculations also reproduced the well-known Pt-Ni-Pt surface 'sandwich' in Pt_3Ni and a weaker core-shell arrangement for the

Pt_4Mo cluster (strain arguments would favour Mo surface occupation whilst heats of formation favour Pt). The Pt_4Mo particle surface consisted of Pt covered facets with an alternating PtMo sequence appearing at edges and vertices.[77] Although such simulations are instructive, the number of atoms which can be considered in the system is still limited by computational expense.[64] Much work within the cluster community has been dedicated to producing semi empirical methods which are viable for larger nanoparticles or empirical methods which can accurately reproduce experimental phenomena.[78] The size of systems which can be calculated time efficiently using first principles has also increased significantly over the past decade.[79,80]

The core-shell nature displayed by some alloy systems has many advantages. The presence of the bulk alloy significantly lowers the use of Pt and promotes favourably modified surface electronic structures which can enhance ORR activity. The Pt skin itself has a high surface area due to the nature of its formation maximising Pt availability and serves to protect the core from further dissolution. In short, such systems have the potential to meet our cost, activity and durability targets. Further Pt reductions could be made by exchanging the core for an inexpensive Pt-free alternative. The TMCs have gained much interest for this role due to their electronic structures and mechanical properties.

1.2.4 Transition Metal Carbides for Core-Shell Catalysts

Levy and Boudart's assertion that WC had 'Pt-like' surface electronic structure[81] and exhibited catalytic properties has led to much interest in the TMCs as components for PEMFCs. Alongside some innate activity, the TMCs also exhibit excellent conductivity and better thermal stability than C_{black} making them ideal candidates as catalyst cores. What is more, a number of Pt/TMC systems have shown an enhancement of activity due to the electronic alteration of Pt by the carbide,[82,83]and a degree of resistance to CO poisoning.[84] In this final subsection, the suitability of TMCs for use as a catalyst support or core for fuel cell applications will be discussed as well as recent examples of Pt/carbide systems.

The electrochemical stability of the TMCs under fuel cell operating conditions is a crucial factor in determining TMCs suitability as catalyst supports. The stability of the parent TMs can be visualised in Pourbaix diagrams,[85] identifying regions of stability according to pH and potential. For multicomponent materials such as carbides, chronopotentiometric (CP)-titration measurements can be used to identify regions of immunity, passivation and oxidation under an applied potential,

suggesting which materials may be suitable for a given application.[86]WC has been well studied in this manner by Weidman *et al*.[86,87] indicating instability in neutral and alkaline environments at positive potentials, but stability at low pH(<2) and negative potentials, as seen in figure 5. In the passivation region, stable W_xO_y compounds form at the surface, however it is worth noting that even in the presence of the oxide, the activity of the Pt/WC system remained almost constant over 100 oxidising cycles whilst Pt/C activity dropped substantially after only 20.[88] WC then, is proposed as a good candidate for the catalysis of the Hydrogen Evolution Reaction (HER) and HOR at all pHs and a possible ORR cathode at low pH.[89] TiC, TaC and ZrC were also identified as stable ORR catalysts by Kimmel *et al.*[47]Doping WC with Ta has proven to increase its stability in PEMFC operating conditions whilst also enhancing its electrochemical activity toward ORR.[90] Dopant strategies may prove an effective way of modifying TMCs to improve their longevity under operating conditions.

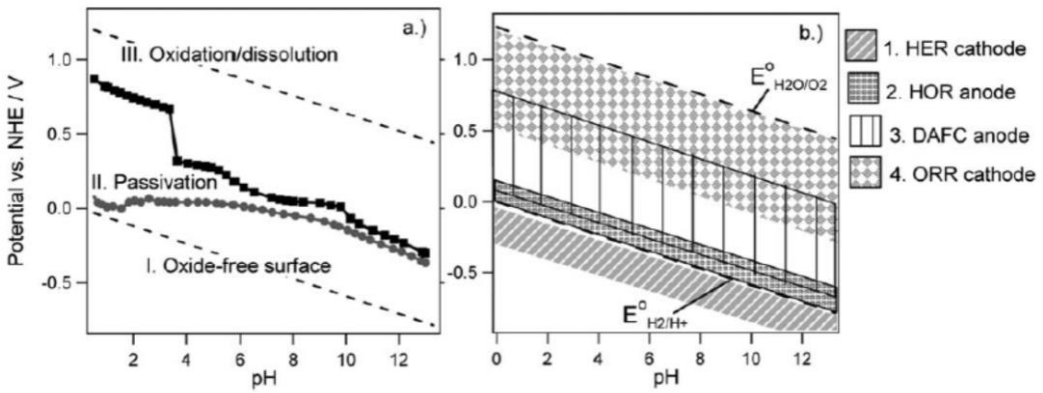

Figure 5 WC E-pH stability map and activity regions as suggested by Esposito[89]

The low surface area of many commercially available TMCs is also problematic when considering them as catalyst supports, WC-Alfa for example has 1.6 m^2/g[91] due to particle sizes of 10-30nm. A novel method for synthesis of TMC nanoparticles with sub 10 nm diameters has been developed using carbon foams as a base. This universally applicable method yielded particle sizes for V_8C_7, MoC and WC of 3.2, 4.9 and 8.4 nm respectively which were then covered with 3nm Pt particles.[92] Subsequent RDE tests found an enhanced activity toward ORR for each of these samples, although the stability of the foam for fuel cell conditions was not addressed. High surface area, 'clean' W_xC has also been produced via a 'polymer route' for the formation of W_2C microspheres for methanol oxidation[93] and WC single phase supports for Pt within the ORR. In this second case, a BET surface area of 89m^2/g was recorded alongside decreased solubility in acidic media. While the surface area measurements were promising, very poor electrochemical stability and low mass activity of Pt suggest that the lowering of C content may have negatively impacted the sample's performance as a catalyst.[91]

Apart from the core itself, application of the Pt shell must also be considered as the core effect will be shell thickness dependent. Methods for the introduction of Pt to TMCs are numerous in the literature; most commonly sputtering and physical mixing are utilised resulting in deposited Pt particle sizes in the range of 5-10nm. Direct reduction of Pt onto the surface as undertaken by Nie *et al.* resulted Pt/WC nanoparticles less than 10nm in diameter and improved activity for ORR in both acidic and alkaline solution. It also resulted in an onset potential 150mV more positive than that of Pt/C, whilst having halved the Pt loading. It was asserted this improvement was caused by high particle distribution and small Pt nanoparticle size although diameters of Pt nanoparticles were not reported due to difficulty in distinguishing between components in TEM images.[82] The geometry of the Pt particles being supported on the WC has also been investigated with novel Pt geometries such as dendrites exhibiting much high activities towards methanol oxidation than cubic Pt nanoparticles.[94]

Density Functional Theory (DFT) calculations showed that 1ML Pt on top of bulk WC markedly changed Hydrogen and Oxygen Binding Energies (HBE/OBE) to be similar to those of pure Pt, highlighting the possible utility of ML or core-shell systems of Pt-TMC. Pt MLs on WC thin film were also created experimentally via thermal evaporation. The HER activity of 1ML Pt/WC was found to be very close that of pure Pt, whilst a 30 ML Pt/WC system exhibited near identical performance to Pt_{bulk}. The core-shell arrangement was also observed to prevent WC oxidation during short term HER testing. Whilst long term durability tests would need to be undertaken, the initial results regarding the maintenance of the atomic ratio at the system surface were encouraging.[95] The testing of such ML Pt-WC foil catalysts for ORR however, revealed significantly lower activities than that of Pt_{bulk}. This lessened activity was suggested to have been caused by ML Pt dissolution or aggregation resulting in a loss of the synergic interaction and overall activity.[89]

Table 1 DFT calculated hydrogen and oxygen binding energies on WC, Pt and Pt ML/WC

Surface	HBE (kcal/mol)[89]	OBE (kcal/mol)[96]
Pt(111)	-10.8	-91.7
WC (0001)	-25.1	-173.2
1ML Pt-WC(0001)	-10.1	-92.9

Whilst Physical Vapour Deposition (PVD) can be used to deposit ML on planar single crystals, as a line-of-sight technique it is inappropriate for treatment of 3D powders. Atomic Layer Deposition (ALD) has been employed in attempts to cover both planar and powder samples. The ALD foils were observed to form from Pt islands and exhibited ORR activity comparable with that of Pt_{bulk}

after 20 ALD Pt cycles.[96] Subsequent use of oxygen as a co-catalyst led to the formation of thinner, although not ML, overlayers. This method was proposed as a viable means of producing core-shell particles on a commercial scale.[97] Recently Kido *et al.* produced Pt MLs on TiC powder using the Incipient Wetness Impregnation (IWI) slurry method. These overlayers were observed to be stable and have activity comparable with Pt/C_{black} for the HER whilst having greatly lessened the Pt loading.[98]

In conclusion there is still a large amount of research to be done in bringing Pt-TMC core-shell systems to PEMFC reality. Phase pure carbides with large surface areas must be synthesised and a reliable method of Pt ML deposition found which can lay down thin layers with precision. Concurrently with this research, increasing our understanding of the nature of Pt-core interactions, predicting stable core-shell arrangements and being able to better explain the enhancement observed for the Pt/TMC systems is essential in order to offer direction and rationalization for synthetic approaches.

1.3 Computational Catalyst Design

Having considered the experimental literature surrounding the subject, the computational methodology of the project must now be addressed. Recent developments in computational theory, capability, and our underlying understanding of surface interactions have made the screening and '*in silico*' design of catalysts possible. Theoretically evaluating system activity, stability, and selectivity saves time and money and can provide data not available via experiment.[99]

The aim of screening is to use quantum chemical methods to identify microscopic material properties which determine macroscopic performance, allowing the creation, evaluation and development of catalysts computationally. Density functional theory (DFT)[100,101] has been widely employed for this purpose due to its ability to efficiently produce accurate estimates of activity and stability for solid surface systems. Quantitative Structure Activity Relationship (QSAR) and descriptor methodologies have both been utilised in computational screening for catalysts[102] for a large range of application from ammonia production,[103]the HER,[104] and Near Surface Alloys (NSAs)[105] to materials for ORR.[106] These examples have all been surveys of bimetallic transition metal compounds which can be treated using the Universality Principle for reactions characterised as 'the activation of a diatomic molecule'.[107]

The Universality Principle states that there is a universal relationship between reaction activation energy, E_a, and the stability of intermediate states, ΔE, which in turn gives rise to a direct relationship between adsorption energy and catalytic activity. The linearity between E_a and ΔE is a Brønsted-Evans-Polanyi type relationship, [108,109] meaning from the plethora of possible calculated intermediate energies and transition state energies, the number of independent descriptors can be reduced to one or two without the introduction of errors greater than those native to DFT simulations.[110] In the creation of an optimal catalyst, low activation energies would be combined with weak intermediate binding to allow removal of dissociation products following the Sabatier principle.[60]Application of kinetic models then allows transformation of the linear adsorption energies into a volcano-plot against catalytic activity, positioning optimal systems close to the maxima. Appropriate descriptors must be chosen for each system as described by Nørskov,[111] in the case of the ORR the binding energy of atomic oxygen at the system surface may be used.[106]

The stability of multicomponent systems may also be considered computationally as exemplified by the work of Greeley *et al.*[104,105,106] For bimetallic systems four calculations were conducted to assess system stability: free energy change due to surface segregation, intrasurface transformations (island formation or dealloying), the free energy of adsorption of oxygen (due to its ability to poison the catalyst) and the likelihood of acidic environment mediated corrosion.

Whilst the d-band model has proven key in the prediction and explanation of TM property trends[57] such as adsorption strengths on alloys and binding strengths at defect sites, catalytic research is branching out to consider TM including compounds such as carbides, oxides and zeolites which provide different theoretical challenges. In addition to the difficulties DFT has in modelling some of these TM systems[112] (in particular Thoria, Ceria, Titania[113] and other TM oxides) due to short comings in the exchange-correlation functional and the delocalisation error,[114] the simple d-band-centre descriptor is not appropriate for explanations of activity in these materials. Nørskov *et al.* suggested that the deviation in the case of the TMCs may be attributed to the incorrect partitioning of electron-density; leading to the DOS projections including low energy C p-bands significantly decreasing the d-band centres. They also noted that the correlation of adsorption energy and d-band centre in the original model neglected band shape, and that the distortion of the bands upon interaction with C in the carbide would be expected to affect this relationship.[115]

Descriptors for carbides and other materials are being developed. Toulhoat *et al.* use Bond Energy Descriptors (BED) from bulk phase carbides, oxides and hydrides to explain and predict trends in activity. The BED were constructed from contributions to the cohesion energy of like and unlike atoms from within the bulk, differing from the pure TM systems previously discussed. The plotting of this BED against kinetic activity data produced a volcano-like relationship allowing selection of optimal solids for different applications from the maxima of the plots.[116] Upon further study of TMC surfaces, electronic surface states or surface resonances (SRs) have been observed to occur on the (111) facet through 'difference DOS plots' of surface and bulk data. Investigations into the nature of atomic adsorption on TiC and TiN have led to the suggestion of a Concerted-Coupling Mechanism (CCM) involving the interaction of the adsorbate with both the TMSR and CSR. The depletion of the TMSR upon adsorption provides proof of concept that surface-localised states are playing a key role in the adsorption process.[117] The mean energy of the TMSR, E_{TMSR}, has been identified as a descriptor for the system as it produces a linear correlation with E_{ads} values; the adsorption getting stronger as the value of the TMSR-centre increases.[118] This descriptor was also found to be applicable for molecular adsorption in extension of the scaling relationships frequently observed on TMs.[110]

1.4 Summary

In order for PEMFCs to meet the requirements necessary for widespread use in vehicles, Pt loading must be decreased whilst the stability and activity of the catalyst must increase. Core-shell nanoparticles are a promising solution exhibiting activities similar to or better than Pt_{bulk} with greatly lessened Pt content. TMCs such as WC and TiC have been identified as being stable in low pH environments and WC has been observed to form strong Pt-WC bonds enabling the possible formation of Pt ML and core-shell nanoparticles.

1.4.1 Research Question

The aim of the current project is to provide computationally rationalized suggestions for core choice in Pt/carbide core-shell systems. We seek to do this by firstly assessing the geometric and electronic factors which effect Pt ML formation and investigating if there is a wetting descriptor which characterises this behaviour. Secondly we wish to understand the synergic effect that Pt/TMC systems exhibit and use this knowledge to discern suitable core materials for the ORR.

Thirdly we wish to investigate the stability of these systems with regards to Pt agglomeration at the surface

2. Methodology

The following chapter seeks to give a brief introduction to the computational methods used throughout this research project. For a fuller treatment of the theories mentioned the reader is directed to Koch and Holthausen [119] or Sholl and Steckel's [120] introductions and the review by Payne.[121]

2.1 Electronic Structure Theory

Electronic structure theory describes where electrons are found in a system and what the energy of the system is as a result. The answer to these questions can be approximated in most cases by the solution of the non-relativistic, time-independent Schrödinger equation:

$$\hat{\mathrm{H}}\Psi = \Psi E \tag{1}$$

where $\hat{\mathrm{H}}$ is the Hamiltonian operator, Ψ is the wavefunction of the system and E the energy. For a system of M nuclei and N electrons, in atomic units, the Hamiltonian takes the form:

$$\hat{\mathrm{H}} = -\sum_{i=1}^{N}\frac{1}{2}\nabla_i^2 - \sum_{A=1}^{M}\frac{1}{2M_A}\nabla_A^2 - \sum_{i=1}^{N}\sum_{A=1}^{M}\frac{Z_A}{r_{iA}} + \sum_{i=1}^{N}\sum_{j>i}^{N}\frac{1}{r_{ij}} + \sum_{A=1}^{M}\sum_{B>A}^{M}\frac{Z_A Z_A}{R_{AB}} \tag{2}$$

Where M_A is the ratio of the mass of nucleus A to the mass of an electron and Z_A is the atomic number of nucleus A. In this equation the first two terms represent the kinetic energies of the electrons and nuclei respectively, the third term is the coulombic attraction between electron and nuclei and the last two terms the repulsive electron-electron and nuclei-nuclei interactions respectively.

Given that the mass of the nuclei is much greater than that of the electrons and thus their relative velocity much lower, it is a good approximation to consider the electrons moving in a field of fixed nuclei (this is the so called Born-Oppenheimer approximation), thereby allowing the separation of the electronic and nuclear components of the Schrödinger equation.

$$\hat{\mathrm{H}}_{ele} = -\sum_{i=1}^{N}\frac{1}{2}\nabla_i^2 - \sum_{i=1}^{N}\sum_{A=1}^{M}\frac{Z_A}{r_{iA}} + \sum_{i=1}^{N}\sum_{j>i}^{N}\frac{1}{r_{ij}} \tag{3}$$

By solving the electronic Schrödinger equation (3), the total energy of the system would be:

$$E_{tot} = E_{ele} + \sum_{A=1}^{M} \sum_{B>A}^{M} \frac{Z_A Z_A}{R_{AB}} \quad (4)$$

In order to fully describe the electrons in the system, spin must be introduced. This results in an electron being described with 3 spatial coordinates **r** and a spin coordinate ω, collectively written as **x.**

$$\mathbf{x}=\{\mathbf{r},\omega\} \quad (5a)$$

Thus an N electron system would be described with a wave function $\Psi(\mathbf{x_1},\mathbf{x_2}\ldots\mathbf{x_N})$. In order to obey Pauli's Exclusion Principle (1925), the wavefunction must also be antisymmetric with respect to the exchange of two electrons as shown in (5b).

$$\Psi(\mathbf{x_1}, \mathbf{x_2}, .., \mathbf{x_N}) = -\Psi(\mathbf{x_2}, \mathbf{x_1}, .., \mathbf{x_N}) \quad (5b)$$

The Hartree-Fock approximation, which allows the construction of the multi-electron wavefunction by creating a Slater determinant of single electron wavefunctions, notably maintains this antisymmetry.

In the course of a calculation, approximate wavefunctions must be assessed with respect to the actual groundstate wavefunction Ψ_0 and groundstate energy E_0 of the system. The Variational Principle states that the expectation value of the Hamiltonian of the trial wavefunctions $\langle\Psi|\hat{H}|\Psi\rangle$ will be the upper bound of the true energy E_0.

$$\langle\Psi|\hat{H}|\Psi\rangle \geq E_0 \quad (6)$$

Thus, if we minimise the functional $E[\Psi]$ until $\Delta E[\Psi]=0$ we obtain the true ground state Ψ_0 and will be able to calculate E_0. However, the complexity of solving this problem is immense.

2.2 Density Functional Theory

Density Functional Theory (DFT), the basis of the calculations presented in this work, developed as the result of the Hohenberg-Kohn theorems which draw a parallel between the electron density and the full wavefunction of a system.[100] The first of their assertions was that the groundstate energy of a system is a unique functional of the electron density of that system E[ρ(r)] such that:

(7) $$E[\rho(\boldsymbol{r})] = \int V(\boldsymbol{r})\rho(\boldsymbol{r})dr + F[\rho(\boldsymbol{r})]$$

where $\rho(r)$ is the electron density, $V(r)$ is the external potential applied by the nuclei and $F[\rho(r)]$ is a unknown universal functional including the electron interactions: the Hartree potential and the exchange and correlation terms. Thus we can calculate the E_0 from the groundstate electron density, a 3 dimensional problem, rather than considering the 3N dimensional full wavefunction. The total energy can now be written as a functional with two constituent functionals, one containing the known kinetic energy, coulomb interaction, electron repulsion and nuclei repulsion terms and a second combining all the unknown terms including the correlation function. This second term is the exchange correlation functional and must be approximated for in order to apply DFT.

The second Hohenberg-Kohn principle, akin to the Variational Principle, stated that the density which minimized the overall functional E is the true electron density, corresponding to the groundstate of the system. Applying the principle to equation 7 we gain the following:

(8) $$\langle \Psi' | \hat{F} | \Psi' \rangle + \langle \Psi' | \hat{V} | \Psi' \rangle > \langle \Psi | \hat{F} | \Psi \rangle + \langle \Psi | \hat{V} | \Psi \rangle$$

and so it follows that

(9) $$\int V(\boldsymbol{r})\rho'(\boldsymbol{r})dr + F[\rho'(\boldsymbol{r})] > \int V(\boldsymbol{r})\rho(\boldsymbol{r})dr + F[\rho(\boldsymbol{r})]$$

(10) $$E[\rho'(\boldsymbol{r})] > E[\rho(\boldsymbol{r})]$$

Building on these theorems, Kohn and Sham[101] developed one-electron equations for a fictitious non-interacting system which has the same density as the interacting system. Please see appendix A for a derivation of this theory.

(11) $$-\left[\frac{\hbar^2}{2m}\nabla^2 + V(\boldsymbol{r}) + V_H(\boldsymbol{r}) + V_{XC}(\boldsymbol{r})\right]\Psi_i(\boldsymbol{r}) = \varepsilon_i \Psi_i(\boldsymbol{r})$$

The three potentials on the left hand side of the equation define the coulomb interaction, the electron-electron repulsion (known as the Hartree potential) and the exchange correlation contributions. The Kohn Sham equations must be solved iteratively, starting from a trial electron density, to calculate the electron density of the system and then compare this new value to the initial one. Upon evaluation, the new density is accepted or rejected and mixed into the new

starting cycle in a self-consistent process which ends when no improvement to the electron density is made. Density mixing can be carried out in CASTEP using the Broyden or Pulay mixing schemes, and is employed to prevent charge sloshing from the output density change.

DFT has developed to allow the calculation of metallic systems since the presence of unoccupied states close to the Fermi level was problematic. Whilst in insulating systems the unoccupied bands have much higher energies than the Fermi level and so can be easily identified and excluded, in metals the removal of these bands using energy minimisation algorithms was inefficient. Instead, higher energy unoccupied bands must be included in the calculation ensuring the orthogonalisation to the lower energy bands was maintained. Since the cost of calculations increased with the number of bands included, the occupancies of the bands were calculated to ascertain which bands were important for the construction of the electron density. Given that real occupancies of 0 or 1 are discontinuous and so render the search algorithm unstable, smearing schemes were employed on the band energies to allow partial occupation. The entropic contribution to the energy could then be removed to retrieve the zero temperature result once the density had been constructed.

2.3 The Exchange Correlation Functional

As noted the exchange-correlation functional must be approximated for in order to solve the Kohn Sham equations. The first exchange correlation functional developed was the local density approximation (LDA) seen in equation 12a.

$$(12a) \qquad E_{xc}[\rho(\boldsymbol{r})] = \int \varepsilon_{xc}(\boldsymbol{r})\rho(\boldsymbol{r})d^3\boldsymbol{r} \quad \text{where} \quad \varepsilon_{xc}(\boldsymbol{r}) = \varepsilon_{xc}^{homo}(\boldsymbol{r})$$

Where the exchange correlation energy per electron in the electron gas $\varepsilon_{xc}(\boldsymbol{r})$ is equal to that in a homogenous electron gas of the same density. The functional is often split with the exchange contribution being accounted for using equation 12b from Dirac and Bloch whilst the correlation portion can be fitted from numerical data.

$$(12b) \qquad \varepsilon_x = -\frac{3}{4}\left(\frac{3\rho(\vec{r})}{\pi}\right)^{\frac{1}{3}}$$

Due to the spreading of electron density, this approximation overestimates binding energies and gives particularly poor results for systems with localised states. In some instances, due to the underestimation of bandgaps, it also produces results indicating that known semiconductors have metallic behaviour.[122]

The generalised gradient approximation (GGA) seen in equation 13 incorporated corrections to the LDA based on the gradient of local electron density.[123] This improved the GGA functional's binding and atomic energies and results in more realistic geometric data although over-correction of LDA values has been observed in some cases.

$$E_{xc}^{GGA}[\rho(\boldsymbol{r})] = \int F_{XC}(\rho, \nabla\rho) d\boldsymbol{r} \quad (13)$$

Within this group, functionals may be fitted to experimental data as in the case of BLYP where selected atomic data formed the basis of the exchange part to improve results for similar systems.[124,125] Another well-known GGA is the PBE functional, where the parameterisation of the functional is done using fundamental constants essential to the energetics of the system.[126] Revision of this method, via the alteration of the form of the local exchange enhancement factor, resulted in the RPBE which was chosen in the following thesis research due to its improved accuracy in the calculation of chemisorption energies .[127]

All DFT implementations are affected by the self-interaction error, the fact that when electron-electron repulsion is calculated an electron is in the potential field created by all the electrons in the system (including itself).[114] By including some exact exchange from Hartree Fock theory, hybrid functionals such as B3LYP[123] were created to improve this aspect of their performance. An alternative method of lessening self-interaction applies energetic penalties for the hybridisation of d or f orbitals, this is known as DFT+U.[128]

$$E_{xc}^{hybrid}[\rho(\boldsymbol{r})] = \int F_{xc}(\rho, \nabla\rho) d\boldsymbol{r} + 0.25 E_x^{HF} \quad (14)$$

2.4 Basis sets and Boundary Conditions

In order to run calculations of the type described here, electronic information about the system under consideration is needed. Finite basis sets, which are sets of functions that describe the electronic composition of atoms in the system, are combined to provide the initial density used in the Kohn-Sham equations. These basis functions can have different forms, such as the localised Gaussian or the plane-wave and can be minimal; containing the fewest functions needed to represent all the electrons in the atom, or more complete to enable more detailed consideration of the structure. The codes used in the current work employ plane-wave (CASTEP)[129] and real space basis sets (GPAW).[130]

Plane-wave basis sets are particularly useful when working with solid systems where a regular lattice defines the structure. Electrons travelling through the lattice will experience a periodically fluctuating potential due to the presence of the nuclei. This is expressed in Bloch's theorem (1928) as:

$$\Psi_r(\boldsymbol{r}) = f_k(\boldsymbol{r})\exp[ik \cdot r] \tag{15}$$

where $f_k(\boldsymbol{r})$ is a periodic function and $\exp[ik \cdot r]$represents an envelope of plane-waves with wave vectors k. The cell-periodic part can be expanded using planewaves whose wave vectors are reciprocal lattice vectors of the crystal:

$$f_k(\boldsymbol{r}) = \sum_G c_{\boldsymbol{k}+G}\exp[i\boldsymbol{G} \cdot \boldsymbol{r}] \tag{16}$$

The substitution of equation 16 into equation 15 therefore allows the electronic wavefunction to be described as a sum of planewaves. Since the wave vectors are unique only until the first reciprocal lattice vector, k, calculations need only consider the first Brillouin zone of reciprocal space to obtain the band structure of a repeating system. Within the Brillouin zone various schemes exist for the selection of sampling points. Throughout this work the popular Monkhorst-Pack approach was used with the k-point mesh decided following convergence tests on the bulk total energy.[131] An infinite number of plane-waves would constitute a complete basis, however to make calculations practical energy cut offs are applied to truncate the plane-wave expansion and set the size of the basis set.

2.4.1 The Pseudopotential Method

Plane-wave basis sets are commonly combined with pseudopotentials, which are approximate potentials used to replace the core electrons of a system. Modelling the all- electron system explicitly would require a large number of planewaves in order to fully describe the nodal behaviour of the valence wavefunctions in the core region. Instead, the core electrons and the strong core region ionic potential are replaced with a smooth pseudopotential and pseudo wavefunctions, see figure 6. The pseudopotential is designed so that outside the core region the pseudopotential and wavefunctions exactly match the actual potential and wavefunction and inside the core region the pseudopotential produces the same effect the ion and core electrons would have on the wavefunction whilst preventing the pseudo wavefunction from having nodes within the core region. The 'softer' or smoother this potential is, the fewer planewaves are needed

to describe the system and hence computational savings are made. In the current work, ultrasoft pseudopotentials of the Vanderbilt type were employed.[132]

Figure 6 Schematic of a pseudopotential (dotted), all electron potential (solid) and wavefunctions, reproduced from Payne[121]

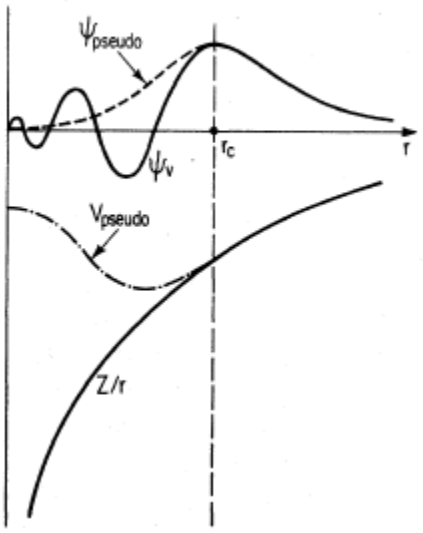

Due to their periodic nature plane-wave basis sets are commonly implemented in calculations with periodic boundary conditions. This is where a small section of a material is modelled and this unit cell is repeated around the original cell to produce an infinitely large system. In this 'tiled' system, if an atom moves through the cell wall on one side it will reappear at the other side travelling with the same velocity. This is useful for bulk systems and surfaces can be treated in this way providing sufficient vacuum distance is left in the direction perpendicular to the plane of the surface to prevent the interaction of the potentials. For molecular and cluster calculations however, non-periodic boundary conditions are preferable for efficiency's sake.

2.4.2 The Projector Augmented Wave Method (PAW)

An alternative to the pseudopotential method is the projector augmented wave method.[133,134] This is based on a transformation, $\hat{T}$, between pseudo wavefunctions $|\acute{\Psi}_n\rangle$ and the all-electron wavefunction $|\Psi_n\rangle$:

$$|\Psi_n\rangle = \hat{T}|\acute{\Psi}_n\rangle \tag{17}$$

The transformation operator is defined in expression 18 where ***a*** is a local contribution around each atom. The transformation maps a set of smooth pseudo partial waves, $|\acute{\phi}_i^a\rangle$, for each atomic valence state *i* to the all-electron eigenstates or all-electron partial waves $|\varphi_i^a\rangle$. These waves are

chosen to be identical outside of the 'augmentation sphere'- a certain value of *a* so that it is only the core region of the atom that is affected.

(18) $$\hat{T} = \hat{1} + \sum_{ai}(|\varphi_i^a\rangle - |\acute{\varphi}_i^a\rangle)\langle\acute{p}_i^a|$$

The third term in the expression represents the projector functions, within the augmentation sphere these functions are non-zero and with the pseudo partial waves form an orthonormal basis set, equation 19.

(19) $$\sum_i \langle \boldsymbol{r}|\acute{\varphi}_i^a\rangle\langle\acute{p}_i^a|\boldsymbol{r}'\rangle = \delta(\boldsymbol{r}-\boldsymbol{r}') \quad \text{where } \langle\acute{p}_i^a|\acute{\varphi}_i^a\rangle = \delta_{ij}$$

Within GPAW different basis sets may be used, either atomic orbital-like functions within LCAO mode or grid based wave functions within Finite Difference (FD) mode. In the first of these the pseudo wave functions $\acute{\Psi}(r)$ are expanded as linear combinations of atom-centered, localised basis functions $\Phi_{nlm}(r)$with coefficients $c_{\mu n}$.

(20) $$\acute{\Psi}(r) = \sum_\mu c_{\mu n}\Phi_\mu(r)$$

The atomic basis functions take the form of a spherical harmonics and radial functions where R^b is the position of nucleus **b**, and $r^b = r - R^b$

(21) $$\Phi_{nlm}(r) = \Phi_{nlm}\left(r^b + R^b\right) = \varphi_{nl}r^b Y_{lm}(\hat{r}^b)$$

The eigenvalue problem can then be defined in equation 22 which maybe be directly diagonalised.

(22) $$\sum_\nu H_{\mu\nu}c_{\nu n} = \sum_\nu S_{\mu\nu}c_{\nu n}\varepsilon_n$$

In the LCAO method the minimum basis set will include one atomic orbital-like function for each valence state of an atom. Extra radial functions can be added for each valence state to improve the quality and the basis set will also include a polarization function corresponding to 'the lowest unoccupied angular momentum quantum number'. The use of the atomic orbital-like functions significantly reduces the computation time although accuracy is significantly affected by the completeness of the chosen basis set. The density and potential are still represented on the real-

space grids and so in this case the calculation time will be dominated by these calculations and not operations on the wavefunctions.

Within the FD method, the pseudo wave functions are represented on real space grids, these values are initially set using an LCAO basis chosen by the user. Finite difference stencils are then applied to the grid to enable the calculation of the gradient at a point from the data of the surrounding points.

The implementation of the PAW method on real space grids within GPAW improves calculation parallelisation and increases the speed of solving the Kohn-Sham and Poisson equations via use of multi-grid algorithms. Use of real space grids also allows for flexible boundary conditions so systems can be treated more sympathetically to their structure. Whilst these are significant improvements over existing implementations of other basis sets, the GPAW method does require 10 times the memory of a plane-wave implementation to describe a wavefunction to the same degree.

In the following thesis, geometry minimisation calculations form the basis of our study of adsorption characteristics. This optimisation process is iterative; after the initial ionic positions are set, electronic minimisation occurs and the Hellmann-Feynman forces within the unit cell are calculated. The atomic forces are compared to a predefined maximum and, depending on whether they meet the standard, a new set of ionic positions are generated and the process repeated. At the end of the second iteration the change in energy between the iterations, the atomic forces and the change in atomic positions are evaluated with regard to pre-set tolerances and the process can repeat until convergence is attained. In CASTEP the geometry minimisation scheme used was the BFGS algorithm which searches local configuration space to locate geometric minima close to the initial starting structure.[135] The BFGS method relies on the first derivative of the energy of the ions which is given by the Hellmann-Feynmann forces.

2.5 Electronic Structure Analysis

To consider the effect of electronegativity in a system and begin to assess bond character, charge density analysis is crucial. Two commonly used methods are Mulliken and Bader analysis, the first concerns population density in electronic orbitals whilst the second considers charge density

distribution.[136] In the case of Mulliken analysis,[137] values from the density matrix of the basis set (usually localised Gaussian type orbitals) are given to the atoms they represents in the system. This method is sensitive to basis set type and is unable to represent metals and other systems where there is a degree of electron delocalisation.

Bader analysis[138] requires segregation of the charge density into atomic basins. Having defined the points along the bond with the least charge density as 'critical points', paths which follow the most rapid decrease in charge density are mapped out. The surface created by these paths is described as having 'zero flux' as the gradient of change in charge density is zero, and provides the boundary between the basins. The atomic regions are then integrated and the charges assigned to the atomic nuclei within them. It is also possible to conduct a more complex analysis of the critical points and their associated density and Lapalacian, this can give insight into the strength and nature of the bond in question although sometimes this is not trivial.[139,140]

Density of states analysis will also be carried out on a wide range of the systems calculated. This method assesses the number of states which are available for occupation at a given energy for the system. States below E_f are filled and those above E_f are unoccupied. Deconvolution of the states by spin channel is possible as is the projection of the states for the s- p- and d-bands enabling identification of the bands most involved in bonding interactions. In the current work optics calculations were run within CASTEP following the geometry optimisation of the systems. The population and 'pDOS weights' were calculated and the resulting output files submitted to LinDOS[141] for the calculation of partial DOS values.

The vast majority of the work conducted in this thesis uses DFT as explained in this chapter. The theory surrounding other methods used briefly in the work will be touched upon in chapter 7

3. Carbide Materials

3.1 Introduction to Carbide materials

Carbide compounds are composed of carbon and metals or metalloids with a lower electronegativity. The bonding of the carbides has been described as having covalent, ionic and metallic character which vary dependent on the metal component used.[142] They are found to form across the periodic table with 'salt-like' carbides formed with the alkali metals, interstitial or intermediate carbides formed with the transition metals and covalent carbides formed with silicon and boron. The interstitial and covalent carbides are refractory materials exhibiting high melting points and extreme hardness[143] as well as excellent conductivity, both electrical and thermal, and corrosion resistance.[144,145] Carbides of group IV and V metals favour MC stoichiometries and form face centred cubic (fcc) materials similar to NaCl with the smaller C atoms fitting into the close packed metal lattice.[49] A variety of stoichiometries and structures are known for WC[146] and SiC[147] however for the purposes of this study 1:1 stoichiometries were selected. Fcc and hexagonal close packed (hcp) WC were included to enable the comparison of behaviour arising from altered structure and β or 3C-SiC[148] was included for a non-transition metal comparison.

The introduction of the C into the metal lattice results in increased electron density at E_f causing the similarity to Pt,[149]which was earlier noted for WC by Levy and Boudart.[81] The 'Pt-like' nature of the TMCs is observed in their reactivity: ethylene on TMCs, for example, forms CCH_3 intermediates instead of dissociating to atomic C and H as would occur on the pure TM. The modified surface activity witnessed more resembles Pt than the TM parent metal. Levy and Boudart highlighted WC's ability to perform PGM specific tasks such as the oxidation of H_2 to form water and the reduction of WO_3 with moist hydrogen,[81] and TMC catalysis of C-H bond transformations in dehydrogenations and isomerisations are also well known.[150]

3.2 Bulk Carbide Calculations

Here we present our bulk and surface carbide models and discuss their structural and electronic properties with reference to the literature.

3.2.1 Computational Methodology

The bulk carbides unit cells were modelled in the Atomic Simulation Environment (ASE)[151] from literature lattice values. Calculations were carried out using density functional theory (DFT) as implemented in the plane-wave code CASTEP.[152] Ultrasoft pseudopotentials[132] were used throughout and the exchange-correlation included using the generalized gradient approximation[126] in the RPBE functional.[127] Following convergence testing a Monkhorst-Pack grid [131]of 10x10x10 k-points was used to sample the Brillouin zone and an energy cut off of 340eV used for the plane-wave expansion. The Pulay mixing scheme[153] was chosen for incorporation of calculated electron density into the SCF cycle in which the electronic energy convergence criteria set at $5x10^{-7}$ eV per atom. Geometry optimisation of the cell was carried out using the BFGS method[135] with a maximum force tolerance of $0.05eVÅ^{-1}$, a stress tolerance of 0.1 GPa and an energy tolerance of $2.0E^{-5}$ eV/atom. Charge density analysis was carried out using Bader[138] analysis in the Topology code[154] and projected density of states calculations were conducted using LinDOS.[141]

3.2.2 Bulk Geometry and Charge Transfer

The modelled bulk systems were found to describe the known features of the carbides well. The calculated lattice parameters (table 2) displayed good agreement with both experimental and theoretical values from the literature. The maximum deviation from X-ray crystallographic data was +2.5% whilst agreement with the GGA theoretical values was generally within 1%.

Table 2 Bulk carbide properties including lattice parameter, metal electronegativity on the Pauling scale[155],χ, charge transfer from the metal, the gap between valence and conduction band centres,Δ, and the d-band centre E_d

Material	Calculated Lattice Parameter (Å)	Literature Lattice Parameter (Å)	Metal χ	Net Bader Charge (e)	Net Mulliken Charge (e)	Δ (eV)	E_d (eV)
TiC	4.37	4.33[a](4.33)[f]	1.5	1.64	0.68	5.68	0.12
NbC	4.50	4.47[b](4.49)[f]	1.6	1.66	0.7	6.50	-1.38
TaC	4.57	4.46[b](4.48)[f]	1.5	1.76	0.74	6.78	-0.44
WC (hex)	2.93, 2.85	2.91, 2.84[c](2.92,2.84)[g]	1.7	1.40	0.6	8.45	0.54
WC (cubic)	4.39	*(4.38)[f]	1.7	1.64	0.69	6.80	-2.29
SiC-β	4.37	4.36[d](4.39)[h]	1.9	3.03	1.24	10.02	-
Pt	4.01	3.92[e](4.02)[i]	2.2	-		-	-2.46

*experimental data unavailable. References: a[156], b[157], c[158], d[159], e[160], Theoretical values in brackets: f[142], g[97], h[161],i[162]

The lattice parameters of the carbides were observed to increase with the metal's atomic[163] and covalent radii[155] down the groups of the periodic table as seen in figure 7. The smaller WC lattice parameter value is due to the Lanthanide contraction reducing the atomic radius of W. SiC was observed to deviate from this pattern as Si is not a transition metal and has a much small atomic and covalent radii due to the lack of d-electrons and the shielding of the nucleus which they provide. SiC is covalently bonded, accounting for the reduced atom-atom distances and lattice parameter.

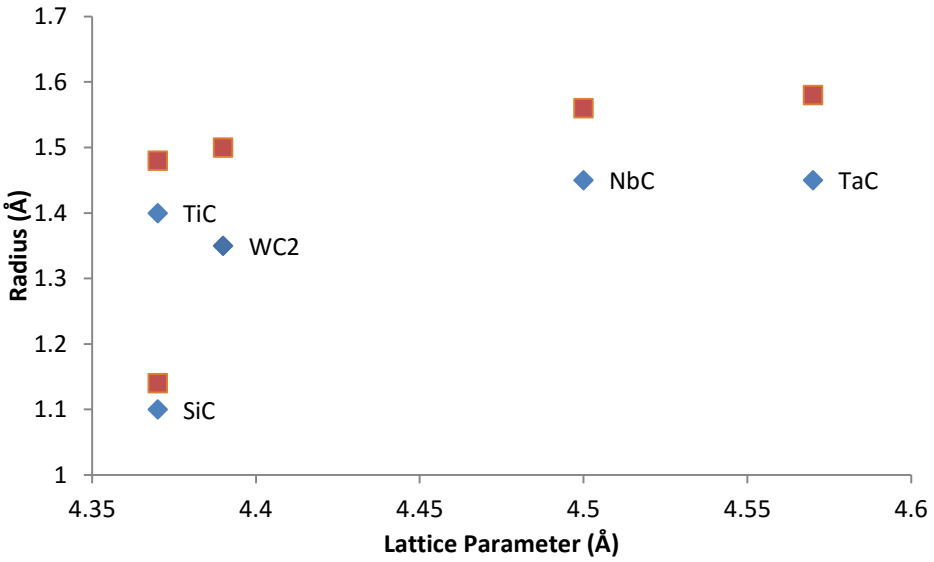

Figure 7 Plot of cubic carbide lattice parameters versus the atomic (blue diamond) and covalent (red square) radii of the parent TM

Topological analysis of the electron density revealed charge being transferred from the metal to the carbon in each of the materials, due to the higher electronegativity of carbon (2.55 on the Pauling scale). For the early transition metals, charge transfer was observed to increase down the group as the electronegativity of the metals decreased. Along the period from Ta to W the charge transfer decreased. For the fcc carbides this trend has been used to assign differing degrees of ionic character to the bonding. [142] Differences in charge transfer were noted between the two crystal structures of WC suggesting that the hexagonal form of WC is more covalent than the cubic given the lessened degree of transfer. The SiC was again very different from the TMCs as it exhibited double the charge transfer indicated in the other compounds. While this was unexpected, the same trend was also observed using an alternative charge partitioning method (Mulliken analysis[137]) suggesting that the phenomenon is not due to a miss-assignment of density to the different atoms and adding credence to result. In the literature, whilst the covalent nature of the compound is well known, calculations for the degree of electron transfer have varied widely with 0.89 electrons[164] and 1.4 electrons [165] being two theoretical examples.

3.2.3 Bulk Carbide Electronic Structure

The electronic structures of the bulk carbides were studied to identify periodic trends amongst the carbides and shed more light on the bonding present in each of the systems. The density of states (DOS) plots shown in figure 8 include partial density of states (pDOS) values for the TM d-band and C p-contributions.

The DOS of the TMCs are comprised of a low lying band at or below -10eV which consists mainly of C s- and TM d-overlap, a filled bonding valence band below E_f and an empty or partly filled antibonding conduction band at or above E_f. The valence band was observed to contain a large amount of TM d- and C p-overlap whilst the conduction band was dominated by empty TM d-states. At E_f the TMC were also characterised by a non-vanishing DOS between the valence and conduction bands.

Figure 8 Density of States (DOS) and partial DOS (pDOS) plots for the bulk carbides a) TiC, b) NbC, c) TaC d)fcc WC e) SiC and f) hcp WC

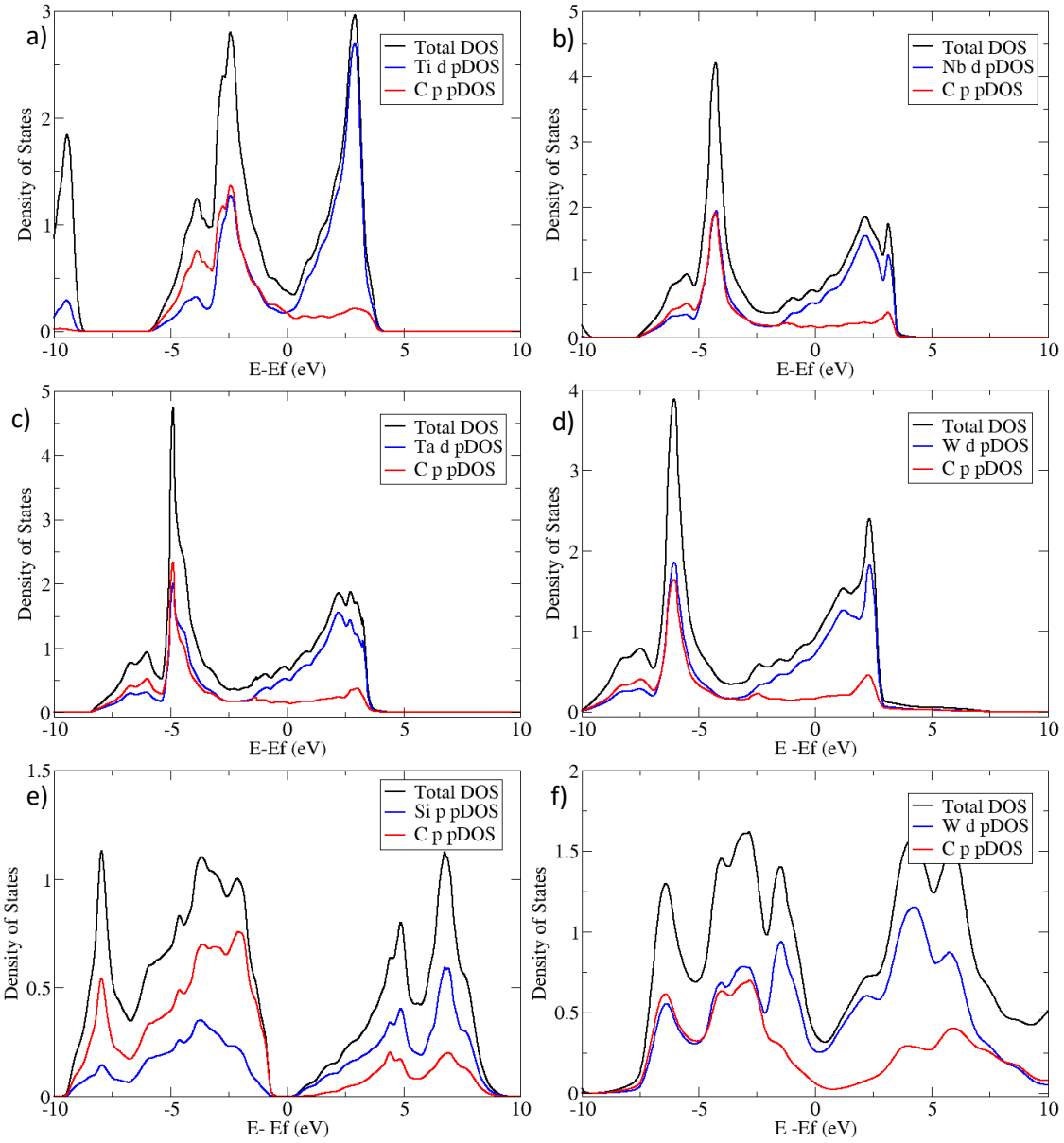

As the d-band filling increased moving across the period, both the conduction and valence bands were shifted negatively in energy resulting in an increased number of states at E_f, and improved conductivity. The gap between the valence and conduction band centres (Δ) increased going down the series from TiC to Nb to Ta signifying a widening in the bonding anti-bonding splitting which is indicative of the compounds' stability.[145] The smaller Δ observed for the cubic WC confirms its relative instability as unfavourable filling of the anti-bonding orbitals was observed.[146]

The hexagonal WC DOS also exhibited valence and conduction bands connected by a 'pseudogap' at E_f. It was similar to TiC in terms of the positioning of the bands with regards to E_f, although with

a much larger Δ value confirming its stability with regard to cubic WC. Unlike in the fcc TM carbides, hexagonal WC was observed to have much broader bands suggesting more electron delocalisation and supporting the assertion of more covalent bond character indicated by the Bader analysis. The E_d of the hexagonal WC was positive due to the higher energy position of the conduction band; this again made it more reminiscent of TiC than the cubic WC.

The electronic structure of SiC differed from that of the TM carbides as it is a semiconductor. Excellent overlap was noted between the C and Si p-bands as expected for a covalent compound with C contributions dominating the valence band and unfilled Si p-states the conduction band. Δ was once again very large as the conduction band was well separated from E_f. The calculated value of the band gap was 1.42 eV which is significantly less than the literature value of 2.39eV.[166] The discrepancy was caused by the oft-cited self-interaction error due to the approximate nature of the GGA exchange correlation functionals, which can lead to band gaps being underestimated.[167]

We confirm therefore that ionic and covalent contributions are indeed present in the bonding of the carbides as evidenced by the charge transfer and DOS data shown. The ionic contributions were seen to increase down the group with decreased electronegativity whilst along a period, filling of the d-band resulted in lowering of the d-band and better overlap with the C 2p states thus resulting in greater covalence. These findings are in agreement with Viñes *et al.*[145] and Vojvodic *et al.*[142]

3.3 Carbide Surface Calculations

After optimisation of the bulk properties, the (100) and (111) surfaces for the cubic systems and additionally the (0001) and $(10\bar{1}0)$ surfaces for the hexagonal system, were cut in ASE (figure 9).[151] 2x2 unit cells were used for the (111) type surfaces and 1x1 for the (100) surfaces. A Monkhorst-Pack grid of 5x5x1 was applied to each of the surfaces whilst all other tolerances were maintained as before. Slab depths were converged to give surface area energies consistent to 0.02 eV and a vacuum distance of 10Å was included to prevent interference between repeated images under periodic boundary conditions.

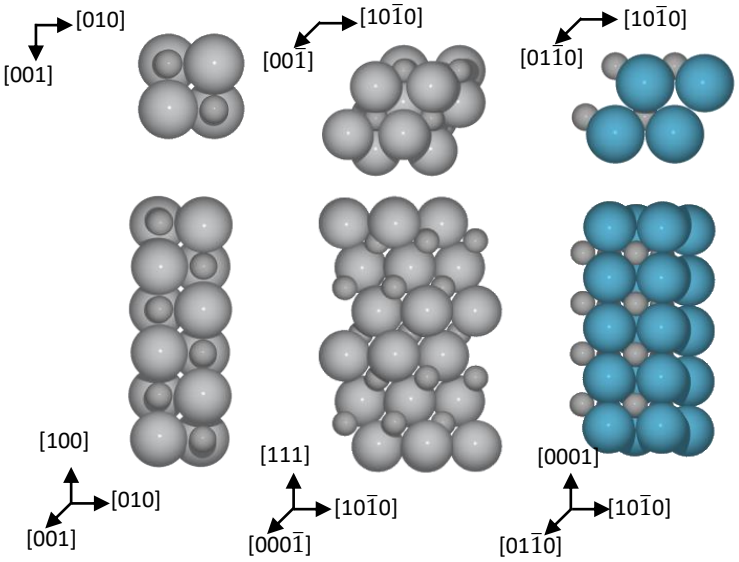

Figure 9 Top and side views of the cubic (100) and (111) surfaces and the hexagonal (0001) surface

Symmetrical double-sided slabs with fixed centre layers were used for the calculation of the surface energies to prevent the creation of a surface dipole. Both carbon and metal rich surfaces are accessible experimentally, therefore a selection of C terminated surfaces were included in our dataset although they are thought to provide less stable metal anchoring.[168] Having calculated the surface energies, single-sided slabs were cut and optimised for adsorption tests. For fcc-(111) surfaces a minimum of five carbide bilayers were used and for fcc-(100) a minimum of three bilayers with the back bilayer in each case constrained to bulk lattice positions. Whilst there are a number of surface reconstructions known for SiC,[147] herein we only considered idealised terminations to facilitate comparison with TM carbide structures.

Surface energies (E_{surf}) were calculated using equation 23. Where E_{system} is the energy of the calculated surface slab, n is the number of units within the system, E_{bulk} is the energy of a TMC unit in the bulk, E_c is the energy of a unit of graphene, E_X is a unit of bulk metal or Si and A is the surface area.

(23) $$\boldsymbol{E_{surface} = \frac{E_{system} - (nE_{bulk} + nE_C + nE_X)}{2A}}$$

3.3.1 Surface Geometry and Relaxations

TMC surfaces are well known to relax, undergoing changes in inter- (relaxation) and intralayer ('rumpling') distances, see figure 10.[144,145,115] The fcc-(111) surfaces exhibited a significant surface contraction of first interlayer spacing whilst the interlayer spacing of the second layer was increased with regard to the bulk value.[117] These alternating 'positive-negative' changes reduced in magnitude as depth increased. The fcc-(100) surfaces 'rumpled', denoting a change in TM-C spacing in the surface layer, the magnitude of associated interlayer changes were typically less than 10%. These effects were seen across the whole spectrum of TMCs. Inclusion of these effects in calculations has been highlighted as crucial in the calculation of exact surface energies, the error induced by neglecting such relaxations is in the order of 10-15%.[145]

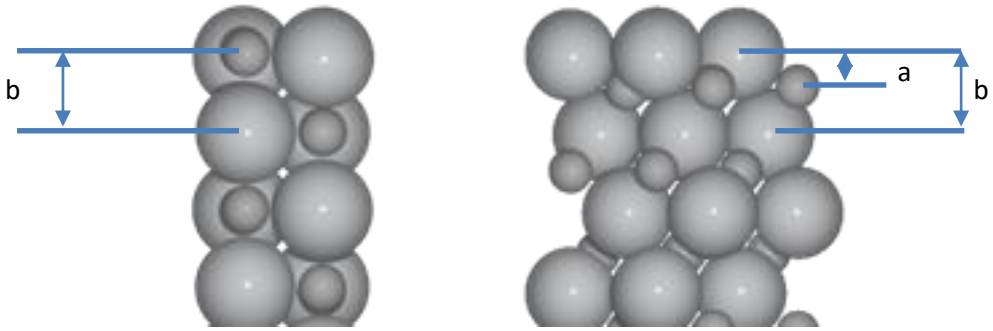

Figure 10 Schematic diagram of a) intralayer and b) interlayer distances in the different surfaces

As seen in Table 3 the fcc-(100) surfaces were the most stable for the fcc carbides. This observation can be rationalised via the bond-breaking model due to the strength of the M-C bonds and the number of these bonds broken to create the (100) and (111) surfaces (1 and 3 respectively).[169] In cases where carbon terminated as well as metal terminated surfaces have been calculated, the carbon terminated surfaces were significantly less stable than their metal counterparts.

The fcc-(111) surfaces were seen to experience alterations of 10-25% in excellent agreement with literature values.[117] For materials where C and TM terminated surfaces were calculated, the C terminations exhibited a much greater degree of contraction as the C atoms were drawn towards the bulk to minimize the surface energy. In the case of hexagonal WC, less contraction was noted for the hcp-(0001) surface[170] than the fcc-(111) surfaces and the hcp-($10\bar{1}0$) surface was observed to expand into the vacuum layer rather than contract as in the other cases.

The SiC surfaces exhibited smaller variations from the bulk than the fcc surfaces, although greater contraction of the C terminated surfaces was still observed. Due to the previously mentioned propensity of SiC to undergo surface reconstructions, comparative experimental SiC data has not been highlighted, however the LEED values for the TMC surfaces in Viñes are in good agreement with our findings. Throughout the dataset, first layer contractions were much greater than those in subsequent layers and bulk layer values were restored within 3 bilayers. For the fcc-(100) surfaces where C and TM were present at the surface it was noted that TM atoms were drawn into the surface whilst C atoms moved away from the bulk to produce the rumpling effect in agreement with Viñes.[145]

Table 3 Carbide surface energies, % change of intra- and interlayer distances and surface iconicity (charge relative to the neutral atom). Intra-layer distances for (100) show TM-C values

Surface	Energy (Jm^{-2})	Intralayer change (%)	Interlayer change (%)	TM charge (e)	C charge (e)
TiC(100)	1.48	-2.1	-0.7	1.64	-1.58
NbC(100)	1.12	-7.7	-4.4	1.61	-1.59
TaC(100)	1.19	-4.8	-1.2	1.66	-1.61
WC($10\bar{1}0$)hc	4.16	12.7	0.5	0.92	-1.40
WC(100)fcc	0.51	-6.2	-7.5	1.53	-1.49
SiC(100)	2.64	-2.0	0.5	1.53	-3.08
CSi(100)	3.24	-12.9	-7.0	3.10	-1.69
Pt(100)	1.72	-	-2.1	-	-
TiC(111)	3.90	-16.1	-2.7	1.10	-1.81
NbC(111)	1.28	-15.4	-4.8	0.94	-1.72
TaC(111)	1.64	-11.7	-5.4	0.98	-1.81
WC($11\bar{2}0$)hc	4.39	0.7	0.2	-	-
WC(0001)hcp	3.17	-4.5	-1.4	0.67	-1.34
WC(111)fcc	2.07	-20.3	-8.1	0.86	-1.63
CW(111)fcc	3.03	-24.3	-6.0	1.70	-0.98
SiC(111)	2.57	-0.4	2.0	0.77	-3.1
CSi(111)	4.09	-12.8	-12.9	2.98	-0.84
Pt(111)	1.40	-	1.1	-	-

3.3.2 Electronic Structure Analysis

In addition to the geometric alterations imposed by surface relaxation, variation in charge transfer was noted between the bulk and the top-most layers of the carbide surface. Upon cleaving the surface, 'dangling bonds' were created where TM-C interactions would have taken place. The electron density at these points was partially redistributed throughout the surface layer to minimize instability. A significant loss of electrons from the surface TM

to the subsurface C layer (just under half the bulk value) was noted for the fcc-(111) surface bilayer. This was expected as the electronegativity of C is much greater than that of the TMs and so the extra density left on the TM was subsumed. For the C terminated (111) surfaces, the topmost C layer exhibited much less accumulated charge than later C layers as it only had one set of TM to draw electrons from. In these cases, the first TM layer was observed to give-up more charge to compensate for this lack of electrons in the surface layer. The fcc-(100) first layer showed little charge alteration in comparison with the bulk as both carbon and metal atoms are present in each layer. The hexagonal WC exhibited a greater loss of TM charge density at the surface than the fcc WC although a similar degree of charge accumulation to the fcc WC was observed in the C layers.

The SiC(100) surfaces showed marked electron transfer difference in their first layer with the topmost component losing half of its bulk charge value. For the SiC(111) surfaces the changes were even more stark due to the loss of electrons from the covalent bonds which would have been formed had the material continued in the z direction. As noted for the geometric alterations, bulk charge values were restored across our subset of studied carbides upon reaching the third bilayer. The surface charge density behaviours of TM terminated fcc-(111) carbides described here are in good agreement with the work of Vojvodic.[117] The data for the top two bilayers of relaxed carbide surfaces are shown in chapter 4 tables 6 and 7 alongside the Pt adsorption data.

DOS diagrams for the carbide surfaces can be seen in figures 11-13. The fcc-(111) surfaces shown on the left-hand side of figure 11 share some common characteristics with the bulk carbides previously discussed. Low lying bound states were observed at or below -10 eV, a filled valence band was observed below E_f and at and above E_f the conduction band was dominated by TM states. In comparison to the bulk DOS of figure 8, the surface valence bands have finer structure at the shoulder seen at lower energies and contain more C density as was suggested by the charge transfer results. The conduction band was observed to be much wider than in the bulk material and was structured in three parts. As d-band filling increased, the conduction bands were shifted negatively in energy towards E_f and became partially filled which may have been due to the surface contraction resulting in better orbital overlap and the subsequent shift of the bands. Due to this shifting of the conduction band the pseudo-bandgap was lessened which may have caused the higher surface energies observed for these slabs.

The fcc-(100) DOS on the right hand side of figure 11 also show the low lying bonding band, the valence band below E_f and the conduction band. The valence band was widened comparative to the bulk materials and shifted positively in energy towards E_f. Since the rumpling effect on the surface (where the surface C atoms move out of the plane of the surface) resulted in greater C-TM bond lengths the orbital overlap was reduced which led to a destabilization of the bonding states.[145] Unlike the fcc-(111) DOSs, the fcc-(100) valence bands are comprised of almost equal TM and C contributions, following the lessened degree of charge transfer observed earlier.

In comparison, the C terminated fcc-(111) surfaces seen in the top row of figure 12 were dramatically positively shifted resulting in increased DOS at E_f. In the case of CTi(111) the shift resulted in the valence band crossing E_f and being only partially filled whilst for CW(111) the dramatic reduction of the pseudogap resulted in a delocalised DOS suggesting more covalent bonding at the surface. The hexagonal WC surfaces also displayed broadened DOS for the bonding and antibonding bands with undiscernible pseudogaps for the WC(11$\bar{2}$0) and WC(10$\bar{1}$0) systems. For the WC(0001) surface, which is comparable to the fcc-(111) in its appearance, the TM:C ratio below E_f was even in keeping with the lessened degree of charge transfer observed. Above E_f the DOS was still dominated by unfilled TM states although the C terminated CW(10$\bar{1}$0) surface was observed to contain a high degree of C character at E_f.

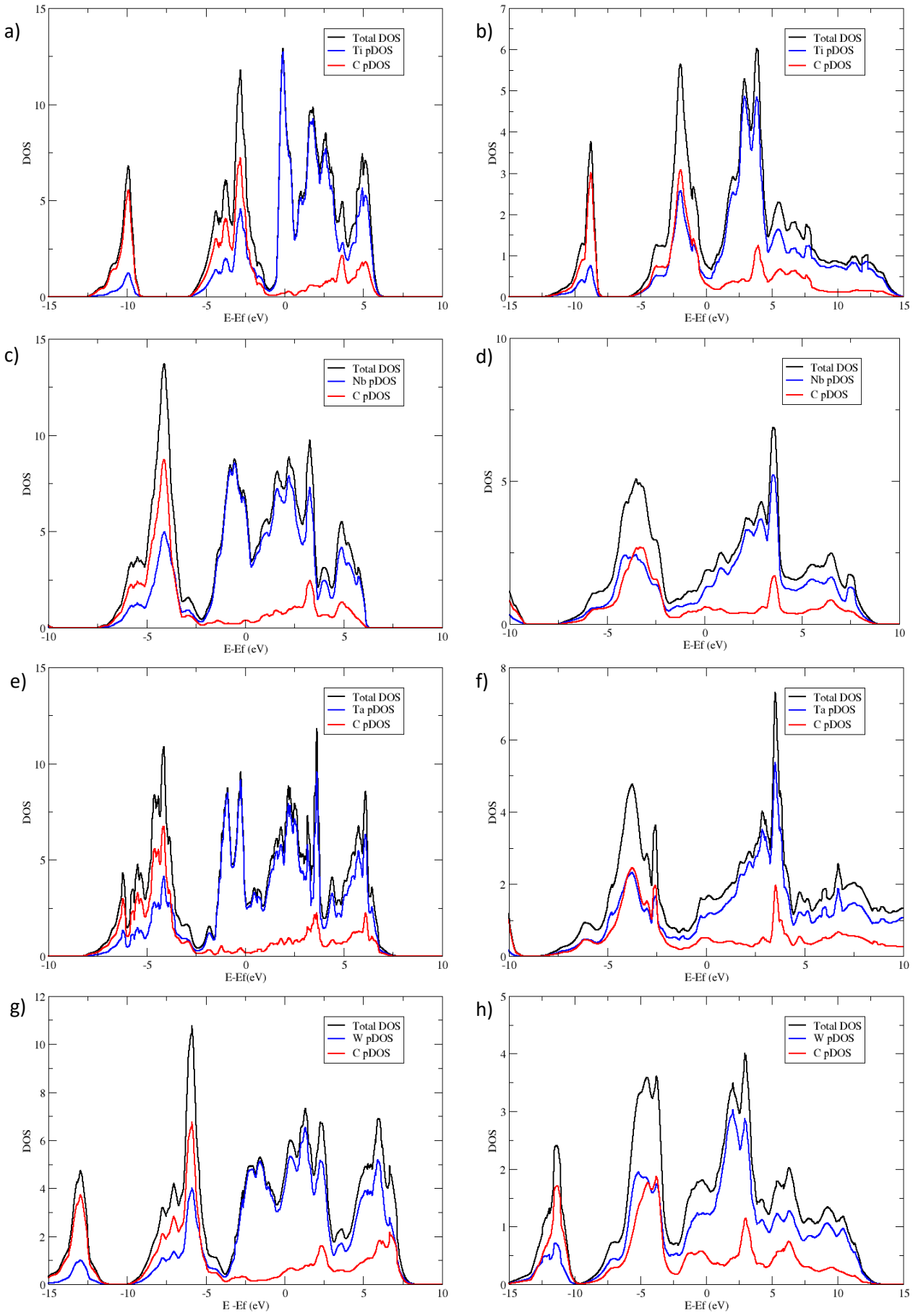

Figure 11 DOS plots of fcc carbide surface bilayers a) TiC(111), b) TiC(100), c)NbC(111), d) NbC(100), e)TaC(111), f)

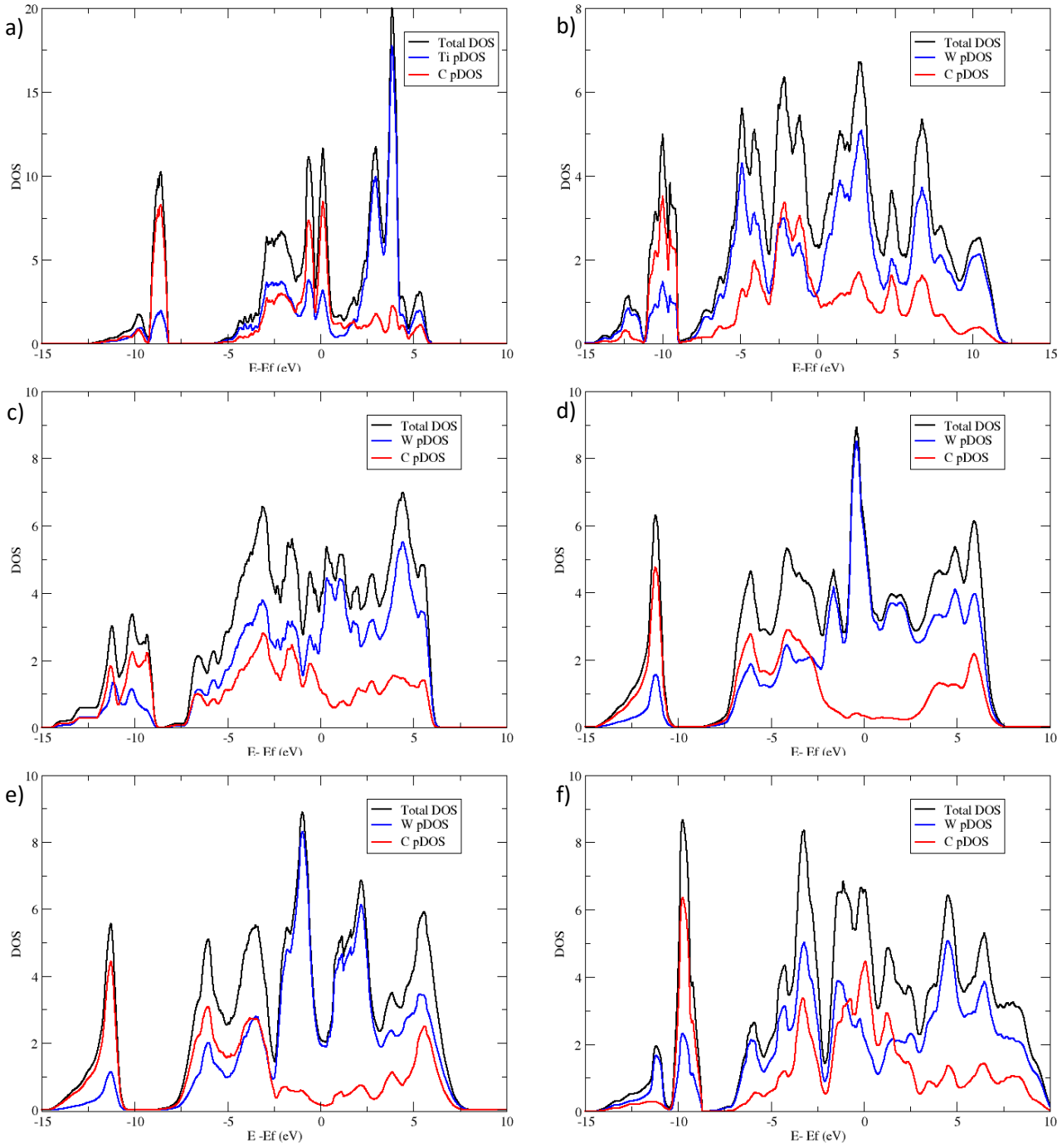

TaC(100), g) WC(111)fcc and h) WC(100)fcc

Figure 12 DOS plots of surface bilayers, a) CTi(111), b) CW(111)fcc, c) WC(11$\bar{2}$0) hcp, d) WC(10$\bar{1}$0) hcp e) WC(0001) hcp and f) CW(10$\bar{1}$0) hcp

The SiC surface DOSs shown in figure 13 displayed broadened bands in comparison with those of the bulk material in figure 8. Whilst bulk SiC had a clear bandgap at E_f and was designated a semi-conductor, the SiC surfaces exhibited differing characteristics at E_f. SiC(111) was observed to have Si density present at E_f whilst the C terminated CSi(100) displayed a discrete DOS peak of TM density just above E_f. Whilst the SiC(100) valence band

was mostly constructed of C contributions, due to the charge transfer from the surface Si atoms noted previously, the CSi(100) surface was more evenly constructed below E_f.

Figure 13 DOS plots of SiC surface bilayer a) SiC(111), b) SiC(100) and c) CSi(100)

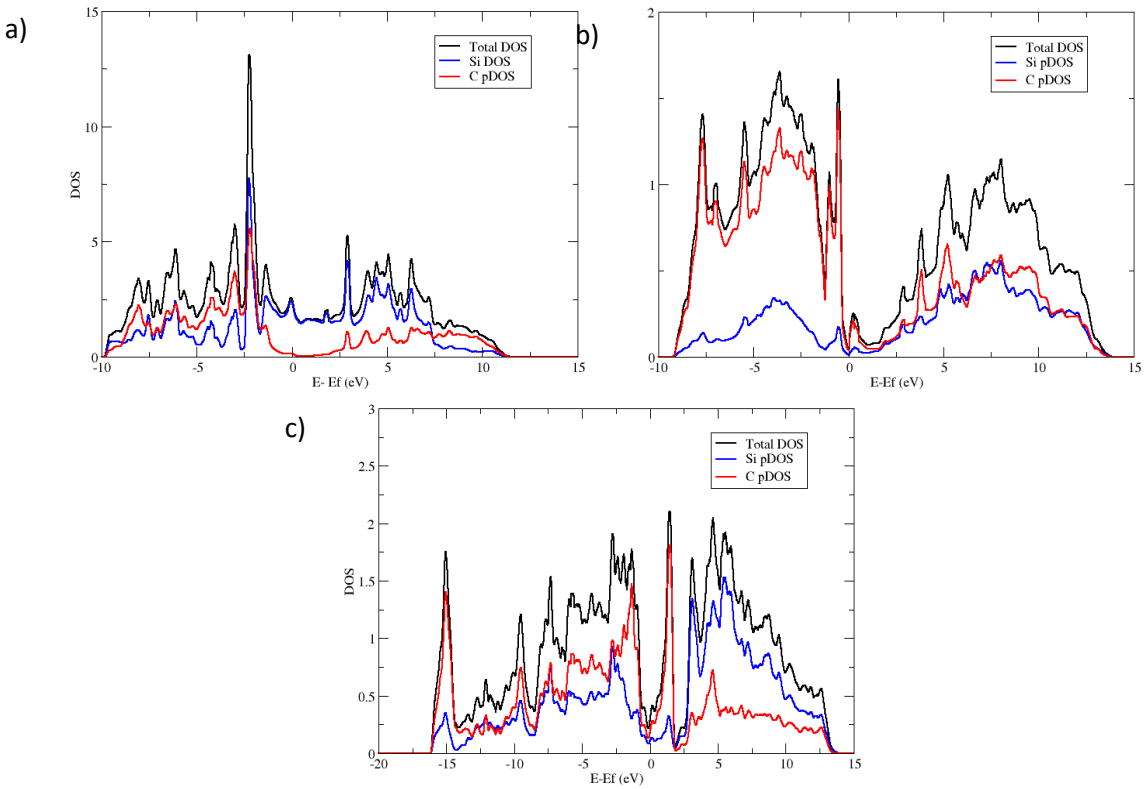

Surface specific electronic structure contributions of the carbides were found upon subtracting the bulk DOS from the calculated first bilayer DOS as shown for the fcc carbide surfaces in figure 14. The positive peaks represent surface resonances (SR), or accumulations of density. For the fcc-(111) surfaces at or around E_f a resonance with mainly TM nature was observed, whilst below E_f in the valence band a mixed TM-C resonance was found and lower still in energy, a C resonance was seen. Since the C resonance was low lying and contained significant core s- and p-contributions it was assumed not to play a significant role in the activity of the surface and so will not be described further.

The TMSRs are highlighted in blue for ease of identification. As observed in the bulk DOS, with increased d-band filling the valence and conduction bands of the surface shifted negatively in energy, leading to the same shift being observed for the TMSRs.

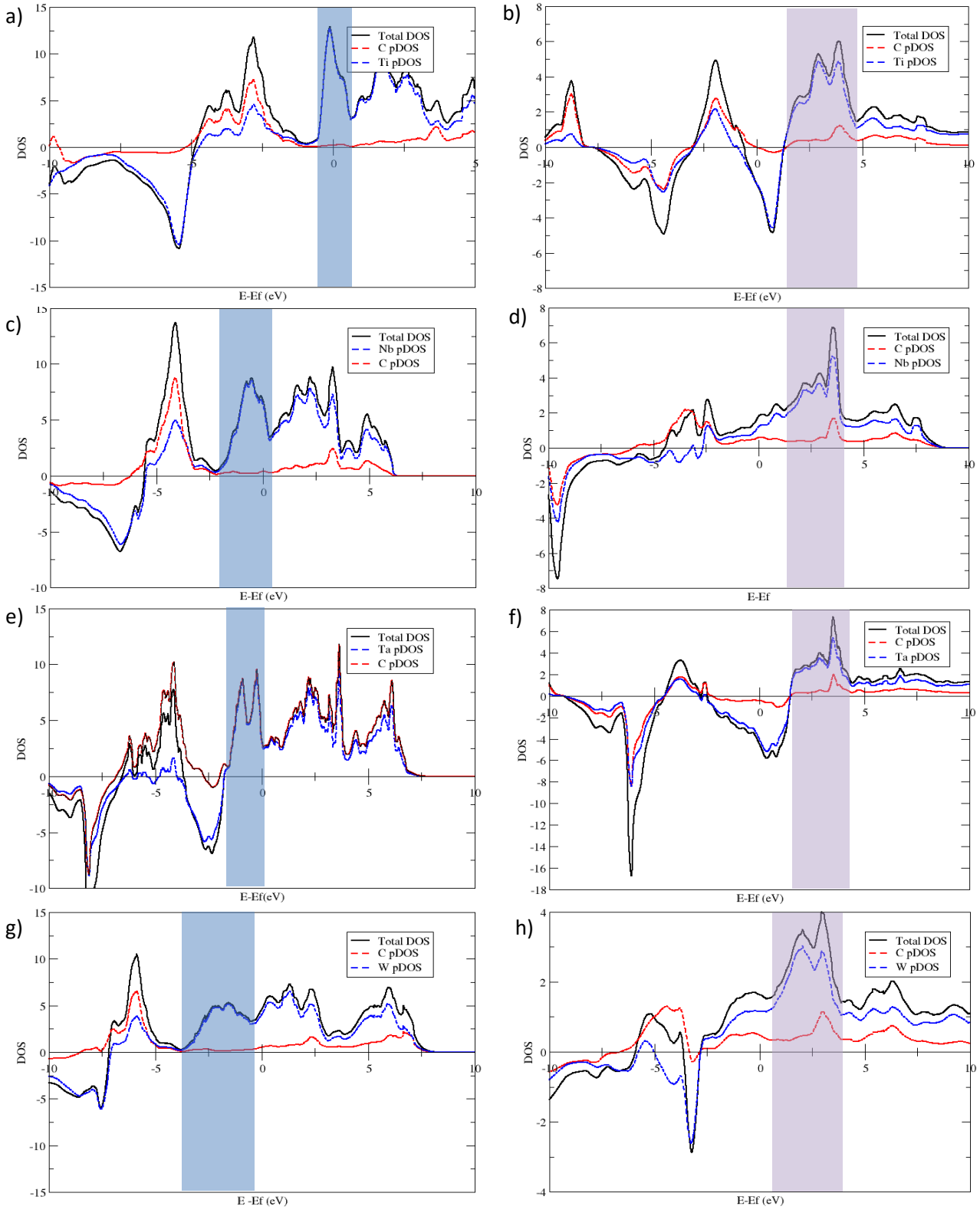

Figure 14 Difference DOS plots (surface-bulk) a) TiC(111), b) TiC(100), c) NbC(111), d) NbC(100), e) TaC(111), f) TaC(100), g) WC(111)fcc and h) WC(100)fcc. TMSRs are highlighted in blue and other regions of interest in purple

Moving down the groups the amplitude of the TMSRs decreased and their width broadened. The mean energy of the TMSR, E_{TMSR}, shifted from 0.008eV for TiC(111) to -1.092eV for cubic WC(111). The mixed TM-C resonance remained at a constant separation

from the TMSR preceding a sharp C depletion in each of the plots. The WC and NbC(111) mixed resonances appeared narrow and well defined whereas the TiC and TaC mixed resonances included finer structure at lower energies and formed a broadened band

For the fcc-(100) surfaces, the difference DOS was dominated by unfilled TM bands above E_f which shifted negatively in energy as the d-band was filled, these regions are highlighted in purple. Below E_f small TM-C maxima between -5 and -2 eV were noted which contained more C character for NbC(100) and cubic WC(100). These bands were also shifted negatively in energy when descending the TM groups.

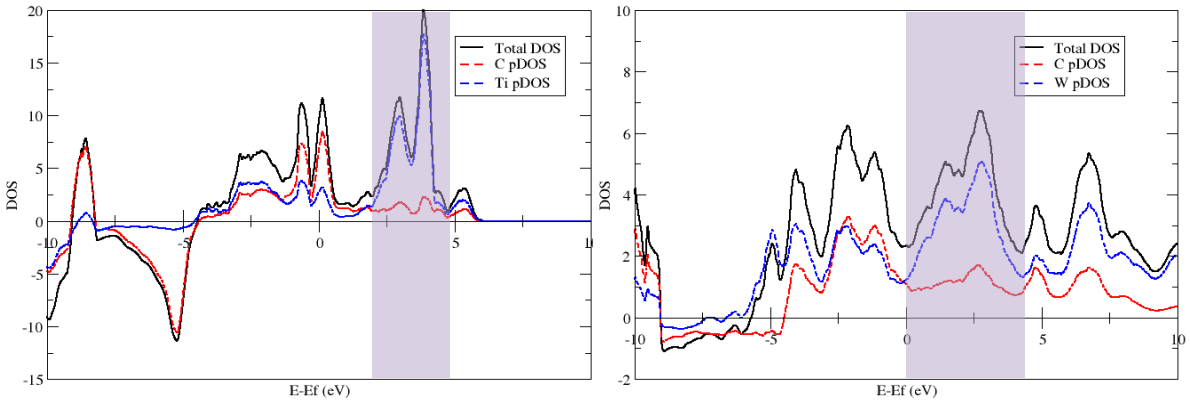

Figure 15 Difference DOS plots (surface-bulk) of surface bilayers CTi(111) and CW(111)fcc

The C terminated fcc-(111) surfaces shown in figure 15 did not exhibit TMSRs at E_f. Whilst they have unfilled TM character resonances above E_f, in the bonding region more C character was observed as previously noted.

TMSRs were observed in the TM terminated hexagonal WC surfaces shown in figure 16 plots a) to d). The (0001) surface contained a well-defined peak just below E_f whilst the $(10\bar{1}0)$ TMSR was narrowed and shifted towards E_f. The WC$(11\bar{2}0)$ difference DOS contained a small TM character resonance just above E_f whilst CW$(10\bar{1}0)$ had more C character at E_f in agreement with previous plots. The SiC difference DOS plots e), f) and g) showed no evidence of TMSRs although C surface resonances were noted for SiC(100) just below E_f and for CSi(100) just above E_f. Surface mixed bands were noted at higher energies above E_f although these bands were dominated by Si character just as such bands are dominated by TM in the case of hexagonal WC.

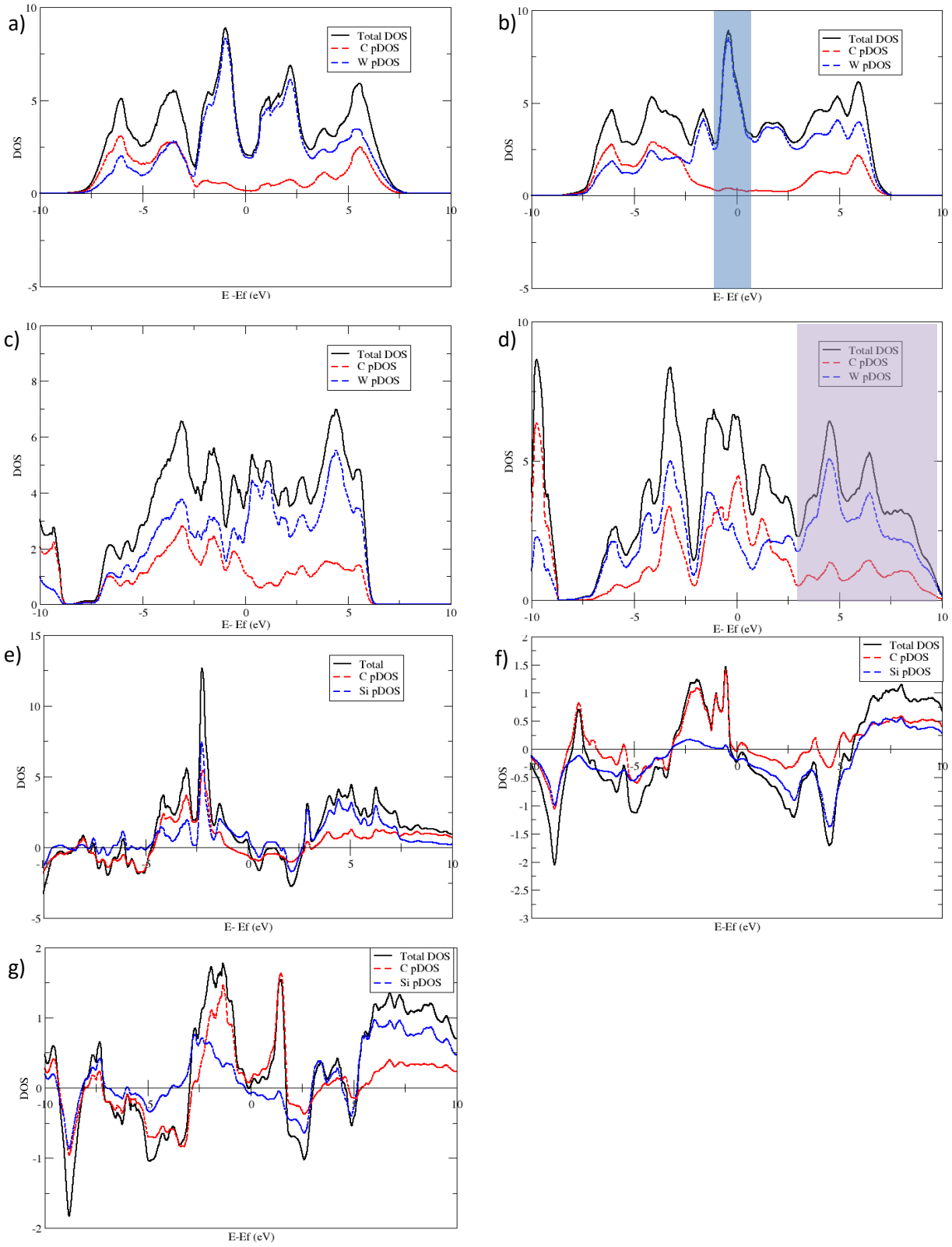

Figure 16 Difference DOS plots (surface-bulk) of surface bilayers, a) WC(0001) hcp, b) WC(10$\bar{1}$0) hcp, c) WC(11$\bar{2}$0) hcp, d) CW(10$\bar{1}$0) hcp, e) SiC(111), f) SiC(100) and g) CSi(100). TMSRs are highlighted in blue and other regions of interest in purple.

3.4 Conclusions

The geometric and electronic structures of our carbide selection have been successfully modelled and analysed. The optimised lattice parameters of the carbides agreed well with previous theoretical work and the experimental values. The bonding of the fcc carbides was found to contain significant ionic contributions as noted in the topological Bader analysis and localised bonding and antibonding bands in the bulk DOS. Hexagonal WC by comparison contained more covalent character and SiC was classified as a covalent compound due to the excellent Si-C overlap given the lessened degree of difference in their electronegativities.

Among the fcc-(111) surfaces, significant surface relaxation was observed and charge transfer from the surface to the bulk occurred to minimize surface energies and compensate for the creation of a surface charge-dipole. Surface specific TM resonances were observed in difference DOS plots. These shifted lower in energy upon the filling of the d-band. Hexagonal WC was noted to have electronic structure features similar to fcc-carbides of earlier TM groups and also exhibited TMSRs in its (0001) and $(10\bar{1}0)$ surfaces. The fcc-(100) surfaces exhibited surface rumpling with TM metals drawn into the surface resulting in the destabilisation of the bonding bands. Small, C dominated surface resonances were noted below E_f though well-defined TMSRs were absent. In general the covalently bonded carbides exhibited less geometric rearrangement, less charge transfer and more orbital overlap resulting in their bonding bands having a more mixed nature. The geometric and electronic findings here are in good agreement with the work of Vojvodic and Viñes.

It has previously been shown that the mean energy of TMSRs (E_{TMSR}) can be used to explain atomic and molecular adsorption on the TMC fcc-(111) surfaces.[118] We will consider the effect of TMSRs upon Pt ML adsorption in the next chapter.

4. Platinum Monolayer Adsorption and Characteristics

In this chapter the Pt wetting behaviour of the carbides is explored via Pt adsorption calculations. Links were sought between the underlying carbide and the observed Pt adsorption trends. The effect of the carbides upon the Pt overlayer was also investigated in terms of electronic structure and charge transfer in the system.

It has been suggested that if full encapsulation of the supporting nanoparticles with Pt were possible, the required specific surface area of the catalyst material would decrease by 80% as conventional catalysts use Pt particles covering approximately 20% of the support surface.[89] Furthermore, the stability of the core-shell under ORR conditions is also reliant on complete encapsulation as the Pt overlayer provides protection for the non-noble core.[171] Defects in the overlayer have been highlighted as providing a possible route for the leaching of core material.[62]

In order for the possible PGM thrifting and activity enhancement benefits of carbide core-shell particles to be realised, strong Pt adsorption to the carbides must be observed and the formation of monolayers (MLs) theoretically assessed. Overly strong interactions with the core must be avoided however, in order to prevent a bulk alloy being formed as in the case of Si and platinum silicate. The presence of the C in the carbide has previously been observed to make metal diffusion into the bulk less likely.[172]

Overlayer coverages of 0.5 - 3ML were calculated for each of the carbides to assess adsorption behaviour and carbide induced changes in the Pt overlayer. The ability to screen the carbides for their Pt wetting capability was also considered in this section via study of geometric and electronic surface properties and trial of the d-band centre[57] and transition metal surface resonance models.[118] The work contained in this chapter was published.[173]

4.1 Pt Adsorption and Monolayer Formation

To determine the preferred Pt adsorption sites, Pt atoms were placed at high symmetry locations on the fcc-(100) and fcc-(111) surfaces as seen in figure 17 as well as the analogous positions on the hcp-(0001) and hcp-(10$\bar{1}$0) surfaces.

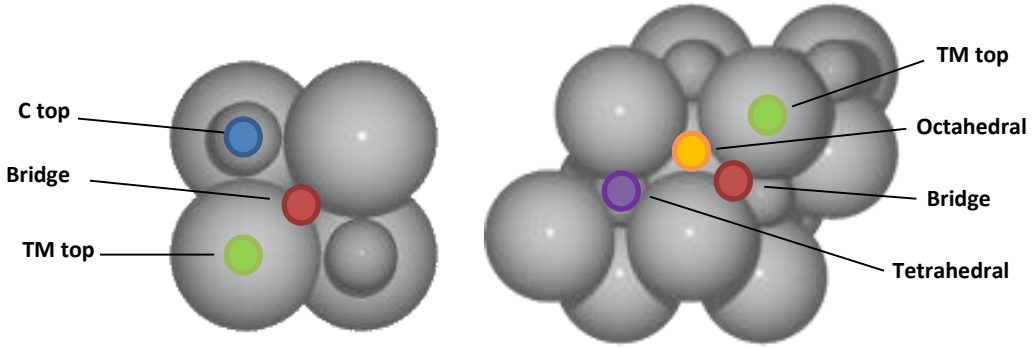

Figure 17 Schematic of high symmetry adsorption positions on fcc-(100) and fcc-(111) surfaces

The adsorption energies on the carbides were calculated using equation 24.

$$E_{ads} = \frac{E_{N\cdot Pt\,/TMC} - (E_{TMC} + N \cdot E_{Pt})}{N} \tag{24}$$

Where $E_{N\cdot Pt/TMC}$ is the energy value for the adsorbed system, E_{TMC} is the energy of the clean, relaxed carbide surface, N is the number of Pt atoms included in the ML and E_{Pt} is the energy of bulk Pt. The use of Pt bulk as a reference in this case enables the alternative to ML adsorption to be Pt agglomeration at the surface.

4.1.1 Pt Adsorption Energetics

Here we present the E_{ads} values for the Pt at its preferred adsorption sites. Trends through the carbide group are discussed as well as the role of Pt-Pt and Pt-TMC interactions ($E_{Pt\text{-}Pt}$ and $E_{Pt\text{-}TMC}$) in the overall adsorption.

As can be seen in Table 4, adsorption of Pt was not favoured on the TMC fcc-(100) surfaces. The C top site proved to be the least unstable site however and was therefore included for further testing. The WC(10$\bar{1}$0)hcp surface proved favourable towards Pt adsorption as did as SiC(100) and their C-terminated equivalents. In these cases the bridge sites were selected as the most stable. On the (111) type surface, all the carbides produced favourable E_{ads} at the 3-fold hollow sites. The difference in E_{ads} between 3-fold sites was generally small, less than 0.05eV in the majority of cases, however for TiC and WC fcc the difference was 0.15eV. Although, as stated in the first chapter, some experimental examples of Pt on TMCs do exist, adsorption energies for sub ML amounts of Pt have not been reported in the literature, instead the current model maybe compared with other theoretical studies. Collaboration with our industrial sponsors will hopefully yield such data in the future which would be most beneficial to the field.

Table 4 Table of preferred Pt adsorption sites for carbide surfaces at 0.5 ML coverage

Surface	0.5 ML E_{ads} (eV/atom)	Position
WC(0001)hcp	-1.01	Tetrahedral
SiC(111)	-1.81	Octahedral
TiC(111)	-1.68	Octahedral
CTi(111)	-3.31	Octahedral
WC(111)fcc	-1.34	Tetrahedral
CW(111)fcc	-0.11	Octahedral
NbC(111)	-1.05	Tetrahedral
TaC(111)	-0.96	Tetrahedral
WC(10$\bar{1}$0)hcp	-1.58	C top
CW(10$\bar{1}$0)hcp	-1.26	C bridge
SiC(100)	-1.67	Si bridge
CSi(100)	-2.80	C bridge
TiC(100)	0.93	C top
WC(100)fcc	0.45	C top
NbC(100)	0.61	C top
TaC(100)	1.03	C top

An alternative method of assessment for the stability of the initial Pt ML is the comparison of $E_{Pt\text{-}Pt}$ and $E_{Pt\text{-}TMC}$ values as used by Esposito[174] and Vasić.[175] Here the $E_{Pt\text{-}TMC}$ expression of equation 25 uses isolated Pt as the reference and $E_{Pt\text{-}Pt}$ defined in equation 26 is the cohesive energy.

$$E_{Pt-TMC} = \frac{(E_{Pt/TMC} - (E_{TMC} + N \cdot E_{Pt\ isol.})}{N} \quad (25)$$

$$E_{Pt-Pt} = \frac{(E_{NPt} - N \cdot E_{Pt\ isol.})}{N} \quad (26)$$

Instances where $E_{Pt\text{-}Pt} > E_{Pt\text{-}TMC}$ should result in Pt agglomeration whereas when $E_{Pt\text{-}Pt} < E_{Pt\text{-}TMC}$, stable Pt ML should be preferentially formed. The $E_{(Pt\text{-}TMC)}$-$E_{(Pt\text{-}Pt)}$ values are identical to E_{ads} values for 1ML as subtraction of equation 26 from 25 results in the cancellation of E_{Pt_isol}. This can be seen from the identical trends in Table 5 with the fcc-(100) and CW(111)fcc surfaces having positive (and thus unstable) $E_{(Pt\text{-}TMC)}$-$E_{(Pt\text{-}Pt)}$ values. We note that the $E_{(Pt\text{-}TMC)}$-$E_{(Pt\text{-}Pt)}$ calculated for WC(0001)hcp matches that calculated by Esposito *et al.* exactly and so include the literature $E_{(Pt\text{-}C(0001))}$-$E_{(Pt\text{-}Pt)}$ value describing Pt adsorption on graphitic carbon for direct comparison to our calculated data in the following discussion.[174]

Table 5 Comparison of $E_{Pt\text{-}TMC}$ to $E_{Pt\text{-}Pt}$ where $E_{Pt\text{-}Pt}$ is 4.59 eV/atom

Material	1ML $E_{Pt\text{-}TMC}$ (eV/atom)	1ML $E_{Pt\text{-}TMC}$- $E_{Pt\text{-}Pt}$ (eV/atom)
WC(0001)hcp	-5.76	-1.16
SiC(111)	-5.56	-0.97
TiC(111)	-6.03	-1.44
CTi(111)	-7.15	-2.56
WC(111)fcc	-5.78	-1.19
CW(111)fcc	-4.37	0.22
NbC(111)	-5.63	-1.04
TaC(111)	-5.52	-0.92
WC(10-10)hcp	-6.07	-1.47
CW(10-10)hcp	-6.24	-1.64
SiC(100)	-5.98	-1.39
CSi(100)	-6.68	-2.08
TiC(100)	-4.34	0.25
WC(100)fcc	-4.26	0.33
NbC(100)	-4.49	0.10
TaC(100)	-4.16	0.43

The $E_{Pt\text{-}TMC}$ values for the fcc-(111) type surfaces were 20-35% greater than the $E_{Pt\text{-}Pt}$ values in agreement with the literature,[174] suggesting a layer-by-layer growth mechanism should be favoured. This was indeed found to be the case for thermally evaporated Pt on WC(0001) as shown experimentally using AES.[172] As before, the C-terminated carbides were observed to produce stronger binding values in comparison to their TM terminated counterparts. It is noted that the literature $E_{(Pt\text{-}C(0001))}\text{-}E_{Pt\text{-}Pt)}$ value of 1.31 eV is significantly more positive than the calculated $E_{(Pt\text{-}TMC)}\text{-}E_{Pt\text{-}Pt)}$ values, suggesting that the carbides should prove more favourable supports for wetting than graphitic carbon.[174]

Having ascertained the preferred sites of Pt adsorption at low coverage, the MLs were built up by repetition from these sites. For SiC(111) both the octahedral and tetrahedral 1ML and 2 ML systems were constructed and the adsorption energies compared. A preference for the octahedral site for the 1 ML system was contrasted by a preference for the tetrahedral site in the first layer of the 2 ML and 3ML systems. However the differences in E_{ads} were within 0.005 eV, well below possible margins of error associated with DFT, and so the initially assigned preferred site was carried forward for further study.

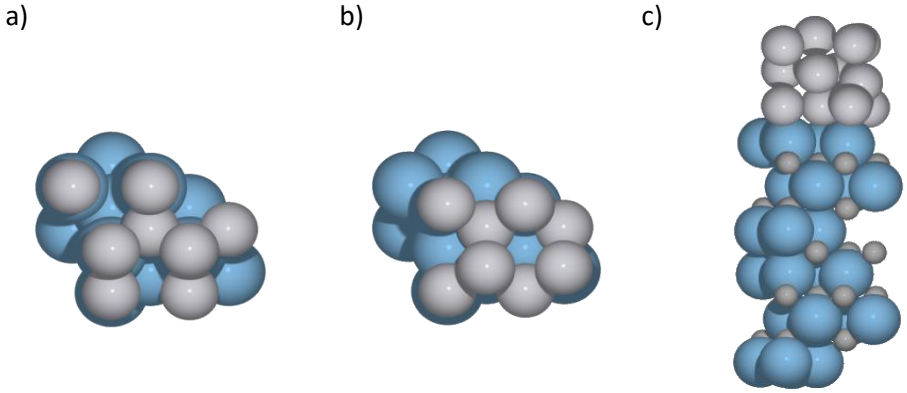

Figure 18 2ML and 3ML structures for TaC(111) a) the preferred TM alignment b) hollow alignment c) 'ABA' stacking

For the (111) surfaces, the positioning of the second and third Pt monolayer was again decided following the optimisation of the different options with the most stable layering also being carried forward for further analysis. In the case of SiC, WC fcc, TaC and WC hcp surfaces the preferred alignment was a second Pt layer placed directly above the TM of the surface as seen in figure 18 a). In the third layer, the majority of fcc carbides took the 'ABA' structure, figure 18 c), whilst both forms of WC and SiC exhibited 'ABC' Pt stacking.

Figure 19 displays the energetics of the Pt monolayer adsorption on the carbide surfaces. In the case of hcp WC and SiC, each of the surfaces exhibited favourable Pt adhesion suggesting total encapsulation of nanoparticulate carbide may be possible. The Pt E_{ads} converged towards E_{Pt} as the overlayer thickness increased due to the increased number of Pt-Pt interactions being included in the system. For these materials, the order of surface preference for monolayer adsorption is:

C terminated > (100) > (111)

following the trends of the $E_{surface}$ recorded previously (see Chapter 3 Table 3).

It was generally observed that less stable surfaces proved more reactive towards Pt adsorption. In the case of the fcc carbides, the (100) surfaces remained unfavourable towards Pt adsorption throughout Pt build-up while the (111) surfaces were preferentially coated again following $E_{surface}$ trends.

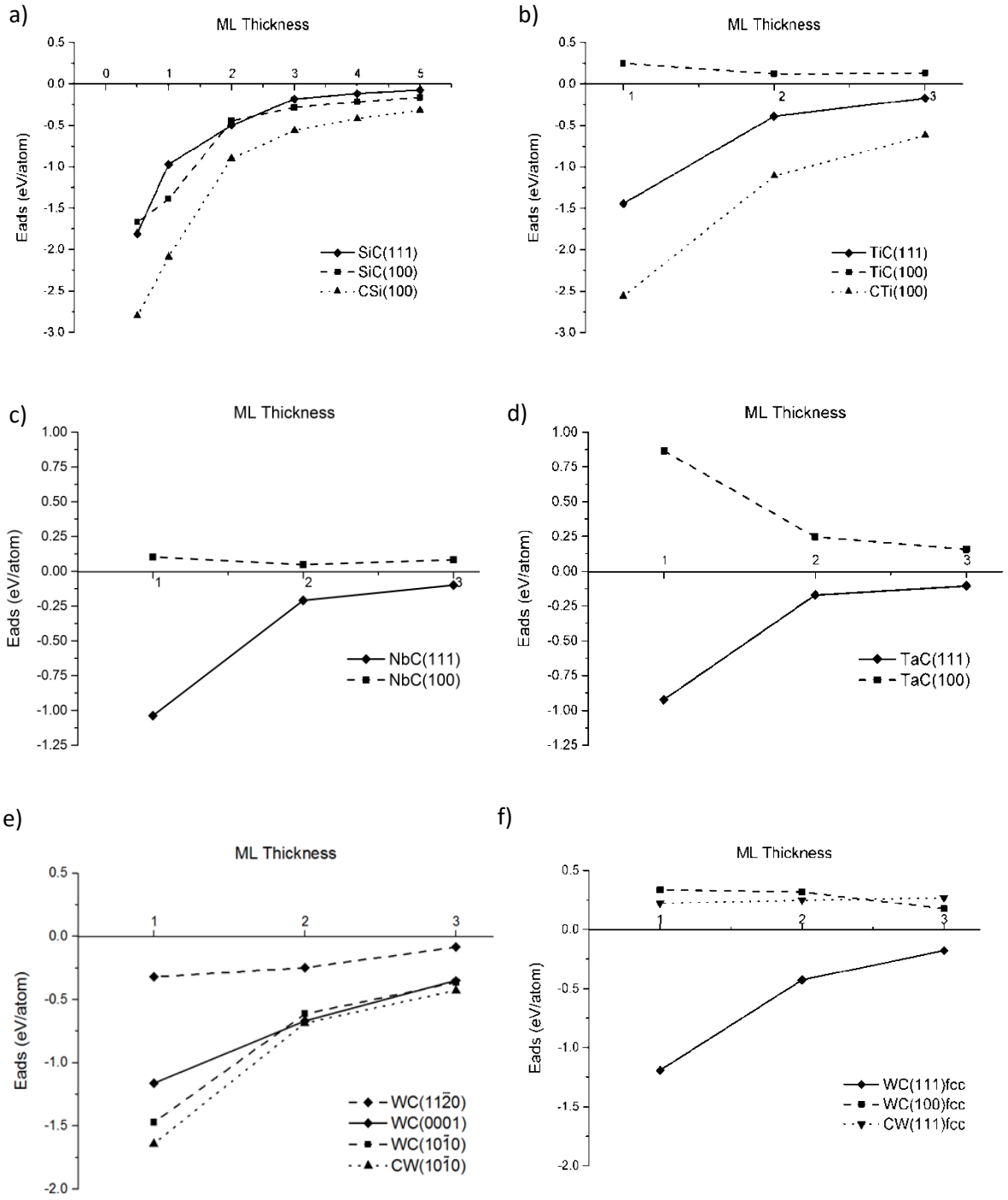

Figure 19 Pt adsorption energies for ML build-up on a) TiC, b) SiC, c) NbC, d) TaC, e) WC hcp and f) WC fcc

No obvious periodic trends were observed for fcc-(100) E_{ads} upon descent of group or transition along the periodic table from Ti to W. The most unfavourable single surface was TaC(100) with a 1ML adsorption value of +0.87 eV. For the fcc-(111) type surfaces the 1 ML E_{ads} decreased upon descent from TiC to NbC to TaC however the WC fcc E_{ads} was found to be more negative.

4.1.2 Pt Adsorption Charge Transfer

Charge transfer at the carbide surface and onto the Pt overlayer was calculated in an effort to understand the interactions occurring at the materials' interface and identify trends in the carbides' wetting behaviour. Topological analysis of the electron density within the Bader paradigm[138] was used to calculate the charge transfer within the Pt/carbide systems using the Topology code[154] (Tables 6 and 7). A negative value is indicative of a gain of electrons at the atom (or layer) and a positive value with their loss.

For the fcc carbides, charge transfer onto the Pt was observed for all TM terminated surfaces. In the case of the fcc-(100) surfaces, the electron density was observed to be mainly from the C atoms whereas for the fcc-(111) surfaces it was from the TM surface layer. The degree of charge transfer observed was greater for the fcc-(111) than for the fcc-(100) ranging from -0.6 to -0.47 and -0.3 to -0.15 electrons respectively. For the C-terminated surfaces, density moved from the Pt overlayer to the electronegative C atoms in the surface and subsurface layers leaving a +0.12 to +0.14 charge on the overlayer in each case. The degree of charge transfer was similar for the hcp WC surfaces, with the (0001) surface acting like an fcc-(111) surface. As for the clean surfaces, a much greater degree of charge transfer was noted for SiC with -1.3 and -1.8 electrons being transferred to the Pt atoms on the (100) and (111) surfaces respectively.

The most significant alteration of charge density distribution within the Pt overlayer was found in the first ML which was in direct contact with the carbide. Any subsequent MLs were observed to have minimal charge at the surface as a significant charge build-up would be expected to result in instability. As in the clean systems, bulk charge transfer values had been recovered by the third bilayer of carbide.

Table 6 Charge density distribution in carbide and Pt/carbide systems for TiC, WC fcc and WC hcp, colour bar for density ranges shown below

3.5 3.0	2.99 2.5	2.49 2.0	1.99 1.5	1.49 1.0	0.99 0.5	0.49 0.0	0.0-0.5	-0.5-1.0	-1.0-1.5	-1.5 -2.0	-2.0-2.5	-2.5 -3
TiC	100	1	2	3	111	1	2	3	C111	1	2	3
Pt3				-0.08				-0.05				-0.07
Pt2			-0.14	-0.03			-0.10	0.00			-0.15	-0.04
Pt1		-0.29	-0.16	-0.24		-0.61	-0.52	-0.56		0.14	0.32	0.26
1	1.64	1.63	1.64	1.66	1.10	1.58	1.56	1.48	-0.80	-0.88	-0.91	-0.92
2	-1.58	-1.36	-1.38	-1.33	-1.81	-1.70	-1.71	-1.64	1.53	1.58	1.63	1.62
3	1.60	1.64	1.61	1.60	1.60	1.62	1.63	1.61	-1.55	-1.66	-1.66	-1.65
4	-1.65	-1.64	-1.63	-1.68	-1.68	-1.67	-1.66	-1.67	1.64	1.66	1.62	1.63

WC fcc	100	1	2	3	111	1	2	3	c111	c1	c2	c3
Pt3				-0.07				-0.04				-0.04
Pt2			-0.13	-0.01			-0.11	-0.01			-0.13	0.00
Pt1		-0.14	-0.14	-0.17		-0.47	-0.35	-0.39		0.15	0.31	0.24
1	1.53	1.46	1.65	1.60	0.86	1.31	1.28	1.26	-0.98	-0.85	-0.92	-0.94
2	-1.49	-1.31	-1.39	-1.39	-1.62	-1.61	-1.60	-1.59	1.70	1.46	1.51	1.48
3	1.52	1.55	1.56	1.54	1.58	1.60	1.60	1.59	-1.40	-1.53	-1.53	-1.52
4	-1.47	-1.54	-1.53	-1.52	-1.60	-1.61	-1.57	-1.57	1.59	1.58	1.58	1.60

WC hcp	w$10\bar{1}0$	1	2	3	0001	1	2	3	c$10\bar{1}0$	1	2	3
Pt3				-0.06				-0.04				-0.05
Pt2			-0.09	0.01			-0.1	-0.01			-0.13	-0.02
Pt1		-0.46	-0.33	-0.38		-0.46	-0.35	-0.38		0.12	0.27	0.2
1	0.92	1.32	1.28	1.28	0.67	1.15	1.14	1.13	-0.6	-0.67	-0.72	-0.72
2	-1.4	-1.37	-1.37	-1.36	-1.34	-1.37	-1.37	-1.37	1.49	1.5	1.51	1.51
3	1.4	1.41	1.41	1.4	1.36	1.37	1.37	1.37	-1.34	-1.4	-1.38	-1.38
4	-1.39	-1.39	-1.39	-1.38	-1.38	-1.38	-1.38	-1.38	1.35	1.35	1.36	1.36

Table 7 Charge density distribution in carbide and Pt/carbide systems for SiC, TaC and NbC

SiC	100	1	2	3	111	1	2	3	c100	1	2	3
Pt3				-0.04				-0.06				-0.04
Pt2			-0.13	-0.03			-0.16	-0.04			-0.13	-0.03
Pt1		-1.33	-1.15	-1.18		-1.76	-1.73	-1.73		0.12	0.25	0.20
1	1.53	2.86	2.80	2.77	0.77	2.60	2.70	2.64	-1.69	-1.67	-1.70	-1.71
2	-3.08	-3.06	-3.07	-3.05	-3.11	-3.12	-3.10	-3.12	3.10	3.07	3.07	3.06
3	3.08	3.07	3.10	3.06	3.08	3.07	3.08	3.08	-2.96	-3.04	-3.05	-3.04
4	-3.08	-3.07	-3.09	-3.07	-3.07	-3.08	-3.08	-3.08	3.07	3.08	3.07	3.07

TaC	100	1	2	3	111	1	2	3
Pt3				-0.05				-0.03
Pt2			-0.09	-0.05			-0.07	-0.01
Pt1		-0.27	-0.18	-0.18		-0.61	-0.47	-0.52
1	1.66	1.71	1.73	1.74	0.98	1.52	1.46	1.49
2	-1.61	-1.40	-1.45	-1.45	-1.81	-1.77	-1.78	-1.79
3	1.68	1.69	1.70	1.71	1.70	1.74	1.74	1.74
4	-1.74	-1.74	-1.73	-1.72	-1.73	-1.74	-1.74	-1.74

NbC	100	1	2	3	111	1	2	3
Pt1				-0.05				-0.03
Pt2			-0.13	-0.06			-0.09	-0.02
Pt3		-0.33	-0.18	-0.21		-0.58	-0.46	-0.48
1	1.62	1.66	1.67	1.70	0.94	1.44	1.40	1.42
2	-1.59	-1.36	-1.40	-1.40	-1.72	-1.69	-1.69	-1.70
3	1.62	1.68	1.70	1.65	1.60	1.65	1.65	1.64
4	-1.66	-1.66	-1.64	-1.64	-1.67	-1.67	-1.67	-1.67

3.5 3.0
2.99 2.5
2.49 2.0
1.99 1.5
1.49 1.0
0.99 0.5
0.49 0.0
0.0-0.50
-0.5-1.00
-1.0-1.50
-1.5-2.00
-2.0-2.50
-2.5-3.00
-3.0-3.50

4.1.3 Pt Adsorption Electronic Structure Alteration

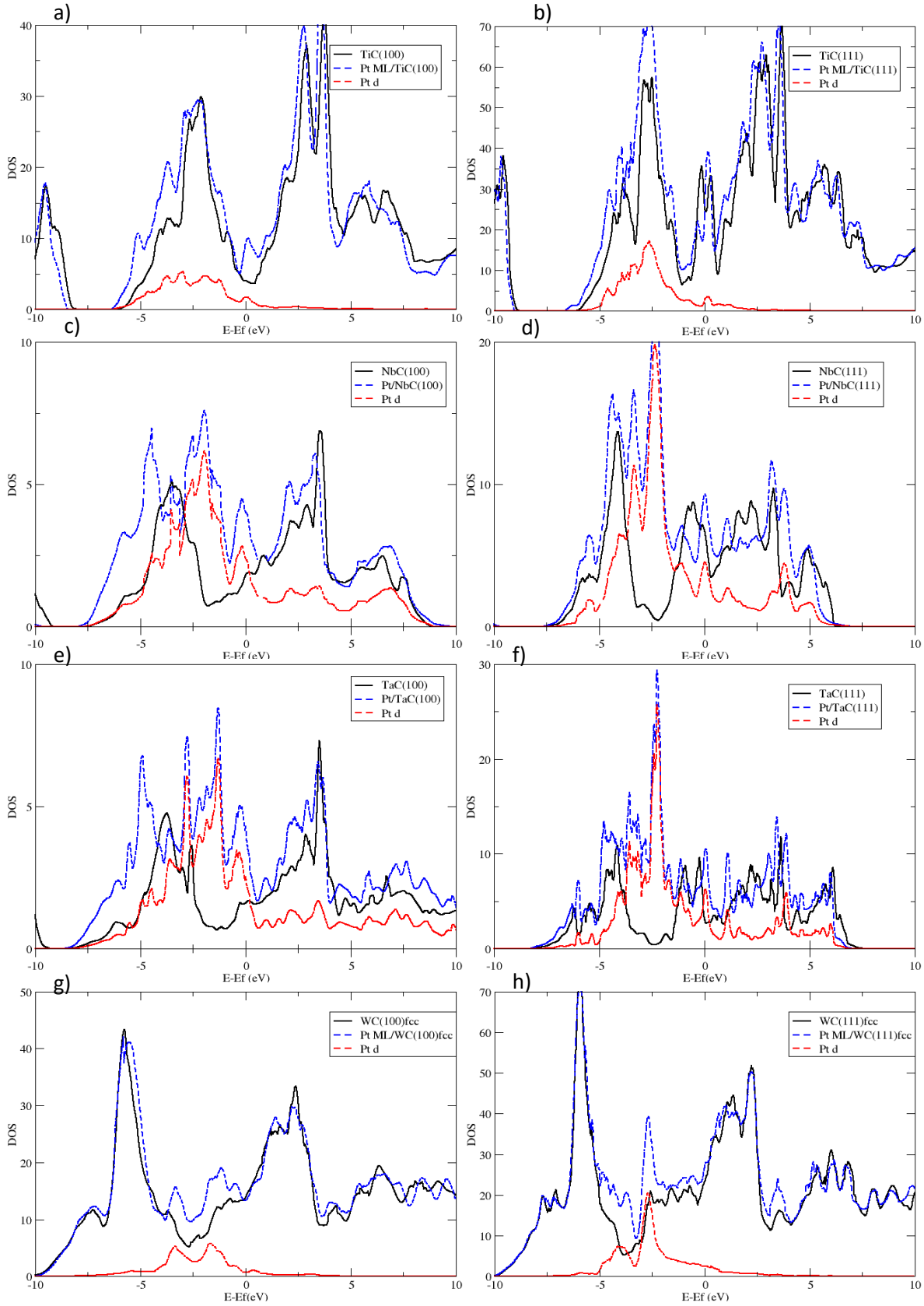

Figure 20 Total and partial DOS plots for the adsorption of Pt on clean carbides surfaces a) TiC(100), b) TiC(111), c) NbC(100), d) NbC(111), e) TaC(100), f) TaC(111), g) WC(100)fcc and h) WC(111)fcc

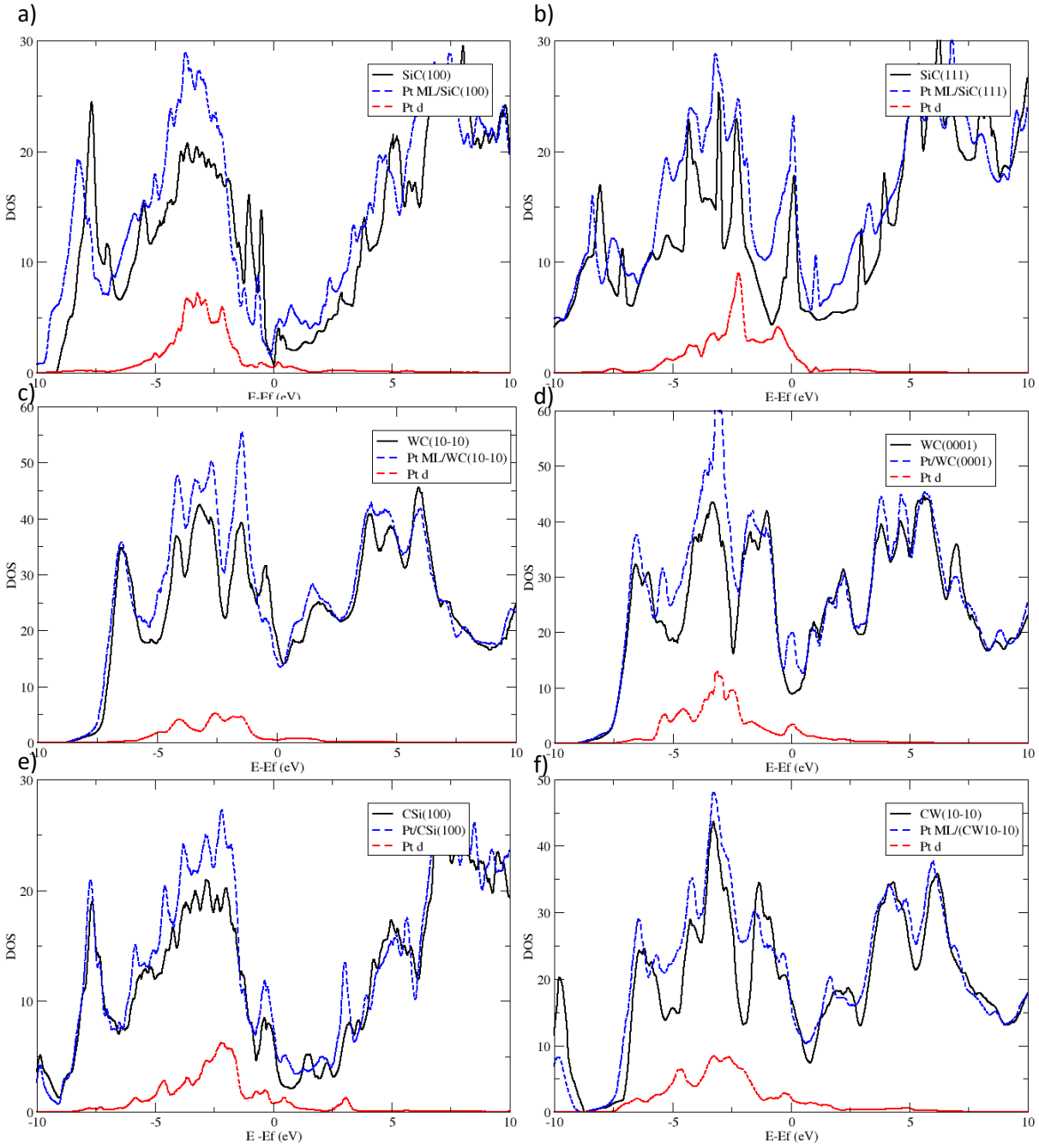

Figure 21 Total and partial DOS plots for the adsorption of Pt on clean carbides surfaces a) SiC(100), b) SiC(111), c) WC(10$\bar{1}$0)hcp, d) WC(0001)hcp , e) CSi(100) and f) CW(10$\bar{1}$0)hcp

At its most fundamental the adsorption of Pt on to carbide surfaces resulted in a negative shift in energy of the total DOS as the Pt introduced more electrons into the system (figures 20 and 21). The effect of this upon system stability will be discussed shortly. Throughout the dataset, the shift in valence states due to the change in TMC metal constituent (see chapter 3) also led to differences in the overlap of the Pt d-band and the carbide DOS.

For TiC, the Pt contributions fell well within the valence band of the carbide DOS, figure 20 a) and b). In the case of TiC(100) there was an increased DOS in the pseudogap at E_f whilst this was not the case for the (111) or C- terminated systems. Here the gap Δ between valence and conduction band was maintained. On descent through the periodic table to NbC, the Pt contribution was observed to fall partially in the pseudogap increasing the DOS in this region, resulting in a considerably reduced Δ in the (100) case. This trend was also exhibited by the TaC surfaces seen in figure 20 plots e) and f). As electronic filling of the metal d-band continued, the Pt contribution was closer to the centre of the pseudogap as in the case of WC fcc, figure 20 plots g) and h). Due to the similarities in band position with regard to E_f, the Pt d-overlap with WC hcp was very similar to that of TiC (figure 21 plots c) and d)). For SiC systems a good overlap between the Pt d- and carbide p-states was consistently observed within the valence band leading to little alteration of Δ although a small negative shift was noted (figure 21 a) and b)).

For the fcc-(100) surfaces then, the inclusion of Pt resulted in a gradual reduction of Δ values and an increased DOS within the carbide pseudogap region. Given that the stability of the carbides is known to depend heavily on the bonding- antibonding splitting signified by Δ,[145] the reduction of this marker upon Pt inclusion indicates the instability of the ML system. In contrast, the cases where (100) type surfaces proved favourable towards Pt adsorption (figure 21 a) and c)) exhibited a good overlap between the carbide C p-states and the Pt d-states. Whilst this overlap criteria appeared to be met in the case of TiC(100), the greater covalence of the WC hcp and SiC surfaces noted earlier also played a role in the stability of adsorbed Pt.

Having previously identified surface specific resonances for the fcc-(111) surfaces, the effect of Pt adsorption on these TMSRs and regions of interest was studied using difference DOS plots (figure 22) where $DOS = DOS_{Pt/TMC} - DOS_{TMC}$. Upon Pt adsorption, a depletion of the TMSRs was noted in all cases, indicating that these resonances were involved in the adsorption process. Based on this observed involvement, Vojvodic *et al.* developed the TMSR centre, E_{TMSR}, as a descriptor for atomic and molecular adsorptions at TMC(111) surfaces .[118] The usefulness of this model for the current system will be discussed under section 4.2.

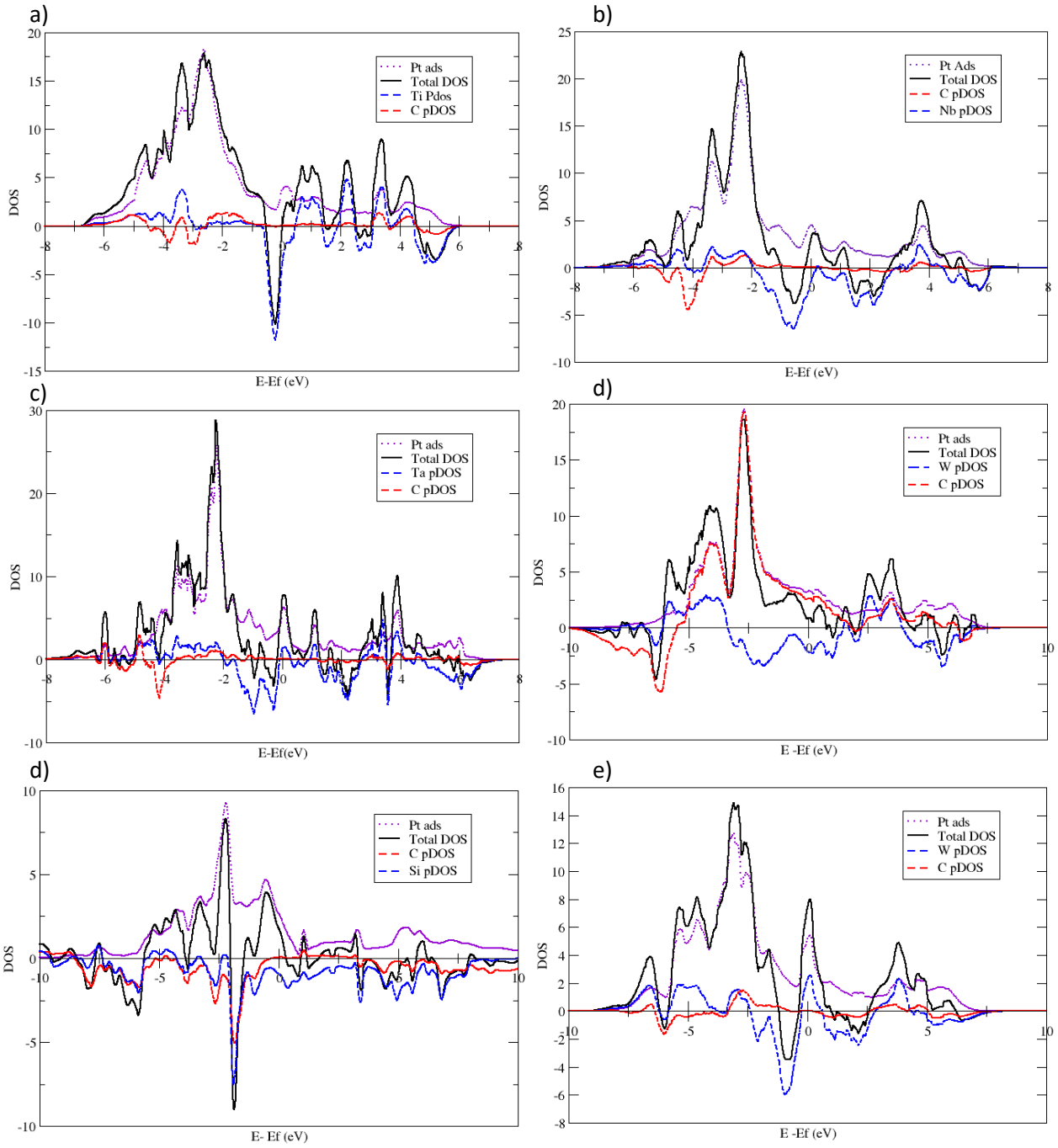

Figure 22 Difference DOS plots of carbide surface bilayers upon Pt adsorption a) TiC(111), b) NbC(111), c) TaC(111), d) WC(111)fcc, e) SiC(111) and f) WC(0001)hcp

For the Pt itself the electronic structure was affected by the geometric strain created by the lattice mismatch with the carbide, as well as the interaction with the electronic structure of the carbide surface. These changes are exemplified by the DOS plots shown in figure 23.

Figure 23 pDOS of Pt d-bands for Pt overlayers of varying thicknesses adsorbed on to a) TiC(111) b) WC(0001)hcp and c) SiC(100). The pDOS traces are offset vertically for clarity.

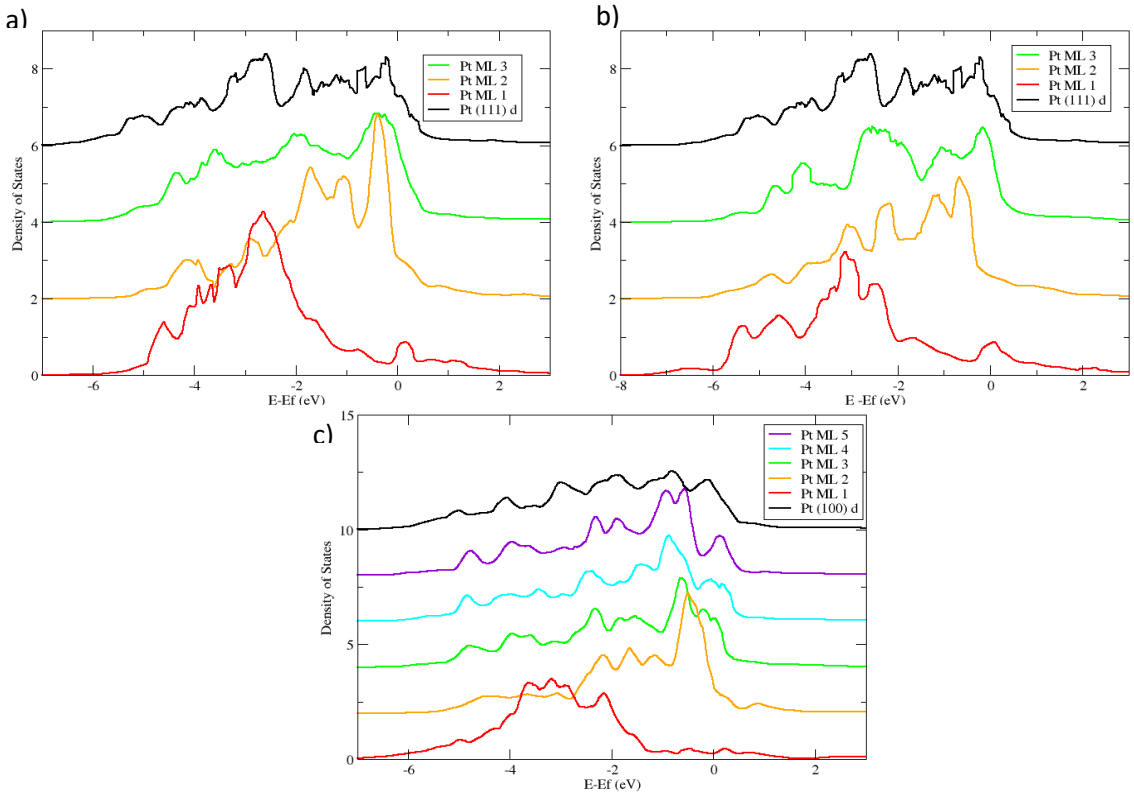

Both orbital overlap and the presence of hetero-bonds (i.e. Pt-X rather than Pt-Pt) are known to alter the d-band width. Consequently, to maintain the filling of the d-band, the d-band centre, E_d, shifts towards or away from E_f.[55] For example, ML adsorption onto a support with a larger lattice constant than Pt results in reduced Pt-Pt orbital overlap and so narrows the d-band width resulting in E_d moving towards E_f.

The effect of the carbide was felt most strongly by the ML nearest the carbide as can be observed in the significant changes to the d-band shape in the red, 1ML pDOS traces above. As the overlayer thickness increased, the DOS for the outer layer of Pt in the overlayer became more reminiscent of that for the pure Pt; E_d moved back towards the Pt surface value and the bandwidth increased. In the case of SiC, 5ML of Pt were analysed and the surface pDOS for the 3ML showed significant similarity to the pure Pt(100) trace. Given this convergence, the thickness of our subsequent overlayers was limited to 3 ML as at N>3 any benefit from the underlying support would be negligible. These findings were in agreement with work from Abruña's group which indicate that overlayer thicknesses of 1-2ML provided the optimum ORR activity for Pt/AuCu systems.[176] The convergence of the surface Pt layer E_d by 3ML can be seen in figure 24a). Within pure Pt slabs, E_d variation between the relaxed surface and the bulk slab interior also takes 3-4 layers as observed in 24 b).

Figure 24 a) Plot showing the variation of E_d in Pt/SiC(100) as the Pt overlayer thickness is increased. Legend colours represent ultimate overlayer thickness b) variation in E_d on descending into Pt(111) and (100) slabs

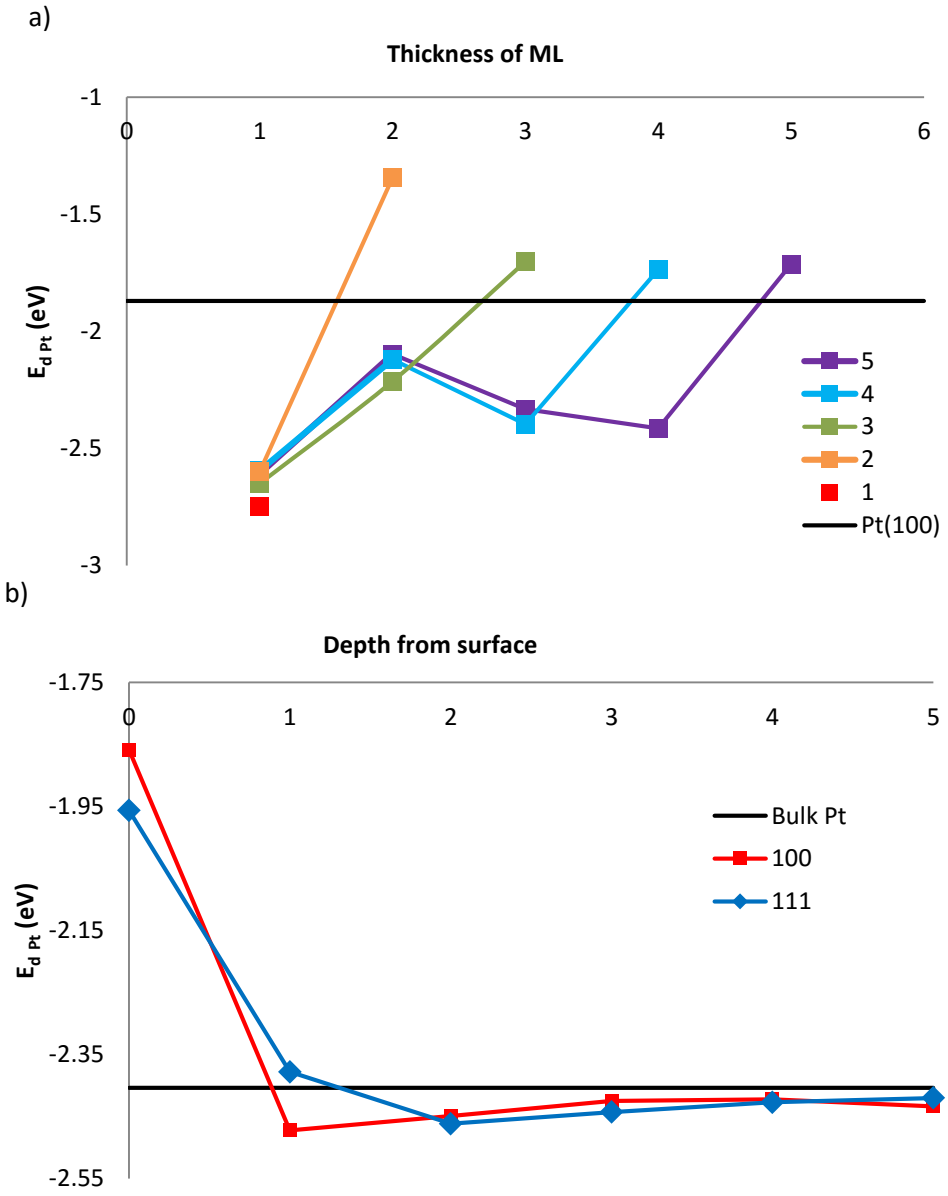

It must be noted that the use of periodic boundary conditions in the presented model leads to the continuation of lattice parameter mismatch throughout the monolayer regardless of thickness. This is due to the fact that the unit cells used are constrained to the carbide lattice parameters. In experiment, self-healing has been reported which would allow the Pt lattice constant in very thick overlayers to be bulk-like,[59] however as can be seen in figure 24, a discrepancy, in this case ~0.15 eV, remain between the 3ML Pt E_d and that of the pure Pt surface.

To assess the extent by which the geometric effect caused the alteration of the Pt electronic structure, Pt(100) and Pt(111) surfaces were expanded to cover the same areas as the carbide unit cells. The area mismatch between bulk Pt and the carbides studied is

due in large part to the radius of the metal involved in the structures and the expansion varied from +4 to +30% . It is necessary to note that the more significant mismatches resulted in several of the overlayers being in a transitional state *i.e.* having an intermediate character between two surface structures.

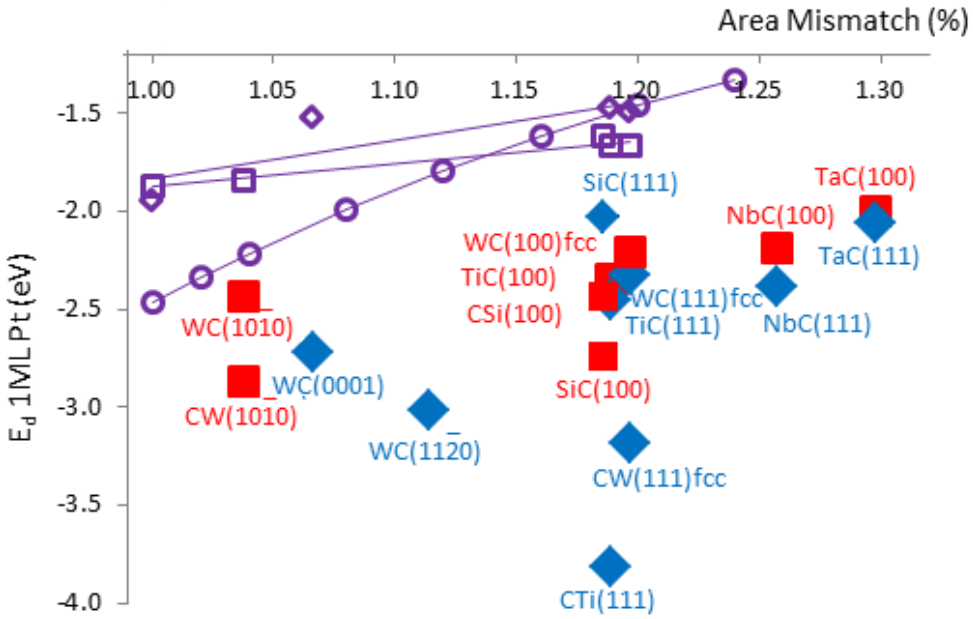

Figure 25 Plot of Pt E_d versus lattice mismatch, solid data point represent Pt/carbide data, hollow purple data points depict unsupported, expanded Pt surfaces.; circles denote bulk Pt, diamonds Pt(111) and squares Pt(100)

In figure 25 the expansion of the Pt lattice parameter was observed to decrease the value of E_d, shifting it closer to the E_f. In the case of Pt expansion to the SiC(100)area the E_d of the unsupported Pt was lowered by 0.2 eV which is in keeping with the E_d discrepancy noted for figure 24. The supported Pt E_d values were consistently more negative than the unsupported Pt values due to the ligand effect exerted by the various carbide metal constituents. For the fcc carbides, Pt MLs on the C terminated surfaces had more negative E_d values than those on the corresponding TM or Si terminated surfaces. The C terminated surfaces had an increased DOS at the pseudogap and greater C p-density below E_f which resulted in greater C p-character in the adsorption orbital overlap and the resultant shift in energy.

For the fcc carbides E_d(100) values were consistently 0.1-0.2eV more positive than E_d(111) values for the same carbide. The C terminated (111) surfaces for TiC and fcc WC did not produce a regular E_d difference within the general trend. The Pt/hcp WC E_d were arranged in the same order as the other surfaces although the difference between the $E_d(10\bar{1}0)$ and E_d (0001) was greater at 0.25eV. The hcp WC results exhibited different behaviour with regards to area mismatch. Increased unit cell area resulted in increasingly negative E_d

values with the symmetry of the surface aiding Pt d- W d-orbital overlap to overcome the lattice expansion effect.

The Pt/SiC surfaces exhibited the opposite trend in E_d ordering with the Pt/SiC(100) system having a less negative E_d than Pt/SiC(111). The interaction of the Pt with the SiC(100) surface was dominated by C p-states whilst that with the SiC(111) surface had more Si p-character due to the termination of the surface. DOS analysis showed the C states in the SiC(100) surface were further in energy from E_f than the filled Si bands in the SiC(111) and a further negative shift of the total Pt/SiC(100) DOS upon Pt adsorption gave rise to the more negative E_d value.

Figure 25 suggests that overall the metal content and carbide surface electronic structure had the most significant impact on the resultant E_d of the Pt ML as a range of E_d values were observed with little lattice mismatch variation. Whilst the effect of the lattice expansion appears regular in nature, the effect of metal content seems less predictable and full Pt adsorption calculations appear necessary to ascertain the values. In the following section, the search for a single factor from the carbide electronic structure which could rationalise Pt adsorption is detailed.

4.2 Possible Descriptors for Pt Adsorption

Given the preferential binding of Pt on to many carbides surfaces and the suggestion that formation of 2D layers should be possible, a wetting descriptor for Pt on the carbides was sought to allow rapid computational screening of carbide materials. Descriptors are 'microscopic material properties which can be used to predict macroscopic catalytic activity'[110] or more generally to predict macroscopic behaviour. Having considered the electronic structures of the carbides surfaces, we began with the d-band centre model,[57] in an attempt to relate TMC electronic structure to E_{adsPt}.

It must be noted first of all that the choice of the d-band centre limits this possible descriptor to TM containing carbides as Si for example does not possess d-electrons. Atomic adsorptions at transition metal carbide surfaces have also been observed to diverge from the d-band centre model. Kitchin *et al*. have suggested that this may be due to the miss-assignment of C electrons to metal centres causing overly negative E_d values. In this case, some improvement was noted upon

the introduction of a 1 Å cut off radius for the projection of the one-electron states onto the atomic orbitals. This minimised the contribution from neighbouring sites in the DOS, however the correlation between E_d and the adsorption energy of hydrogen $E_{ads\ H}$ remained weak in comparison to that observed for TM metallic and bimetallic systems. The neglect of the change in shape of the d-band due to C insertion was also highlighted as a possible source of error in the model as applied to TMCs.[115]

Figure 26 Correlation of $E_{ads\ Pt}$ at high and low coverage limits, red squares represent 0.5ML and blue diamonds 0.25 ML

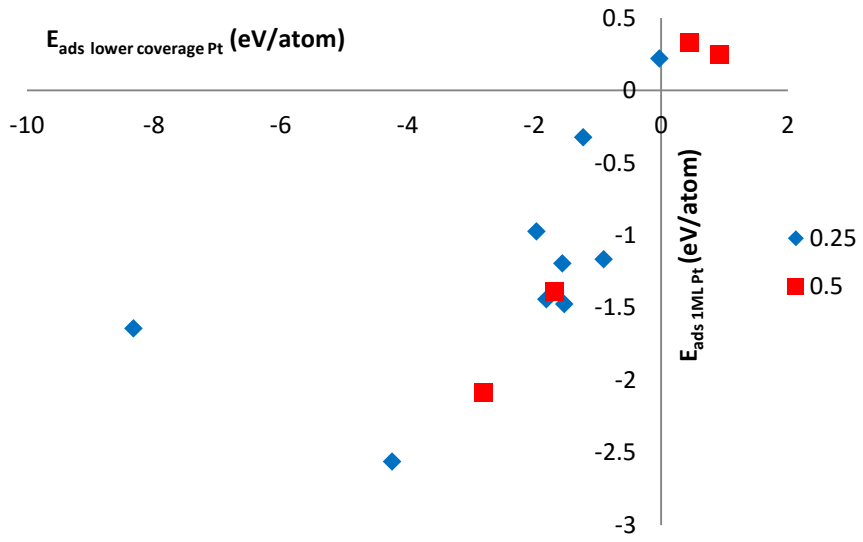

The following model evaluation was carried out with 0.25, 0.5 and 1ML coverages in order to ascertain whether Pt-Pt interactions affected the correlation to $E_{d\ carbide}$.[177] Throughout the set of carbides, the E_{ads} values at the lower Pt coverage were stronger than those at 1 ML, however from figure 26 a strong correlation can be observed between the E_{ads} at different coverages. The outlier in the plot represents the C-terminated WC hcp surface where the Pt atom nestled between the surface Cs forming very short, strong bonding interactions. For the model evaluation, no significant effect upon the strength of correlation between $E_{ads\ Pt}$ and E_d carbide was noted relative to the coverage and thus the 0.5 ML plot is included here as representative of the trends observed.

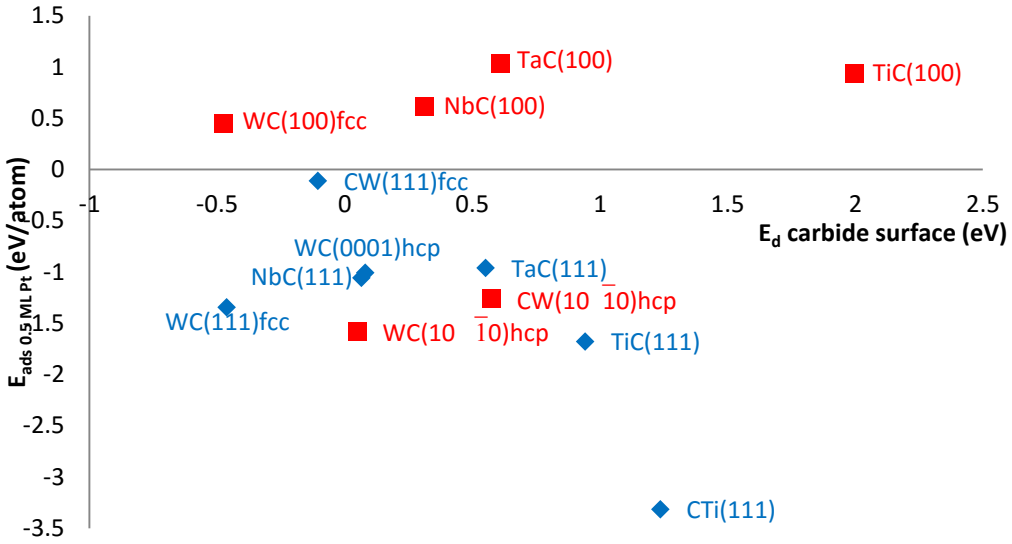

Figure 27 Plot of E_{ads} 0.5ML Pt versus E_d of the clean carbide surfaces

As can be seen in figure 27, the behaviours of the (100) and (111) surfaces were quite different. The fcc-(100) surfaces had varying E_d values and yet exhibited similar adsorption properties giving no indication of a trend, whilst the WC $(10\bar{1}0)$hcp surfaces exhibited significantly lower E_{ads} values. Considering the (111) surfaces, with the inclusion of the C terminated data points the expected relationship of increasingly negative E_d to weakened E_{ads} was observed. However, this correlation was weak, with no obvious pattern connecting C-terminated and TM-terminated surfaces and as such the model could not be used to predict Pt adsorption for TMC surfaces.

Pt coverage was observed to affect the $E_{ads\ Pt}$ of the SiC surfaces. At lower coverages Pt atoms nestled into the top Si layer of the carbide slab, whereas at higher coverages the additional Pt-Pt interaction prevented such close proximity with the surface and the Pt-SiC distances were observed to increase (table 8). Testing for the sequestration of the Pt into the SiC was carried out after similar calculations on Pt/Si had revealed subsurface Pt collection and the formation of bulk silicates. The presence of C in the core lattice was observed to make such subsurface Pt unfavourable in this case.

Table 8 Pt coverage dependence of the vertical Pt-SiC distance for SiC(111)

Coverage (ML)	Pt-SiC (Å)
0.25	1.02
0.5	1.15
0.75	1.31
1	1.44
2	1.43

To test Vojvodic *et al*'s E_{TMSR} as an alternative descriptor for the (111) surfaces[118] in figure 28 we present both lower limit and 1ML coverage trends. It must be noted that SiC was included as a non-TM carbide, using the centre of the Si SR, and as such its divergence from TM electronic descriptors was expected.

Figure 28 Plots of E_{ads} Pt versus E_{TMSR} for a) 0.25ML Pt and b) 1ML Pt

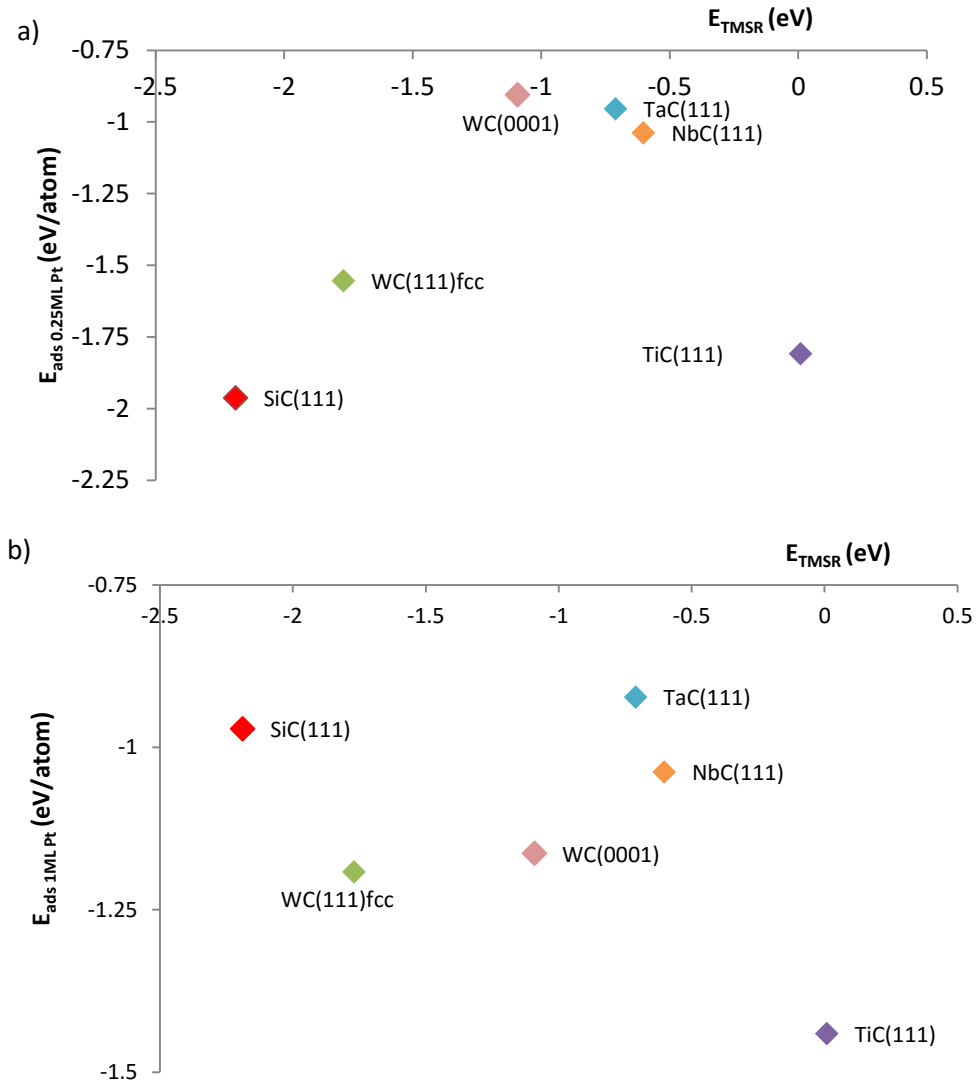

Neither plot in figure 28 provides a well evidenced trend for weakening Pt adsorption with decreasing E_{TMSR}, this is in part due to the small dataset chosen for the work. Although the E_{TMSR} model has successfully been used to study atomic and molecular adsorption onto the TMC and identify scaling relations between similar molecular fragments (i.e. NH, NH_2 and NH_3)[117] we conclude that it cannot be used to predictively describe the Pt wetting of the carbide in this case.

4.3 Conclusions

In this chapter we have seen proof of concept that carbide core-shell nanoparticles should theoretically be possible since Pt can adsorb to carbide surfaces. Due to the difference in the $E_{(Pt-TMC)}$ and $E_{(Pt-Pt)}$ values, layer by layer overlayer formation was predicted for Pt on the fcc-(111) surfaces and total encapsulation was predicted for the WChcp and SiC materials. In the case of SiC it was noted that the C in the carbide prevented Pt sequestration into the bulk and so maintained the Pt layer at the surface- as required for catalytic activity.

Charge transfer calculations showed that the inclusion of Pt led to electron transfer from the carbide to the Pt ML with the exception of C-terminated surfaces where the topmost C layer withdrew electrons from the Pt in contact with it. Charge transfer was most significant for the Pt in direct contact with the carbide and diminished at the surface as Pt thickness increases. The d-band of the Pt was significantly affected by contact with the carbide surface; being narrowed and shifted negatively as a result of the extra electron density present. This shift of the E_d was normalised by the 3rd ML suggesting that catalytic enhancement from the carbide support would be nullified at N≥3 ML. Lattice mismatch and electronic structure were observed to have separable and to some extent predictable roles in the alteration of the Pt ML E_d however possible periodic trends from the metal component of the carbide could not be observed due to the small sample group size.

Surface specific resonances were found to be present for the fcc-(111) carbides and difference DOS plots revealed their involvement in Pt adsorption. The search for a predictive descriptor for Pt adsorption strength using E_d and E_{TMSR} proved inconclusive due to the carbides' complex bonding and electronic dissimilarities with the TMs. Currently then, in the screening of carbide materials it appears that the calculation and assessment of $E_{ads\ 1ML\ Pt}$ and its associated electronic structure will be of most use when assessing the suitability of cores for wetting and subsequent reagent adsorption.

5. Metallic Tie-Layers to aid Pt Adsorption

As previously discussed in chapter 4, the encapsulation of the carbide core is seen as essential for its survival in the hostile PEMFC environment. Given the unfavourable wetting of the fcc-(100) like surfaces towards Pt, this chapter explores the use of metallic tie-layers as a possible strategy to improve Pt adsorption. As shown in figure 29, the tie-layers considered herein are atomically thin layers of a second metal that are located between the carbide and Pt resulting in a sandwich type structure. To be a suitable tie-layer, the trialled metals must adsorb to the carbide surfaces and also prove stable to forming a Pt-outer skin rather than favouring reconstruction to give subsurface Pt.

Practically, it was necessary to consider the long term question of whether such materials could be synthesised, therefore candidate tie-layer metals were chosen for which either atomic layer deposition (ALD) or chemical vapour deposition (CVD) precursors are already known.[178] Metals known to form alloys with Pt and therefore likely to bind Pt to the carbide were preferred although Au was also investigated whilst being known not to alloy with Pt for comparison of behaviour. As reported in the course of the following chapter we chose to test group 9, 10 and 11 TMs (Co,Ni,Cu[179] Rh, Ir, Pd, Ag[180] and Au[181]), in addition to excess layers of the non C component of the carbides themselves (Ti, Ta, Nb) and the main group metals Al, Sn and Ga.

Figure 29 Schematic showing tie-layer of metal a) between carbide and Pt b) with tie-layer at surface

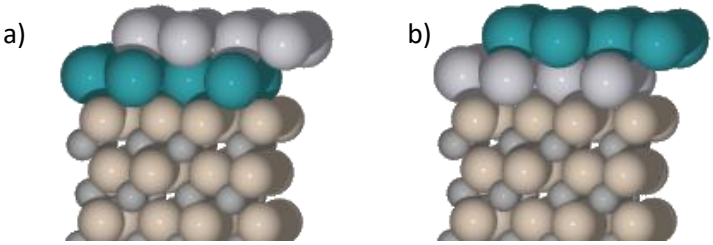

Although numerous examples of Pt and other metals such as Pd and Au as layers on Pt alloy[62,171,182,183,176] or TMC supports[174,175,48] are available in the literature, very few instances of multi-metal overlayers have been reported. The work of Humbert *et al.* stands out because it shows that by replacing the bulk Pt of a Pt-Ni-Pt bimetallic structure with WC hcp a reduction in Pt loading is possible and that physical vapour deposition techniques may be used to create this metallic bilayer surface.[172] The known predisposition for Ni to sequester into Pt bulk was countered via the inclusion of the WC,[184] thereby maintaining the Pt/Ni bilayer surface and its associated activity. A surface Pt layer was observed regardless of Pt and Ni deposition order

following ‘a flash’ of rapid temperature ramping to 600K. The formation of the Pt-outer layer was attributed to ‘Pt migration to lower the surface energy and strain’. Such atomic rearrangement must be taken into account when testing potential Pt/tie-layer/carbide systems.

The Kirkendall effect,[185] where inequivalent diffusion constants for metals within alloys result in segregation, has been witnessed for nanoparticulate ORR catalysts under PEMFC conditions.[186] Pt_3Co particles were found to form hollow Pt, Pt-Co core-shell, and bulk Pt particles. Hollow Pt nanoparticles formed in this way have been observed to have an increased specific activity due to the lattice contraction present in the system,[186,187] although hollow systems may also collapse in on their voids to produce bulk Pt particles.[188] For core-shell arrangements from alloys this can result in a loss of activity enhancement due to a thickening of the outer shell [182] or, following the collapse of a shell after significant portions of core have been replaced by a void resulting in contracted Pt lattice parameters, an increase in activity.[62]

5.1 Tie-Layer Adsorption Methodology

The adsorption of tie-layer metals was studied on the fcc carbides TiC, TaC and NbC and also on SiC and WC hcp surfaces in an effort to identify common factors in their adsorption behaviours. The metal atoms were placed at the preferred Pt binding sites on the carbide (111) and (100) or equivalent surfaces and geometric optimization was carried out. The Pt preferred site was used as previous calculations had suggested negligible energy barriers existed on the surface and spontaneous migration of Pt to preferred sites was noted. Adsorption energies were calculated using equation 24 from chapter 4.

The tie-layer/carbide surface was then covered with an overlayer of Pt and the resulting system further minimised to attain the ground state geometry. The reverse of the bilayer system Tie/Pt/carbide (see figure 29) was also studied to compare the stabilities of the arrangements. The preference for Pt forming the outer skin of the system is given by equation 27 where a negative value indicates that surface Pt is stable.

$$E_{Pt\ outer\ skin} = \frac{(E_{Pt/X/TMC} - E_{X/Pt/TMC})}{N} \quad (27)$$

As discussed in section 4.1.1, SiC and WC hcp surface calculations predicted the favourable adsorption of Pt, as did fcc-(111) surfaces, whilst fcc-(100) surfaces were observed to have unfavourable adsorption energetics. As we can see in table 9, the adsorption of tie-layer metals

resulted in radically different and sometimes quite promising trends in the adsorption energy which will now be discussed.

Table 9 Adsorption energies for 1ML tie-layer metals on various carbide surfaces, green shading represents tie-metals predicted to favourably adsorb to the carbide.

Tie-Layer Metal	E_{ads} (eV/atom)										
	SiC		TiC		NbC		TaC		WC hcp		
	100	111	100	111	100	111	100	111	$10\bar{1}0$	$11\bar{2}0$	0001
Pt	-1.39	-0.97	0.25	-1.44	0.10	-1.04	0.43	0.92	-1.47	-1.18	-1.16
Co †	-1.18	-1.57	0.17	-0.78	-0.16	-0.52	-0.30	-0.87	-0.99	-2.04	-0.99
Rh	-1.10	-1.38	0.23	-1.06	0.04	-0.69	0.35	-0.61	-1.05	-1.57	-1.14
Ir	-0.51	-0.72	0.96	-0.66	0.71	-0.17	1.15	-0.03	-0.53	-1.06	-0.94
Ni †	-0.40	-0.55	0.60	-0.29	0.26	-0.09	0.44	-0.11	-0.73	-1.29	-0.42
Pd	-1.27	-0.93	0.06	-1.19					-1.30	-1.15	-0.95
Cu	-0.18	0.20	0.58	-0.30					-0.60	-0.74	-0.26
Ag	-0.40	0.24	0.37	-0.67							
Au	-0.74	0.14	0.31	-1.19							
Zn	-0.39	0.26	0.02	-0.63							
Ti			0.22	0.23	0.00	0.23	0.05	0.10	-0.77	-2.43	-0.15
Al			-0.23	-0.73	-0.04	-0.55	0.15	-0.63	-1.11	-1.48	-0.69
Ga			-0.35	-0.94					-1.12	-0.90	-0.66
Sn			-0.49	-1.05					-1.16	-1.18	-0.50
Ta					0.79	0.48	0.95	0.74			
Nb					0.38	0.45					

† Please note the result shown are without spin polarisation being included in the calculation

The adsorption energetics calculated for WC hcp predicted the favourable adsorption of late TMs from groups 9 and 10 and the test set of main group metals. The strongest calculated adsorptions energies were found for the $(11\bar{2}0)$ surface for both the late TMs and the main group elements. In the case of the (0001) surface a preference towards the late TMs was predicted whereas for the $(10\bar{1}0)$ surface the main group metals were predicted to adsorb preferentially. SiC(100) adsorption energetics suggested the favourable adsorption of the group 9-12 late transition metals however the (111) surfaces were predicted to be unlikely to adsorb the group 11 and 12 metals. Conversely, the calculations suggest TiC(100) will not adsorb the late TM at all and favourable adsorption is only predicted for the main group elements Al, Ga and Sn. The TiC(111) surface displayed favourable adsorption energy trends towards both the late TMs and main group metals. For NbC only Co and Al were predicted to adsorb at the (100) surface and group 9 and 10 metals at the (111). Co was the only element within the dataset which calculations predicted had the potential to adsorb to both TaC(100) and (111) although adsorption of other late TMs was also calculated to be favourable on the (111) surface. Analysis of these trends with regards to the electronic structure of the surfaces will be presented in the following section.

After initial analysis, WC hcp was predicted to favour the adsorption of the most tie-metals, followed by SiC which theoretically may be fully encapsulated by the late TMs of group 9 and 10. Al, Sn and Ga may be suitable metals for adsorption on both (100) and (111) TiC surfaces. The adsorption energy trends for NbC predicted Co could adsorb onto both surfaces, however given that the Pt adsorption was found to be stronger than Co on the (111) surface it may be that a bimetallic overlayer could be achieved whereby Co covered the (100) and Pt the (111). It must also be noted at this point that converged spin polarised calculations for Ni and Co should further increase their stability and so experimental trials should not be ruled out. Encapsulation of TaC by Co should also theoretically be possible. The effect of tie-layer introduction on adsorption of reagents will be covered in chapter 6.

5.2 WC hcp

5.2.1 Geometry

The structural properties of the tie-layer metals on the WC hcp surfaces are displayed in table 10. In agreement with the overall E_{ads} previously stated, the $(11\bar{2}0)$ M-WC bond lengths were the shortest followed by the $(10\bar{1}0)$ and then the (0001) values. The adsorption of the tie-layer species resulted in an expansion of the first layer of the carbide. This expansion was observed to be least significant for the (0001) surface with variation from the clean surface here being ≤1%, the $(10\bar{1}0)$ surfaces expanded vertically by up to 3.8% whilst for the $(11\bar{2}0)$ surface the maximum increase of 7% was seen for Al and Ga. The extent of the expansion therefore, was seen to be a reflection of the strength of the tie-layer interaction.

Table 10 Vertical relaxation and $\Delta E_{M\text{-}WC}\text{-}E_{M\text{-}M}$ data for WC hcp surfaces, X-WC and D_{13} distances are measured from the surface M layer.

Tie-layers	(0001)				
	X-WC (Å)	D_{13} (M-M) (Å)	ΔD_{13} (%)	$E_{M\text{-}WC}$ (eV/atom)	$\Delta E_{M\text{-}WC}\text{-}E_{M\text{-}M}$ (eV/atom)
Ti	2.41	2.83	0.9	-5.37	-0.15
Co	1.93	2.84	1.0	-1.77	-0.99
Rh	2.05	2.84	1.0	-4.87	-1.14
Ir	2.08	2.83	0.8	-6.78	-0.94
Ni	1.90	2.84	0.9	-3.88	-0.42
Pd	2.12	2.83	0.6	-4.25	-0.95
Pt	2.12	2.83	0.6	-5.76	-1.16
Cu	2.08	2.82	0.5	-133.55	-0.26
Al	2.26	2.83	0.6	-3.88	-0.69
Ga	2.34	2.82	0.3	-2.91	-0.66
Sn	2.55	2.81	0	-3.52	-0.50

Tie-layers	$(10\bar{1}0)$				
	X-WC (Å)	D_{13} (M-M) (Å)	ΔD_{13} (%)	$E_{M\text{-}WC}$ (eV/atom)	$\Delta E_{M\text{-}WC}$-$E_{M\text{-}M}$ (eV/atom)
Ti	1.99	2.49	0.4	-5.99	-0.77
Co	1.69	2.54	2.3	-1.77	-0.99
Rh	1.87	2.56	3.2	-4.78	-1.05
Ir	1.88	2.58	3.8	-6.36	-0.53
Ni	1.70	2.54	2.3	-4.19	-0.73
Pd	1.92	2.55	2.7	-4.60	-1.30
Pt	1.92	2.57	3.5	-6.07	-1.47
Cu	1.82	2.52	1.7	-132.51	0.77
Al	2.04	2.51	1.1	-4.30	-1.11
Ga	2.17	2.51	1.0	-3.36	-1.12
Sn	2.40	2.52	1.4	-2.82	0.21

Tie-layers	$(11\bar{2}0)$				
	M-WC (Å)	D_{13} (M-M) (Å)	ΔD_{13} (%)	$E_{M\text{-}WC}$ (eV/atom)	$\Delta E_{M\text{-}WC}$-$E_{M\text{-}M}$ (eV/atom)
Ti	1.19	1.28	2.5	-7.65	-2.43
Co	0.93	1.31	4.6	-2.83	-2.04
Rh	1.09	1.30	4.1	-5.30	-1.57
Ir	1.02	1.32	5.9	-6.89	-1.06
Ni	0.91	1.31	5.1	-4.75	-1.29
Pd	1.14	1.31	4.4	-4.45	-1.15
Pt	1.09	1.33	6.4	-5.77	-1.18
Cu	1.02	1.31	4.8	-134.03	-0.74
Al	1.00	1.34	7.0	-4.66	-1.48
Ga	1.18	1.34	7.0	-3.14	-0.90
Sn	1.79	1.30	4.3	-4.20	-1.18

The trends in vertical separation of the tie-layers from the carbide surface were observed to be similar regardless of carbide facet. The M-WC distances appeared to correlate with the atomic radii of the tie-layer metals although non-TM Al and Ga did not follow this trend. Evidence of M-WC varying periodically as one traverses the periodic table can be seen as the Rh:Pd and Ir:Pt distances increased (figure 30). This was in agreement with the work of Vasić *et al*. who reported variation of M-WC with atomic radii along the period.

It was noted that the Cu overlayer values were significantly larger than those of the other metals tested. This was an artefact of the modelling of the Cu itself and so the adsorption energy of the overlayer was in keeping with the other values since the error cancelled across the calculations. In the future, new Cu pseudopotentials should be used to verify these results.

Figure 30 Plot of tie-metal atomic radii[189,190] versus M-WC(0001) vertical distances

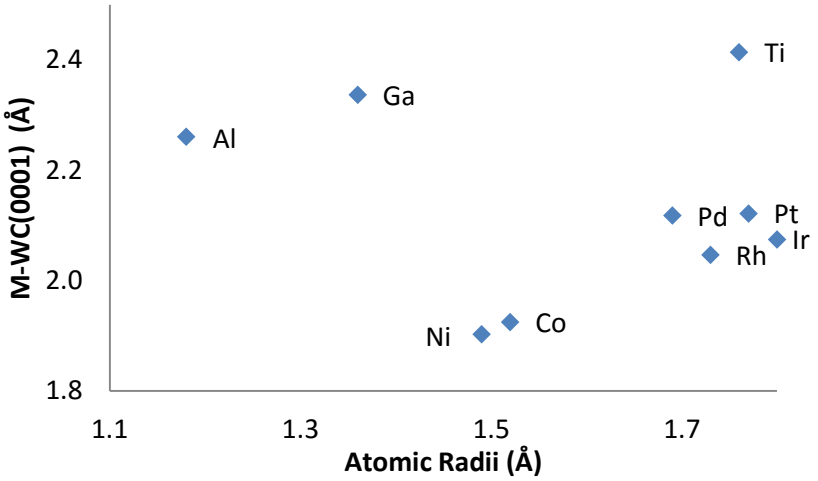

Within the tie-metals tested on WC hcp, Ti, Co and Zn are hcp, the early TMs are body centred cubic (bcc) whilst other the TMs and Al have fcc structures and Ga and Sn are listed as having orthogonal and tetragonal structures respectively.[191] It was proposed that similarity in the surface structure and the tie-metal's natural crystal structure may result in improved adsorption. However, in the case of the WC(0001) surface no such preferences towards the hcp metals were found.

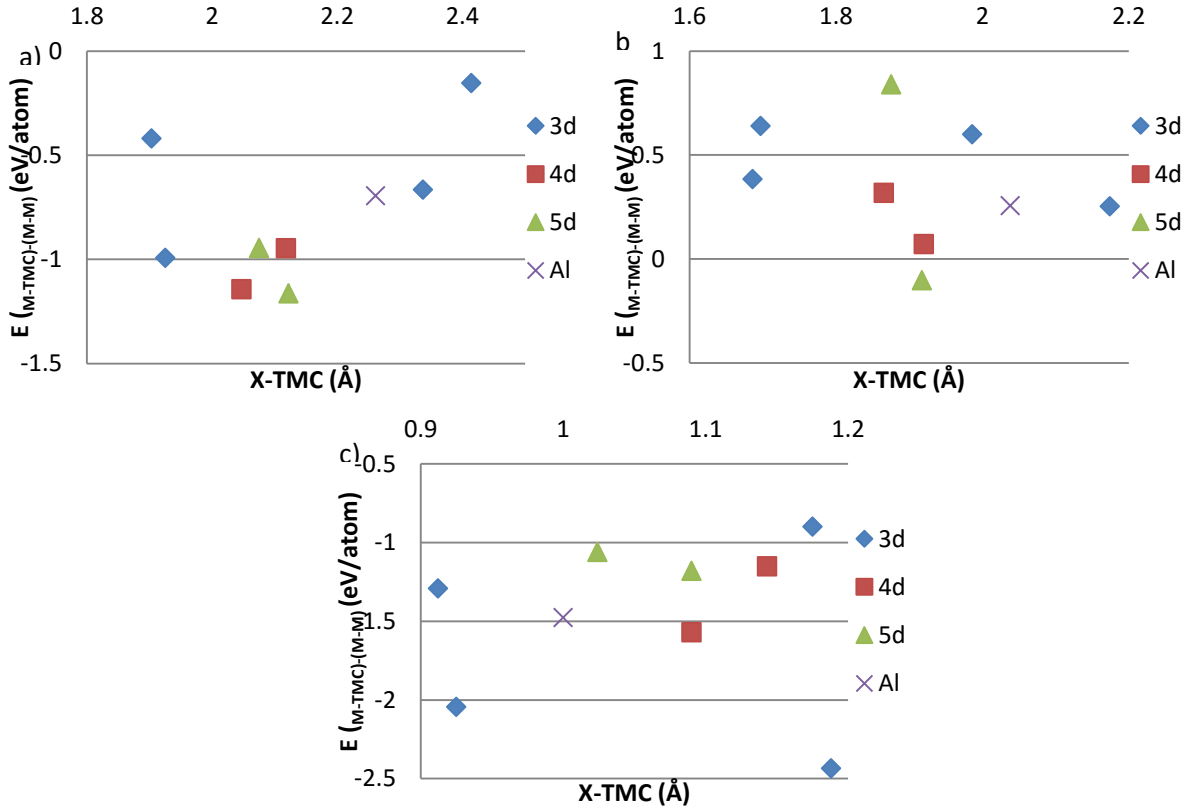

Figure 31 Plots showing X-WC vertical distances with relation to the adsorption strength $E_{(M\text{-}WC)\text{-}(M\text{-}M)}$ a) (0001) b) (10$\bar{1}$0) and c) (11$\bar{2}$0)

In general the M-WC distances for the PGMs on the WC (0001) were in good agreement with those recorded by Vasić *et al.*[175] However, the literature values for the relaxation of the first bilayer (ΔD_{12}) -2.9% and -3.05% with 1ML of Pt and Pd respectively[168] differed by a whole percentage point from the calculations presented in this work (1.9% for Pt and Pd). Given the excellent agreement with the literature observed for the relaxation of the clean carbide slabs (chapter 3) we concluded that our carbide model should be representative of experimentally observed surfaces. It must be noted that the literature methodology utilised a shorter carbide stack and constrained all bar the top bilayer of the carbide. In the current work a 6 bilayer slab was modelled with only the back bilayer constrained to bulk distances. Having repeated the optimisation of our Pt containing slab with constraints matching those of the literature the change in D_{12} was found to be 2.3%. It is therefore suggested that the difference in ΔD_{12} for the overlayered structure partially originates from the lack of freedom for the relaxation of the surface to permeate beyond the first carbide bilayer. The greater degrees of freedom allowed within our model enabled the relaxation to extend deeper into slab and hence the difference in inter-layer distances from the bulk value could be spread throughout the different layers. A small functional effect was also noted; when the newly constrained system was run with PBE and PW91 xc functionals the ΔD_{12} percentages were calculated to be 2.1 and 2.06% respectively for the Pt ML.

5.2.2 Energetics

The trends in $E_{M\text{-}M}$ for the TM tie-layers were highly periodic in nature as can be seen in figure 32. Generally $E_{M\text{-}M}$ weakened as one moved across the period with sharp drops coinciding with changes in period. This observation can be attributed to the fact that across the period, d-band filling increases and atomic radii decrease as the charge on the nucleus increases without the commensurate increase in shielding from the electrons. Further consideration of the periodic changes to bonding observed will be made in the electronic structure analysis for the later carbide materials.

Figure 32 Plot displaying the periodicity of M-M interaction strength where blue represents 3d, green 4d and orange 5d metals

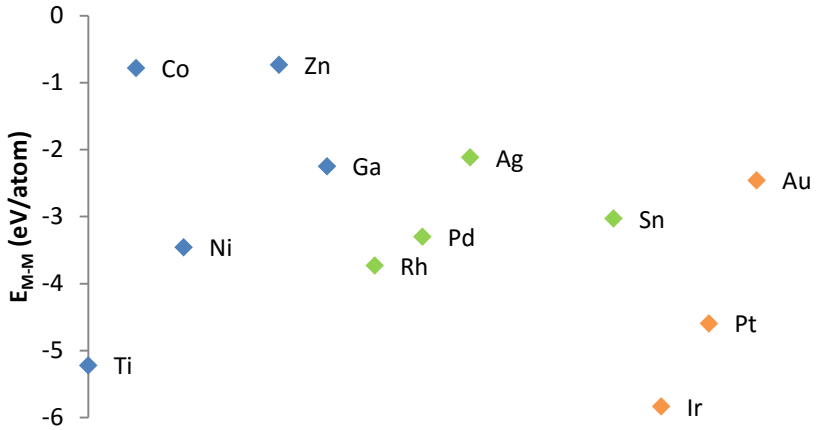

Given the balance between $E_{M\text{-}M}$ and $E_{M\text{-}WC}$, the metals with more negative $E_{M\text{-}M}$, in this case TMs with less d-band filling, were expected to be less likely to form ML on the carbides. Vasić predicted that Ru and Ir on WC(0001) would re-agglomerate to form ad-islands even if initial adsorption were possible.[175]In figure 33 the current calculations are observed to result in favourable adsorption for all the tie-layer metals tested including Ir. The difference in findings may be due to different carbide slab setups as previously discussed or the use of differing xc functionals; the Vasić paper using PBE[126] whilst the current work employs RPBE a revision to the PBE functional made by Hammer, Hansen and Nørskov.[127]

Single point calculations were carried out on the geometry optimised adsorbed structure using PBE to identify the extent to which the xc functional effected the outcome. Whilst use of the PBE functional did yield significantly stronger $E_{(M\text{-}M)}$ and $E_{(M\text{-}WC)}$ values (-6.89 and -7.84 eV/atom as compared to -5.83 and -6.78 eV/atom) these cancelled to give $E_{(M\text{-}WC)\text{-}(M\text{-}M)}$ within 0.003 eV/atom of the RPBE calculations. We therefore conclude that the difference in functional does not account for the behaviours reported. It must be acknowledged that, having used single point calculations, geometric differences between the literature and presented work still remained.

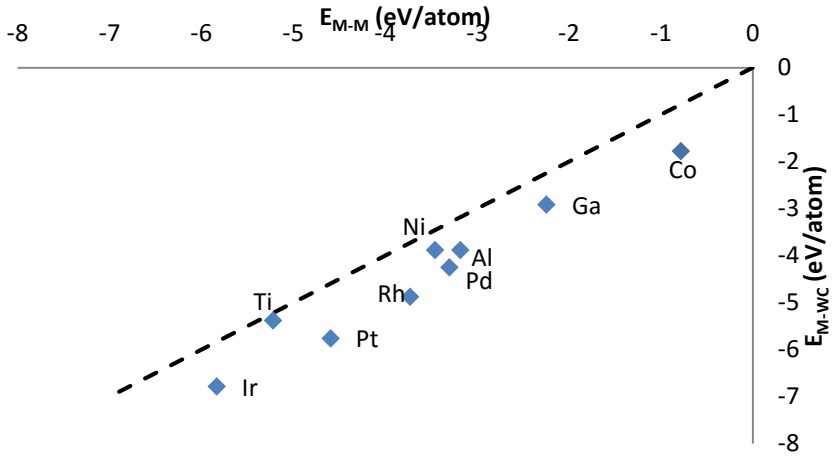

Figure 33 Plot of $E_{M\text{-}M}$ versus $E_{M\text{-}WC(0001)}$ with 1:1 shown as a dashed line

Experimentally, Pt, Pd and Au[174] as well as Ni and Rh[192] monolayers have been formed on WC(0001) surfaces and investigated as hydrogen evolution or methanol reforming catalysts. The coverage of the tie-metals was investigated using Auger electron spectroscopy (AES) which allows calculation of the overlayer thickness. The ML character of the Pt overlayer was further supported by the presence of a core level shift of the Pt 4f $\frac{7}{2}$ peak position relative to bulk Pt in the XPS data, which suggested intimate contact between the Pt present in the system and the carbide substrate.[174]

5.2.3 Tie-Layer Stability

Having ascertained the ability of the tie-layer candidate metals to adsorb to the WC hcp, assessment of their stability relative to Pt was carried out. In figure 34 a) the E_{ads} of the tie-metals are displayed alongside the E_{adsPt} on the same surfaces. From the E_{ads} traces we observed that Pt adsorption was predicted to be more favourable than the tie-layer candidates, except for the adsorption of Co, Rh, Ni, Ti and Al on the $(11\bar{2}0)$ surface. This would suggest that if both overlayer precursors were present, the Pt would preferentially adsorb to the carbide surface. However, each of the tie-metals were predicted to favourably adsorb to all WChcp surfaces allowing for the possibility of full encapsulation in an alternative metal.

Figure 34 a) Tie-layer adsorption energies for 1ML on WChcp surfaces and b) bilayer stability with respect to Pt as the outer layer for WC hcp surfaces

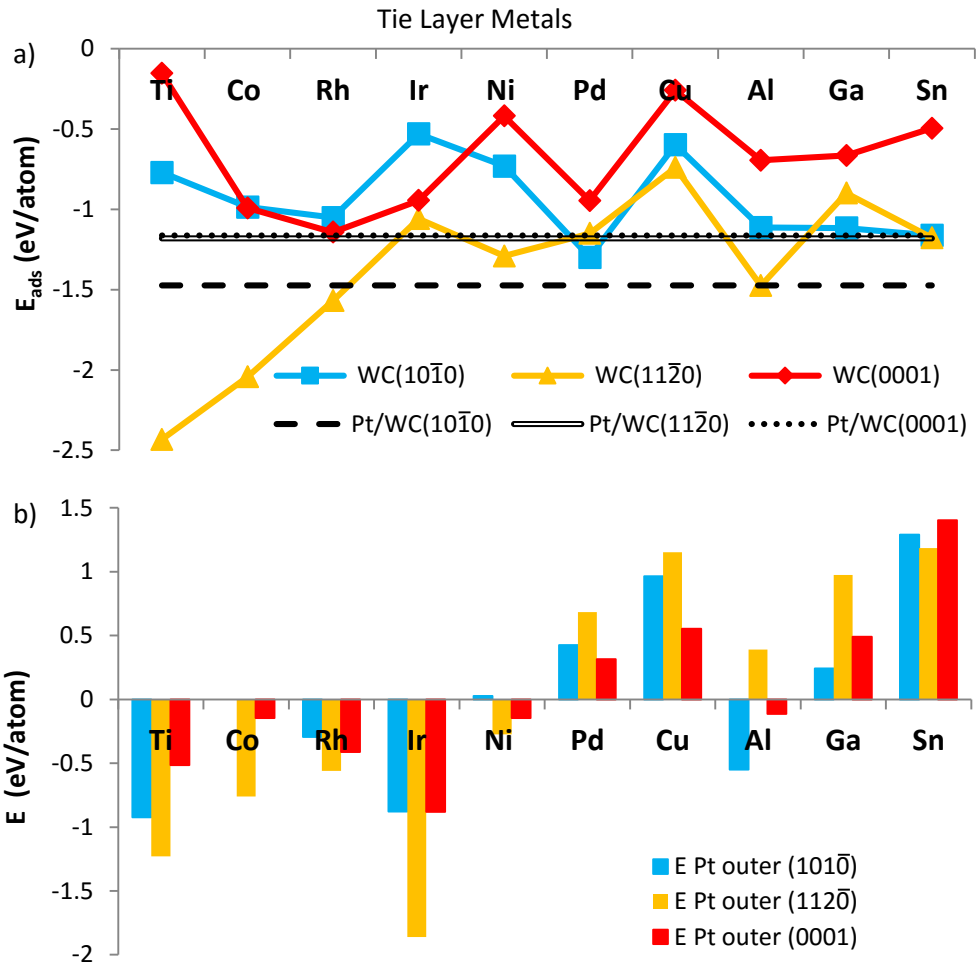

The second plot, figure 34 b), displays the stability of the Pt/tie-layer bilayered systems ($E_{Pt\ outer}$) as defined by equation 27. These $E_{Pt\ outer}$ calculations revealed that the group 9 elements as well as Ni, Ti and Al preferentially supported Pt as the outer layer on some or all facets. Whilst a lack of electronic convergence in the Co/Pt/WC(10$\bar{1}$0) prevented the calculation of a stability value for comparison with the other materials, the Pt/Co/WC(10$\bar{1}$0) system did not undergo significant simultaneous rearrangement and as such appeared to be at least metastable. Accordingly, sequential metal deposition should result in the required Pt/X/WC structure. For these metals, exposure to temperature should also result in segregation of a Pt-X alloy to give the desired tie-layer structure; this would be driven by the reduction of strain at the surface due to the larger Pt atomic radius.

As mentioned in the introduction, the work of Humbert *et al.* currently appears to be the only verification of the calculations at hand as Pt/Ni/WC(0001) was synthesised and Pt was found in the outer layer of the system as investigated using AES prior to and post annealing.[172] This is

encouraging since the predicted relative stability of Ir and Ti were much higher in the current work and so we propose that their ordering should prove to be thermally stable.

5.3 SiC

Given that Pt was predicted to adsorb to both SiC facets, a reduced group of tie-metals were selected for testing on SiC with the aim of altering Pt activity rather than promoting Pt adhesion. The main group elements were not included to allow for further calculations to be undertaken for the fcc carbides.

5.3.1 Geometry

Table 11 Vertical relaxation and $\Delta E_{M\text{-}SiC}$-$E_{M\text{-}M}$ data for SiC surfaces, X-SiC and D_{13} distances are measured from the surface M layer.

Tie-layers	(100)				
	X-SiC (Å)	D_{13} (M-M) (Å)	ΔD_{13} (%)	$E_{M\text{-}SiC}$ (eV/atom)	$\Delta E_{M\text{-}SiC}$-$E_{M\text{-}M}$ (eV/atom)
Co	1.58	2.21	0.4	-1.96	-1.18
Rh	1.68	2.20	0.2	-4.83	-1.10
Ir	1.69	2.20	0.4	-6.34	-0.51
Ni	1.54	2.19	-0.3	-3.86	-0.40
Pd	1.71	2.18	-0.8	-4.58	-1.27
Pt	1.67	2.19	-0.4	-5.98	-1.39
Cu	1.69	2.18	-0.7	-133.47	-0.18
Ag	1.82	2.14	-2.5	-2.51	-0.40
Au	1.84	2.17	-1.3	-3.19	-0.74
Zn	1.53	2.17	-1.4	-1.12	-0.39

Tie-layers	(111)				
	X-SiC (Å)	D_{13} (M-M) (Å)	ΔD_{13} (%)	$E_{M\text{-}SiC}$ (eV/atom)	$\Delta E_{M\text{-}SiC}$-$E_{M\text{-}M}$ (eV/atom)
Co	1.30	2.51	0.1	-2.35	-1.57
Rh	1.41	2.50	-0.3	-5.11	-1.38
Ir	1.41	2.49	-0.8	-6.56	-0.72
Ni	1.28	2.52	0.4	-4.01	-0.55
Pd	1.49	2.50	-0.6	-4.23	-0.93
Pt	1.44	2.49	-0.8	-5.56	-0.97
Cu	1.51	2.51	-0.3	-133.09	0.20
Ag	2.01	2.51	0.0	-1.88	0.24
Au	1.82	2.52	0.5	-2.31	0.14
Zn	2.16	2.51	0.0	-0.47	0.26

The X-SiC distances were observed to follow periodic trends lengthening upon descent of the groups and across the periods as seen in figure 35. Trends in the X-SiC bond lengths were mirrored regardless of facet although the (100) surface bond lengths were consistently shorter than those for (111) despite the lesser adsorption energies for tie-layers on the (100).

Figure 35 Trends in the X-SiC bond length for tie-layer metals on SiC(111)

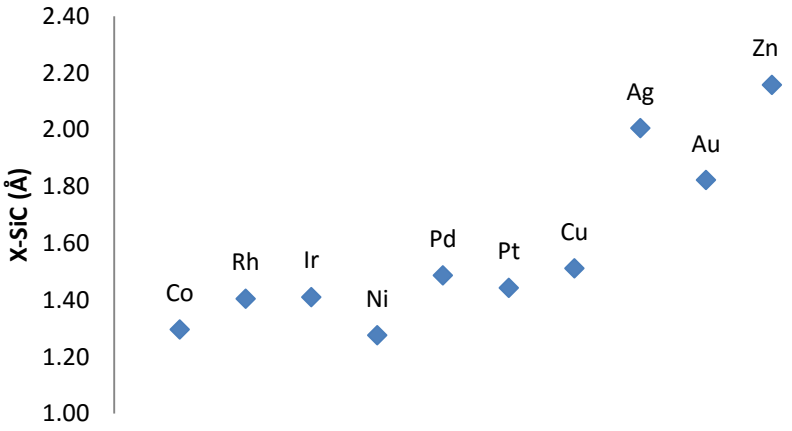

The geometry optimisation of Rh and Zn layers resulted in rippled overlayer structures, see figure 36. This rearrangement was undertaken to minimise the surface energy however this was not simply due to steric interaction; the calculated atomic radii of Rh and Zn are 1.73Å and 1.42Å respectively compared to the Pt radius of 1.78Å.[190]

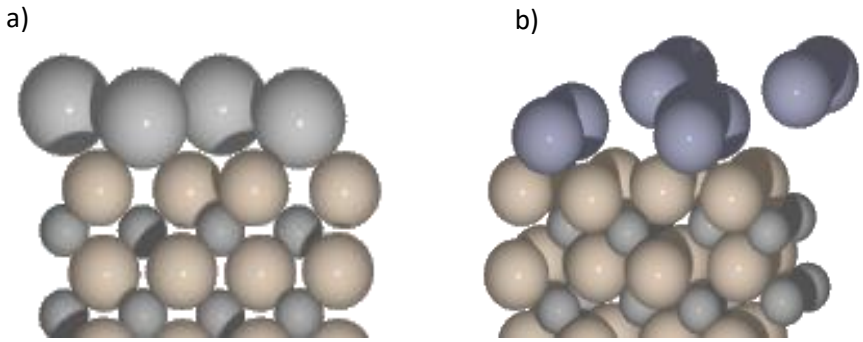

Figure 36 Trial tie-layer metals forming rumpled overlayers on SiC(100) a) Rh and b) Zn

From figure 37 significant differences could be observed between the electronic structures of the two systems. The Rh d-band in plot a) was partially filled, with a small amount of the valence band above E_f. This suggested that the metal could act as an electron acceptor as well as an electron donor in charge transfer with the surface. It was noted that the differences in the DOS plots of the higher and lower Rh layers were negligible and so that the small rumpling of the surface had not created Rh atoms in significantly different environments.

In contrast Zn, as a d^{10} metal had a fully filled d-band which was situated well below E_f. The Zn d-band also has a much narrower bandwidth signifying more localisation of the electrons. Topological analysis of the charge distribution revealed a minimal transfer of charge from the Zn to the carbide, with both Zn atoms experiencing a loss of 0.07-0.08 electrons. The rearrangement of the Zn surface resulted in the Zn closer to the carbide having a more negative d-band centre and therefore being more stable. In this case electronic stabilization was considered to be the driving force for the surface relaxation.

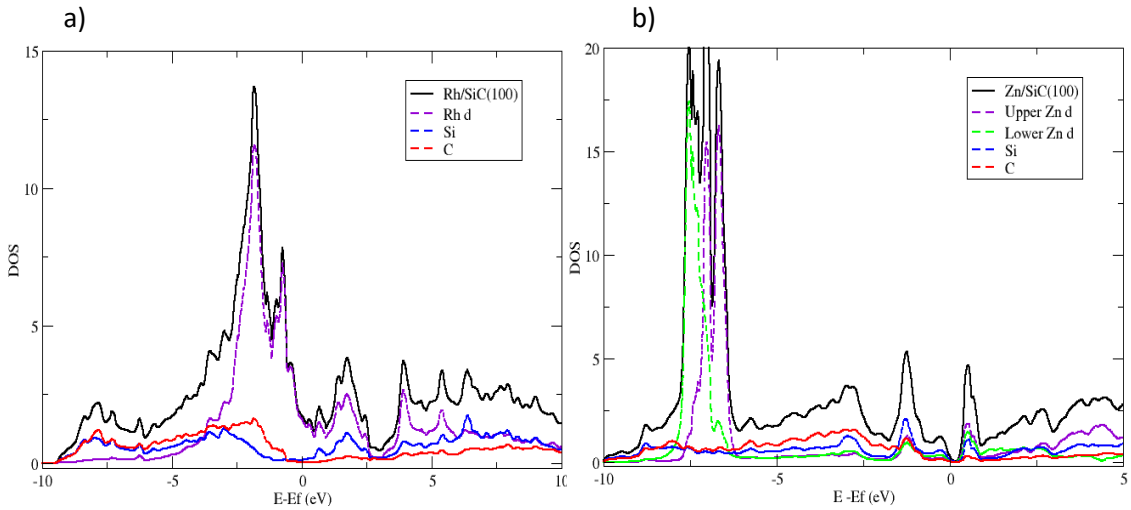

Figure 37 DOS plots for SiC(100) surface with adsorbed a) Rh 1ML and b) Zn 1ML

5.3.2 The Role of Electronic Structure in Adsorption

Having identified metals which were unfavourable to adsorption on the SiC(111), further investigation of the Zn and Ag monolayers was undertaken. Links between their electronic structures and adsorption behaviour were sought through comparison to the successfully adsorbed Pt and Rh/SiC(111) systems. Figure 38 displays the DOS plots for the X/SiC(111) systems with the tie-metal highlighted in purple in each case. Immediately noticeable was the difference in bandwidth for the d-band of the tie-metal. The Rh and Pt systems had bandwidths of 6 and 7 eV respectively whilst the Ag and Zn had bandwidths of 1 and 2 eV.

The surface specific characteristics of SiC were highly dependent on facet. Whilst the (100) surface formed a broad valence band covering -10 to 0eV, the SiC(111) had a strong surface resonance at -2 eV as identified in chapter 3 figure 16. In chapter 4 figure 22 we observed that it was involved in the adsorption of Pt. The excellent overlap between the Pt and Rh d-bands and the SiC SR was the reason for the very strong adsorption. The fact that the Ag and Zn d-band are located so

negatively, leaving no electron density at the resonance would suggest that overlap here was impossible; hence the failure to adsorb.

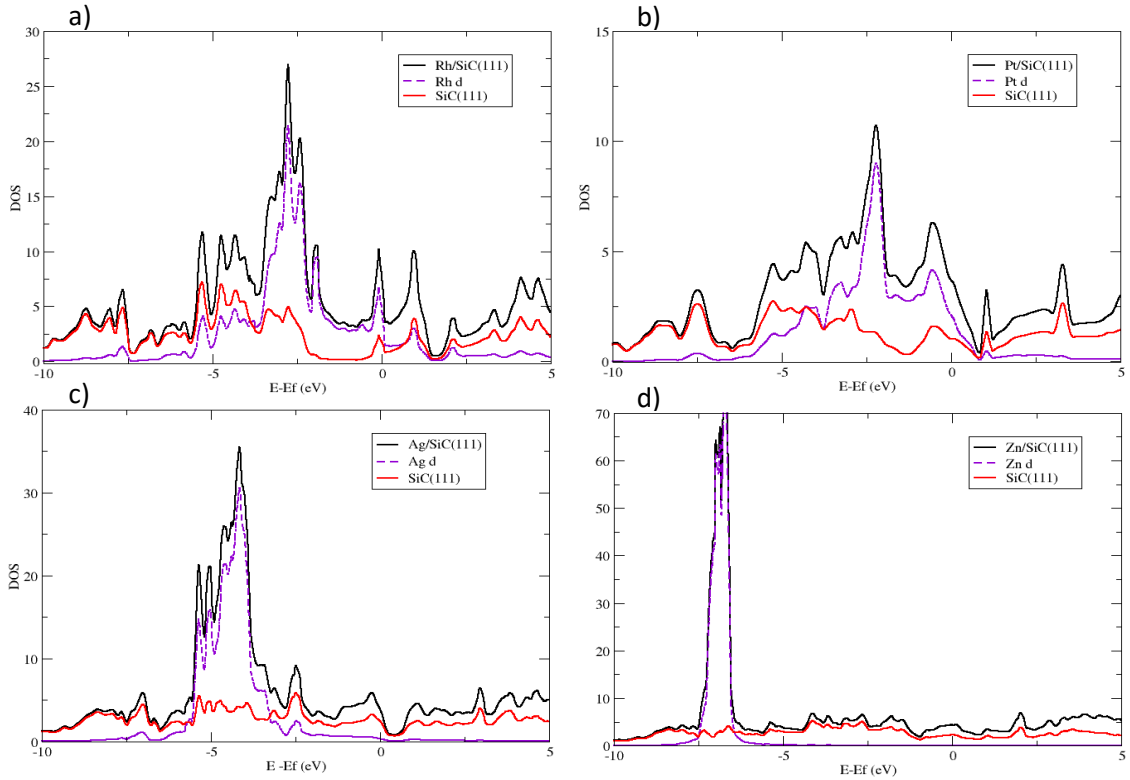

Figure 38 DOS plots for tie-metals on SiC(111) surfaces a)Rh b)Pt c)Ag and d) Zn

It was therefore suggested that the bandwidth and positioning of the proposed tie-layer metal d-band were key, and that E_d within a certain range of the carbide surfaces E_{TMSR} might be a descriptor for overlap and adsorption. To test this, the DOS for the bulk tie-layer metals were calculated and their E_d values collected. The effect of the electron filling could clearly be seen in the E_d values for the TMs in table 12. Across the period, as the number of d electrons increased the E_d became more negative, the bandwidth was also reduced which can be observed in figure 39.

Table 12 E_d values for the tie-layer metals, for main group metals, the value given is the centre of the valence band

Metal	E_d (eV)
Ti	1.27
Nb	1.43
Ta	1.76
W	0.49
Co	-1.13
Rh	-1.93
Ir	-2.35
Ni	-1.28

Metal	E_d (eV)
Pt	-2.47
Cu	-2.38
Ag	-3.95
Au	-3.34
Zn	-7.12
Al	0.90
Ga	-0.99
Sn	-0.24

Figure 39 d-band DOS for bulk 1st 2nd and 3rd row TM. Top row: Ti, Co, Ni, Cu, Zn, second row: Nb, Rh, Pd, Ag, bottom row: Ta, W, Ir, Pt and Au. Structures are shaded according to crystal structure, red: BCC, orange: hcp and yellow: FCC. Red line denotes E_f , green the -2eV SiC SR

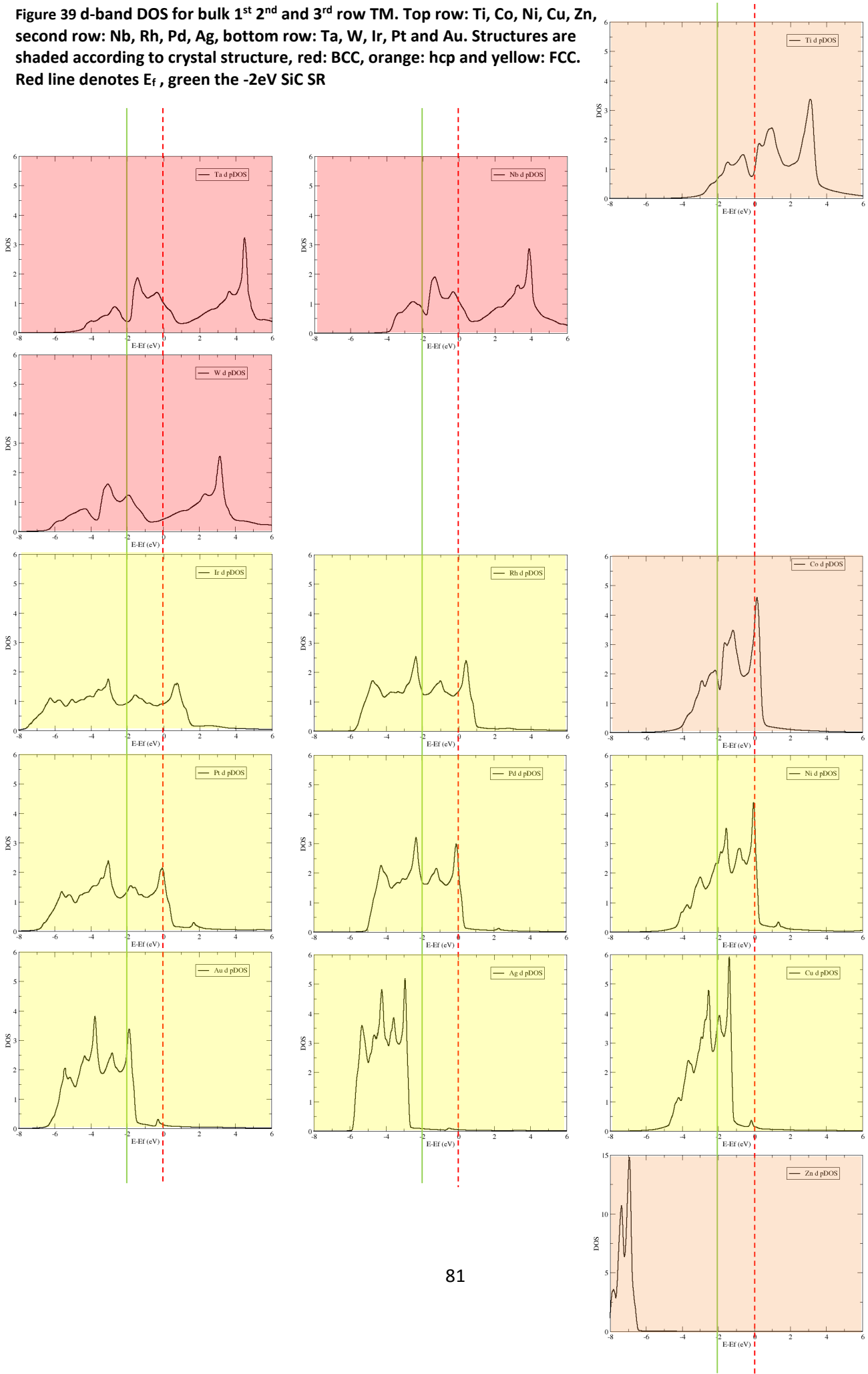

Whilst it was facile to discount metals for which the valence band was below -2 eV (denoted by the green line in figure 39) such as Ag and Zn as no orbital overlap was possible, it was instructive in this case to consider elements with similar E_d but different adsorption outcomes. In the case of Pt (-2.47) and Cu (-2.38) the bandwidth and the proximity of the 'top' of the valence band to the SR of the support were crucial to the resultant adsorption. At this point, it should be noted again that the values presented here are for the bulk metals. From Chapter 4 we are aware that surfaces have less negative E_d values, for Pt this difference is in the range of 0.5 eV, whilst the general appearance of the states remains unchanged.

Figure 41 DOS plots showing the shift of the metal d-band for Au/SiC(111) and Cu/SiC(111)

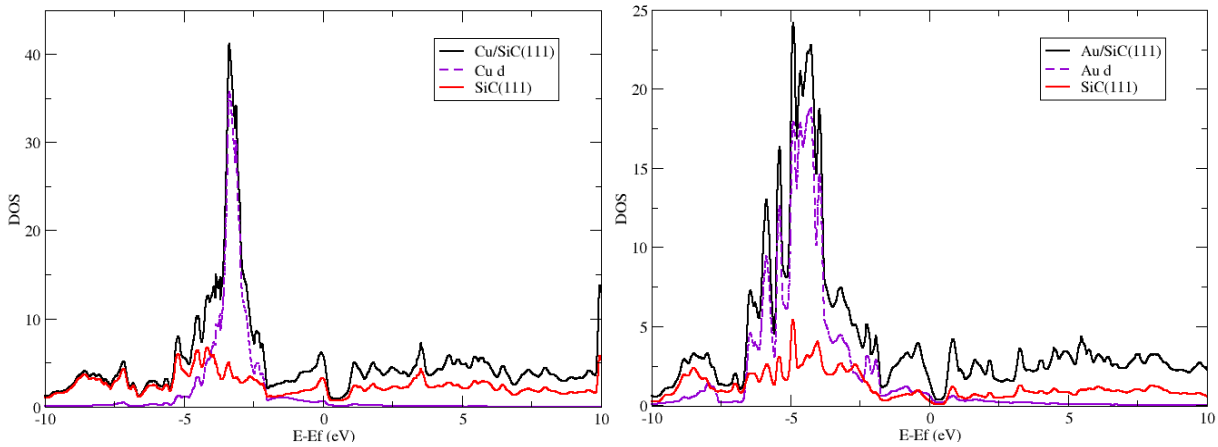

Since placing the tie-layer on the carbide surfaces resulted in a negative shift and narrowing of the d-band, as previously noted, the Cu d-band could not sustain overlap with the SiC SR. Figure 40 clearly shows a lack of DOS at -2eV for both Cu and Au and explained their failure to adsorb. From these examples it was clear that more than 1eV overlap was necessary between the metal DOS and the clean surface SR. As we considered the later carbides, this idea was further developed. Initially however we could state that the adsorption of the early and mid TMs on SiC was expected as these metals exhibited broad d-bandwidth and unfilled valence bands which should allow for electron acceptance as well as donation. The group 11 elements share the d^{10} s^1 configuration and so their filled valence bands descend below E_f meaning they are only available for electron donation whilst also limiting the potential overlap with carbide surface resonances.

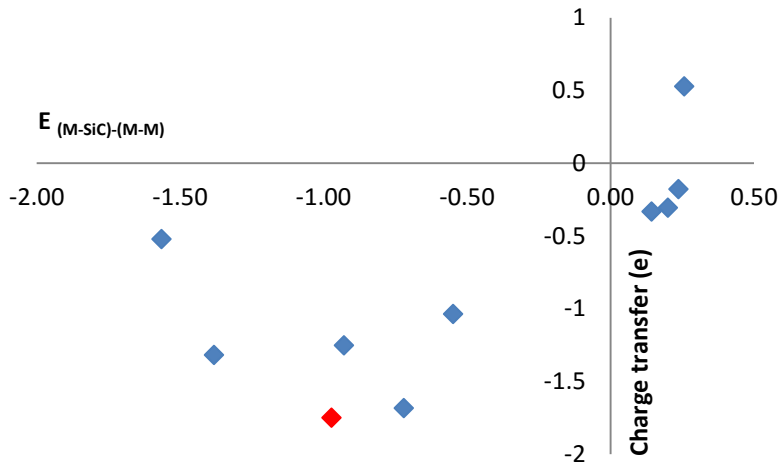

Figure 42 Plot of charge transfer from SiC(111) surface to tie-layer metals shown relative to $E_{(M\text{-}SiC)\text{-}(M\text{-}M)}$, the red data point signifies Pt.

Charge transfer analysis shown in table 13 suggested that in the majority of cases where significant electron donation to the tie-metal was possible, a stable X-SiC bond was formed. Conversely, when charge transfer to the tie-layer was minimal or electron donation occurred from the tie-layer (as in the case of Zn) adsorption was predicted to be unfavourable.

Table 13 Charge Transfer data for Pt/X/SiC systems.

Layer	Co		Rh		Ir		Ni		Pd	
	100	111	100	111	100	111	100	111	100	111
Pt	-0.36	-0.28	-0.21	-0.20	-0.16	-0.16	-0.29	-0.28	-0.16	-0.19
Tie	0.07	-0.52	-0.62	-1.32	-1.01	-1.68	-0.14	-1.04	-0.79	-1.25
Si	1.82	1.57	2.35	2.32	2.68	2.65	1.96	2.09	2.48	2.26
C1	-3.05	-3.08	-3.06	-3.12	-3.06	-3.12	-3.07	-3.08	-3.07	-3.11
Si	3.07	3.07	3.07	3.10	3.08	3.10	3.08	3.07	3.07	3.09
C2	-3.07	-3.08	-3.08	-3.09	-3.08	-3.09	-3.08	-3.08	-3.09	-3.09

Layer	Cu		Ag		Au		Zn	
	100	111	100	111	100	111	100	111
Pt	0.11	0.07	-0.04	0.09	-0.15	-0.10	-0.46	-0.37
Tie	-0.34	-0.30	-0.24	-0.18	-0.89	-0.33	0.53	0.53
Si	1.79	1.06	1.85	0.83	2.58	1.16	1.53	0.64
C1	-3.08	-2.91	-3.10	-3.06	-3.08	-3.05	-3.10	-3.10
Si	3.08	2.90	3.09	3.08	3.06	3.07	3.08	3.09
C2	-3.08	-2.90	-3.08	-3.09	-3.08	-3.07	-3.08	-3.09

5.3.3 Tie-Layer Stability

We then moved to consider the probability of Pt surface tie-layer systems being formed. As shown in figure 42 a), on the SiC(100) surface, Pt was predicted to adsorb more strongly than any tie-

metal. The Co, Rh and Pd adsorption energies were seen to be comparable to that of Pt which would suggest that Pt would be predominant on the (100) surfaces but that Co, Rh and Pd should also form stable monolayers. Ir and Ni were also predicted to favourably adsorb to the SiC(100) surface but considerably more weakly than Pt. Excellent overlap of the Co and Rh d-bands on the SiC(111) surface led to the prediction of preferential adsorption whilst Pd adsorption was again predicted to be of comparable strength to that of Pt. In the case of Co and Rh Pt/X/SiC(111) arrangements would be expected.

Figure 43 a) Tie-layer adsorption energies for 1ML on SiC compared to Pt and b) stability with respect to Pt as the outer layer on SiC surfaces

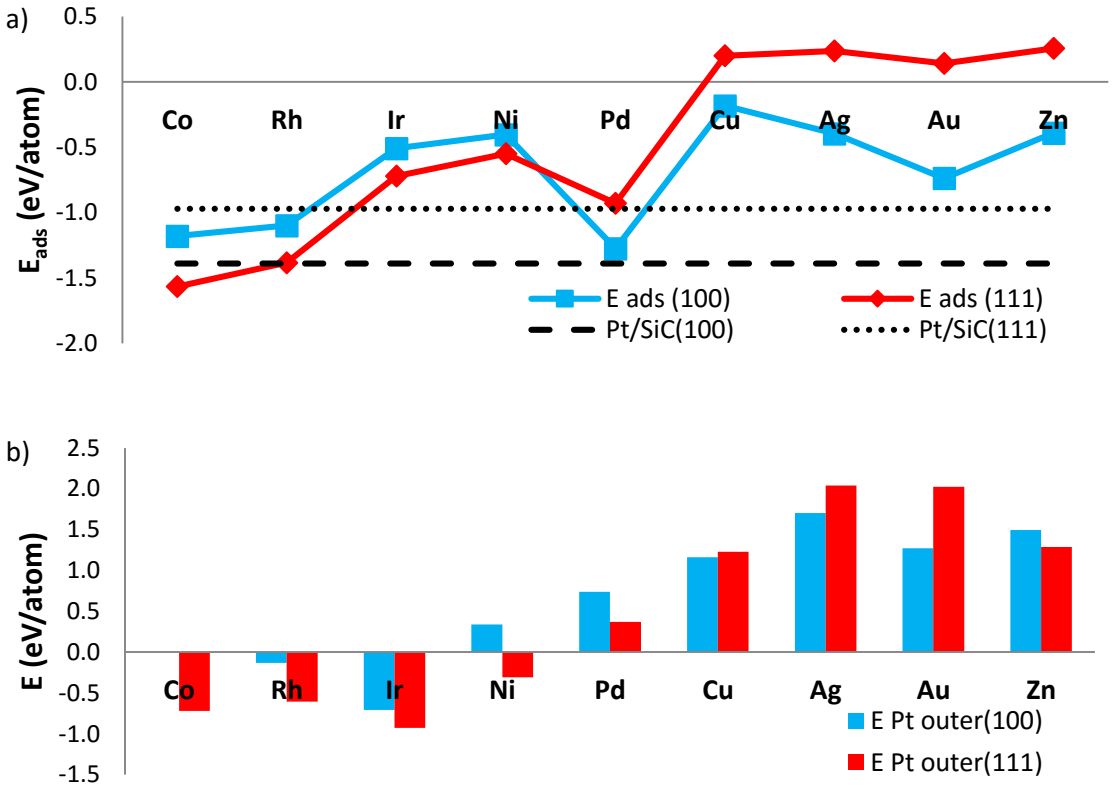

Considering figure 42 b), in addition to stable Co and Rh (111) systems, Ir was also observed to favour Pt-outer skin formation and the Rh/SiC(100) systems was also predicted to be favourable towards the Pt/X/SiC configuration. Closer inspection of the Pt/Co/SiC(100) system revealed mixing within the overlayer to produce PtCo alloys regardless of initial metal ordering. Loss of the bilayer structure prevented a comparative value for the instability of this system but the possibility of excess Pt causing the desired Pt-outer layer was noted.

Whilst the stability of the Pt/Ir/SiC systems initially appeared surprising given Ir's much weaker E_{ads}, Ir and Rh's ability to alloy with Pt are well documented[76] and bilayer and core-shell PtIr and PtRh particles have been widely reported.[61,193] In the case of Ir and Rh then, the strongly favourable bonding interaction with Pt had improved the stability of the system. The (100) surface energies of Rh and Ir are 1.310 and 1.772 eV/atom in comparison to Pt(100) 1.378 eV/atom.[162] The desire to minimise surface energy provided the thermodynamic driving force behind the Pt-outer skin formation and high Pt/Ir/SiC(100) stability.

Figure 44 DOS plots for Rh applied as a tie-layer on SiC surfaces a) Rh/Pt/SiC(100) b) Pt/Rh/SiC(100) c) Rh/Pt/SiC(111) d) Pt/Rh/SiC(111) e)Pt/Ir/SiC(100) and f) Pt/Ir/SiC(111)

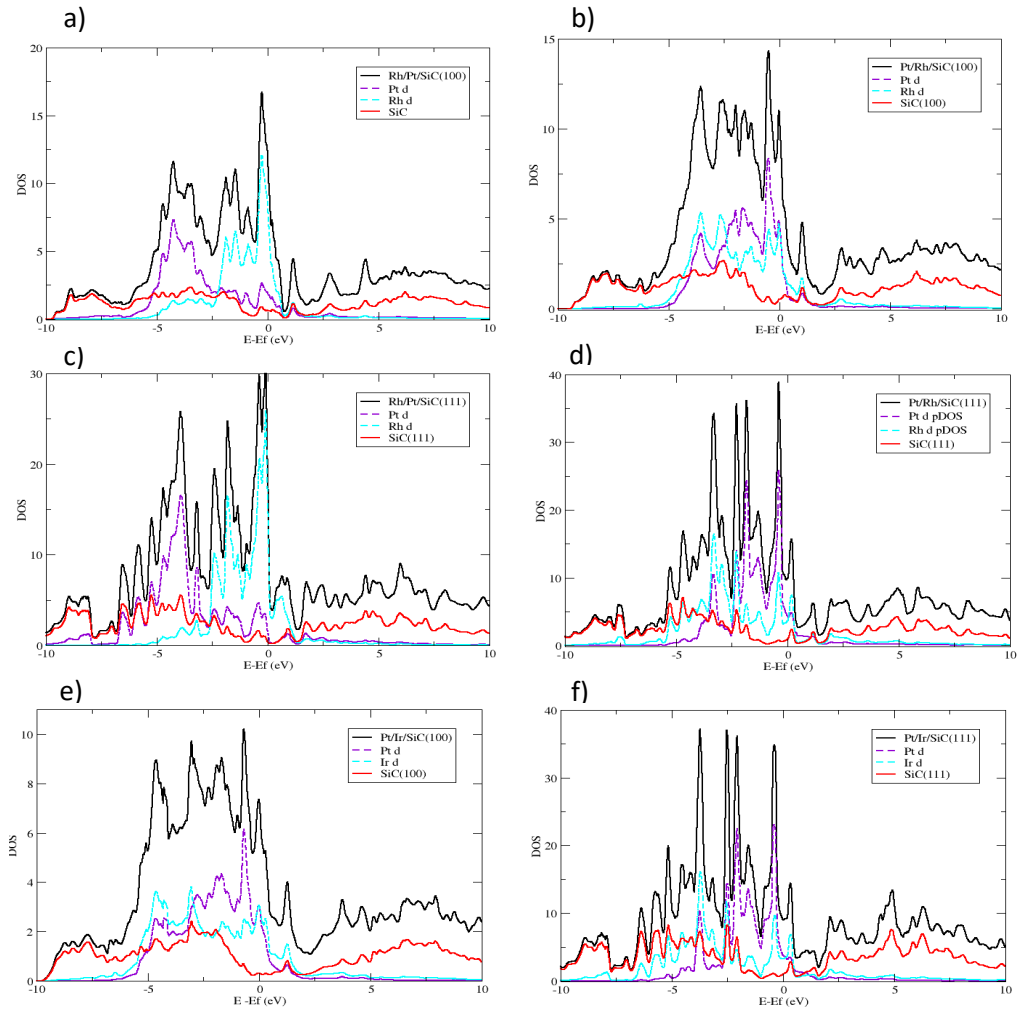

For the Rh systems we turned to consider the electronic structure of the alternative metal orderings. The DOS plots in figure 43, revealed that when that when the tie-metal was in contact with the carbide, the d-band remained broad, allowing excellent overlap with the outer layer Pt and the surface resonance in the case of the (111) facets. By contrast, when Pt was in contact with the carbide its d-band narrowed and shifted negatively, allowing little overlap with the other metal. In this respect then it appears that intermediate E_{ads} coupled with a broad tie-metal bandwidth are essential for stable Pt-outer layer formation.

5.4 TiC

The TiC(100) surface specific features were noted at -2 and +3 eV whilst the TiC(111) surface was observed to have a TMSR at 0eV and a mixed C/TM SR centred at -3eV . The fcc TMCs were previously noted not to adsorb Pt on the (100) surface and this was found to extend to all the TM tie-layer metals trialled on TiC(100) although the $E_{M\text{-}M}$ of Pd and Zn were only marginally greater than $E_{M\text{-}TiC}$. Alternative metals with a range of physical properties and available ALD precursors were chosen from the p-block: Al, Ga and Sn. These metals were observed to adsorb on TiC(100) with Sn having the greatest E_{ads}. For the (111) surface Pt adsorption was stronger than those calculated for the possible tie-layer metals. Whilst the other PGMs and main group metals tested had intermediate to strong E_{ads} values, additional Ti was not adsorbed at the surface.

5.4.1 Geometry

Table 14 Vertical relaxation and $\Delta E_{M\text{-}TiC}$-$E_{M\text{-}M}$ data for TiC surfaces, X-TiC and D_{13} distances are measured from the surface M layer.

Tie-layers	(100)				
	X-TiC (Å)	D_{13} (M-M) (Å)	ΔD_{13} (%)	$E_{M\text{-}TiC}$ (eV/atom)	$E_{(M\text{-}TiC)\text{-}(M\text{-}M)}$ (eV/atom)
Ti	2.167	2.105	-0.3	-5.00	0.22
Co	1.87	2.13	0.8	-0.61	0.17
Rh	1.93	2.13	1.0	-3.50	0.23
Ir	1.89	2.15	1.6	-4.88	0.96
Ni	1.86	2.12	0.5	-2.85	0.60
Pd	2.06	2.13	0.8	-3.24	0.06
Pt	1.98	2.15	1.5	-4.34	0.25
Cu	2.03	2.13	0.7	-132.70	0.58
Ag	2.368	2.125	0.6	-1.74	0.37
Au	2.284	2.133	1.0	-2.15	0.31
Zn	2.196	2.122	0.5	-0.72	0.02
Al	2.15	2.107	-0.2	-3.41	-0.23
Ga	2.333	2.107	-0.2	-2.60	-0.35
Sn	2.395	2.096	-0.8	-3.52	-0.49

Tie-layers	(111)				
	X-TiC (Å)	D_{13} (M-M)	ΔD_{13} (%)	$E_{M\text{-}TiC}$ (eV/atom)	$E_{(M\text{-}TiC)\text{-}(M\text{-}M)}$ (eV)
Ti	2.396	2.457	-0.1	-4.99	0.23
Co	1.88	2.50	1.7	-1.57	-0.78
Rh	1.94	2.50	1.4	-4.79	-1.06
Ir	1.95	2.50	1.4	-6.49	-0.66
Ni	1.87	2.51	2.1	-3.75	-0.29
Pd	2.02	2.46	0.1	-4.49	-1.19
Pt	1.99	2.46	0.2	-6.03	-1.44
Cu	2.04	2.44	-0.7	-133.59	-0.30
Ag	2.303	2.432	-1.1	-2.78	-0.67
Au	2.171	2.437	-0.9	-3.65	-1.19
Zn	2.166	2.441	-0.7	-1.37	-0.63
Al	2.261	2.448	-0.4	-3.91	-0.73
Ga	2.224	2.445	-0.6	-3.19	-0.94
Sn	2.559	2.433	-1.1	-4.07	-1.05

The fcc carbide surfaces also exhibited periodic trends in the bond length of the transition metals to the TiC surfaces with the length increasing down the group and across the period. However, little relation was observed between the bond length and the adsorption energy of the tie-layers to the TiC. The successful adsorption of the main group metals led to a contraction of the carbide (100) surface whilst moderate surface expansion was noted elsewhere.

5.4.2 Electronic Structure Contributions to Adsorption

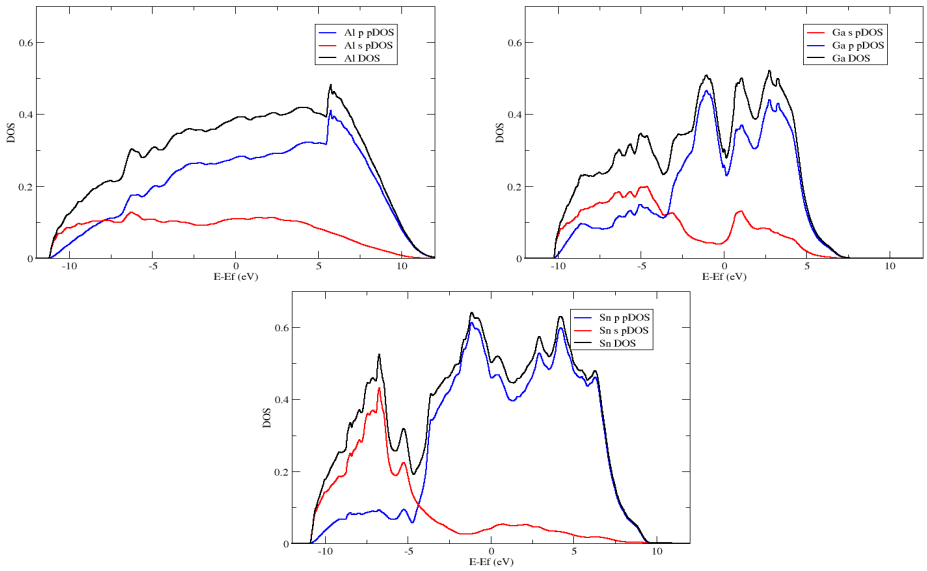

Figure 45 DOS plots for Al, Ga and Sn bulk metals

The lack of adsorption of extra Ti onto the TiC surface can be understood in light of the limited possible overlap with the SR suggested by the positioning of the d-band (see figure 39). Strong adsorption of the group 9 metals was expected given the increased d-band filling leading to more negative E_d values proximate to the CSR. However, the increased bandwidth down the group did not favour the strong adsorption of Ir. Increased d-band filling across the periodic table resulted in the descent of the completed Cu, Ag and Au d-bands well below E_f and prevented overlap with the TiC TMSR at 0eV. The strong adsorption of Au was unexpected and suggests that the adsorption was principally through an interaction with the C/TM SR. Given these results the prediction of adsorption behaviour in relation to a single SR would not seem to adequately describe the necessary interactions. The very broad bands of the main group metals seen in figure 44 would allow overlap with both the TM and C/TM SRs.

5.4.3 Tie-Layer Stability

From table 14 we observed that Ti and Ir have stronger $E_{M\text{-}TiC}$ values than Pt, however due to their higher $E_{M\text{-}M}$ values this did not result in favourable 1ML adsorption. Figure 45 a) shows that only the main group metals are predicted to adsorb to the TiC(100) surface. In the case of the (111) surface, bar Ti all of the metals were predicted to adsorb to the TiC surface although none of them as strongly as Pt itself.

Calculations of the stability of the Pt-outer layer shown in figure 45 b) suggested that of the metals which are predicted to adsorb on to TiC(100)surface, Al and Ga were most likely to form Pt-outer layer structures. Although Al and Ga were predicted to adsorb to the TiC(111) surface, the adsorption preference for Pt resulted in a subsurface Pt layer in contact with the carbide support. Ti, Rh and Ir were also calculated to favour Pt/X/TiC structures on both facets, however given the unfavourable adsorption energetics for the (100) surface it is unlikely that the adsorption of the overlayer would take place and agglomeration of the metal would be more likely. Ir/TiC(111) was predicted to be the most favourable system to support a Pt-outer skin. Co containing systems experienced significant Pt mixing with the Co layer suggesting instability of the bilayer system but preventing a numerical comparison of $E_{Pt\ outer}$ values.

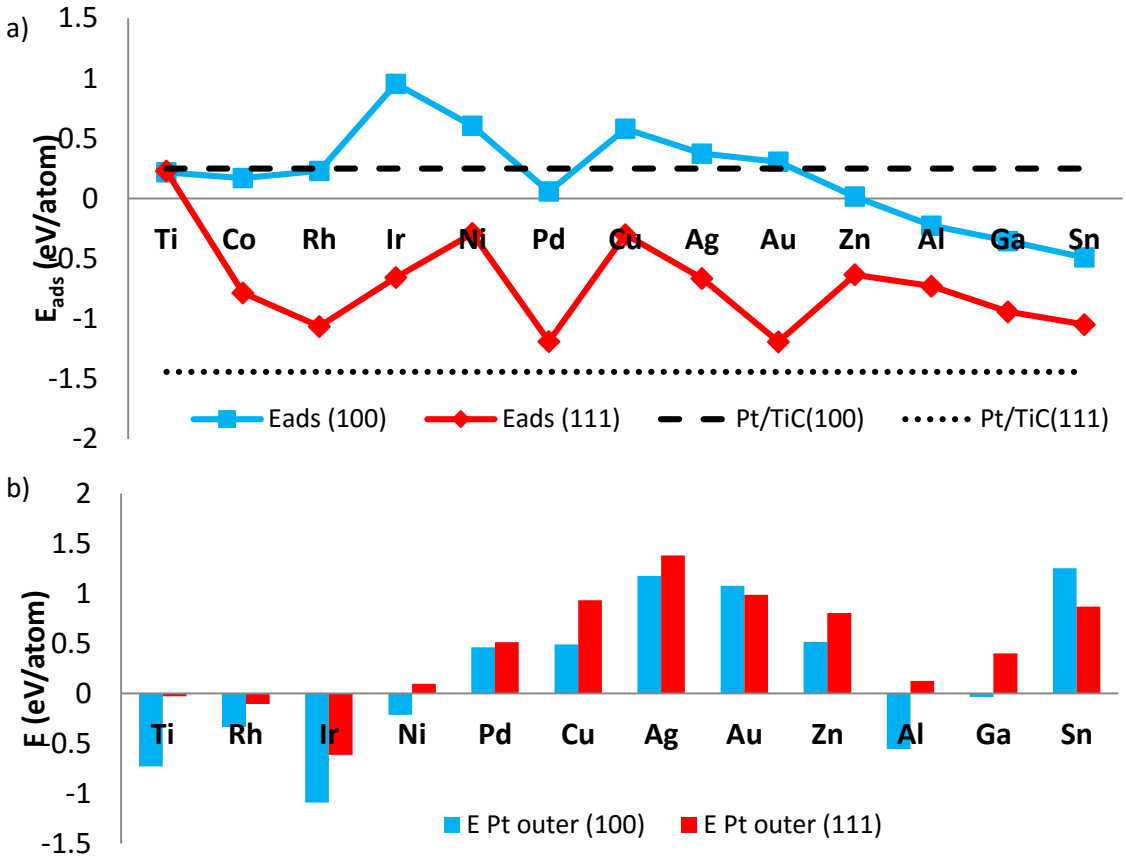

Figure 46 a) Tie-layer adsorption energies for 1ML on TiC surfaces and b) stability with respect to Pt as the outer layer on TiC surfaces. Failure of electronic convergence in the Co/Pt/TiC systems prevents data report

From the DOS plots of figure 46 we can observe the alteration in bonding between the Pt, tie-metal and TiC surfaces for each of the (100) systems favourable towards Pt-outer skin formation. The $E_{Pt\ outer}$ values indicated stabilities in the order Ir>Al>Rh. For the TM tie-layers we can see bandwidth maintained in the tie-layer and excellent overlap with the Pt indicating a large degree of covalence. This was also borne out by the broadening of the TiC valence band. In the case of Al, the valence electronic structure of the tie-layer led to good overlap with the TiC s- and p-contributions whilst the Pt overlapped strongly with the SR at -2eV. In this case the pronounced valence and conduction bands of the TiC(100) surface were largely maintained as the Al did not interact significantly with the Ti d-band to result in band broadening.

The (111) stability results indicated Ir>>Rh whilst Al was unfavourable to Pt-outer layer structure formation. The previously suggested link between stability and the larger bandwidth at the TMSR was corroborated by the comparison of Ir and Rh DOS. The Ir d-band provided overlap through the whole length of the valence band whilst Rh overlapped with the CSR at -3eV. In these cases the pseudogap at E_f was maintained for the TiC. In the case of Al where the Pt/Al/TiC(111) system

was unstable, the conduction band of the TiC was shifted below E_f causing the instability. The Pt in this system also seemed to be strongly overlapped with the CSR rather than the TMSR.

Figure 47 DOS plots showing variation in tie-layer stability to Pt forming the outer shell a) Pt/Rh/TiC(100) b) Pt/Rh/TiC(111) c) Pt/Ir/TiC(100) d) Pt/Ir/TiC(111) e) Pt/Al/TiC(100) and f) Pt/Al/TiC(111)

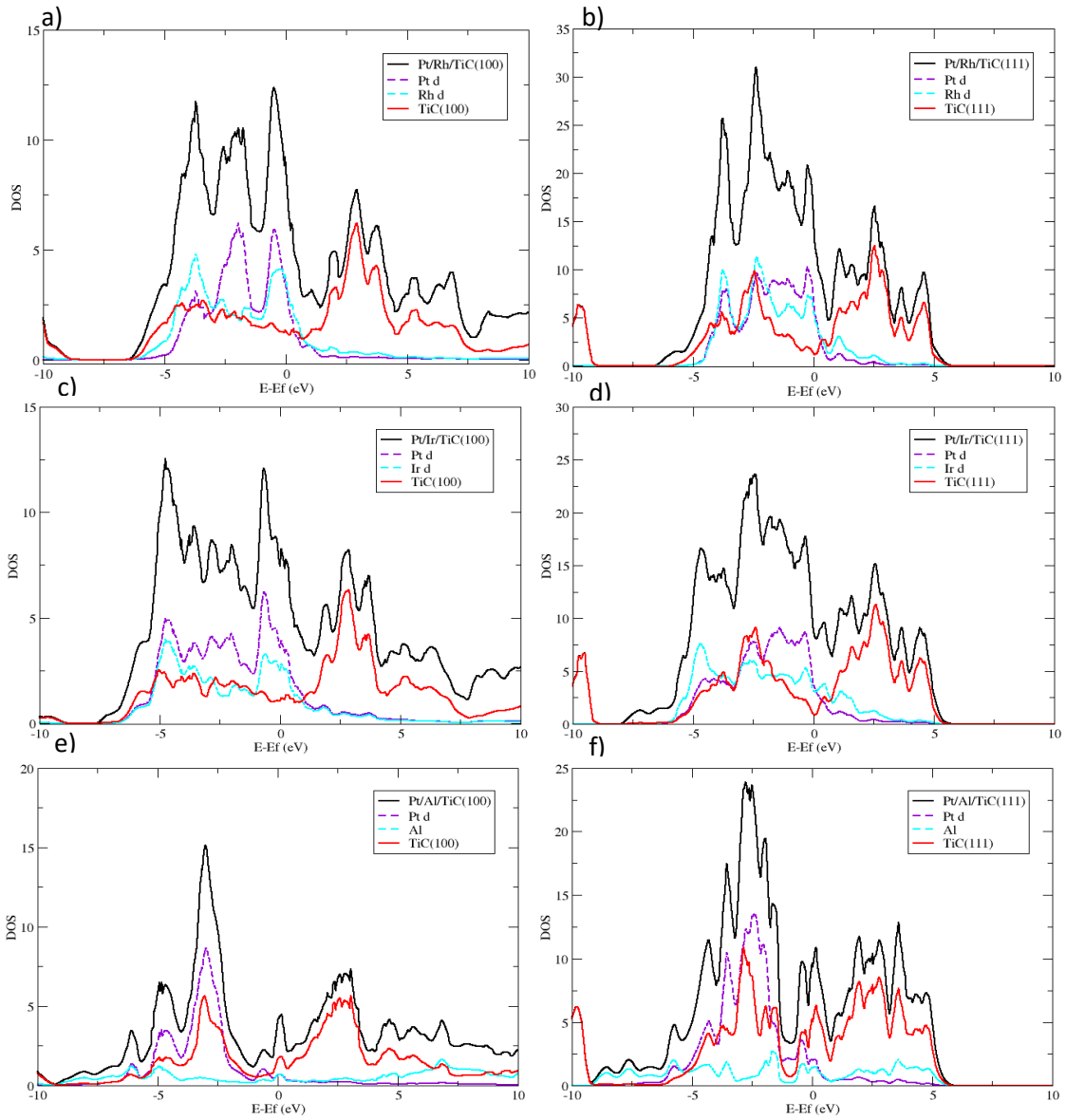

Tie-layer metals with unfilled d-bands were observed to donate rather than accept electron density whilst in contact with the TiC surfaces. The most promising systems with regard to stable Pt/X/TiC(111) formation (Ir and Rh) experienced minimal charge transfer to the tie- layer, see table 15, in keeping with the large degree of covalence previously mentioned. Charge build-up was noted on the Pt surface for the PGM tie-layers, with (100) surfaces calculated as being more negative than the (111). Ti and the main group metals were observed to lose a considerable amount of charge to the surface Pt due to excellent orbital overlap with the (100) surfaces.

Table 15 Charge Transfer data for Pt/X/TiC systems

Layer	Ti		Rh		Ir		Pd		Cu		Ag	
	100	111	100	111	100	111	100	111	100	111	100	111
Pt	-1.06	-0.67	-0.25	-0.17	-0.19	-0.13	-0.20	-0.14	-0.41	-0.25	-0.25	-0.18
Tie	1.35	0.55	0.04	-0.39	-0.04	-0.47	-0.04	-0.41	0.32	-0.20	0.13	-0.25
Ti 1	1.57	1.10	1.63	1.49	1.61	1.53	1.64	1.51	1.64	1.44	1.66	1.43
C 1	-1.78	-1.73	-1.44	-1.70	-1.44	-1.70	-1.43	-1.71	-1.55	-1.72	-1.53	-1.74
Ti 2	1.59	1.63	1.60	1.63	1.61	1.64	1.60	1.62	1.61	1.62	1.60	1.62
C 2	-1.68	-1.66	-1.63	-1.66	-1.61	-1.66	-1.63	-1.67	-1.63	-1.67	-1.66	-1.67

Layer	Au		Zn		Al		Ga		Sn	
	100	111	100	111	100	111	100	111	100	111
Pt	-0.10	-0.46	-0.57	-0.37	-1.94	-1.45	-0.72	-0.46	-0.95	-0.64
Tie	-0.14	-0.11	0.61	0.00	1.61	1.32	0.87	0.09	1.22	0.31
Ti 1	1.66	1.53	1.65	1.38	1.62	1.62	1.63	1.38	1.58	1.33
C 1	-1.44	-1.72	-1.64	-1.75	-2.10	-1.73	-1.69	-1.74	-1.80	-1.73
Ti 2	1.61	1.62	1.62	1.62	1.62	1.64	1.59	1.62	1.58	1.62
C 2	-1.64	-1.67	-1.66	-1.67	-1.66	-1.67	-1.67	-1.67	-1.67	-1.67

Whilst Ir theoretically favoured the formation of Pt-outer layered structures on both surfaces, the initially unfavourable adsorption of Ir on the (100) surface suggests that this would be experimentally unviable. However, the use of Al on the (100) facet might may be able to improve Pt adsorption allowing for full encapsulation with Pt covering the (111) to protect the carbide.

5.5 NbC

As with other fcc carbides, NbC was predicted to have favourable adsorption for Pt on the (111) facet but not the (100). The (111) TMSR was centred at -1eV whilst for the (100) surface a mostly C-character SR was previously noted at -3eV (see chapter 3 figure 14). The tie-layer adsorption data shown in table 16 revealed that only Co and Al were predicted to favourably absorb onto the (100) surface although the $E_{(M\text{-}NbC)\text{-}(M\text{-}M)}$ values of Ti and Rh were less unfavourable than Pt . The group 9 TMs and Ni adsorbed preferentially to the (111) surface as did Al, although Pt was still predicted to be the most strongly adsorbed metal.

5.5.1 Geometry

Table 16 Vertical relaxation and $\Delta E_{M\text{-}NbC}$-$E_{M\text{-}M}$ data for NbC surfaces, X-NbC and D_{13} distances are measured from the surface M layer.

Tie-layers	(100)				
	X-NbC (Å)	D_{13} (M-M) (Å)	ΔD_{13} (%)	$E_{M\text{-}NbC}$ (eV/atom)	$\Delta E_{M\text{-}NbC}$-$E_{M\text{-}M}$ (eV/atom)
Ti	2.12	2.15	-0.1	-5.22	0.00
Nb	2.135	2.153	0.1	-7.27	0.38
Ta	2.21	2.16	0.4	-5.82	0.79
Co	1.77	2.24	3.8	-0.94	-0.16
Rh	1.89	2.28	5.8	-3.69	0.04
Ir	1.80	2.32	7.2	-5.12	0.71
Ni	1.86	2.21	2.7	-3.19	0.26
Pt	1.96	2.27	5.2	-4.49	0.10
Al	2.21	2.16	0.4	-3.23	-0.04

Tie-layers	(111)				
	X-NbC (Å)	D_{13} (M-M) (Å)	ΔD_{13} (%)	$E_{M\text{-}NbC}$ (eV/atom)	$\Delta E_{M\text{-}NbC}$-$E_{M\text{-}M}$ (eV/atom)
Ti	2.39	2.48	0.3	-4.98	0.24
Nb	2.391	2.492	0.8	-7.20	0.45
Ta	2.40	2.50	1.0	-6.12	0.48
Co	1.90	2.53	2.1	-1.29	-0.51
Rh	1.98	2.52	1.7	-4.42	-0.69
Ir	2.00	2.52	1.8	-6.01	-0.17
Ni	1.84	2.51	1.5	-3.55	-0.09
Pt	2.04	2.51	1.4	-5.63	-1.04
Al	2.28	2.49	0.6	-3.74	-0.55

X-NbC distances increased down the group whilst across the period of 3d metals for the (111) surface there was a decrease in bond length. For the (100) 3d metals however the order of Co and Ni bond lengths was reversed. On the (100) surface, whilst no significant vertical rumpling was observed, there was noticeable horizontal rearrangement as the overlayer optimised during the calculation run. The Ti, Co and Ni atoms shifted relative to their initial sites above C in order to reduce the distance to the next tie atom. This shift occurred most significantly for Co and Ni leaving intra-layer tie-metal distances of 2.791Å and 2.624Å respectively and resulting in the formation of tie-layer 'chains' on the carbide surface as shown in figure 47. These rearrangements stabilized the system surface energies, promoting adsorption. Addition of the tie-layer metals also resulted in the expansion of the first bilayer of the carbide, this was most pronounced for the (100) surface, particularly in the cases of Rh and Ir.

Figure 48 Ni and Co surface layer relaxations

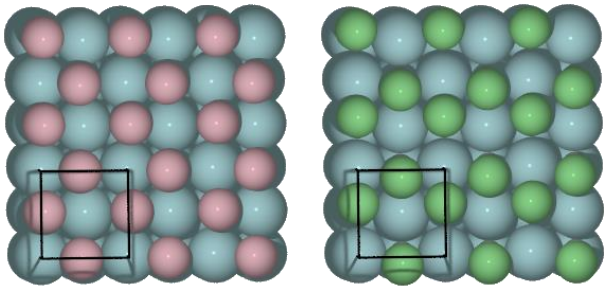

5.5.2 Electronic Structure Contributions to Adsorption

Electronically, the metals that adsorb to the (100) surface are diverse; main group Al as seen in figure 44 has a broad featureless DOS with partially filled s and p bands whilst around the E_f d^7 Co consists mostly of filled d-bands with an E_d of -1.13. Using overlap with the -3eV CSR as our adsorption criteria, the analysis suggested that Rh, Ir , Ni, Pd and Pt should also be adsorbed on to the carbide however this was not the case. Whilst the Rh-carbide interaction was calculated to be more favourable than that of Pt, the adsorption of Ir was predicted to be strongly disfavoured.

Figure 48 shows the DOS of the preferentially adsorbed metals and those which show some potential of being more favourable towards adsorption than Pt as well as the previously mentioned Ir system. Plot a) shows the strong overlap and interaction of the Al and Nb d-band in the valence band between -7 and -2eV and the contribution of density in the pseudo bandgap. Significant NbC peak broadening was noted below E_f indicating covalence in the bonding. For the each of the TM tie-layers, some TM d-band overlap with the CSR at -3eV was observed but the major feature of all the plots was a significant narrowing of the tie-metal d-band and the alteration of the carbide pseudogap size.

It appears the positioning of the tie-metal d-band maximum in relation to the NbC valence and conduction bands governs the strength of the interaction with the carbide surface. In the case of Co, plot c), the d-band contribution fell in the centre of the pseudogap, avoiding interaction with the conduction band maximum above E_f or significant contribution to the pseudogap minimum at -2.5eV. The only difference between this and Rh, plot d), which exhibited the same d-band filling as Co, was a contribution of density to the pseudogap minimum due to Rh's larger initial bandwidth. These unfavourable characteristics were further developed in the Ir plot e).

The adsorption of Pt DOS, which can be seen in chapter 4 figure 20, involved overlap with the NbC valence band, significant reduction of the pseudogap and increased density at the E_f. The

other extreme was observed for Ti as the d-band contribution was shifted towards E_f due to the lesser d-filling which allowed greater overlap with the NbC conduction band maximum and resulted on a significantly reduced pseudogap. It was suggested therefore, that increasing the DOS at E_f by overlapping with the pseudogap was key to adsorption whilst overlap with the valence or conduction band which increased density at the pseudogap minimum and shifted either of the total system's band centres towards E_f destabilised the interaction.

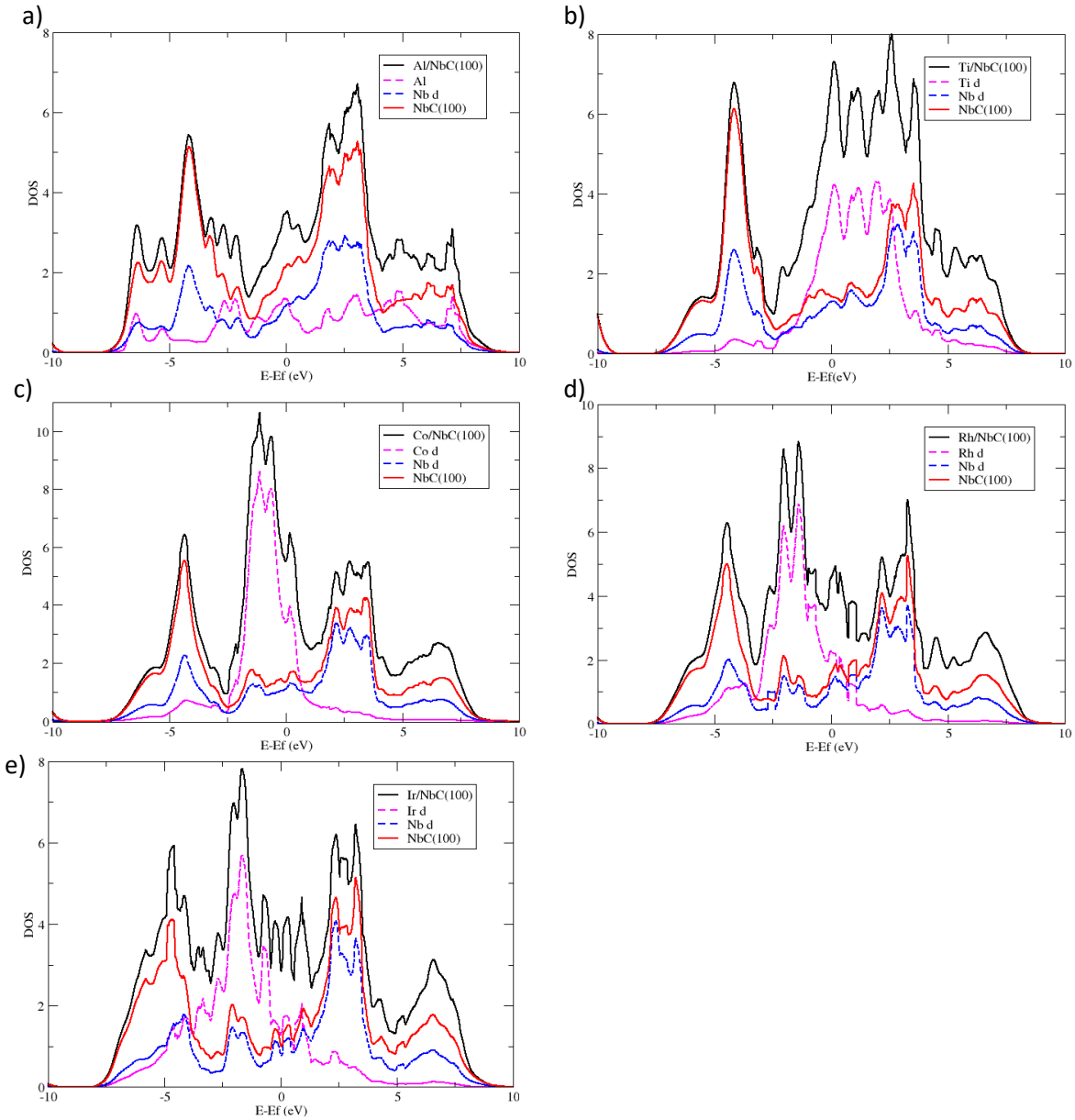

Figure 49 DOS for a) Al/NbC(100), b) Ti/NbC(100), c) Co/NbC(100), d) Rh/NbC(100) and Ir/NbC(100)

5.5.3 Tie-Layer Stability

The predicted bilayer stabilities shown in figure 49 b) suggested that Pt-outer skin formation would be favoured for all the tie-metals trialled. However, as before, the limited selection of

metals predicted to adsorb onto the carbide surface reduces the number of Pt/X/NbC structures that are likely to be synthetically attainable. Whilst Co was predicted to favourably adsorb to the carbide, the failure of some Co containing calculations to converge electronically has rendered comparison of the structures impossible. From initial calculated geometries however, significant rearrangements of the Pt/Co(111) systems suggested that this ordering was unstable. Mixing of the Pt into the Ni layer for the Pt/Ni/NbC systems was also observed rather than stabilisation of the required bilayer structure. Given the propensity of these metals to form alloys with Pt, an extension of the overlayer model to consider alloys would be worthwhile and potentially more representative of experimentally accessible systems.

Figure 50 a) Tie-layer adsorption energies for 1ML on NbC surfaces and b) stability with respect to Pt as the outer layer on NbC surfaces

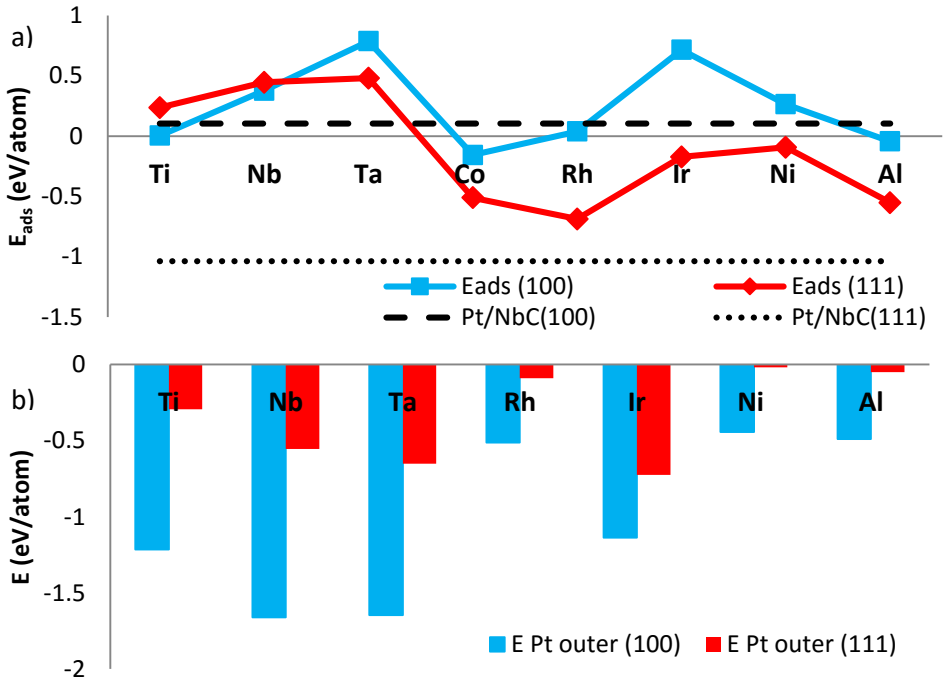

The calculations predicted that full encapsulation by Pt/Al and Co should be possible. The minimal adsorption energies of Ti and Rh on the NbC(100) surface may allow for formation of overlayers and Pt was predicted to be stable at the surface this being the case. For the NbC(111) facet, Rh, Ir and Ni were predicted to provide stable Pt-outer layers, the most favourable of which is predicted to be Pt/Ir/NbC(111). Vertical relaxation was also noted in this case with Pt rows forming a rippled surface.

It was previously noted from table 16 that Ir, Ti, Ta and Nb were all predicted to have stronger $E_{M\text{-}NbC}$ values on NbC(100) than Pt. The eventual unfavourable $\Delta E_{(M\text{-}NbC)}\text{-}E_{(M\text{-}M)}$ values were

observed to be due to the strength of $E_{(M-M)}$; -7.6 eV/atom for Nb and -6.6 eV/atom for Ta compared to Pt's -4.6eV/atom. However, the strength of metal-metal interactions may provide some justification for the observed Pt-outer bilayer stability. For example, in a competitive binding environment, the excellent overlap with Pt afforded by the broad d-band of Ir resulted in covalent Pt/Ir interactions. Table 17, containing charge transfer data for the Pt/X/NbC systems shows other evidence for Pt/X interactions. In the case of Ti, Ta and Nb, significant charge transfer from the tie-metal to the Pt occurred.

Table 17 Charge transfer data for Pt/X/NbC systems

Layers	Al		Ti		Co		Ni	
	100	111	100	111	100	111	100	111
Pt	-1.73	-1.50	-1.03	-0.77	-0.49	-0.38	-0.40	-0.37
Tie	2.48	1.42	1.37	1.01	0.36	-0.05	0.19	-0.10
Nb1	1.61	0.94	1.47	0.63	1.63	1.30	1.63	1.34
C1	-2.05	-1.68	-1.80	-1.71	-1.53	-1.69	-1.49	-1.69
Nb2	1.60	1.64	1.60	1.65	1.67	1.64	1.66	1.64
C2	-1.69	-1.67	-1.66	-1.66	-1.68	-1.67	-1.66	-1.67

Layers	Nb		Rh		Ta		Ir	
	100	111	100	111	100	111	100	111
Pt	-0.80	-0.61	-0.25	-0.17	-0.82	-0.61	-0.17	-0.14
Tie	1.12	0.56	0.03	-0.29	1.11	0.57	-0.11	-0.40
Nb1	1.45	0.93	1.66	1.32	1.47	0.91	1.65	1.39
C1	-1.65	-1.70	-1.46	-1.69	-1.76	-1.69	-1.41	-1.69
Nb2	1.63	1.64	1.65	1.65	1.67	1.64	1.69	1.66
C2	-1.77	-1.66	-1.65	-1.67	-1.67	-1.66	-1.63	-1.67

The localised charge resulted in the narrowing and stabilisation of the Pt bands observed in figure 50 plots a)-d). However in the cases where initial tie-layer adsorption was unfavourable, such as TiC/NbC(111) and TaC, significant filling of the carbide conduction band was also noted. This was energetically unfavourable and suggested that while Pt may be favoured as the outer metal by comparing bilayer structures, the whole adsorbed overlayer was unlikely to be stable.

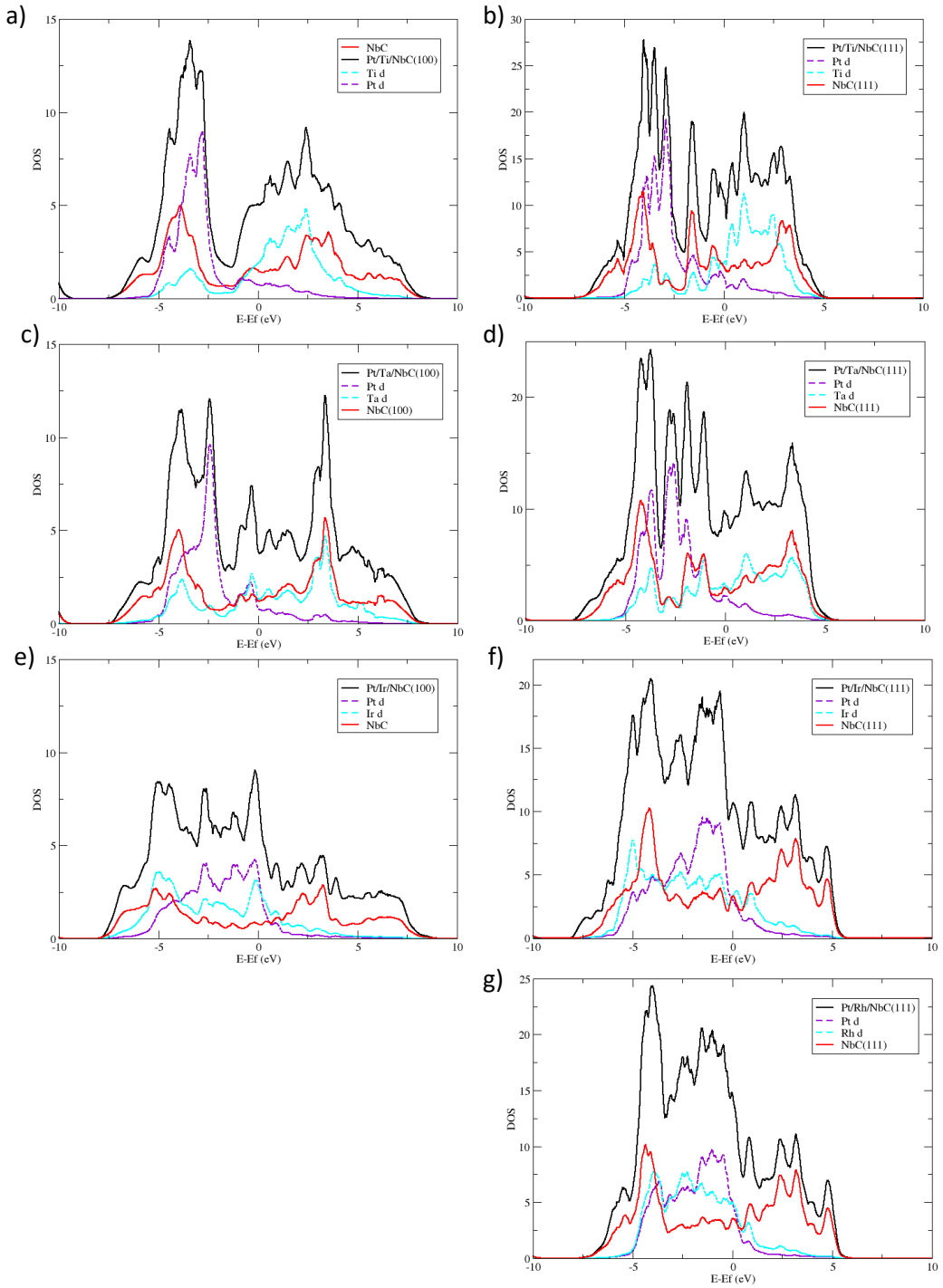

Figure 51 DOS plots showing variation in tie-layer stability to Pt forming the outer shell a) Pt/Ti/NbC(100) b) Pt/Ti/NbC(111) c) Pt/Ta/NbC(100) d) Pt/Ta/NbC(111) e) Pt/Ir/NbC(100) f) Pt/Ir/NbC(111) and g) Pt/Rh/NbC(111)

5.6 TaC

The TaC(111) surface contained a mixed character SR at -1eV and surface specific features on the (100) facet at +3eV and -4eV which were better defined than their NbC counterparts. Addition of the tie-metals revealed Co was the only metal to adsorb to the TaC(100) surface although Ti and Rh were noted to behave more favourably than Pt. On the (111) surface all the metals trialled bar

Ti and Ta successfully adsorbed at the surface although Co was the only candidate with an adsorption energy approaching that of Pt.

5.6.1 Geometry

Table 18 Vertical relaxation and $\Delta E_{M\text{-}TaC}$-$E_{M\text{-}M}$ data for TaC surfaces, X-TaC and D_{13} distances are measured from the surface M layer.

Tie-layers	(100)				
	X-TaC (Å)	D_{13} (M-M) (Å)	ΔD_{13} (%)	$E_{M\text{-}TaC}$ (eV/atom)	$\Delta E_{M\text{-}TaC}$-$E_{M\text{-}M}$ (eV/atom)
Ti	2.14	2.15	-2.5	-5.17	0.05
Ta	2.22	2.15	-2.2	-5.65	0.95
Co	1.90	2.18	-0.9	-1.08	-0.30
Rh	1.92	2.29	3.8	-3.38	0.35
Ir	1.85	2.32	5.0	-4.68	1.15
Ni	1.89	2.21	0.3	-3.01	0.44
Pt	2.07	2.26	2.4	-4.16	0.43
Al	2.29	2.13	-3.2	-3.03	0.15

Tie-layers	(111)				
	X-TaC (Å)	D_{13} (M-M) (Å)	ΔD_{13} (%)	$E_{M\text{-}TaC}$ (eV/atom)	$\Delta E_{M\text{-}TaC}$-$E_{M\text{-}M}$ (eV/atom)
Ti	2.32	2.53	1.1	-5.12	0.10
Ta	2.47	2.51	0.5	-5.86	0.74
Co	1.83	2.56	2.5	-1.65	-0.87
Rh	2.00	2.56	2.3	-4.34	-0.61
Ir	2.03	2.57	2.8	-5.86	-0.03
Ni	1.84	2.56	2.3	-3.57	-0.11
Pt	2.05	2.55	2.2	-5.52	-0.92
Al	2.20	2.60	3.9	-3.81	-0.63

X-TaC lengths were observed to follow periodic trends as for the previous carbides, again with Al as an anomaly within the dataset. For the (100) surface both contractions and expansions of the first bilayer were observed with no clear link to the adsorption behaviour of the metal layers. The (111) surface expanded upon introduction of the tie-layer metals although again without correlation to the metal $E_{M\text{-}TaC}$-$E_{M\text{-}M}$.

On TaC(100) horizontal surface rearrangements were noted for Co, Ni and Ta leading to the formation of chains of the tie-metal as shown in figure 51. Vertical displacement of alternate Al rows was observed on the TaC(111) surface, however the difference was less pronounced than on the SiC surfaces being just 0.07Å.

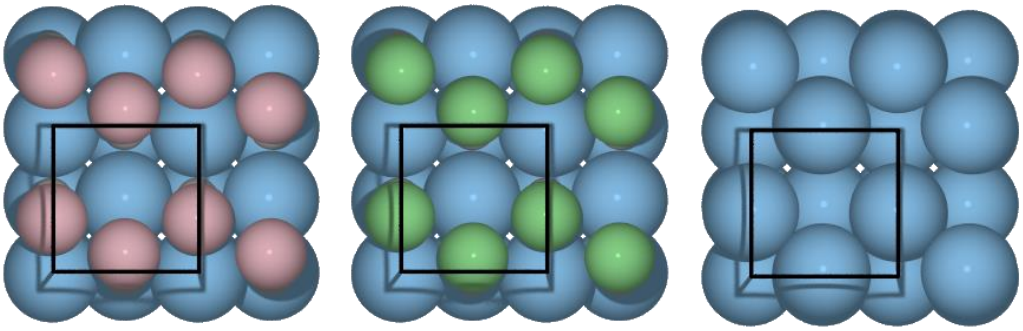

Figure 52 Ni, Co and Ta surface rearrangement on the TaC(100)

5.6.2 Electronic Structure Contributions to Adsorption

For NbC, the DOS plots in figure 52 show the adsorption of Co through overlap with the carbide pseudogap at and below E_f. The addition of Pt (chapter 4 figure 20) involved more valence band overlap whilst the addition of Ti resulted in Ti d-band overlap above E_f with the TaC conduction band. For the (111) surfaces, the lack of Ti d-band filling prevented significant overlap with the TaC(111) valence bands and thus disfavoured adsorption. Co was observed to have a larger $E_{M\text{-}TaC}$-$E_{M\text{-}M}$ than Rh whilst Pt was stronger than both of these.

All three of these cases involved the tie-metal d-band overlapping the TaC(111) pseudogap. The Co maximum was seen to be closer to E_f than that of Rh, which suggested better overlap with the TaC(111)SR at -1 eV. Whilst the Pt d-band maximum lay further still from E_f, the Pt d-band was observed to have a much great bandwidth allowing significant overlap with the valence band and interaction with the conduction band. These interactions shifted the valence and conduction bands negatively, with the filled bands below E_f becoming stabilized. From the charge density information in chapter 4 table 7 we know this coincided with electron donation to the Pt.

Figure 53 DOS plots for the adsorption of a tie-layer ML a) Ti/TaC(100) b) Ti/TaC(111) c) Co/TaC(100) d) Co/TaC(111) and e) Rh/TaC(111)

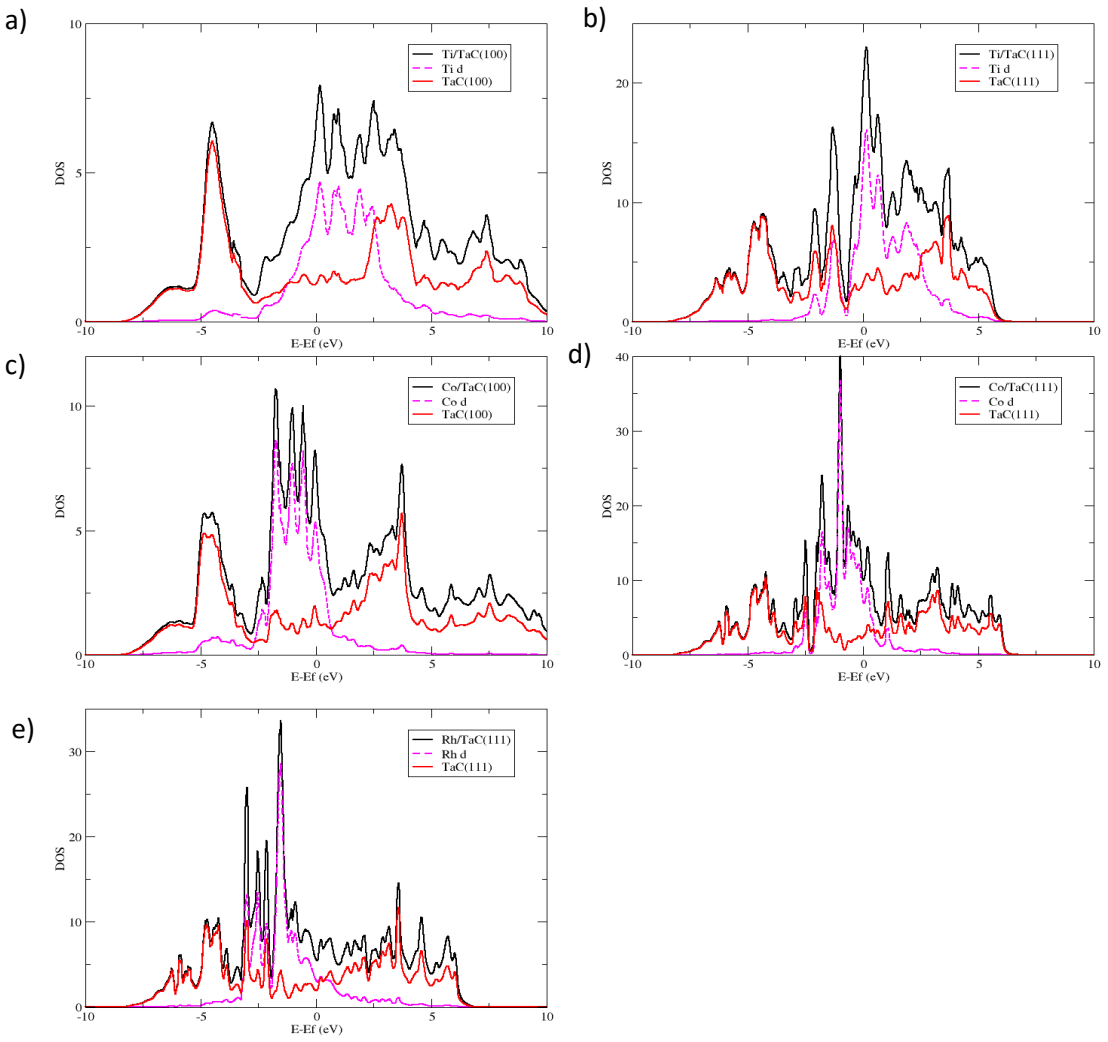

5.6.3 Tie-Layer Stability

Given the initial tie-metal adsorptions, whilst the bilayer stability calculations predicted good Pt-outer layer formation in figure 53 b), Co was the only candidate predicted to be suitable for encapsulation of the TaC. Again the failure of Co containing X/Pt/TaC systems to converge results in no segregation value, however significant surface rearrangement for both bilayer arrangements shown in figure 54 strongly suggested instability with regards to an Pt-outer skin being maintained. The Ni(111) experienced similar mixing of the bilayer again rendering it unstable under the current analysis.

Figure 54 a) Tie-layer adsorption energies for 1ML on TaC surfaces and b) bilayer stability results with respect to Pt as the outer layer on TaC surfaces

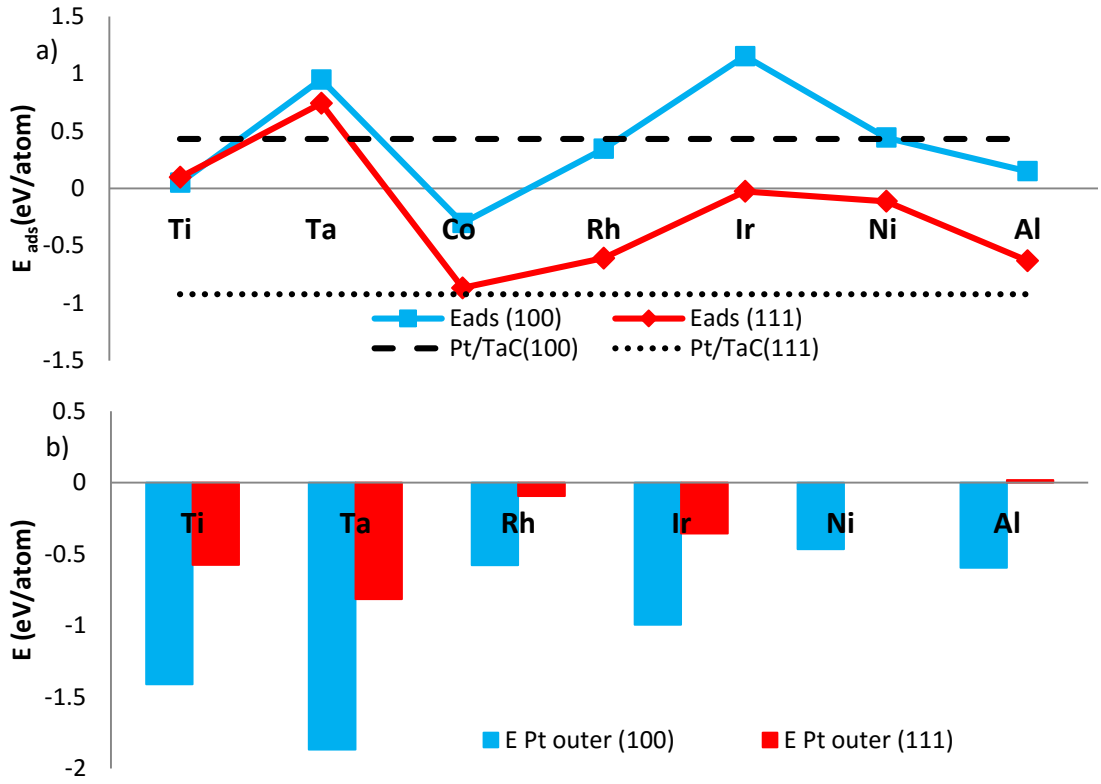

Considering the (100) surfaces which had previously been calculated to undergo surface rearrangement (figure 51), the Co and Ni systems were predicted to maintain the tie-layer chains within the bilayer. This resulted in a larger degree of accessibility to the tie-layer than for the other (100) surfaces, see in figure 54 b). Whilst an idealised bilayer was not predicted to be stable, the predicted adsorption of the PtCo alloy to TaC on both facets is still of interest in the current work since this method should allow Pt introduction to a previously unfavourable carbide facet. The addition of more Pt may also result in an active catalytic surface (since the enhanced activity of Pt/TM alloys is well documented[32]) and although the effect of the carbide may be lost, the thrifting effect of a non PGM core would still apply.

Figure 55 a) Pt/Co/TaC(111) and b)Pt/Co/TaC(100) are predicted to undergo significant rearrangement exposing Co at the surface

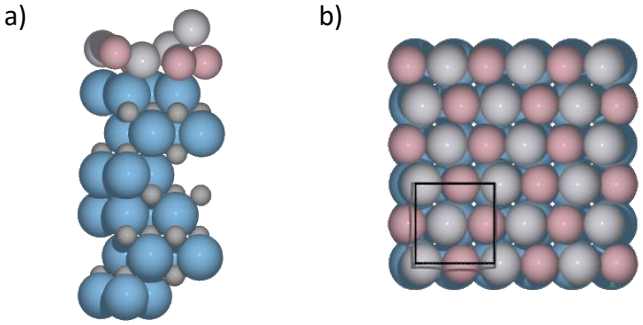

Of the other tie-metals predicted to adsorb at the (111) surface, Rh and Ir(111) bilayers were predicted to favour Pt-outer layer formation. The resultant bilayers were calculated to undergo surface relaxation resulting in rippled Pt surface layers. This was likely to have occurred to reduce surface strain due to the carbide's expanded lattice parameters. The Pt/ Ni bilayer, as previously mentioned, was predicted to mix forming an alloy however the Al bilayer structure was predicted to favour sub-surface Pt. On consulting Vitos *et al*,[162] the surface energy of Al(111) was found to be significantly less than that of Pt(111) 0.531 eV/atom in comparison to 1.004 eV/atom, thus we conclude that the surface Al was favoured to minimise the system surface energy.

On inspection of the DOS in figure 55, with the addition of Pt we observed enhanced tie-layer- TaC valence band overlap and a dramatic reduction in the width of the pseudogap as the Pt density was localised around -3eV for the (100) surfaces. This localisation coincided with significant charge transfer to the Pt from the tie-layer metals. The lesser degree of charge transfer for the Ir(100) data suggested greater covalence, as less charge localisation was suggested and the Pt and Ir DOS traces retained their broad bandwidths. Among the (111) systems a lesser degree of charge transfer was noted across the dataset. For Rh and Ir on the (111) surface, charge transfer from the carbide Ta to the tie-layer as well as the Pt surface was noted. In the cases of Ti and Ta(111) partially filling of the carbide conduction band was observed suggesting that adsorption would be unfavourable even though a Pt-outer bilayer may be preferred to Pt subsurface.

Figure 56 DOS plots a) Pt/Ti/TaC(100) b) Pt/Ti/TaC(111) c) Pt/Ta/TaC(100) d) Pt/Ta/TaC(111) e) Pt/Ir/TaC(100) and f) Pt/Ir/TaC(111)

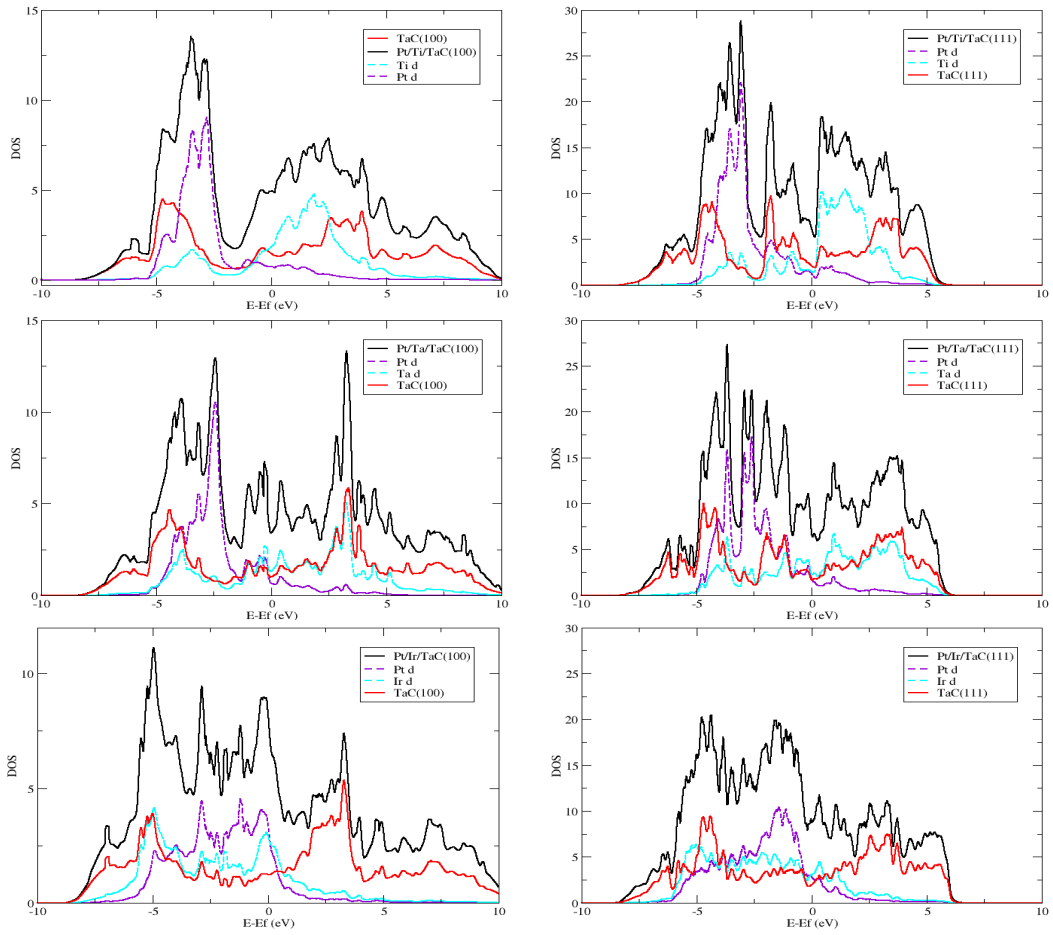

Table 19 Charge Transfer data for the Pt/X/TaC systems, Co(111) and Ni(111) data is noted reported due to the mixing of the bilayers

Layers	Ti		Ta		Co	Rh	
	100	111	100	111	100	100	111
Pt	-1.05873	-0.76508	-0.85081	-0.77	-0.46664	-0.24387	-0.16648
Tie	1.422623	1.127471	1.200133	1.13	0.344327	1.669227	-0.29259
Ta1	1.51095	0.595806	1.495215	0.60	1.70031	0.042431	1.377365
C1	-1.84624	-1.80267	-1.84353	-1.80	-1.55818	-1.50461	-1.77498
Ta2	1.660997	1.742858	1.683227	1.74	1.728322	1.705731	1.74648
C2	-1.73402	-1.73235	-1.72218	-1.73	-1.75357	-1.73308	-1.73631

Layers	Ir		Ni	Al	
	100	111	100	100	111
Pt	-0.17639	-0.12493	-0.402	-2.02219	-1.36274
Tie	-0.07768	-0.42693	0.248332	2.484167	1.327483
Ta1	1.715844	1.454695	1.718038	1.678809	0.952934
C1	-1.46997	-1.77002	-1.53391	-2.08708	-1.77022
Ta2	1.716889	1.750594	1.694622	1.655813	1.737341
C2	-1.71297	-1.73945	-1.72703	-1.76686	-1.73386

5.7 Conclusions

In this chapter we have shown that through the incorporation of other metallic MLs it may be possible to improve Pt adsorption and ensure the full encapsulation of carbide nanoparticles. Our initial goal was to produce stable Pt-outer layers within the metallic bilayer.

Whilst WChcp has already been predicted to favourably adsorb Pt on all facets, tie-layers were trialled as the first steps to investigating the tunability of Pt towards the ORR. WC hcp was calculated to favourably support Pt with Ti, Ir and Rh tie-layers for full encapsulation. Given previous experimental evidence of stable Pt/Ni/WC(0001) overlayer formation,[172] Ir and Ti were highlighted for synthetic development as the current model predicted greater stability over all surfaces than for Ni. Rh and Ir bilayers were also highlighted as promising tie-metal structures for SiC surfaces. Co and Ni were both predicted to adsorb strongly to SiC facets, however due to their propensity to mix with Pt to form alloys, Pt-outer skin structures were not achieved for these metals on either carbide.

Although the fcc (100) surfaces still proved unfavourable towards the majority of tie-layer adsorptions, Co was supported on both facets of NbC and TaC, whilst main group metal Al was predicted to adsorb favourably on the TiC and NbC(100) facets. The creation of a competitive adsorption environment with the addition of Pt resulted in Pt-outer skin systems being favoured in many cases due to the reduction of surface strain. Strong Pt-M interactions may also reduce the effect of $E_{M\text{-}M}$ within the bilayer and improve overlayer adsorption. The fcc(111) carbide surfaces also favoured Ir and Rh bilayers and encountered Co and Ni alloying as previously mentioned.

In the case of the WC hcp and SiC systems then, Rh, Ir and Ti are promising tie-layers for full encapsulation whilst Ni and Co show potential for forming Pt alloys. For the fcc carbides, Al and Co offer possible routes to include Pt on to the previously unfavoured (100) surfaces whilst Rh, Ir and Ni are predicted to favourably form Pt/X/TMC(111) structures. Given the known activity and tunability of Pt containing alloys towards the ORR,[106,69] further investigation of Co and Ni containing Pt alloy overlayers would be worthwhile although the electronic effect of the carbide layer would soon be lost with the addition of more Pt layers.

6. Adsorption of ORR intermediates

In this chapter the effect of the carbide core material in terms of Pt oxygen reduction activity was considered via the adsorption strength of key reaction intermediates. As mentioned in the introductory chapter, Sabatier's optimal catalytic activity is achieved when the activation energy and the strength of bonding of reaction intermediates are balanced.[60] These requirements allow for both reagent dissociation on the surface and the removal of subsequent products. The linear correlation between these factors has been found to be a Brønsted-Evans-Polanyi relationship.[108,109] The relation is independent of reactant and thus Nørskov *et al*.'s 'Universality Principle'[107] can be used to relate adsorption energies to catalytic activity[194] for TM surfaces[107] as well as TMCs [118] and TM oxides.[195] In addition, scaling relations between adsorbates which bond through the same atom (i.e. O, OH and OOH)[196, 197,118] enable predictions of activity for a whole reaction to be made from a selected adsorption energy[198] i.e. the oxygen adsorption energy in the case of ORR.[106]

Figure 57 Trends in oxygen reduction activity relative to oxygen binding a) calculations on pure metal (111) surfaces, Nørskov *et al.*[15] b) experimental data including Pt ML on single crystal metals (circles), polycrystalline alloys annealed under UHV (diamonds) and bulk alloys annealed under UHV (squares) Greeley *et al.*[32]

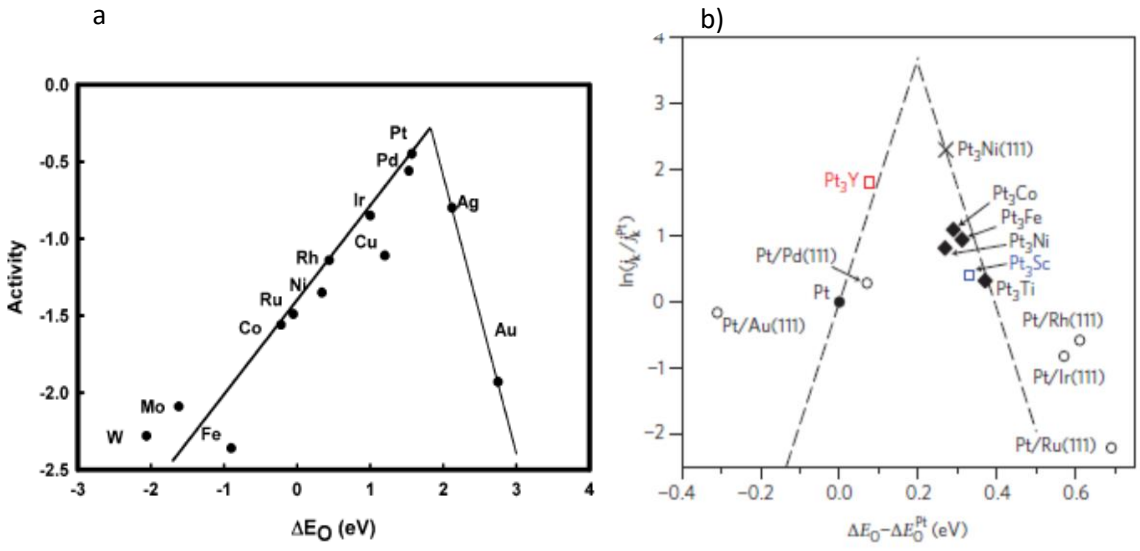

Volcano plots relating the oxygen adsorption energy to oxygen reduction activity reveal scope for catalytic optimisation as pure Pt is not at the pinnacle of the plot either by calculation or from single crystal data as can be seen in figure 56. A reduction in the O adsorption energy of 0.2eV would result in the maximum possible activity although weakening the binding by up to 0.4 eV would still allow improvement over pure Pt.[199] Thus weakened oxygen adsorption energies within this range were sought for the identification of promising core-shell systems.

6.1 Adsorption Methodology

Given the scaling relationship between O bonded molecules previously stated, the adsorption of atomic O and OH were investigated on the surface overlayer structures. Prior to adsorption, isolated O_2 and H_2O molecules were modelled to provide reference states. Geometry minimisation was carried out in CASTEP using ultrasoft pseudopotentials with an energy cut off of 340eV. Unit cells of 10Åx11Åx12Å were used for the isolated molecule calculations to break the symmetry and a minimal smearing width of 0.001 eV was applied. In the case of O_2, spin polarisation was necessarily taken into account.

The target adsorbates were then placed at high symmetry locations (see chapter 4 figure 17) on relaxed pure platinum and overlayered carbide systems. The final support bilayer was constrained to bulk coordinates as before whilst the rest of the system was allowed to optimise during geometry minimisation. The reagent adsorption energies were then calculated using equation 28.

$$E_{ads\ reagent} = \frac{E_{Ads\cdot Pt/TMC} - (E_{Pt/TMC} + N \cdot E_{Ads})}{N} \quad (28)$$

Where *N* is the number of adsorbates present and E_{Ads} represents the reference energy of the atomic or molecular reagent. The reference states used were $½E_{O2}$ for atomic O and $½E_{H2}$ for atomic H, whereas for OH, E_{H2O} - ½ E_{H2} was employed throughout. Convergence of the pure Pt slab depth led to (100) and (110) slab depths of six atomic layers and a (111) slab depth of five atomic layers.

6.2 Adsorption on Pure Platinum

Atomic and molecular adsorptions were carried out on the (100), (110) and (111) surfaces of the pure Pt to provide a comparison with the carbide supported Pt monolayers. Molecules were placed in vertical and horizontal orientations and allowed to rotate and move freely with relation to the Pt surface.

Table 18 Adsorption energies for reagent atoms and molecules on Pt(100) and (110) surfaces, 0.5ML coverage

100

Adsorbate	Position	Angle (°)	X-Pt (Å)	E_{ads} (eV)
H	Bridge	-	1.77	1.22
O	Bridge	-	2.00	-0.67
O2	Bridge	46.6	2.20	0.11
OH	Bridge	19.7	2.14	0.48
H2O	Atop	18.2	2.84	-0.09

110

Adsorbate	Position	Angle (°)	X-Pt (Å)	E_{ads} (eV)
H	Bridge	-	1.76	-0.49
O	Bridge	-	1.99	-0.89
H2O	Atop	15.1	2.45	-0.20

The bridging adsorption site was favoured by all adsorbates except H_2O which was predicted to bond preferentially at the atop site. For the (100) surface this water binding was in agreement with molecular dynamics (MD) simulations at 300K undertaken by Raghavan *et al.*[200] The H_2O molecule held a tilted geometry in relation to the Pt surface in both cases with the hydrogens not parallel to the surface. The current work also suggested that adsorption would be more favoured on the (110) surface than the (100).

Table 19 Adsorption Energies for reagent atoms and molecules on Pt(111), 0.25ML

111

Adsorbate	Position	Angle (°)	X-Pt (Å)	E_{ads} (eV)
H	Octahedral	-	1.88	-0.39
O	Octahedral		2.09	-0.82
O2	Octahedral	8.8	2.07	-0.26
OH	Octahedral	81.8	2.26	1.28
H_2O	Atop	5.7	2.542	-0.05

For the (111) surface, the predicted favoured adsorption site was the octahedral 3-fold site except for H_2O which again was predicted to bond most favourably at the atop position. This finding was in agreement with Michaelides *et al.*'s work on H_2O at TM surfaces which states that atop binding of H_2O is favoured for a wide range of TMs and that the water molecules are predicted to bind approximately parallel with the metal surface. H_2O on Pt(111) surfaces has previously been calculated with an O-Pt distance of 2.36Å and an angle of 7° to the surface which was in general agreement with the geometries calculated in the present work.[201] The hydroxyl findings differ as Michaelides *et al.* in their 2001 paper report a preference for the bridge and atop sites at low (0.25) and high (0.5) coverages respectively.[202] The literature method does differ from the setup in the current work; a low energy cut off of 300eV and a 3 layer Pt slab constrained in the bulk positions were used. Michaelides' use of a selection of larger unit cells and coverages also allowed for the formation of 'chains' of OH or an hexagonal 'flat ice' H_2O layer.[203] These may account for part of the difference between the literature adsorption energy for OH, -2.49eV at 0.5 ML,[202] and H_2O, -0.35eV[201] on Pt(111) and those calculated here. The significant difference between the literature and current OH values however would suggest a more systematic problem with the H_2O model, possibly stemming from the pseudopotentials employed. As stated in the introduction of

the chapter, the current work seeks to identify a reduction in oxygen binding strength and so the values of ΔE_{ads} from the proposed model were deemed to be sufficient for this investigation.

In order to allow comparison at similar coverages, the E_{ads} of atomic oxygen on Pt(111) at 0.5 ML was also calculated and found to be -0.45 eV/molecule. The drop in adsorption strength came as a result of repulsive inter-adsorbate interactions.

6.3 Adsorption on Pt/Carbide Surfaces

6.3.1 Atomic Oxygen

6.3.1.1 Single Monolayer Surfaces

The adsorption site preferences and adsorption energies of atomic oxygen were considered with respect to the high symmetry adsorption sites present at the surface. Spontaneous migration from site to site was noted in some cases, as indicated in table 20. This suggested that no significant energy barriers were present on the surface. The final adsorbate position after these migrations was often the overall minimum for the surface. The bridge site was predicted to be the most stable adsorption site for the (100) surfaces although in the case of CW(10$\bar{1}$0) the 4-fold hollow was favoured. The fcc(100) surfaces for TaC, TiC and NbC were predicted to have the strongest adsorption energies towards oxygen followed by the SiC, and hcp and fcc WC surfaces.

Table 20 Adsorption energies of atomic oxygen on (100)-type surfaces, values with an asterix denote movement from the initial adsorption site towards or to the overall most favoured site

Starting Position	Surfaces							
	SiC(100)	CSi(100)	TiC(100)	WC(10$\bar{1}$0)	CW(10$\bar{1}$0)	WC(100)fcc	NbC(100)	TaC(100)
atop	xxx	-0.76*	-0.46	0.71	-0.44	-0.09	-0.47	-0.62
bridge	-0.82	-0.69	-1.03	-0.34	-0.31	-0.69	-1.01	-1.23
4-fold	-0.83*	-0.51	-0.91*	0.03*	-1.16	-0.58*	xxx	xxx

The same method of charge transfer analysis carried out for the Pt overlayers in chapter 4 was carried out for these structures and is displayed in table 21. The density distribution indicated that the electron density donated from the carbide surface to the Pt overlayer was subsequently transferred to the O. Analysis of the favoured adsorption sites revealed a calculated charge of between 0.70 and 0.82 electrons resting on the adsorbate on the (100)-type surfaces and between 0.72 and 0.97 electrons on the oxygen for the (111)-type surfaces. Whilst calculations for the SiC surfaces indicated that a charge build-up was maintained in the Pt overlayer, in the majority of cases the Pt layer was left with a small charge deficit. No correlation can be drawn between the

charge of the clean Pt overlayer and O adsorption strength which is unsurprising given the propensity for oxygen atoms to form covalent bonds.

Table 21 Charge density distribution on the adsorption of atomic oxygen on various Pt/Carbide surfaces

Layer	Surfaces							
	SiC(100)	CSi(100)	TiC(100)	WC(1010)	CW(1010)	WC(100) fcc	NbC(100)	TaC(100)
O	-0.79	-0.76	-0.74	-0.73	-0.82	-0.70	-0.72	-0.74
Pt	-0.96	0.48	0.09	-0.29	0.29	0.13	0.05	0.05
X1	3.07	3.08	1.61	1.31	1.45	1.64	1.75	1.68
C1	-3.04	-1.65	-1.37	-1.35	-0.61	-1.40	-1.45	-1.41
X2	2.87	3.07	1.64	1.41	1.37	1.57	1.73	1.70
C2	-3.07	-3.05	-1.65	-1.41	-1.38	-1.55	-1.71	-1.67

Layer	Surfaces						
	SiC(111)	TiC(111)	CTi(111)	WC(0001)	WC(111) fcc	NbC(111)	TaC(111)
O	-0.80	-0.96	-0.83	-0.75	-0.78	-0.97	-0.91
Pt	-1.63	-0.36	0.34	-0.28	-0.28	-0.34	-0.37
X1	2.67	1.58	1.59	1.16	1.30	1.46	1.52
C1	-3.11	-1.72	-0.89	-1.37	-1.59	-1.69	-1.77
X2	3.07	1.61	1.65	1.36	1.57	1.64	1.73
C2	-3.09	-1.67	-1.65	-1.38	-1.58	-1.67	-1.74

Figure 57 displays the oxygen adsorption energies for the carbide supported Pt surfaces plotted against the d-band centres, E_d , of the Pt ML all relative to O adsorption on the pure Pt(100) surface. The calculations identified WC(10$\bar{1}$0)hcp as the only (100)-like surface with a lessened oxygen adsorption strength relative to pure Pt, however the Pt-like values of WC(100)fcc and CSi(100) were also of interest. Whilst these surfaces may not enable improved activity, the prediction of Pt-like activity with vastly reduced Pt loading is still a step forward to realising the first of the DOE fuel cell catalyst targets.[204] It must also be noted that C-terminated carbide surfaces were found to be less stable (chapter 3) and as such, whilst the CSi(100) result is Pt-like it is not a viable ORR catalyst surface.

Figure 58 Δ oxygen adsorption energies for 1ML Pt on carbide (100)-type surfaces relative to E_{ads} O/Pt(100) at 0.5 ML, circles denote C-terminated carbide surfaces

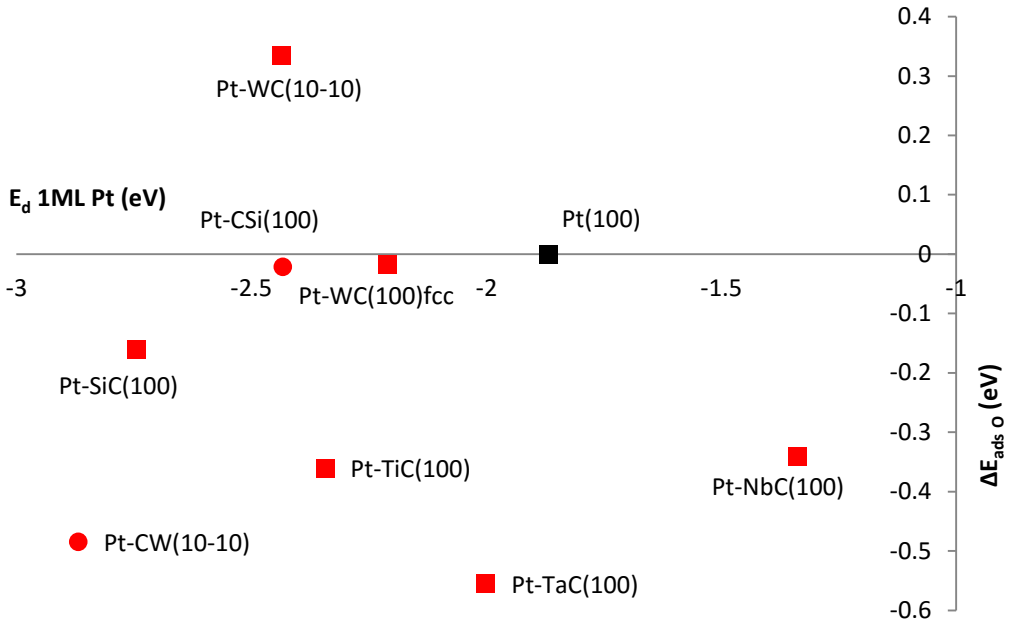

For the (111)-type surfaces, the spontaneous migration of the adsorbate across the surface during geometry optimisation was less frequently observed. The oxygen was predicted to preferentially adsorb at the 3-fold hollow sites. The tetrahedral site was favoured in all cases except the WC(0001)hcp although for SiC(111), WC(0001) and WC(111)fcc the difference in adsorption strength between the sites was less than 0.15 eV/atom which is within DFT error.

Table 22 Adsorption energies of atomic oxygen on (111)-type surfaces, values with an asterix denote movement from the initial adsorption site towards or to the overall most favoured site

Starting Position	Surface						
	SiC(111)	TiC(111)	CTi(111)	WC(0001)	WC(111)fcc	NbC(111)	TaC(111)
atop	-0.44	0.74	1.11	-0.24	-0.01	0.55	0.32
tet	-1.14	-1.05	*	-0.73	-0.66	-1.61	-1.83
oct	-1.11	-0.61	-0.48	-0.84	-0.52	-0.84	-1.04

Figure 58 below shows the predicted adsorption energies of O relative to pure Pt(111). Again, two carbide systems which exhibited reduced O adsorption were noted, with WC(111)fcc being close to the 0.2eV optimum catalytic O binding value previously mentioned. It must however be highlighted that WC fcc is an unstable phase of the material included for comparison with WC hcp. The hexagonal WC(0001) produced a Pt-like O adsorption, 0.02 eV stronger than the pure Pt value. This behaviour of the Pt/WC(0001) system was in excellent agreement with Hsu *et al,* who calculated a 0.05eV difference in oxygen binding energy at a coverage of 1/9 ML. [96] This suggests

that for the (111)-type surfaces our 2x2 unit cells can adequately model behaviour at the low coverage limit.

Figure 59 Δ oxygen adsorption energies for 1ML Pt on carbide (111)-type surfaces relative to E_{ads} O/Pt(111) at 0.25 ML, triangle denotes C-terminated carbide surface and dashed black line the optimum O adsorption energy for (111) surfaces

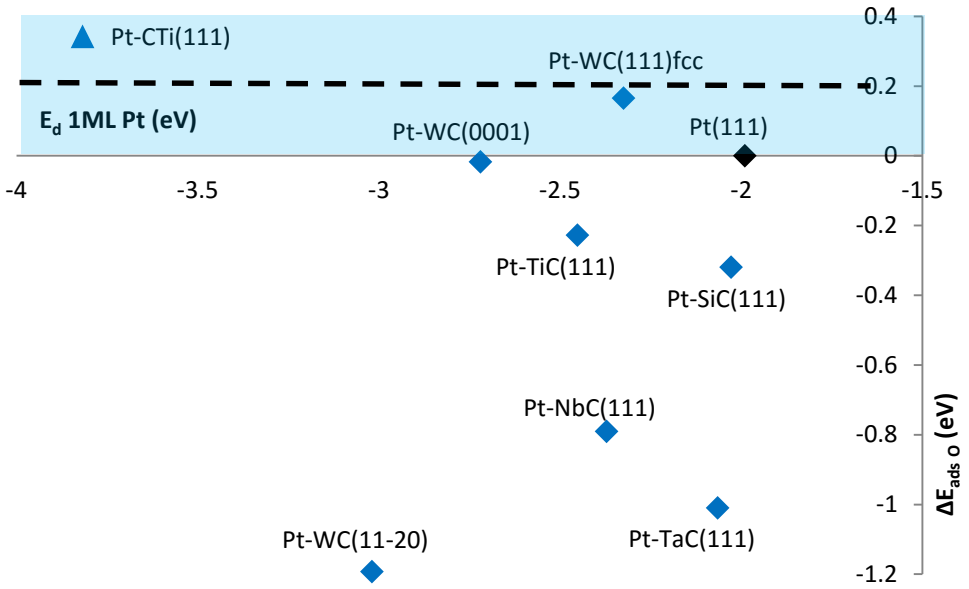

The wide range of adsorption behaviour over a small range of E_d values for both the (100) and (111) surfaces suggested that the d-band centre model is inappropriate for the prediction of O adsorption strength on the Pt overlayers. The presence of the carbon in the support means the alteration of the Pt d-band is more complex than in simple bimetallic systems. Since the O was observed to bind to the Pt overlayer over the entirety of its trace as can been observed in figure 59, and to overlap particularly with maxima in the structure of the valence band and just above E_f, the shape of the Pt d-band is expected to be highly influential on the binding. Given the charge transfer which was observed in table 21 as well, the d-band centre model was deemed too simplistic to cope with these different bonding contributions.

Figure 60 DOS plot for O adsorption on Pt/WC(0001)

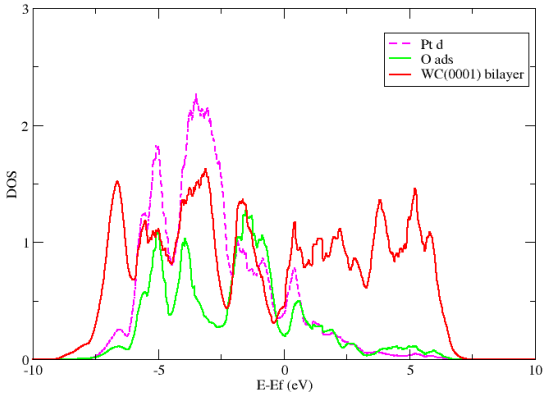

6.3.1.2 Multiple Monolayer Surfaces

Increasing the thickness of the Pt overlayer was observed to lessen the modification of the Pt surface due to the carbide's electronic structure which was noted in the Pt overlayer DOS plots seen in chapter 4. This led us to expect a return of O adsorption strength towards that predicted for the pure Pt surfaces. As figure 60 illustrates however, for both sets of surfaces, 3ML adsorption energies were observed to be significantly stronger than those on pure Pt. This was due to the fixed unit cell dimensions of the model, preventing lattice mismatch from healing, maintaining the geometric effect of the core. This continuing geometric strain effect was observed in the failure of the Pt E_d to attain pure Pt surface values previously investigated in chapter 4.

The addition of multiple Pt layers weakened the adsorption of O for NbC and TaC. For the (100) surfaces this was a minor effect however in the case of the (111) surfaces, the large lattice expansion caused by the underlying carbide had resulted in the carbide metal being accessible from the surface under 1ML Pt. Inclusion of further Pt MLs prevented the adsorbate from approaching the carbide and resulted in the O remaining accessible as seen in figure 61.

Figure 61 Relative O adsorption energies on a) Pt(100)-type overlayers and b) Pt(111)-type overlayers of differing thickness, black dashed line represents the pure Pt surface references.

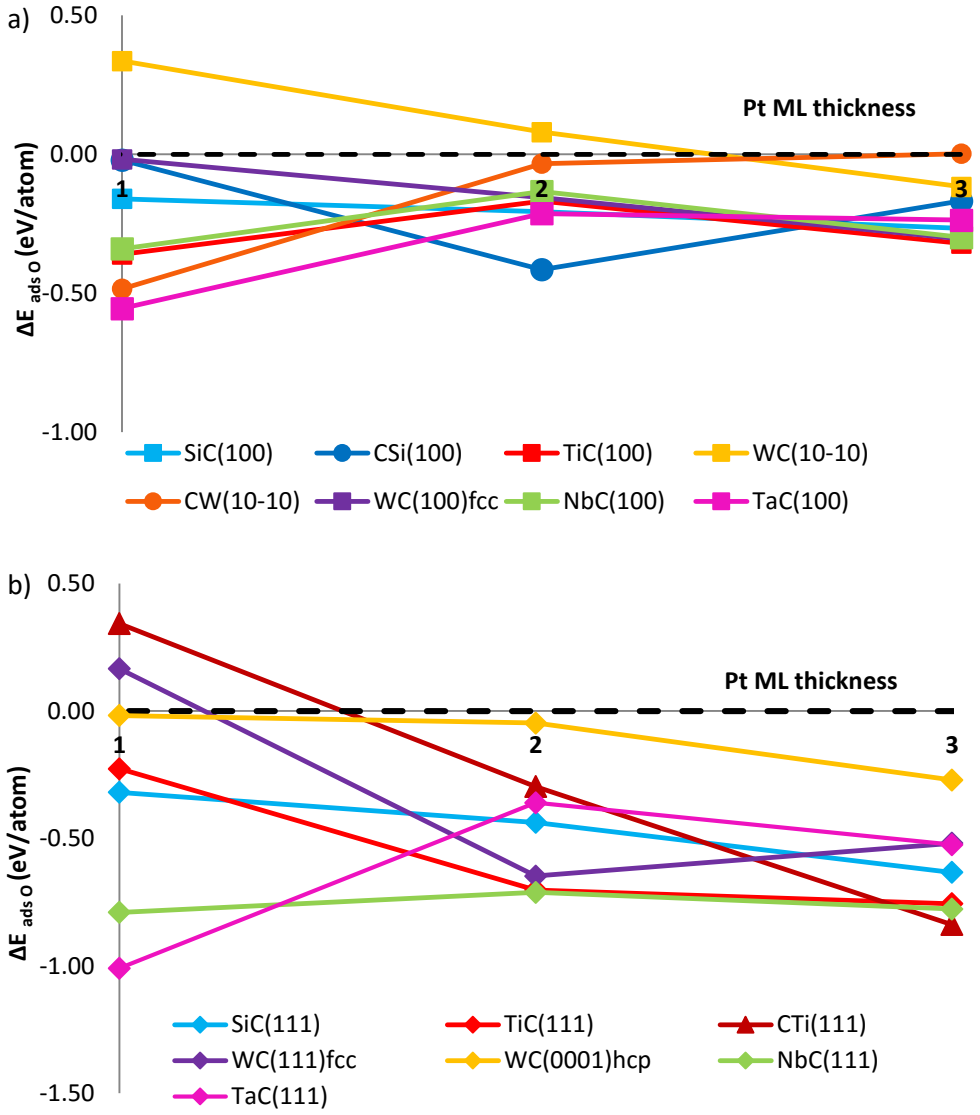

Figure 62 O atom position following optimisation on the Pt/TaC(111) system for 1, 2 and 3ML

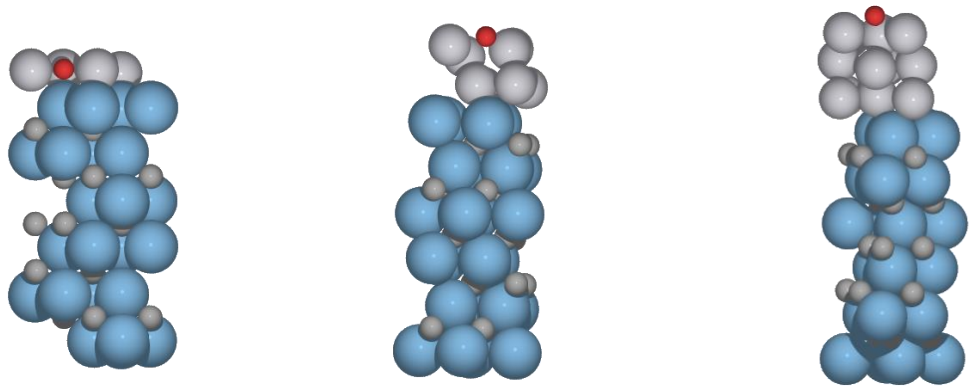

The increased adsorption energy at 2ML Pt for CSi(100) coincided with significant minimisation of the Pt positions to stabilise the whole system. Since the $E_{ads\ o}$ was calculated as a difference

between the clean and adsorbed surfaces, a single point calculation of the relaxed 2ML Pt/CSi(100) was run in which the surface was found to have only a 0.015eV energy difference to the initial clean state. This would suggest the more negative calculated $\Delta E_{ads\ o}$ value is due to improved interaction with the surface as a result of the Pt relaxation. Whilst it would have been possible to optimise only the Pt-O distance and constrain the Pt/carbide surface during adsorption, surface relaxations are essential to accurately modelling materials.

Of the carbides under investigation, hexagonal WC gave the most Pt-like O adsorption behaviour at increased Pt thicknesses for a variety of surfaces. This result suggests that hexagonal WC would provide the best activity, of the materials studied, as a nanoparticle core. At 1ML Pt, the fcc WC surfaces also displayed Pt-like behaviour although with increased thickness this effect was lost and stronger O adsorption was predicted. With increased Pt thickness the SiC core was predicted to become less promoting as the O adsorption strength increases. Both SiC surfaces were in the middle of the adsorption energy range calculated. Whilst the TiC(100) surface retained a similar binding strength throughout the depths of Pt overlayer considered, the remaining TiC surfaces bound O more strongly placing it lowest in this group in terms of possible ORR promotion.

6.3.2 Hydroxyl group

6.3.2.1 Single Monolayer Surfaces

The adsorption of OH followed similar patterns to that of atomic O. On the (100) surfaces the bridging site was again calculated to be the most favourable except for the 4-fold hollow again favoured by CW($10\bar{1}0$). OH adsorption on to the (111) surfaces was predicted to occur most frequently at the octahedral sites and in several cases the E_{ads} values for the tetrahedral and octahedral sites differed by only 0.02eV/. For WC(0001) the atop site was favoured whilst for TiC(111) the bridge site was predicted to be favoured.

Figure 63 Adsorption energies for O and OH at their most stable adsorption sites on the 1ML Pt carbide surfaces, red squares represent (100)-type surfaces whilst blue diamonds represent (111)-type surfaces

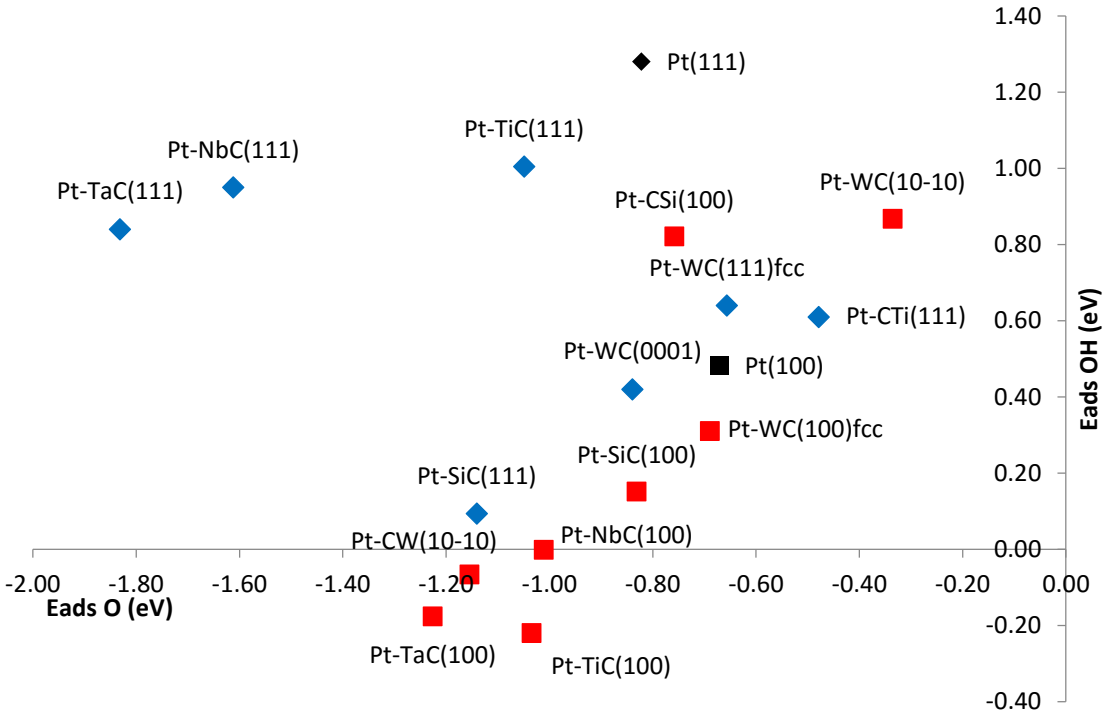

As can be seen in figure 62 the scaling relationship for O and OH adsorption which had been identified on TMs[198] and TMCs[118] was also present for the Pt-TMC surfaces. The (111)-type dataset contains significant deviations from the trend as for TaC, NbC and TiC the $E_{ads\ OH}$ were much more positive in energy than expected. Atomic O was predicted to adsorb very strongly on these surfaces due to the fact that upon relaxation the reagent spontaneously migrated to the interface between the carbide surface and Pt. For OH no movement through the Pt ML was witnessed although the spontaneous diffusion of the OH molecule across the Pt/TiC(111) surface to the bridging site suggested that local energy minima may play a role in the surface adsorption and that more initial adsorption sites should be investigated.

6.3.2.2 Multiple Monolayer Surfaces

The adsorption behaviour of OH was observed to alter radically on increasing the Pt overlayer thickness. For the (100)-type overlayers as seen in figure 63 a), increasing ML thickness resulted in a significant weakening of adsorption energies on TiC, TaC and NbC followed by convergence of the adsorption energies towards strain affected Pt values. This coincided with a reduction in the angle of adsorption of the OH to the surface from 29° to 19° for TiC(100) and 23° to 17° for TaC(100) going from 1 to 2ML Pt. In the cases of CSi(100) and WC($10\bar{1}0$), where 2ML Pt was

observed to strengthen the OH adsorption energy, reductions of 0.1Å in the O-Pt bond distance and 8-10° in the adsorption angle were noted.

Figure 64 OH adsorption on to a) Pt (100) overlayers and b) Pt(111) overlayers of differing thickness, black dashed line represents the pure Pt surface references

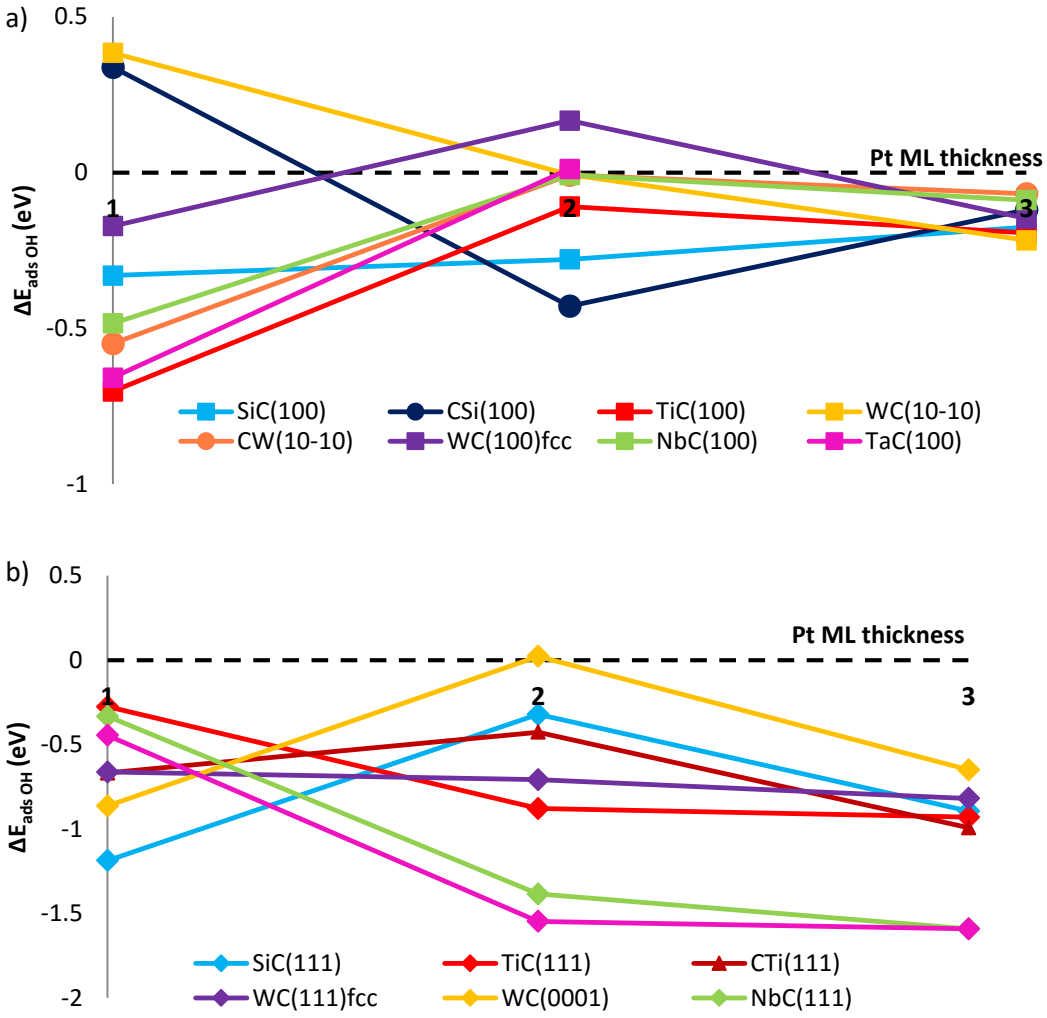

However, the (111)-type surfaces exhibited different overall trends with the final 3ML $E_{ads\ OH}$ covering a wider range. The TaC and NbC datasets were observed to undergo significant strengthening of adsorption as the Pt overlayer thickens resulted in OH adsorption energies far stronger than those for pure Pt. The energy minimised structures, for the 2 and 3ML structures showed the OH binding through shorter O-Pt bonds. In all cases the OH bond angle shifted from 90° at the 1ML to 20°-30°. In the TaC(111) 3ML case, migration to the bridging position upon relaxation was also noted. This would suggest that at 1ML Pt, the carbide was playing a significant role in directing the adsorption of the OH, whilst at increased thicknesses the OH adsorbed in a similar fashion to pure Pt surfaces. The other carbides were observed to converge towards strain affected adsorption energies once an overlayer thickness of 3ML had been reached. The hcp WC

and SiC adsorption strengths were observed to weaken from 1ML to 2ML, in the case of WC(0001) this coincided with a change in the predicted adsorption site from atop to bridge. The fcc WC and TiC systems exhibited less alteration in adsorption energy, experiencing only slight changes in Pt-O bond length. It was generally observed that the increased thickness of Pt resulted in more 'Pt-like' bonding to the surface both in terms of adsorption energy and the angle of binding.

6.3.3 Other Adsorbates on Pt/WC(0001)

As previously noted, the adsorption energies of O and H on Pt(111), WC(0001) and Pt/WC(0001) have previously been reported in the literature.[89] The difference in E_{ads} between Pt(111) and Pt/WC(0001) was calculated to be 0.04eV/atom (+1%) and 0.05eV/atom (-8%) for O and H respectively whereas the difference in E_{ads} between Pt(111) and WC(0001) were +88% and +132% respectively. The addition of the single ML of Pt rendered the WC(0001) much more 'Pt-like'.

In the present work a larger group of adsorbates were tested on the Pt/WC(0001) surface with respect to clean WC(0001) and Pt(111), see table 23.

Table 23 Adsorption energies for a range of adsorbates on Pt(111), Pt/WC(0001) and WC(0001) surfaces

Adsorbate	E_{ads} (eV)					
	WC(0001)	Position	Pt/ WC(0001)	Position	Pt(111)	Position
O	-4.31	C top	-0.85	Oct	-0.82	Oct
N	-2.14	C top	1.15	Tetra	0.50	Oct
CO	-1.62	W top	-1.30	Pt top	-1.50	Tet
NO	-3.31	Bridge	-1.10	Bridge	-1.50	Oct

It can be immediately observed that for all the adsorbates tested, adsorption on the WC(0001) surface was very strong whilst the adsorption was much weaker on Pt(111). Atomic N was predicted not to adsorb on the Pt surfaces while its adsorption was predicted to be favourable on WC(0001). For both the N and NO calculations on Pt(111), spontaneous diffusion from the bridging site to the octahedral hollow was observed. For the CO adsorption on Pt(111), the tetrahedral, octahedral and bridge positions all minimised to within 0.01eV of eachother which is well within the error of DFT. The fractionally lower energy tetrahedral site was reported as the preferred site, however occupation of the other two is also possible.

Addition of the Pt ML was observed to significantly reduce the E_{ads} relative to the WC(0001) surface. The greatest similarity to adsorption on Pt(111) was calculated for atomic oxygen on Pt/WC(0001), E_{ads} values for the other adsorbates were also found to be more 'Pt-like' than 'WC-like'. In terms of predicted adsorption site, the addition of the Pt monolayer resulted in the atomic species binding at the 3-fold hollow sites similar to Pt(111) whilst the small molecules favoured adsorption at the bridge and Pt top sites, which were observed to be meta-stable for Pt(111). The 'Pt-like' findings corroborated the more detailed work on O adsorption for the ORR suggesting the tuning of catalytic activity of the carbides with very little PGM outlay may be considered for many other reactions.

6.4 Adsorption on Pt/Tie-layer/Carbide Surfaces

6.4.1 Atomic Oxygen

Following the identification of promising tie-layer candidates in the previous chapter, O adsorption was carried out on a selection of these Pt/X/carbide systems. The purpose of these calculations was to assess the extent to which the tie-metal would impact O adsorption strength and what effect, if any, the underlying carbide contributed. From figure 56, we note that the activity of a material towards the ORR reaction can be correlated with the O adsorption energy and so $E_{ads\ O}$ is our chosen descriptor in this case.

Atomic oxygen was placed at the bridging site for the (100) surfaces and in the 3-fold hollow sites for the (111) type surfaces and the $E_{ads\ O}$ values calculated according to equation 24 as previously.

Figure 65 O adsorption energies for the Pt/X/carbide(100) surfaces relative to the adsorption of oxygen on pure Pt(100) at 0.5ML. $E_{Pt\ outer}$ is the predicted stability of the tie-layer to favour a Pt outer skin

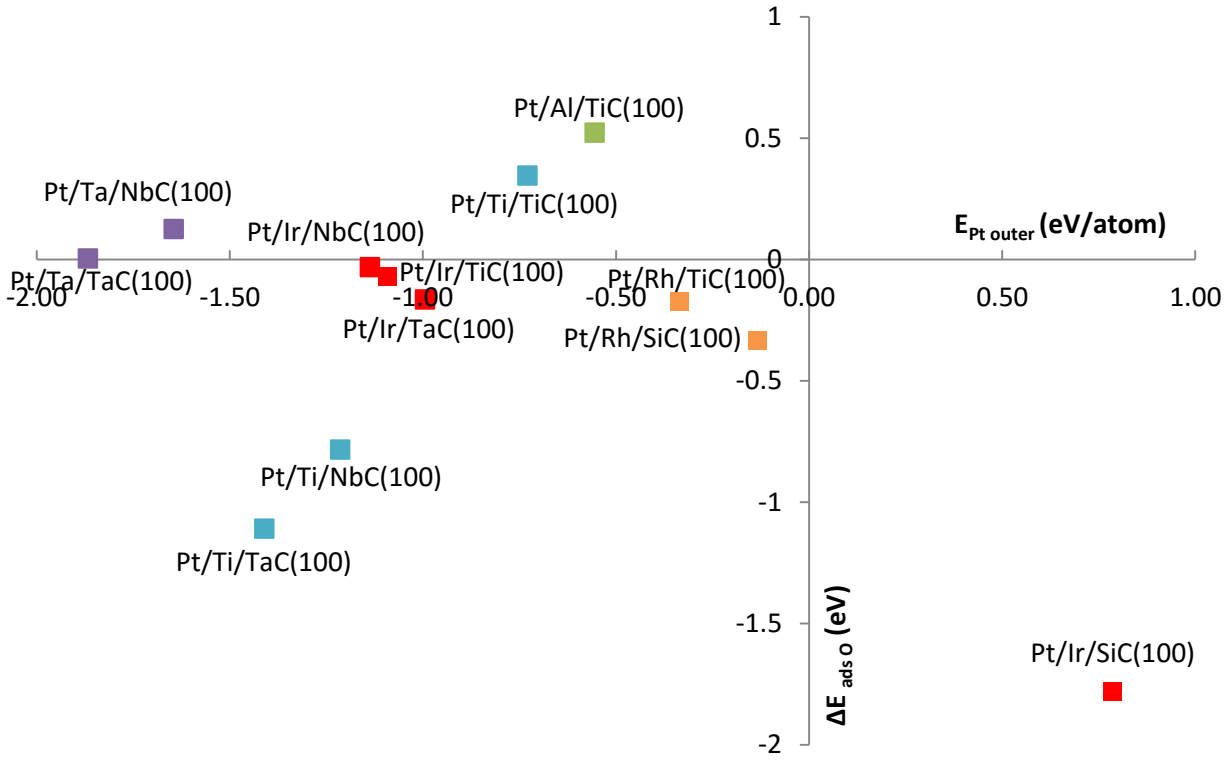

For the (100) surfaces in figure 64, a significant adsorption effect caused by the tie-layer metals was suggested by the grouping of $E_{ads\ O}$ in tie-metal clusters. Notable exceptions to this trend were the very strongly adsorption energies on Pt/Ti/TaC/, Pt/Ti/NbC and Pt/Ir/SiC. In the Ti tie-layer cases, the oxygen atoms were observed to spontaneously migrate through the Pt layer toward the tie-layer resulting in increased adsorption strength as more interactions with surface atoms occurred. This migration can be explained by the oxophilic nature of Ti and would prove detrimental to the system activity since it reduces the availability of the O to react at the overlayer surface. The very strong adsorption of O on Pt/Ir/SiC(100) was observed to coincide with a surface rearrangement which improved the stability of the system and hence resulted in the very negative $E_{ads\ O}$ value.

Of the tie-layer metals trialled, Al was observed to lessen the $E_{ads\ O}$ on TiC by 0.88 eV resulting in a weaker adsorption than that of pure Pt. This is significant as the addition of the Al had significantly altered the Pt behaviour, bringing it close to the region of the volcano plot (figure 56) that was predicted to improve activity. Of the other tie-metals tested on the TiC(100) surface, Ti was predicted to weaken the adsorption energy relative to pure Pt, whilst the Rh and Ir tie-layers were expected to weaken the adsorption in relation to the Pt/TiC(100) value but not that of Pt. The Ta tie-layer containing systems were also calculated to have significantly weakened O

adsorption in the 'improved activity' region, however Ta was not predicted to adsorb favourable to the fcc(100) surfaces and so achieving a stable overlayer experimentally is unlikely.

Figure 66 DOS plots for O adsorption on a) Pt/Al/TiC(100), b) Pt/Ti/TiC(100), c) Pt/Ir/TiC(100) and d) Pt/Rh/TiC(100), only the top bilayer of carbide is included

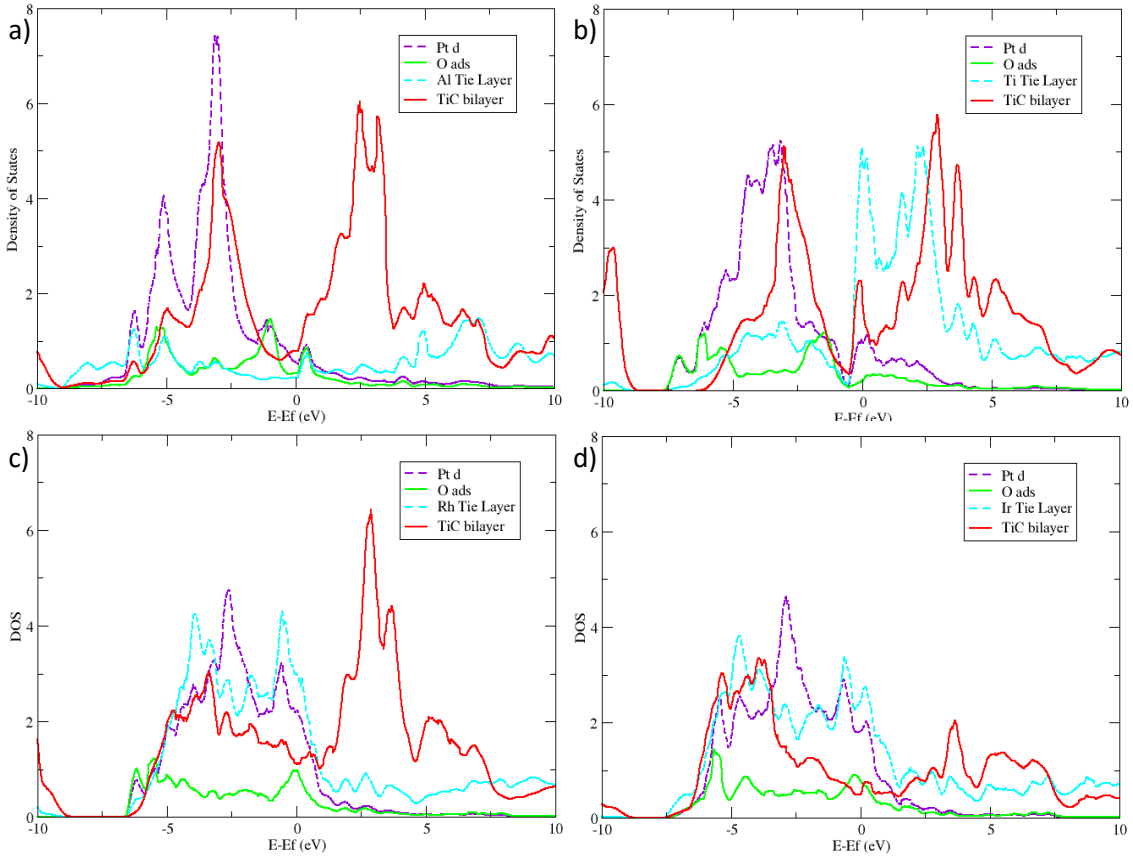

To investigate the effect of the tie-layers, DOS plots for the O adsorbed systems were constructed, see figure 65. Immediately noticeable was the difference in bandwidth and band shape for the Pt (marked in dashed purple) adsorbed on the different tie-layers. The Al and Ti tie-layer systems, a) and b) respectively, exhibited a narrowed Pt band indicative of charge transfer to the Pt as calculated in table 15 chapter 5. This is significant since O adsorption onto the Pt/carbide systems was universally observed to involve significant charge transfer to the O.

The O DOS trace, shown in green, was observed to interact differently with these surfaces. For the Al tie-layer over TiC the Pt maximum was noted to fall exactly in the centre of the O pseudogap and overlap was observed with Pt for the full extent of the O trace. Above E_f a smaller, separate Pt peak was noted to occur around 0.5 eV which coincides with the start of the carbide conduction band. The O trace has two clear maxima, the first of which was shifted negatively from E_f, indicating the relative stability of the interaction. The plots for the later TMs Rh and Ir show broader Pt bands with excellent overlap maintained between the tie-layer and Pt-layer. In these

cases the O bands were broadened, suggesting more covalence in the character of the bonding, and the first maxima was located at E_f. The Pt/Ti/TiC system appears to combine aspects of both of these groups; the lesser degree of d-band filling resulted in the narrowing of the Pt trace and whilst the O band at E_f was broadened it had also been shifted negatively in energy. These findings again suggest that the distribution of the DOS throughout the d-band is of crucial importance in the explanation of reagent adsorption and the E_d value is not sufficient.

Figure 67 O adsorption energy for the Pt/X/TMC(111)-type surfaces relative to O adsorption on Pt(111) at 0.25ML. $E_{Pt\ outer}$ is the predicted stability of the tie-layer to favour a Pt outer skin

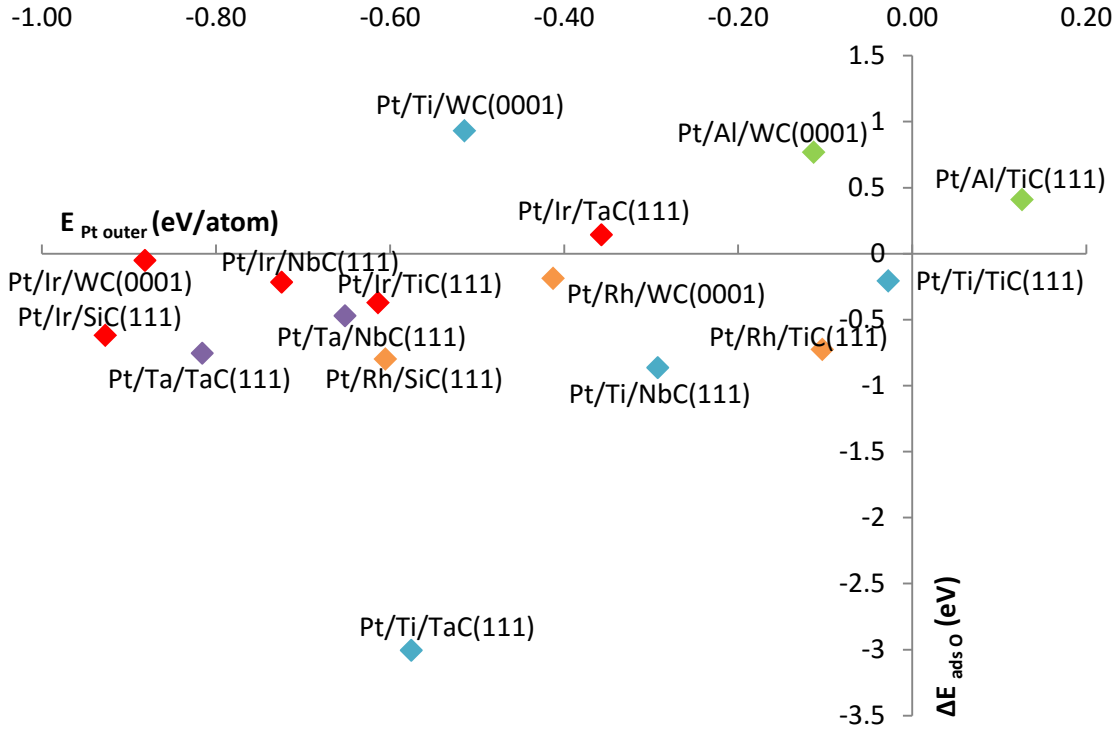

For the (111)-type surfaces, less grouping of $E_{ads\ O}$ by tie layer was observed. Increased activity toward ORR was predicted for Pt/Ir/TaC(111) as the $E_{ads\ O}$ was calculated to be 0.14 eV less than that of Pt(111). Pt/Al/TiC(111) was also predicted to weaken the $E_{ads\ O}$, by 0.41eV, although Pt at the surface of the bilayer had previously been predicted to be unstable. The Pt/Ti/WC(0001) and Pt/Al/WC(0001) systems were also predicted to have $E_{ads\ O}$ significantly weaker than Pt, however in these cases, the $\Delta E_{ads\ O}$ was greater than the calculated 0.4eV region for improved ORR activity.

Spontaneous O migration through the Pt layer to bond with Ti was observed in all of the Ti containing systems due to the oxophilicity of Ti, and resulted in strengthened O adsorption for the TaC and NbC systems whilst for Pt/Ti/TiC $E_{ads\ O}$ remained unaffected. O descent into the Pt layer was noted for the Ta-tie systems, however the overall $E_{ads\ O}$ were reduced by 0.25eV in each case.

The Rh containing systems were all calculated to have a strengthened $E_{ads\ O}$ making them less favourable for application in ORR settings.

The Ir containing systems produced a wide range of $E_{ads\ O}$ for the (111) systems. The Pt/Ir/NbC and Pt/Ir/TaC systems were both observed to give rise to rippled Pt surfaces on the introduction of O and both calculated to produce a weakened $E_{ads\ O}$ as the O was associated with the Pt out of the surface plane. The Pt/Ir/WC adsorption was predicted to be slightly stronger than without the tie layer as the O was observed to approach the Pt surface more closely (2.07Å compared to 2.25Å without the tie-layer). Lastly the Pt/Ir/SiC $E_{ads\ O}$ was doubled in strength compared to its non-tie-layer version as the O again moved towards the Pt surface (2.10Å from 2.26Å). In Chapter 5 table 15 it was noted that significant charge transfer from the SiC(111) to the Ir occurred which may provide an explanation for the strengthened O adsorption as localised charge could be transferred via the outer Pt to the electronegative oxygen.

The lack of correlation between the $E_{ads\ O}$ values of systems based on the same carbide would suggest that the tie layer electronic structure was playing a significant part in the O adsorption. However the expansion wrought by the carbide as a support was still active in altering the adsorption behaviour as the variation in $E_{ads\ O}$ with the same tie-layer metal attested. The surface with the least expansion from lattice mismatch, WC(0001) is identified to be the system most likely to produce Pt-bilayer-like $E_{ads\ O}$. However, chapter 4 figure 25 also suggested that due to their electronic structure contributions the SiC(111) and TaC(111) had the most similar E_d to Pt(111). The prediction of Pt/Ir/TaC(111) in the improved ORR activity region suggests that, if stability concerns could be overcome, tie-layers could mitigate the over-binding of O on Pt/carbide surfaces.

6.4.2 Stability Concerns in Oxygen-Rich Environments

Given the propensity for O diffusion into the surface of Ti and Ta-containing systems, the stability of the overlayer and its predicted ordering was questioned. $E_{Pt\ outer}$ were recalculated for a selection of the tie layer systems in the presence of adsorbed O. The results, shown in figure 67 below, revealed that a number of systems which had previously been predicted to favour a Pt/tie-layer/carbide ordering were reversed under O-rich conditions. Of particular note were the Pt/Al/WC(0001) and the Pt/Al/TiC(111) surfaces which had both been predicted to produce weakened $E_{ads\ O}$ values.

Figure 68 The stability of the bilayer for Pt outer configuration in the presence of adsorbed oxygen

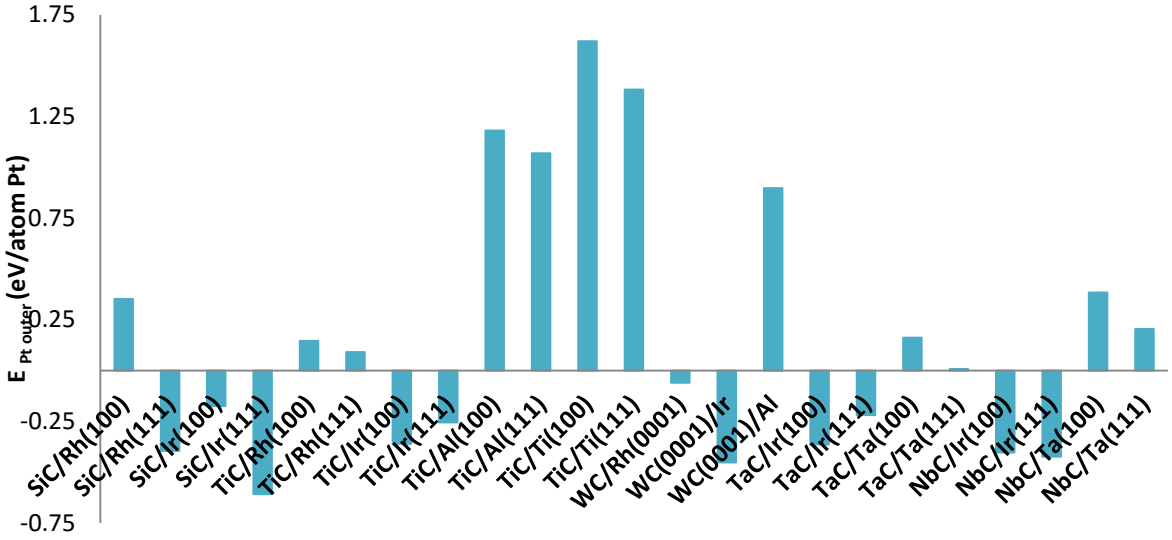

It was suggested that an increased Pt outer layer thickness might reduce the ability of the O to sequester into the oxophilic tie layers and reduce the over-weakening of O adsorption on other surfaces. In order to investigate this, a second Pt ML was positioned on top of the Pt/tie-layer/carbide structures and allowed to minimise prior to O adsorption being carried out.

The $E_{ads\,O}$ of the 2 ML Pt/tie-layer/carbide overlayered systems were compared to the 1ML Pt/tie-layer/carbide systems in figure 68. All of the 2 Pt ML systems were observed to result in adsorption energies stronger than those of pure Pt although the Pt/Ir/TaC(111) and Pt/Ir/NbC(100) values were 'Pt-like'. The smallest influence from the additional Pt was observed for the Rh-containing systems and some of the Ir-containing systems. This suggested that the underlying support and Rh were having little effect on the O adsorption.

Figure 69 $\Delta E_{ads\ O}$ values for single and double Pt ML/tie-layer/carbide systems on the a) (111)-type systems and the b) (100)-type systems, relative to the $E_{ads\ O}$ on Pt(111) and Pt(100) respectively

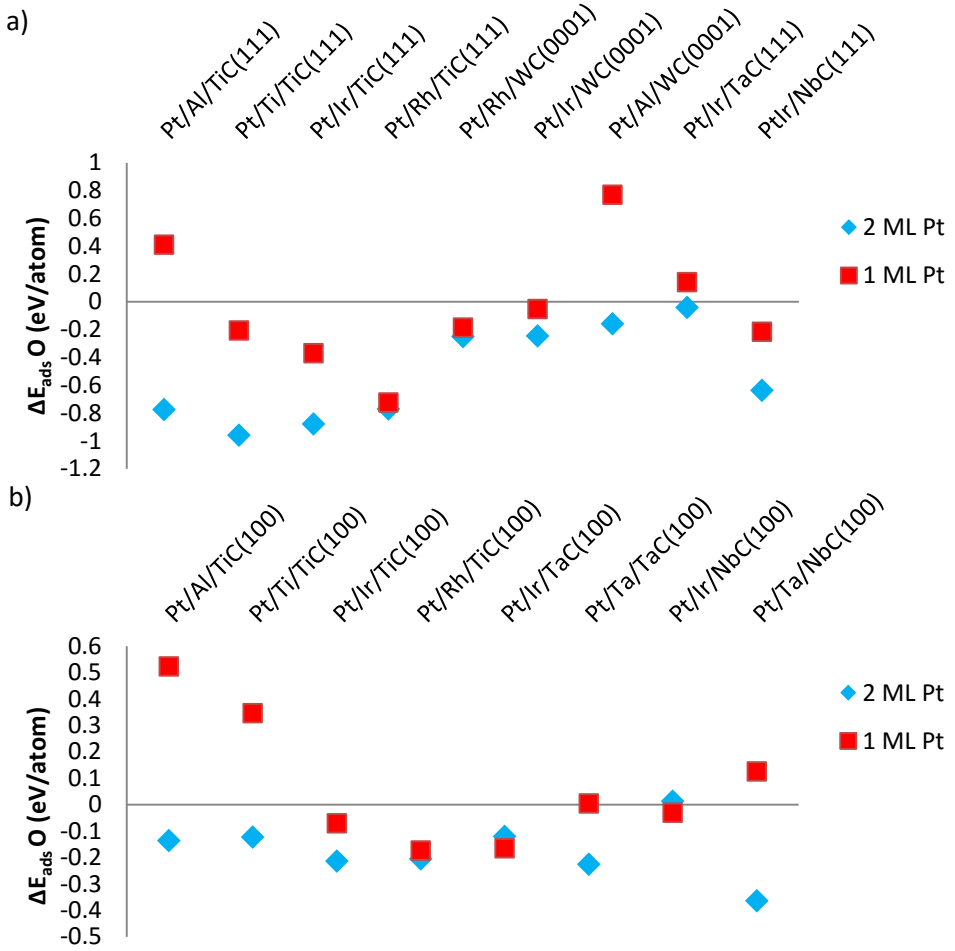

For Pt/Ti/TiC(111) where the oxophilic tie-layer had resulted in O diffusion through the first Pt layer, the addition of extra Pt led to the O settling in the first Pt layer and not binding to the tie-layer atoms. In the Pt/Ir/TiC(111) structure where significant rippling of the Pt layer has previously been noted, the addition of Pt reduced the surface distortion although as previously mentioned this had a minimal effect on the $E_{ads\ O}$ value. Whilst 2MLs of Pt were successful in reducing the diffusion of O through the overlayer, any benefit of the tie-layers in terms of weakening the $E_{ads\ O}$ was lost by the addition of extra Pt. This suggested that the positive, adsorption-weakening effect of the tie-metal's electronic structure was being lost through attenuation as the number of intervening layers increases. Furthermore, as shown earlier, once the system tends toward 2 or 3 ML layers (and ultimately the bulk) the expansion of the Pt lattice by the underlying carbide dominates the results.

Figure 70 Trialled 2 ML Pt/X/carbide systems, bars represent stability towards Pt outer skin formation whilst lines indicate $\Delta E_{ads\ O}$ relative to pure Pt

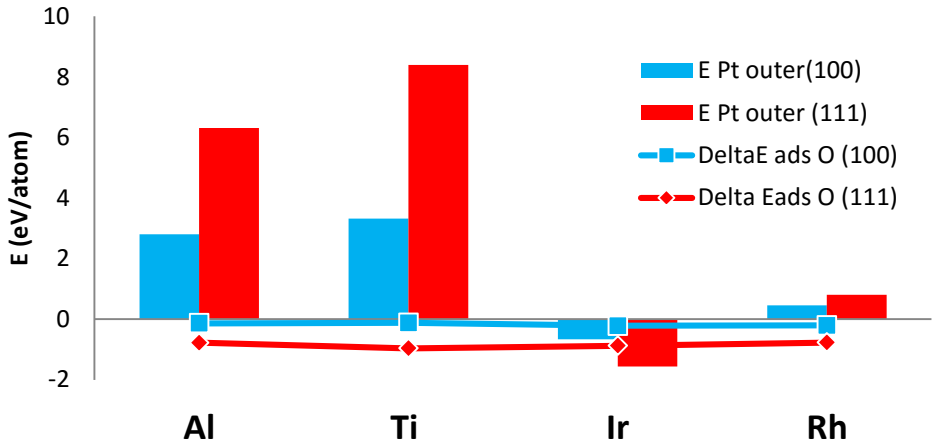

The ability of the bilayer system to retain Pt at the surface was tested for the TiC surfaces and tie-layer metals, see figure 69. Whilst the Ir tie layers were predicted to favourably form the Pt outer layer, the Al, Ti and Rh systems were predicted to favour Pt sequestration. It was noted however that the simple comparison of geometry minimised structures does not provide evidence for the diffusion mechanism by which this process would occur. Whilst TM leaching is known to occur from Pt bulk alloys[205] and Pt surface alloys[206], equally the creation of Pt-skins on bulk Pt alloys has been observed to lessen overall dissolution.[71] The implication is thus that when considering practical application, through a suitably thick deposition of Pt, loss of tie-metal from the core could be limited. Whilst processes such as the Kirkendall effect have been used to explain the dissolution of Co from PtCo nanoparticles observed in experiment,[186] to solve the problem from a theoretical perspective, computationally intensive Nudged Elastic Band (NEB) calculations would be needed to investigate the diffusion of the tie-layer metals throughout the system.

6.5 Conclusions

In this chapter, an assessment of whether carbide and tie-layer inclusion could positively influence O adsorption was undertaken. Reagent adsorption on the Pt/WC(0001) surfaces revealed that the addition of 1ML of Pt significantly weakened E_{ads} values in comparison to the clean carbide surface making the adsorptions more 'Pt-like' than 'carbide-like'. Pt/WC surfaces were calculated to produce $E_{ads\ O}$ that were 'Pt-like' or weaker than Pt suggesting that they may maintain or improve activity towards ORR. Whilst C-terminated TiC and SiC also produced weakened $E_{ads\ O}$ values, their comparative instability rendered them unsuitable surfaces to pursue for fuel cell applications.

A strong correlation was observed between the adsorption of molecule through the same atom (O and OH) for the (100) type surfaces whilst for the (111) surfaces significant divergence was seen. This was caused by the migration of O through the 1ML Pt overlayer towards the oxophilic Ti, Ta and Nb components of the carbides in question. The addition of extra layers of Pt was observed to reduce O migration to the carbide surface and shifted $E_{ads\,O}$ to converge at strained-Pt values. This implied that, discounting the strain effect imposed by our model, the $E_{ads\,O}$ values of the Pt/carbide systems would return to pure Pt values at thicknesses greater than 3ML.

The addition of tie-layers resulted in WC hcp, TiC and TaC surfaces with $E_{ads\,O}$ values weaker than those of pure Pt. For the (100)-type surfaces, $E_{ads\,O}$ were clustered by tie-metal whilst the (111)-type surfaces exhibited no obvious trends by carbide or tie-metal. Oxophilic tie-layers such as Ti and Ta were observed to cause spontaneous O migration through the Pt layer on the (111)-type surfaces. The addition of O was also predicted to reverse the Pt outer formation preferences for many of the most promising Pt/X/carbide structures. Increase of the Pt overlayer thickness was calculated to prevent O diffusion to the tie-layer but also resulted in strengthened $E_{ads\,O}$ values for the systems that at first showed potential improvement towards the ORR reaction.

The calculation of spontaneous O migration to the carbide surface and tie-layer provokes questions of the effect of oxidation upon the catalyst surface. Purposeful addition of excess oxygen to model the formation of oxide layers within the structure would be instructive, allowing further investigation of the predicted activity of the materials. Likewise, the computed thermodynamic instability of the ordering of the bimetallic over-layers raises the question of whether the kinetic trapping of desired structures would be possible given the activation energy necessary for segregation to the surface to occur. Following on from the previous chapter, the investigation of alloy overlayers is necessary future work to better understand the stability of these systems. Although any synergic effect of the carbide would be lost through increased overlayer thickness, use of the carbide core would still allow the reduction of PGM loading and could stabilize the formation of alloyed catalytic surfaces.

7. Pt Clusters and Stability towards Aggregation

The instability of Pt nanoparticles at the cathode plays a significant role in both the loss of performance and the shortening of fuel cell lifetimes. As such, tackling instability has been identified as the key to optimising PEMFC catalysts.[18,14] Pt dissolution and agglomeration to form large Pt particles results in the loss of electrochemically active surface area, an increase in the activation overpotential and a reduction in the cell voltage produced.[17] Smaller nanoparticles have been observed to be less stable with 2 and 3nm Pt/C_{black} nanoparticles losing surface area and hence mass activity more rapidly than particles of 7nm and larger.[40]

Improved stability may be achieved through structural and component based approaches. Nanostructured thin film catalysts, of the type developed by 3M, utilise comparatively large Pt crystallites to form a thin Pt film which fully encapsulate the organic support.[53] Experiment has also indicated that expansion of the Pt lattice parameter (in a core shell nanoparticle structure for example) can reduce the chemical potential of the surface and hence reduce Pt dissolution.[207] The use of alloying metals to aid binding to the support has also been discussed a possible means to reduce Pt surface area loss,[205] and tie-layer structures of the type introduced in the last two chapters may also have similar effects.

To assess the stability of our Pt/carbide systems towards roll-up and the formation of Pt nanoparticles, Pt clusters were modelled to provide a comparison with the modelled Pt thin films. The modelling of these clusters gave opportunities to investigate the electronic structure of Pt clusters of varying sizes. It was also possible to observe their differences from bulk Pt with a view to understanding their properties for comparison with core-shell particles. Energy relationships between the number of atoms and coordination of atoms in the clusters and their total energies were drawn up as a basis for the evaluation of cluster stability. The Pt cluster energies were also compared to the Pt/carbide interaction strengths to identify cases in which ML vs. cluster formation might be expected. Lastly, simulations using effective medium theory, EMT,[208] were also carried out to investigate the surface structures which could be expected with increased Pt loading and a modulated support interaction.

7.1 Methodology

7.1.1 Cluster Calculations

Given the large number of atoms we wished to include in our clusters the fact that traditional Kohn-Sham DFT scales at N^3, where N is the number of atoms in the system, was problematic. A well scaling, highly parallelisable code was needed to make the calculations computationally viable. The projector augmented wave DFT code GPAW[209] was chosen since its real-space-grid basis set scales well for large computational resources[79] and it can be applied without periodic boundary conditions. The GPAW code also gave the option of using a localised atomic orbital basis set, which is highly efficient, allowing geometry optimisation to be carried out more quickly with the ability to then switch to the more accurate grid basis set for the final steps. At the time of code selection ONETEP[210] was also considered, however the initial method was not suitable for metallic systems. The treatment of thousands of metal atoms using ONETEP is now possible and near perfect agreement is witnessed between CASTEP and ONETEP simulations.[211]

Geometry minimisation calculations were run using the linear combination of atomic orbitals, LCAO, method within the GPAW code. After minimisation, the last run was carried out using the finite difference, FD, grid method. In both sets of calculations the following parameters remained unchanged; the RPBE exchange correlation functional was used and the double zeta polarized basis set was specified. A grid spacing of 0.18 was chosen following convergence testing and a Fermi temperature of 0.1eV was used for all the cluster sizes. The clusters were included in cells with at least 5Å of vacuum to the nearest boundary which was confirmed via convergence testing, see appendix B. During convergence testing, numerical oscillations of energy were noted and were traced to the application of inconsistent grid spacing. As a result of this, the unit cell parameters were chosen to be divisible by 1.8 to ensure a consistent grid spacing of 0.18. In this case, zero boundary conditions were applied instead of periodic boundary conditions. The BFGS algorithm was applied for geometry minimisation until the atomic forces were less than 0.05 eV/Å.

Following the work of Xiao and Wang[212] and Nie *et al.*[213] a range of planar and 3D structures were trialled for the 2-12 Pt atom clusters. For the larger structures, cuboctahedron and derived clusters were cut from bulk Pt with a lattice parameter of 4.002Å using ASE.[151] The cuboctahedral clusters were chosen to allow comparison with the (100) and (111) extended surfaces and to follow the alteration of characteristics due to cluster size. Following the geometric minimisation, the average cluster binding energy, E_{bind}, was calculated using equation 29

(29) $$E_{bind} = \frac{N \cdot E_{atom} - E_{cluster}}{N}$$

where N is the number of atoms in the cluster, E_{atom} is the total energy of a single Pt atom and $E_{cluster}$ the total energy of the cluster. The average bond energy, E_{bond}, was calculated using equation 30 for the comparison of bond strengths and the average bond length of the structures was also attained.

(30) $$E_{bond} = \frac{N \cdot E_{atom} - E_{cluster}}{N_{bond}}$$

Electronic structure analysis was carried out via density of states (DOS) plots whilst the electron density was plotted from the real space wavefunction data.

7.1.2 Overlayer Stability Calculations

To investigate overlayer stability towards entropy, a set of Pt overlayer configurations were geometry optimized in order to estimate the entropy of a system. This was achieved by applying statistical thermodynamics to a population of structures at different energy levels. Whilst Metropolis Monte Carlo simulations or molecular dynamics would provide excellent data for this type of investigation, the slow convergence of these methods led us to seek alternative solutions and after consideration effective medium theory, EMT,[208] was used on a set of randomly generated configurations that were optimised within a local structure optimization scheme (as opposed to global minimisation).

EMT is based on the fact that the total energy of any atom is determined by its interactions with the surrounding atoms (in a similar manner to DFT using the electron density of the system).

(31) $$E = \sum_i \left\{E_{c,i}(n_i) + \frac{1}{2}\left[\sum_{j\neq i} V_{ij}(r_{ij}) - \sum_{j\neq i}^{ref} V_{ij}(r_{ij})\right]\right\}$$

$$V(r) = -V_0 exp\left[-k\left(\frac{r}{\beta - s_0}\right)\right]$$

Using the interaction energy of an atom embedded in a homogenous electron gas as a reference, expression 31, and with the inclusion of corrections (i.e. for d-d hybridization in TMs) EMT potentials may be used to work out the Pt interaction energies for very large systems very simply. The interatomic potentials can be fitted with DFT and experimental data by minimising the functional in expression 32.

(32) $$f(\{p\}) = \sum_i q_i \cdot |C_i^{th}(\{p\}) - C_i^{target}(\{p\})|^2$$

This enables EMT to reproduce realistic material properties including for TM metals and their alloys.[214] Such potentials are then suitable for use in molecular dynamics simulations where the calculation of the electron density would result in huge computational expense such as for low symmetry systems with large numbers of atoms. Within ASE, the Pt, Pd, Ag, Au, Al, Ni and Cu potentials are parameterised to give realistic representations whilst those for H, C, N and O offer less rigorous answers. Whithin this elemental subset then, alloy and surface adsorptions maybe tackled.

To represent the Pt-carbide interaction term, a Morse potential,[215] which relates internuclear separation to potential energy, was employed. In this case, r is the internuclear distance, r_0 is the equilibrium bond distance, D is the well depth and a the constant which determines the well width.

(33) $$E(r) = De^{-2a(r-r_0)} - 2De^{-a(r-r_0)}$$

As can be seen in figure 70, the potential combines a short range repulsion, so that as nuclei move together the potential energy increases, and a long range attractive term.

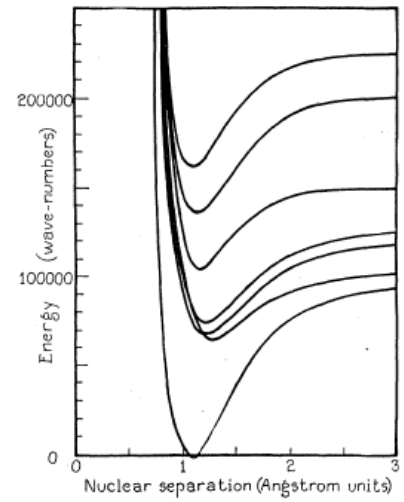

Figure 71 Potential energy curves of nitrogen species, reproduced from Morse[215]

In order to reproduce the 'egg-box' like potential of a cubic surface, the Morse potential was modulated using sine and cosine functions to coincide with outer layer surface atoms, as seen in figure 71. The egg-box effect mimics the potential energy surface when moving from a binding site, through a peak, to an adjacent site. It is recognised that this potential is a significant

simplification of a the real surface potential energy, however it provides us with a model system whereby we can explore the influence of 'strong', 'moderate' and weak' Pt adsorption on a surface of cubic symmetry. Importantly this will give us an idea of the magnitude of the entropy associated with these systems to enhance our thermodynamic analysis.

Figure 72 Schematic illustrating the egg-box potential at the simulation floor, colour range represents the differing potential energies.

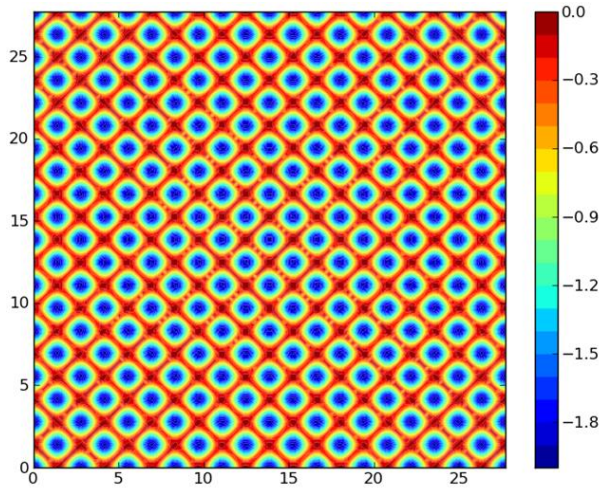

For the calculations a 10x10xNL grid, where NL is the initial number of layers, was created and set to the inter-Pt_{bulk} distances with a vertical vacuum of 20Å. The modulated potential was applied to the lower boundary of the simulation cell to mimic the interaction that the Pt could have with the carbide surface. Pt atoms were randomly placed in the grid to produce starting structures which were then optimized using the FIRE[216] optimiser from ASE with convergence for the atomic forces set to 0.075 eV/Å. As an initial trial for the model, 2500 initial structures were created and minimized.

For the statistical thermodynamics calculations the following expressions were used for the partition function, Z, Helmholtz free energy, A , probability of finding a specific state, P_s, and Entropy, S where E_s is the total energy of the system in state *s*.

(34) $$Z = \sum_{s} exp^{\frac{-\Delta E_s}{k_B T}}$$

(35) $$A = -k_B T lnZ$$

(36) $$P_s = \frac{1}{Z} exp^{\frac{-\Delta E_s}{k_B T}}$$

(37) $$S = k_B \sum_s P_s ln P_s$$

7.2 Small Pt Clusters N=2-12

Following the literature evidence that for clusters between 2-9 atoms planar structures were of similar stability to their 3D counterparts,[212] a range of small cluster geometries including the minimum energy geometries calculated by Nie *et al*[213] were constructed and minimised according to the methodology described previously.

Figure 73 Geometry optimized small Pt clusters, from left to right, top row: 2, 3, 4 flat, 4 tet, 5 flat, 5 tet, six, second row: 7, 8, 8b, 9, 9b, third row: 9c, 10, 10b, 11 and 12

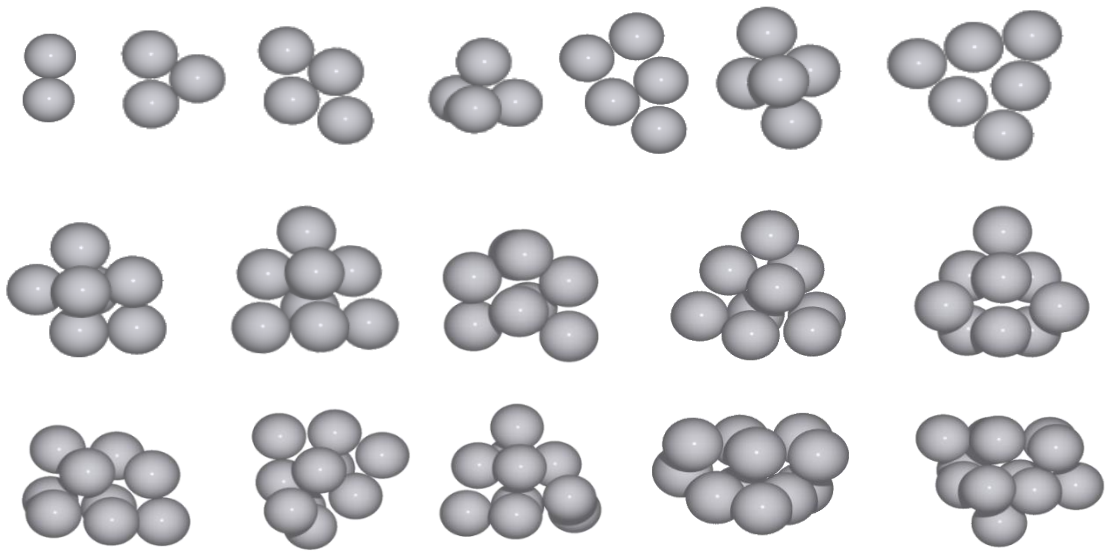

The Pt dimer was calculated to have a bond length of 2.37Å and a binding energy per atom of 1.77eV which were in good agreement with the experimental bond length of 2.34 Å and dissociation energy of 1.83± 0.08 eV/atom,[217] and previous theoretical values of 2.34 Å and 1.76 eV/atom.[212] As expected the energy per atom became increasingly negative as the number of atoms increased, moving towards the bulk Pt value.

Table 24 Total energies, energies per atom, binding energies, bonding energies and average bond length for the FD 2-6 Pt atom clusters. Literature values are taken from Xiao and Wang[212]

Cluster Size	Total Energy (eV)	Energy (eV/atom)	E_{bind} (eV/atom)	E_{bond} (eV)	Ave. bond length (Å)	Literature E_{bind} (eV/atom)
2	-4.23	-2.12	1.77	3.55	2.37	1.76
3	-8.32	-2.77	2.43	2.43	2.5	2.33
4flat	-11.91	-2.98	2.63	2.11	2.53	2.62
4tet	-11.89	-2.97	2.63	1.75	2.62	2.68
5flat	-16.17	-3.23	2.89	1.81	2.49	2.89
5tet	-15.7	-3.14	2.8	1.55	2.64	2.91
6	-20.75	-3.46	3.12	2.08	2.54	3.08

For the very small clusters (N=2-7) the binding energies were observed to be in very good agreement with the Xiao values, although for the 5 atom clusters the relative order of stability was reversed. It must be noted however that the energy differences between these structures were small and well within the accuracy of standard DFT calculations, suggesting at the very least a meta-stability for the planar structures of this size. The planar 6 Pt arrangement calculated here was also observed in the literature to be the most stable 6 atom structure. The planar structures (N= 2, 3, 4, 5 and 6) all exhibited stronger bond energies and shorter bond distances than their 3D counterparts. The strong correlation between bond length and bond strength for all of the small clusters can be seen in figure 73. Given these findings, layered structures were included in the medium sized cluster structures.

Figure 74 Plot showing the increase in bond strength with decrease in bond length for the small clusters

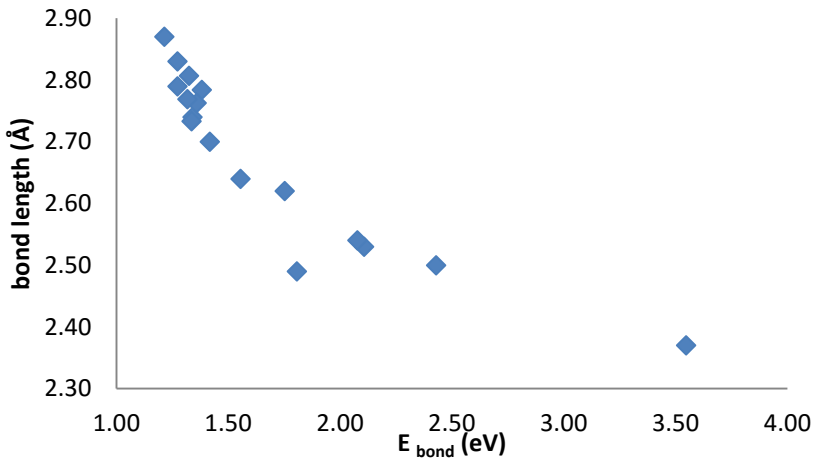

For the 7-12 atom clusters, ad atoms were placed on to facets of the octahedral and tetrahedral structures as well as layered structures constructed from the combination of smaller, planar

arrangements. The addition of ad-atoms to the tetrahedral and octahedral structures resulted in quite significant distortions of the base structures and increased average bond lengths. For N=9, structure 9a was found to have the lowest energy, however the layered structure 9c was found to have a comparable energy with the more spherical 9b. The 11 and 12 atom clusters calculated here were the lowest energy structures previously reported and based on a layering of the 6 and flat5 arrangements. The N=7-12 clusters E_{bind} values were in good agreement with the literature values, the maximum deviation being 0.15eV and the average deviation 0.02eV.

Table 25 Total energies, energies per atom, binding energies, bonding energies and average bond length for the FD 7-12 Pt atom clusters. Literature values are taken from Xiao and Wang[212] except those denoted with † taken from Nie et al.[213]

Cluster Size	Total Energy (eV)	Energy (eV/atom)	E_{bind} (eV/atom)	E_{bond} (eV)	Ave. bond length (Å)	Literature E_{bind} (eV/atom)
7	-23.84	-3.41	3.06	1.34	2.74	3.21
8	-29	-3.62	3.28	1.38	2.78	3.19†
8b	-28.12	-3.52	3.17	1.34	2.73	3.15†
9	-33.56	-3.73	3.39	1.32	2.81	3.33†
9b	-32.85	-3.65	3.31	1.42	2.7	-
9c	-32.98	-3.66	3.32	1.36	2.76	-
10	-37.78	-3.78	3.43	1.27	2.83	3.49†
10b	-37.69	-3.77	3.43	1.32	2.77	-
11	-41.95	-3.81	3.47	1.27	2.79	3.67
12	-46.61	-3.88	3.54	1.21	2.87	3.58†

7.3 Medium Pt Clusters N=13-201

From N=13 onwards, structures solely based on the cuboctahedron were calculated, however it is noted that icosahedral Pt_{13} clusters are also stable as are a number of layered Pt_{13} clusters. Structural searches using genetic algorithms for larger atomic numbers suggest a shift at N=19 from triangular based structures to icosahedral ones and then at N=38 towards 'fcc-like' clusters.[213] However, for this investigation cuboctahedral clusters were chosen to the highlight the alteration of characteristics due to cluster size.

Previous work on the cuboctrahedral Pt clusters ranging from N=13 to 1415 carried out by Li *et al.*[79] concluded that after reaching 147 atoms, the adsorption characteristics of Pt clusters were similar to those on extended Pt surfaces. This was explained as a result of the screening of the adsorbate by the Pt d-electrons, localising the interaction of the adsorbate at the surface and thus

preventing it 'feeling the effects' of the under-coordinated edge and vertex atoms. The electronic structure of the clusters was also reported and, given the partially filled d-bands providing electron density at E_f, quantum size effects from gaps in the DOS around E_f were not observed. It must be noted that these calculations took place with clusters of fixed geometry, whereas the geometry minimization used in the current work should allow geometric factors to influence the electronic structure and adsorption behaviour of the clusters.

Figure 75 Cuboctahedral based Pt clusters from left to right, top row: 13, 19, 43, 55, 79, second row: 135, 165 and 201 atoms

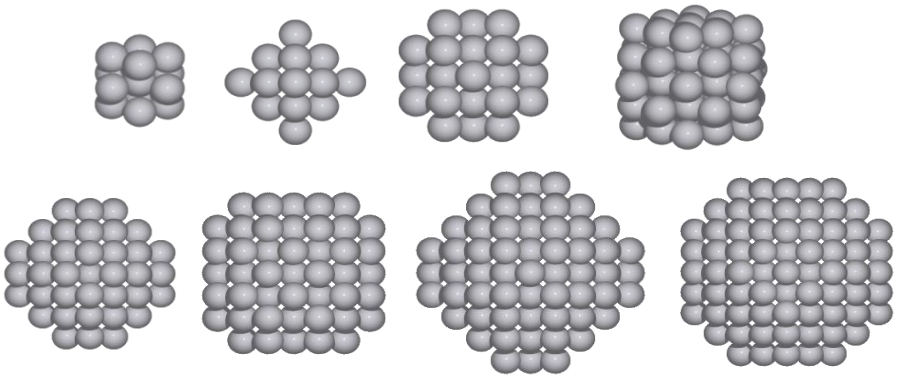

The two-phase minimisation of the medium clusters gave an opportunity to compare the lcao and fd mode outcomes for energy and geometry. Table 26 displays the average movement of an individual atom from its position in the converged LCAO geometry to its position in the FD geometry. Considering these changes in light of the differing number of layers or shells of atoms involved was helpful in identifying trends.

Table 26 Average change in position from LCAO geometry to FD geometry

Cluster Size	13	19	43	55	79	135	165
Change in atomic position (Å)	0.05	0.06	0.02	0.03	0.01	0.10	0.10

For the smaller clusters in the range, 13 and 19 atoms, a large scale contraction was noted towards the central atoms. The increase in position change for the 19 atoms cluster may be due to its under-coordinated vertex atoms being particularly susceptible to relaxation. For the 43 atom cluster, a lesser degree of movement was registered for the first 13 atoms, then moderate motion for the majority of 2nd shell atoms. 6 surface atoms experienced significantly altered positions (0.045Å), these were the 8-coordinate atoms in the centre of the (100) facet, displayed in the centre of the third image in figure 74. This general pattern was repeated for the 55 atom cluster and the vertex atoms experienced changes of 0.029Å, the edge atoms 0.034Å and the centres of the (100) facets again experienced the largest alteration of 0.072Å.

The 79 atom cluster experienced the least average relaxation, with the edge and (100) facet atoms moving 0.019Å and 0.015Å respectively. The 135 and 165 atom clusters showed an order of magnitudes increase in average position change, possibly due to the incomplete nature of the shell (complete shell cuboctahedra or 'magic number clusters' are seen at 13, 55, 147 and 309 atoms). The largest degrees of motion were again observed for the (100) facets on the cluster surface.

The total energies of the LCAO and FD mode calculations varied for a number of reasons. The use of the finite basis set in LCAO mode left these calculations susceptible to basis set supposition error (BSSE) where the basis functions of nearby atomic components overlap to provide a more complete basis set. This results in over binding and the lowering of system energy. This problem can be dealt with in GPAW with the application of 'ghost atoms' to produce a 'mixed basis set' and mimic the degrees of freedom which the system would have if it were adsorbed at a surface (the calculated error then being subtracted from the uncorrected value). The FD values differ from since the FD grid is not susceptible to superposition. However, with the isolated Pt value in each mode subtracted from the cluster value, as can be seen from figure 75, the FD energies were still on average 0.16eV/atom more negative than the LCAO mode values ±0.09eV. This would suggest that the more significant factor in energy difference was actually the further geometric relaxation of the cluster upon conversion from LCAO mode to FD mode.

Figure 76 The energy per atom for LCAO and FD mode geometric optimisations of cluster sizes 13-201 minus the isolated Pt atom value

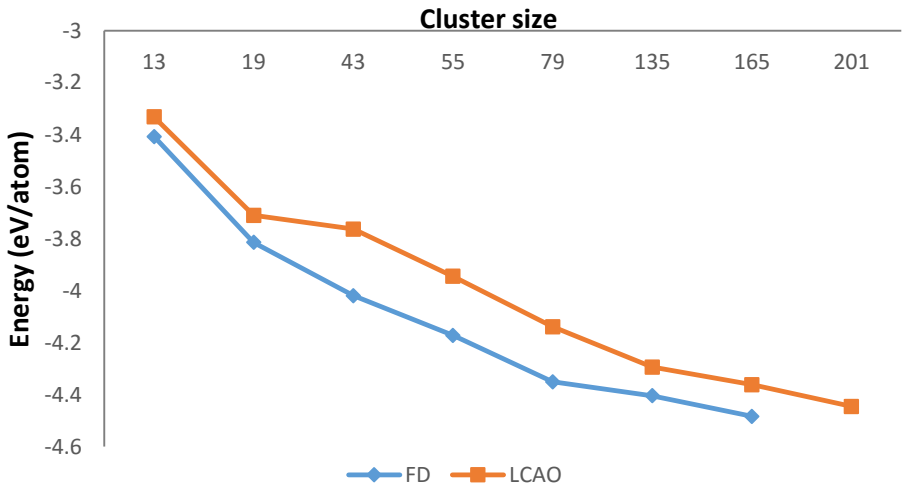

For the medium clusters as the number of atoms increased the energy per atom and binding energy of the Pt decreased towards the bulk Pt figures of -5.43 eV/atom as can be seen in Table 27.

Table 27 Total energy, energy per atom, binding energy and average bond energies for the FD 13-201 atom clusters

Cluster Size	Total Energy (eV)	Energy (eV/atom)	E_{bind} (eV/atom)	E_{bond} (eV)
13	-48.77	-3.75	3.41	1.23
19	-79.01	-4.16	3.81	1.21
43	-187.61	-4.36	4.02	1.11
55	-248.37	-4.52	4.17	1.06
79	-370.87	-4.69	4.35	1.02
135	-640.99	-4.75	4.40	0.99
165	-796.56	-4.83	4.48	0.99
201	-988.04	-4.92	4.57	0.97

7.3.1 Electronic Structure Results

DOS analysis for the cluster electronic structures revealed the transition from 'molecular-like' to 'metal-like' Pt as the cluster size increased. The molecular systems possessed discrete states which were well defined by narrow peaks in the DOS plot. Bulk and metallic systems were observed to produce large numbers of closely lying states overlapping and leading to broad bands being formed in the DOS. In the cluster dataset of figure 76 we observed that between 43 and 55 atoms the localised, narrow peaks became broadened into a wide valence band. The form of this valence band was then further modified as the cluster size continued to increase. The transition from discrete energy states to bands was noted at 147 atoms in the work of Li *et al.* however as previously noted this was calculated from static clusters.

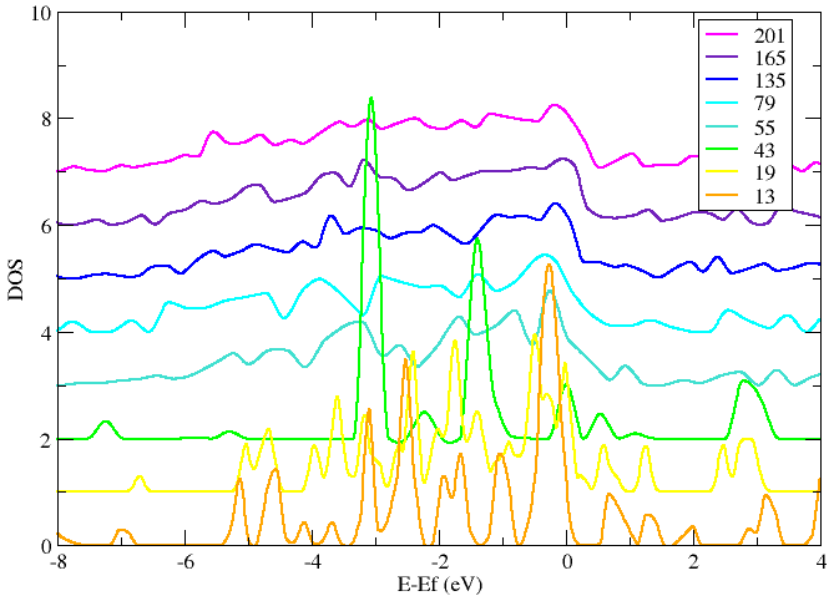

Figure 77 DOS plot for LCAO whole clusters normalised by the number of atoms and offset vertically by 1 unit for clarity

A comparison of the DOS from LCAO and FD converged clusters was made to assess their compatibility and can be seen in figure 77. Although a clear negative shift was visible for the lower portion of the DOS, which is keeping with the 0.5eV more negative energy per atom observed in the previous section, the overall form of the DOS traces were very similar. The maxima at E_f overlapped exactly and a great deal of the finer structural detail was maintained although the relative occurrences of the states at specific energies are observed to differ between modes. Given the high degree of similarity, LCAO mode DOS were judged representative of the cluster data.

Figure 78 Comparison of LCAO and FD converged DOS for the central atom of the 165 atom cluster

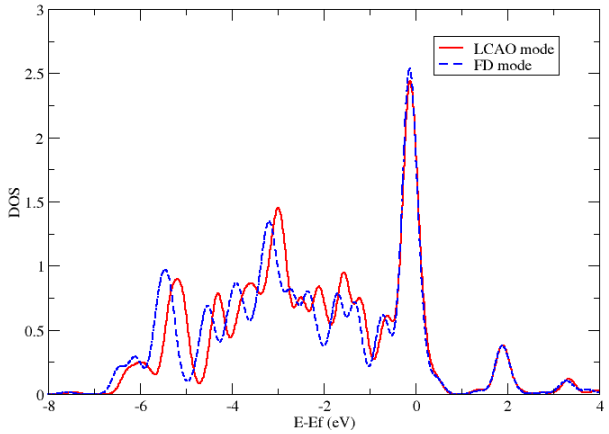

In order to assess how many Pt shells were required for a 'Pt_{bulk}-like' core to be present in a cluster, the central atom d-band pDOS and E_d were also calculated. Since the 12 CN atoms at the centre of the clusters were in the most 'bulk-like' environment it was expected that, as the shell thickness increased, rapid convergence towards Pt metal would be observed.

Figure 79 DOS plot of the LCAO central atom d-band with isolated Pt and Pt bulk d-bands for comparison, traces are offset vertically by 1 unit for clarity

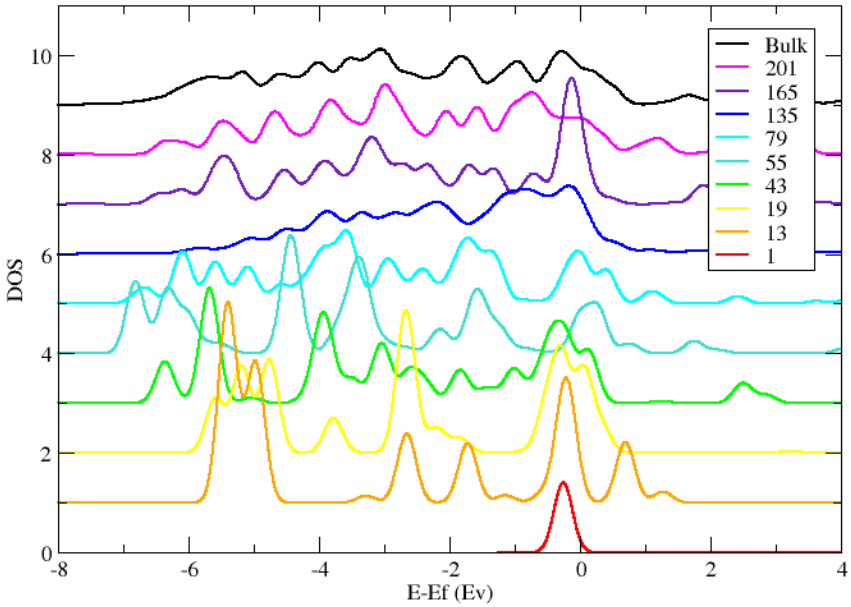

Whilst broadening of the d-band did occur as cluster size increased, as can be seen in figure 78, several unusual features were noted. Whilst the E_d for the 13 atom cluster was expected to be shifted from the bulk value due to the contraction of the surrounding outer shell, the 55 atom cluster has a dramatically lowered E_d of -4.1 eV. From the pDOS we observed that the 43 and 55 atom clusters had distinct bands located between -6 and -7eV which were considerably lower than those of the smaller clusters. As the cluster size increased and more density was located at the top of the valence band near E_f, the band was observed to narrow. Since the band filling had not been altered, the E_d value became more stable around -2.7 eV which was reminiscent of the Pt_{bulk} value, see figure 79.

Figure 80 E_d values for the medium cluster central atoms

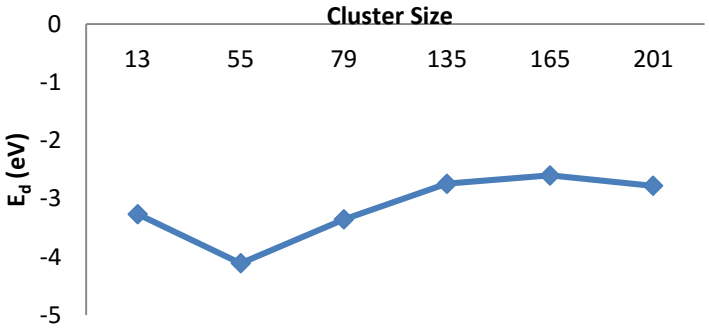

The most eye catching feature of the pDOS however was the large density maximum observed at E_f for the 165 atom cluster. This localisation of density was unexpected given the evolution of the electronic structure from the 79 atom cluster to 135 atoms. A thorough and detailed investigation

of the DOS at E_f throughout the cluster shells was undertaken in an attempt to better understand this behaviour.

Figure 81 DOS for the d-band of 12CN atoms in the a) 55, b) 79, c) 135, d) 165 and e) 201 atom clusters

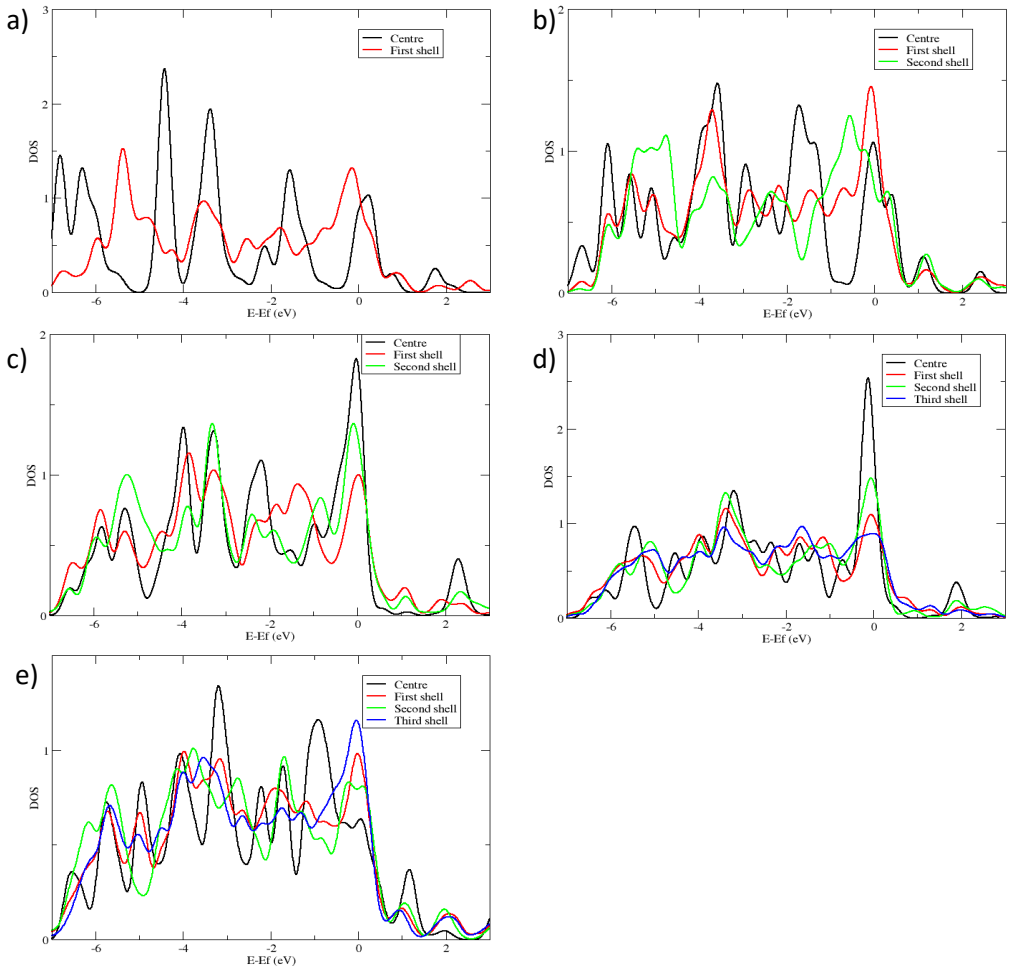

Figure 80 displays the DOS for the CN 12 atoms of the medium sized clusters. Each of the traces depicts the atoms for a different shell of the cluster allowing for a comparison of characteristics through the particle. For the 55 and 79 atom clusters, a significant shift was noted for the E_f peak between the central atom and subsequent shells. This was consistent with the significant shift from the structure cut from the bulk observed after geometry minimisation, resulting in environments experiencing different strain in the different shells. The trend altered for the 135 and the 165 atom clusters as density maxima for the different shells were observed to overlap each other neatly at E_f though the outer shells were subject to peak broadening. Unlike the density of states for the smaller clusters, here the central atom had a much greater density magnitude than the outer shells. In each of these cases the central atom was followed by the second and then the first shell in order of magnitude. The 201 atom cluster seemed to revert to the same

trend as the smaller clusters with the central atom peak exhibiting the least magnitude at E_f with the third, first and second shells being present in that order.

Figure 82 Integrated DOS at ±0.2eV from E_f on the central Pt atom to the outer shell along the a) [100] direction and b) [111] direction

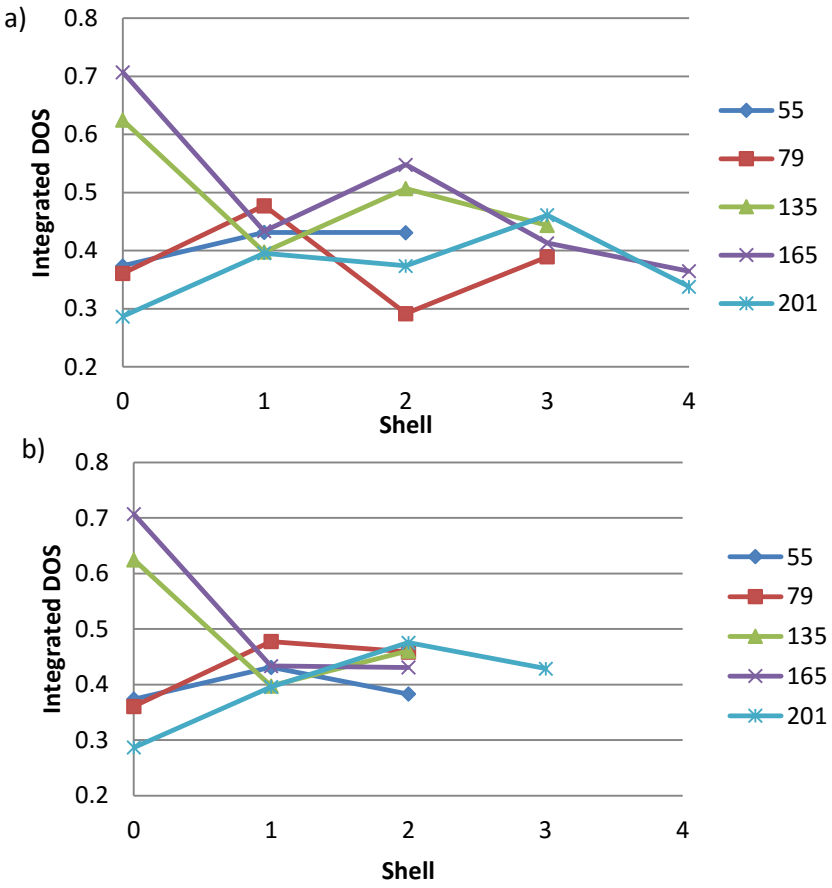

The integrated DOS at E_f for each of the cluster shells including their under coordinated outer layers are presented in figure 81. As can be seen, in the [100] direction the density was observed to oscillate through the cluster with decreasing amplitude; Friedel oscillations.[218] A possible explanation of this behaviour would be the presence of surface states, which may be indicated by the presence of bands just above E_f (0-2eV), which are not present in the Pt_{bulk} d-band shown in figure 78 . Whilst in a slab these states would be observed to decay exponentially into the bulk, it is possible that in a nanoparticle there is not enough depth for the oscillation to be damped and instead constructive interference with the oscillations coming from the other surface facets may result in the enhancement observed at the centre of the cluster.

Inspection of the 2D density slices through the larger clusters shown in figure 82 does support the idea of charge oscillation through the different shells of the cluster. The plots also suggest that

the addition of extra atoms at the surface (forming incomplete shells) has a significant effect on the charge distribution.

Figure 83 2D visualisations of electron density ±0.1 eV from E_f for a) 13, b) 55, c) 135, d) 165 and e) 201 atoms, axis units are grid points from the original GPAW calculation

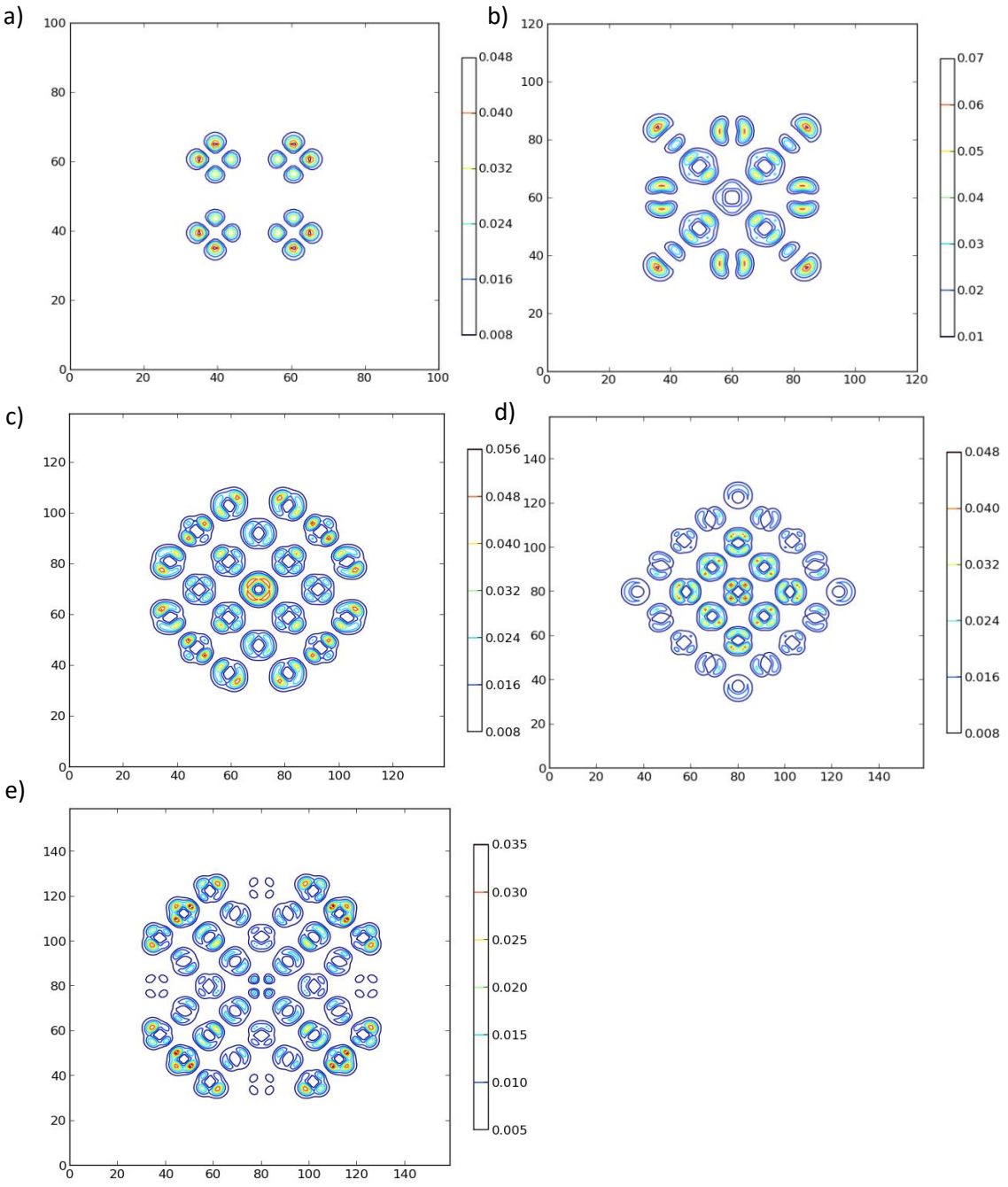

Consideration of the effective potential through the largest clusters revealed a very slight decrease in the potential well depth for the central atom of the 135 and 165 atom clusters,

indicating a slightly lessened stability. A greater change was noted in the form of the smaller interatomic peaks, which may indicate directional bonding interactions along the cluster diagonal.

Figure 84 Effective potentials through the a) 135, b)165 and c)201 atom clusters.The potential is for a 1 atom wide 'core' cut through the unit cell so that the atomic contributions of the different shells were equally displayed

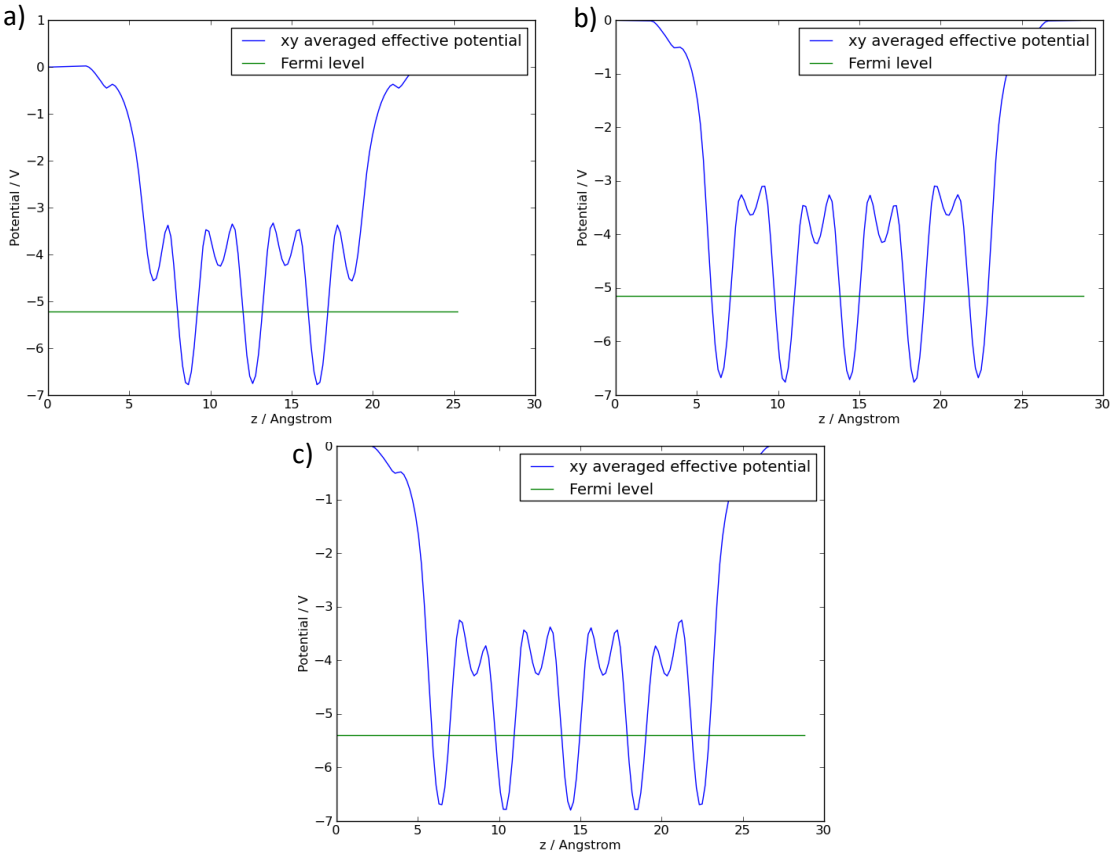

7.4 Rh and Pd Clusters

In order to assess whether the density oscillations witnessed in the Pt clusters were a feature of material or symmetry, medium sized Rh and Pd clusters were also calculated using the prescribed methodology for comparison.

Although a smaller dataset, the Rh and Pd values allowed for useful comparisons to be made. Initially, we observed that the energy per atom of the clusters continued to increase with increasing cluster size. The E_d values for the clusters' central atoms also initially had more negative values and then converged towards the bulk value as the number of atoms increased. In the case of the Rh 55 atom cluster though, the E_d value jumped towards E_f rather than away from it as in the case of Pt.

Table 28 Energy per atom for the LCAO mode Pt, Rh and Pd clusters

Cluster	Energy (eV/atom)		
	Pt	Rh	Pd
13	-3.33	-3.80	-1.33
19	-3.71	-4.40	
43	-3.76	-4.71	
55	-3.95	-4.89	-1.93
79	-4.14	-5.10	
135	-4.29	-5.24	-2.13
165	-4.36	-5.31	
201	-4.45		

Table 29 E_d for the central atoms of the Pt, Rh and Pd clusters

Cluster Size	E_d (eV)		
	Pt	Rh	Pd
13	-3.27	-3.50	-2.20
55	-4.11	-2.69	-2.56
79	-3.36	-3.20	
135	-2.74	-3.00	-2.27
165	-2.60	-2.90	

Unfortunately too few Pd clusters were fully optimised within the timeframe of the project to allow for oscillation trends to be well defined and so further analysis was only carried out on the Rh clusters. The integrated DOS ±0.2eV around E_f for the Rh clusters displayed no sign of the oscillation present for the Pt data. Upon inspection of the Rh DOS, the maximum of DOS was found to be just above E_f and so the integration was repeated for the region +0.2 to +0.6 eV. This data, seen in figure 84 b), did exhibit oscillation in the density through the cluster shells, resulting in density enhancement or depletion at the central atom. This evidence therefore suggested that the phenomenon occurred independent of material. This would in turn suggest that it would be possible through cluster shape and size to engineer the electronic structure of bulk atoms to be more reminiscent of under-coordinated atoms which might enable applications in catalysis or electronics.

Figure 85 Rh Cluster integrated DOS in the [100] direction a) ±0.2eV around E_f b) 0.2 to 0.6eV

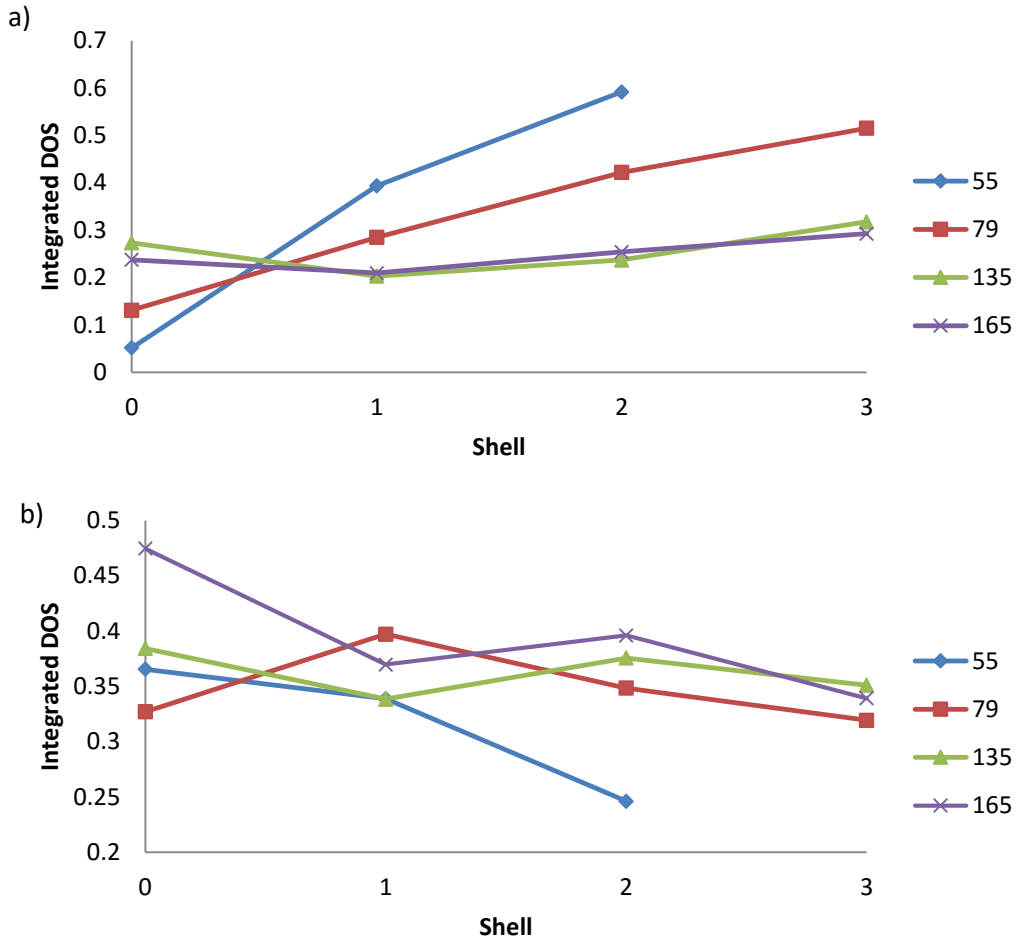

7.5 Numerical Models for Energy Prediction

Having calculated a range of small to medium Pt clusters using DFT, numerical models were developed and tested for their ability to reproduce the data
set and predict future Pt cluster energies. A potential relating coordination number, CN, to energy was also developed in contribution towards simulating the growth of nanoparticulate structures from overlayers on carbide surfaces.

7.5.1 The Cluster size to Energy Relationship

Initially it appeared there was a linear relationship between the energy of a cluster and the number of atoms it contained see figure 85 a). However, given equation 35, at the bulk limit the gradient of the plot should equal the bulk energy of Pt.

(38) $$E_{cluster} = m \cdot N + c \text{ where N>>c} \qquad \frac{E_{cluster}}{N} = m = E_{bulk}$$

The bulk limit was assumed to be at 10000 atoms. This was deemed reasonable given the linear constant, c, is of the order of 10-100, resulting in an uncertainty in the fitted bulk value of 0.0001-0.001eV per atom which is better than DFT accuracy. Augmenting the dataset with this value resulted in figure 85 plot b) which clearly shows that a linear fit no longer provided a good correlation.

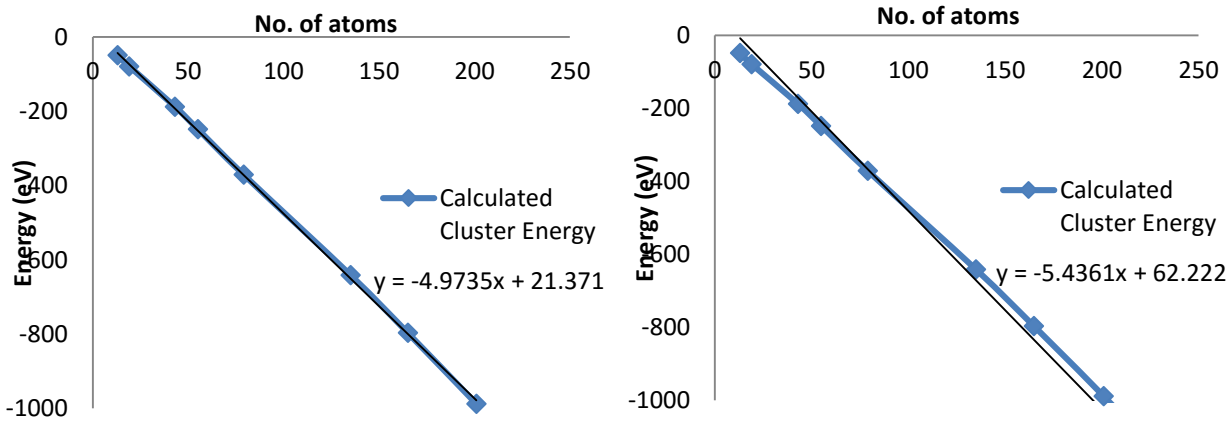

Figure 86 Plots of Energy verses cluster size for a) 13-201 atom clusters b) dataset including the bulk limit at 10000 atoms

The dataset, with added values for N=10000 and N=100000, was then used as a model dataset to test different fitting functionals. A variety of functional forms were trialled and the following functional form chosen:

(39) $$f(x) = E_{particle} = -5.43N + \sum_i \frac{a_i}{N^i}$$

In this form, for very large particles the energy would be given by the bulk value multiplied by the number of atoms, N. Since N is in the denominator for the polynomial part, its contribution to the energy would be negligible for large particles but become more significant as particle size decreased.

The fitting was trialled for values of i ranging from 1 to 6, the fit got progressively better until i=5 after which no discernible improvement was observed. The values of coefficients obtained were 3602.9, -4.36402e+6, 1.92689e+8, -3.3779e+9 and 1.99146e+10. As can be seen from the results in table 30, the agreement between the fitting and calculated values was generally good with the maximum difference being 3.6%. It must be noted that this fitting was not suitable for predicting

the energy of small particles (N<13) however, given their size there is no barrier to calculating these using DFT as previously shown.

Table 30 Calculated and modelled total energy values and % difference for medium to large clusters

Cluster Size	DFT Energy (eV)	Numerical model (eV)	ΔE (%)
13	-48.8	-49.0	0.5
19	-79.0	-79.1	0.1
43	-187.6	-184.5	-1.7
55	-248.4	-257.4	3.6
79	-370.9	-361.4	-2.5
135	-641.0	-636.9	-0.6
147	-	-701.3	-
165	-796.6	-799.3	0.3
201	-988.0	-998.4	1.0
235	-	-1187.9	-
2869	-	-15566.6	-
10179	-	-55268.5	-

7.5.2 The Coordination Number to Energy Relationship

Numerical modelling of the relationship between cluster-atom CN and energy was carried out through fitting a series of linear equations with the form:

$$\sum_{i=1\ or\ 4}^{12} n_i e_i \tag{37}$$

Where the sum is over the atomic coordination numbers present in a given cluster, e_i is the energy of the given CN (to be fitted) and n_i is the frequency of occurrence of that coordination in a particular nanoparticle. It must be noted that CN≠10 in the calculated dataset. The fitting was achieved using the linear least squares fit algorithm implemented in scipy.

Table 31 shows the different e_i energies resulting from the fitting. Model 1 used the CN values from the medium clusters only with the inclusion of the *i*=10 whilst i=10 was removed from linear equations for the model 2. Models 3 and 4 also did not contain i=10 but used dataset containing the lowest energy N=2-201 data and all 2-201 cluster results respectively. It was expected that the lower the coordination number of the atom the less stable it would prove, and this is generally observed to be the case although the CN 11 and CN 2 values are observed not to follow this trend.

Table 31 CN to energy coefficients from different calculated cluster datasets

CN	model 1	model 2	model 3	model 4
12	-4.32	-5.30	-5.35	-5.37
11	-6.03	-5.51	-5.49	-5.48
10	0.00	0.00	0.00	0.00
9	-3.93	-5.10	-5.04	-5.02
8	-3.68	-4.88	-4.77	-4.73
7	-5.24	-4.45	-4.43	-4.42
6	-5.48	-3.94	-3.96	-3.98
5	-3.70	-3.62	-3.64	-3.66
4	-1.98	-3.39	-3.35	-3.38
3			-2.93	-2.95
2			-3.16	-3.14
1			-2.12	-2.12

In the following table 32 we can see the model cluster energies in comparison to the calculated DFT energies. Immediate improvement in accuracy from model 1 to 2 was observed for the larger clusters as the CN 12 value was significantly increased. The error in energy per atom was reduced from 0.4eV to nil via the exclusion of the CN 10 variable. With the addition of the lower CN variables, the smaller clusters could also be calculated although over-binding was noted throughout the dataset. For the larger clusters in the dataset, the re-balancing of the CN9, 11 and 12 values in the model provided accurate energies, with the average energy error per atom being less than the anticipated DFT error. The average energy error per atom for models 2, 3 and 4 were 0.01, 0.02 and 0.02eV respectively; comparing just the answers for the 12-201 data, the 0.01eV value was universal. The CN=12 value was noted to be significantly less than the Pt_{bulk} value, so for large clusters where the cluster interior energy contributions render the energy contributions of the surface atom negligible, an underestimation of the total energy was expected in the order of 0.06eV per atom.

Table 32 Numerical model and DFT Pt cluster energies

Cluster Size	Calculated Energy (eV)	Model 1 (eV)	Model 2 (eV)	Model 3 (eV)	Model 4 (eV)
2	-4.23	-	-	-4.23	-4.23
3	-8.32	-	-	-9.49	-9.43
4	-11.91	-	-	-12.19	-12.20
5	-16.17	-	-	-15.72	-15.81
6	-20.75	-	-	-19.54	-19.57
7	-23.84	-	-	-24.53	-24.65
8	-29.00	-	-	-28.39	-28.52
9	-33.56	-	-	-33.28	-33.39
10	-37.78	-	-	-38.13	-38.18
11	-41.95	-	-	-42.32	-42.41
12	-46.61	-44.11	-48.07	-47.76	-47.81
13	-48.77	-48.77	-48.77	-49.08	-49.24
19	-79.01	-79.01	-79.01	-78.61	-78.70
43	-187.61	-187.61	-187.61	-187.33	-187.26
55	-248.37	-248.37	-248.37	-248.23	-248.15
79	-370.87	-370.87	-370.87	-370.83	-370.88
135	-640.99	-640.99	-640.99	-641.00	-641.04
165	-796.56	-796.56	-796.56	-796.65	-796.66
201	-988.04	-903.74	-988.04	-988.02	-987.99
225		-1002.0	-1112.9	-1112.4	-1112.2

There are a number of ways in which the existing model could be improved for the accurate prediction of larger cluster energies. Firstly, an energy parameter for CN=10 must be included in future models to enable its use on all cluster data. The balance of the CN parameters would undoubtedly be further improved with a wider DFT dataset including a wider variety of calculated structures. To remedy the under-binding expected for larger clusters, it would be possible to use the small degree of geometric alteration observed at the centre of large particles and treat a certain number of CN=12 atoms with the Pt_{bulk} parameter value of -5.43eV. In each of these cases, larger Pt clusters must be optimised and their total energies calculated to enable an assessment of the predictive powers of the model at hand.

7.6 Overlayer Stability

7.6.1 Overlayer to Cluster Energy Comparisons

Following the modelling of Pt clusters reported above, a comparison of the GPAW clusters with CASTEP overlayers was undertaken in an effort to identify systems which would preferentially

support overlayers rather than Pt agglomerates. To make this possible the Pt-Pt interaction from the GPAW clusters, $E_{Pt\_cluster}$, and Pt-carbide interaction E_{ads} (chapter 4 equation 24) were both calculated with respect to their bulk values.

$$E_{Pt\_cluster} = \frac{E_{cluster} - (N \cdot E_{Pt\ bulk})}{N} \quad (38)$$

As can been seen from figure 86 however, since the smaller clusters are not stable with regard to the bulk and favourable interactions are necessarily negative in energy, no indication to the relative behaviours of the Pt could be extracted from these values. It was noted that, being 0K calculations, no entropic contributions towards the energies had been included. The interaction of the Pt clusters with the carbide was also not included in the comparison.

Figure 87 1ML Pt overlayer adsorption energies plotted against $E_{Pt\ cluster}$ values

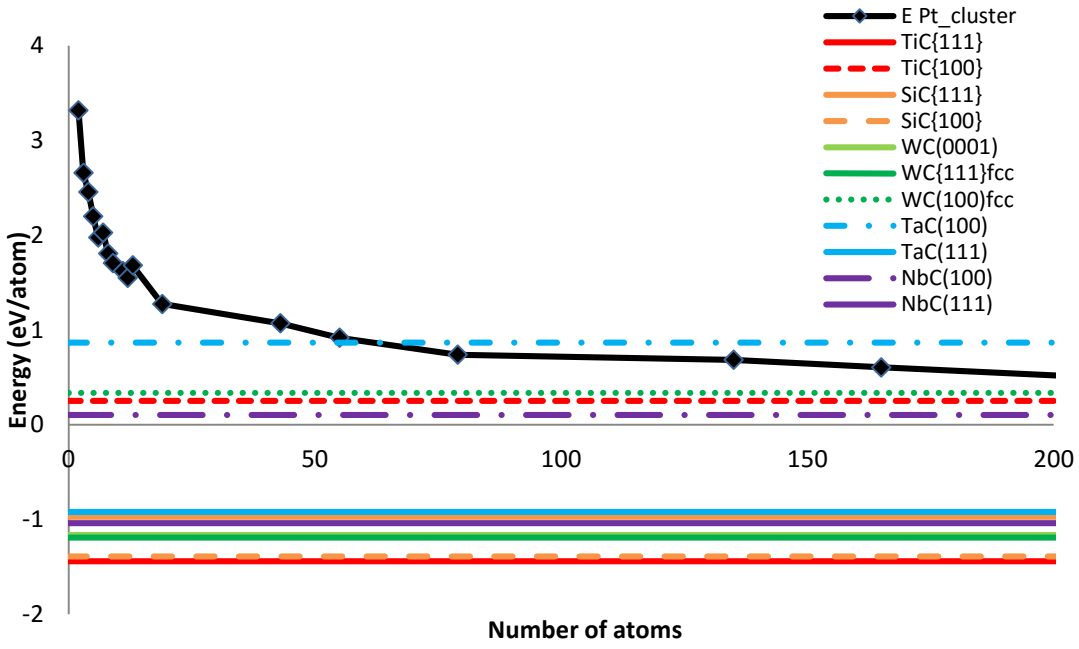

To allow comparison of interacting overlayers and clusters, a hemispherical Pt cluster/carbide model was developed. The interfacial energy $E_{Interface}$ was calculated from the optimised Pt overlayer/carbide structure and portions of the calculated clusters were included having been calculated using the following expressions:

$$E_{Interface} = \frac{E_{Pt\ 3ML/TMC} - (E_{TMC} + E_{Pt\ 3ML})}{N_{Interface}} \quad (39)$$

$$E_{Hemisphere} = \frac{E_{cluster}}{N} \times N_{Hemisphere} \quad (40)$$

$$E_{Interaction} = \frac{E_{Hemisphere} + N_{Interface} \cdot E_{Interface} - N_{Hemisphere} \cdot E_{Pt\ bulk}}{N_{Hemisphere}} \quad (41)$$

Where $E_{Interface}$ differed from the previous calculation of E_{ads} as the E_{TMC} value used was calculated from the fully optimised Pt adsorbed system having deleted the Pt atoms (as opposed to the clean, relaxed carbide system). $N_{Interface}$ is the number of Pt atoms in contact with the carbide (the cut side of the hemisphere) and $N_{Hemisphere}$ is the total number of atoms in the hemisphere.

Table 33 Hemispherical cluster data including the number of atoms in the hemisphere and interface and the % on interface atoms relative to the hemisphere

Original Cluster	$N_{Hemisphere}$	$N_{Interface}$	$N_{Interface}$ (%)	$E_{Hemisphere}$ (eV)
55	34	13	38	-153.54
79	50	21	42	-234.73
135	78	21	27	-370.35
165	95	25	26	-458.62
201	119	37	31	-584.96

This interaction model does make significant assumptions. Using the 3ML Pt $E_{Interface}$ for the whole interaction area will introduce errors since atoms at the outer edge of the particles are likely to be more similar to a 1ML interface. Whilst the majority of $E_{interface}$ values decreased with thickening Pt overlayers, in noticeable cases such as WC(0001), the 3ML $E_{Interface}$ was in fact stronger than the 1ML value, allowing for more variation in the observed adsorption behaviour dependent on the carbide. The relaxations of the carbide surface and the hemispherical cluster have also not been taken into account and there is the possibility that the interface size may vary since Pt ball-up may occur.

However, even given these short comings, the calculated data displayed in figure 87 was still instructive. Of the 5 hemispheres included the 50 atom and 119 atom hemispheres clearly show the most favourable interactions with all the carbide surfaces except WC(100)fcc. The favourable binding of these clusters as opposed to the others was predominantly determined by the ratio of interface and hemisphere atoms. As can be observed in table 33, the 34, 50 and 119 atom hemispheres contained larger proportions of interface atoms, maximising the contribution of $E_{Interface}$ in $E_{Interaction}$ and hence stabilizing the interaction.

The 78 and 95 atom clusters, which had a much lower proportion of interface atoms, were predicted to be unfavourable towards adsorption on the majority of (100) carbide surfaces. The WC(100)fcc facet was not predicted to adsorb any of the Pt clusters, which was also in agreement with the previously calculated carbide facet behaviour discussed in chapter 4. Key to our understanding of the likely Pt structure formation would be the development of larger hemispheres to test the interaction behaviour at the large particle limit.

Figure 88 $E_{Interaction}$ values on various carbide surfaces for hemispherical clusters of size 34-119

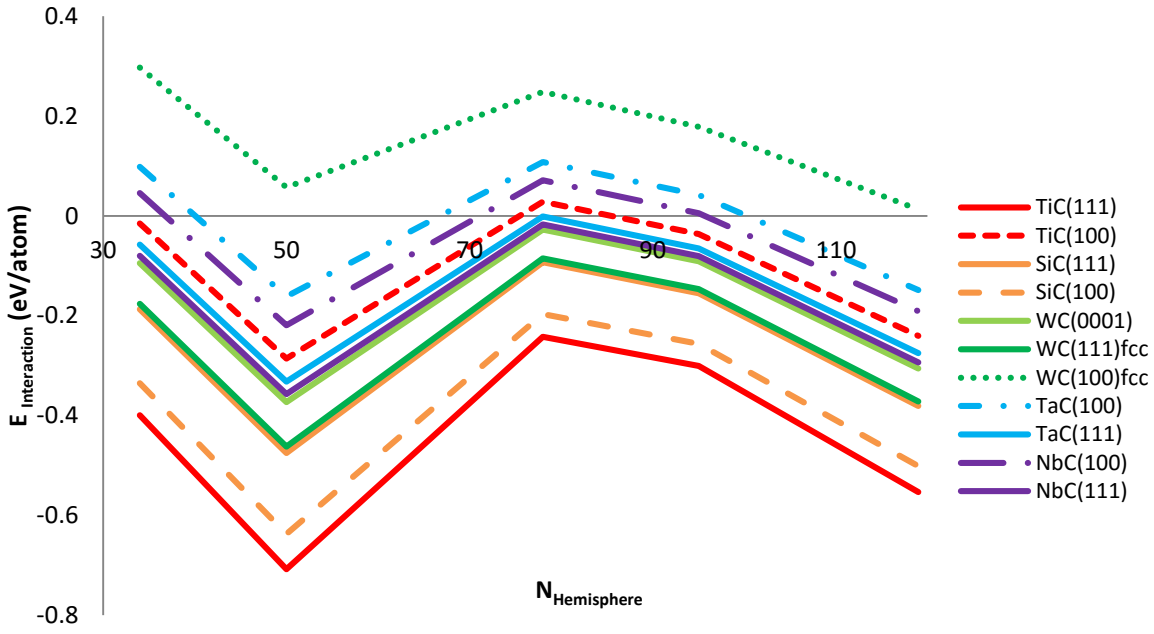

7.6.2 EMT Stability Simulation

In lieu of further GPAW calculations for the inclusion of relaxation effects and the expansion of the numerical models, an EMT potential was used to calculate the energy and geometry of optimized Pt thin layer structures. The aim of this study was to observe the structures resultant from layer geometry minimisation, to consider the effect of layer thickness and in particular attempt to extract an estimate for entropic (finite T) effects so as to correct our initial overlayer and cluster comparisons via use of free energies. The reference state for the model was a pristine layer of the simulation thickness as seen in figure 88. The initial simulation runs were conducted with 100 Pt (enough to make 1ML) randomly distributed over 2 or 3 layers for the initial Pt positioning.

As can be seen in figure 88, the number of layers on which the initial random Pt allocation as made did affect the final outcome of the optimisation. Large areas of the cell base were left uncovered in both datasets and Pt agglomeration into chains and in some areas clusters was widely observed. For the 3 layer setup structures, an increased frequency of the 3D cluster structures was noted.

Figure 89 Agglomeration model for 1ML Pt, top row depicts one of the optimized structures from the 2 layer initial setup, second row depicts the 3 row initial setup and third row is the 1ML reference state

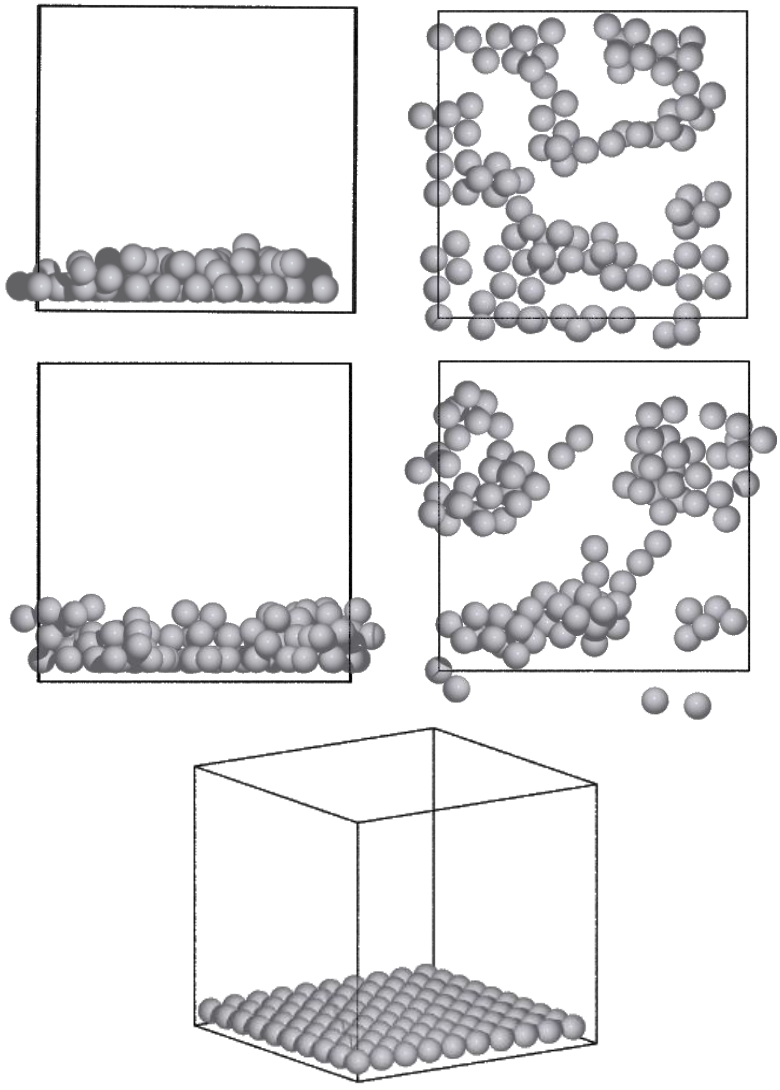

The calculated entropy and Helmholtz free energy values are displayed in table 34. The entropy and free energy of the system were converging by 2500 structures; however an increase in the dataset size would be necessary in order to confirm these values. The 2 layer system was observed to have higher entropy than the 3 layer system, suggesting that the 3 ML system contained a higher degree of bulk-like structure.

Table 34 Entropy (S) and Helmholtz Energy (A) per atom of the 1ML, 2 and 3 layer initial structure datasets at 300K

Sample size	2 Layers		3 Layers	
	S (eV/K)	A (eV)	S (eV/K)	A (eV)
5	0.00014	-0.2533	0.00011	-0.1697
10	0.00022	-0.2643	0.00020	-0.1998
20	0.00031	-0.2748	0.00030	-0.2488
50	0.00053	-0.2948	0.00051	-0.2719
100	0.00076	-0.3140	0.00074	-0.3040
200	0.00102	-0.3319	0.00091	-0.3149
500	0.00144	-0.3559	0.00126	-0.3428
1000	0.00184	-0.3759	0.00156	-0.3591
1400	0.00203	-0.3843	0.00171	-0.3661
1800	0.00218	-0.3910	0.00184	-0.3725
2200	0.00231	-0.3963	0.00194	-0.3770
2500†	0.00239	-0.3997	0.00201	-0.3802

The introduction of enough Pt to form complete multilayers was observed to make a significant difference to the structure of the optimised layers. Immediately noticeable in figure 89 were the smaller void sizes within the Pt layer. The Pt itself was observed to form extended areas of (100) surface and, moving from 2ML to 3ML, regular build-up of Pt resulted in the production of 3ML sections. At the void edges in the 2ML system, the Pt was observed to bunch irregularly to reduce the under-coordination of the atoms. In the case of the 3ML system, two types of defects were observed; a simple void in the layer and secondly an area where atoms missing in the bottom layer of the structure had resulted in disorder in the Pt layers above. In this case the Pt-Pt interaction had enabled the formation of a disordered Pt layer which lessened accessibility to the cell floor.

Figure 90 Optimised structures with top row 2ML Pt and second row 3ML Pt

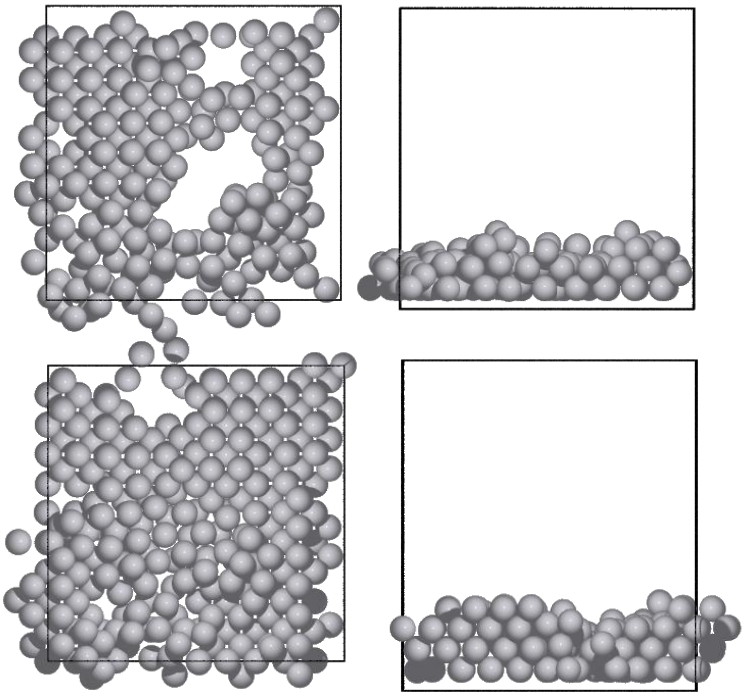

The emergence of such structures at the 3ML thickness suggests that whilst the very thin Pt layers preferred for activity enhancement would be unlikely to form contiguous layers, slightly greater Pt loading could result in contiguous layers which would be able to protect the carbide support.

Following the successful implementation of the EMT potential to thin layer structures, the potential applied to the cell floor of the model may now be altered to incorporate the carbide interaction potentials calculated in chapter 4. This would then provide an alternative method to test the minimum interaction energy necessary to produce contiguous Pt layers. Given the existence of Pd, Ag, Au, Al, Ni and Cu potentials, tie-layer and alloy overlayer systems could also be modelled using this method.

7.7 Conclusions

Geometry optimisation calculations for Pt clusters ranging from 2-201 atoms were conducted in GPAW to provide complementary information for comparison with the CASTEP Pt overlayer structures.

The bonding within the Pt clusters was observed to evolve towards Pt_{bulk} with increased cluster size. For the small Pt clusters, planar and then layered structures were observed to have similar

stability to their 3D counterparts. Unexpected electron density oscillations were discovered in the electronic structures of the cuboctahedral medium sized clusters. The presence of surface states at the cluster edge was suggested and the enhancement in the cluster centre for certain sizes attributed to the constructive combination of the surface state oscillations from multiple facets. Having conducted short studies on Rh and Pd clusters, it was observed that this phenomenon was visible in other materials, although in the case of Rh the DOS maxima was shifted by 0.2eV from the Pt value. The calculation of these clusters also led to the creation of numerical models to allow the prediction of Pt cluster energies from clusters sizes and CNs.

In order to assess Pt overlayer stability, the $E_{interface}$ calculated from Pt overlayer adsorption was incorporated into $E_{Interaction}$ for a series of hemispheres. Interaction was predicted to be most stable for systems with a high proportion of interface atoms. This in turn suggested that the neglected relaxation and possible de-wetting of Pt from the carbide surface would have a significant impact on the stability of the systems. With a view to investigating the likely stability of Pt overlayers with the inclusion of defects and the possibility of agglomeration, EMT potentials were used to geometry optimise Pt thin layers from random initial structures. The results indicated that whilst 1ML Pt was unlikely to form contiguous layers even under the application of a favourable interfacial potential, the addition of more Pt allowed for the formation of Pt overlayers with near complete coverage of the simulation floor. This was a key finding since thicker Pt deposition is attainable experimentally and the integrity of the Pt layer is thought to be crucial for the protection of the carbide from corrosion under operational fuel cell conditions.

There is much scope for further development of the models described within this chapter. The geometry optimisation of larger Pt clusters using GPAW would allow for the accuracy of the numerical energy prediction models to be tested. The distinguishing of different CN 12 environments within the model should enable improved representation of larger Pt particles. The optimisation of adsorbed Pt hemispheres on carbide surfaces would reveal the extent of system relaxation and would lead to an improved understanding of the terms necessary for inclusion in the $E_{Interaction}$ expression. Given this initial proof of concept for the EMT model, there are also a great number of possibilities for further work within this framework. Utilising alternative interfacial potentials at the simulation floor would enable the simulation of Pt structures as if interacting with different carbide surfaces. The introduction of multi-metal systems within using EMT might also provide the information on tie-layer evolution for the 'alloyed' systems discovered in the previous chapter without the large computational cost associated with MD.

8. Conclusions

8.1 Summary

The primary goal of the work presented within this thesis was to use state-of-the-art computational methods to analyse and screen materials for their ability to meet the DOE's central targets for fuel-cell electrode catalysts. Namely, the threefold targets of reduction of Pt loading, improved Pt activity towards ORR and improved stability to allow 5000 hr catalyst lifetimes. To achieve this goal a subset of promising carbide materials were studied to assess whether they would be suitable for use in core-shell nanoparticles. The core-shell structure was chosen as a way to decrease Pt loading whilst maximising Pt availability. The intention of the screening component of project was, firstly, to identify carbide cores that were predicted to adsorb Pt overlayers and secondly, would alter the electronic structure of the Pt surface so as to improve its activity towards the ORR. In the following sections our finding from the various chapters are summarised, highlighting the progress made towards improved ORR catalysts. We will also discuss the extent to which we have been able to predict the stability of these systems and the avenues for future work which have arisen during the project.

8.1.1 Carbide Materials

As the foundations for the investigation, the accurate modelling of our chosen carbide materials was essential. Good agreement was found between our calculated lattice parameters and experimental and theoretical literature values. The electronic structures of the carbides were analysed, revealing electron transfer from the C to the metal in each case and greater degrees of covalence for the SiC and WC hexagonal carbides. Upon the cutting and optimisation of the (100) and (111)-like surfaces, significant relaxation was observed which was in excellent agreement with previous literature findings. Surface specific resonances at or below E_f were identified in the fcc-(111) and (0001) surfaces whilst mixed character peaks were noted for the fcc-(100) surfaces above E_f. The positioning of these resonances was observed to be dependent on d-band filling. It was noted that E_{TMSR} had been used by Vojvodic *et al.*[118] as a descriptor for atomic and molecular adsorption on to TMC fcc-(111) surfaces and this became part of the analysis framework in the results of the following chapters.

8.1.2 Platinum Monolayer Adsorption and Characteristics

The next chapter provided theoretical proof of concept for the formation of carbide core-shell nanoparticles. Pt was predicted to preferentially adsorb on to fcc-(111) surfaces and a layer-by-layer growth mechanism was predicted due to the difference in $E_{(Pt\text{-}TMC)}$ and $E_{(Pt\text{-}Pt)}$ values. Adsorption on all of the studied surfaces was predicted for the hexagonal WC and SiC which suggested that these materials should undergo full encapsulation by Pt. This was of particular interest since the presence of a contiguous overlayer is thought to be necessary to protect the core under the corrosive fuel cell operating conditions. However, the fcc-(100) surfaces were predicted to be universally unfavourable towards Pt adsorption, suggesting fcc carbide nanoparticles could be only partially coated with Pt.

The adsorption of Pt was found to result in charge transfer from the carbide surface to the Pt in contact with carbide. This in turn resulted in the narrowing and negative shift of the Pt d-band away from E_f. The modification of the Pt electronic structure was observed to lessen and revert towards that of Pt bulk as the number of MLs reached 3 and greater. This suggested that any enhancement of activity caused by the underlying carbide would be lost in systems with an overlayer thickness greater than 3 ML.

The identification of a simple descriptor to define Pt adsorption on carbide surfaces proved elusive. The TM surface d-band centre model was unable to account for the change in band-shape that the inclusion of C made to the core. The adsorption of Pt did lead to the depletion of the TMSRs on the fcc-(111) surfaces, proving that they were instrumental in the Pt binding. However, the correlation between E_{TMSR} and $E_{ads\ Pt}$ was not strong enough to allow for the prediction of Pt wetting. It was concluded that the calculation of 1ML Pt on the desired carbide surface followed by the assessment of E_{ads} 1ML Pt and its associated electronic structure was necessary for the elucidation of the carbide adsorption behaviour. This method is still relatively computationally inexpensive as DFT with RPBE provides accurate adsorption energies and the electronic structure codes used are well parallelised to work in high throughput computing facilities.

8.1.3 Metallic Tie-Layers to aid Pt Adsorption

Given the necessity of Pt adsorption for a stable and active ORR catalyst, the introduction of alternative metal MLs was trialled to provide anchoring for Pt at carbide surfaces. For the unfavourable fcc-(100) surfaces, Co and Al were identified as promising tie-layers and predicted to favour the formation of Pt outer layers. These results open the path to extend Pt adsorption onto initially unfavourable materials via the formation of favourable M-Pt interactions. On the fcc-

(111) surfaces, Ir and Rh were predicted to form stable Pt outer skins whilst Co and Ni both migrated spontaneously upon relaxation to form alloy-like surfaces. It is possible that with the addition of further Pt, Pt rich skins could be formed in these systems and, was seen in the introduction, these may well be more active than pure Pt.

Whilst the predicted encapsulation by Pt of all of the carbide nanoparticle facets is a significant step forward in the production of core-shell nanoparticles, as yet, the activity of these systems towards ORR had not been identified. The following chapter sought to shed light on the relative activities of the Pt/carbide and Pt/tie/carbide systems with regards to Pt.

8.1.4 Adsorption of ORR Intermediates

Following the work of Nørskov *et al.*[111] the adsorption energy of O was used as a descriptor for the ORR activity of the surfaces, with weaker predicted O adsorption indicating increased ORR activity and vice a versa. The addition of 1ML Pt to the carbides was found to dramatically lower $E_{ads\ O}$ relative to adsorption on the clean carbide surfaces. Pt/WC surfaces were calculated to produce $E_{ads\ O}$ that were 'Pt-like' or weaker than Pt suggesting that they should maintain or improve activity towards ORR. Whilst C-terminated TiC and SiC also produced weakened $E_{ads\ O}$ values, their comparative instability made them unsuitable surfaces to pursue for fuel cell applications.

Spontaneous migration of the O through the Pt overlayer was noted for the TaC(111) and NbC(111) surfaces due to the oxophilicity of the metals in question and the strained Pt lattice allowing access to the carbide surface. The addition of further Pt layers prevented the O approaching the carbide and significantly weakened the $E_{ads\ O}$, leading it to converge at strained-Pt values. This confirmed that, discounting the strain effect imposed by our model, the $E_{ads\ O}$ values of the Pt/carbide systems should return to pure Pt values at thicknesses greater than 3ML.
Addition of tie-layers resulted in WC hcp, TiC and TaC surfaces with $E_{ads\ O}$ values weaker than those of pure Pt. Oxophilic tie-layers such as Ti and Ta were observed to cause spontaneous O migration through the Pt layer on the (111)-type surfaces. O adsorption was also predicted to reverse the Pt outer layer formation preferences for many of the most promising Pt/X/carbide structures. Increased Pt overlayer thickness was predicted to prevent O diffusion to the tie-layer but also resulted in strengthened $E_{ads\ O}$ negating any improvement of ORR activity shown in the unstable Pt_{1ML}/tie-layer/carbide systems.

Although the results of the study have indicated potential limitations of the stability of the systems in O rich environments, the screening process has identified altered O adsorption characteristics due to the influence of the carbides and tie-layers. These findings suggest that future practical work should include the development of strategies to mitigate this instability. Meanwhile, databases of such systems and the adsorption energies of other reagents would be simple to form and could enable the identification of Pt/core systems for different reaction specifications. Whilst the addition of multiple Pt layers was observed to negate any synergic effect of the Pt/carbide interaction, given the significantly thrifted amount of Pt used in the catalyst the mass activity of the Pt may still be higher than that of Pt/C_{black}. As such the structural motif is still worth investing in, even if electronic structure modification plays only a minor role in increasing the Pt activity.

8.1.5 Pt Clusters and Stability towards Aggregation

The final collection of work considered the stability of the Pt overlayers to Pt agglomeration. GPAW was successfully used to model Pt clusters of varying sizes under non-periodic boundary conditions and an EMT model was employed to simulate surface structures with varying Pt depths. Simple models for the interaction of Pt hemispheres with the carbides surfaces indicated that clusters which offered proportionally large interfaces were more likely to favourably adsorb on to the carbide surfaces. The EMT simulations also suggested that whilst 1ML Pt adsorption was not likely to result in contiguous overlayers, N=3 MLs should be viable.

Unexpected Friedel oscillations of electron density through the cluster were also observed resulting in some clusters exhibiting density enhancements on the central atom. It was suggested that this behaviour may be due to the constructive interference of surface states and seems to occur in Rh as well as Pt clusters.

8.2 Further work

The studies conducted in the course of this research project have suggested many avenues for further work. Whilst our in initial carbide subset was chosen to provide a range of metals and geometries it has become apparent that more non-fcc carbides are necessary for a detailed assessment of the effect of geometry on Pt adsorption. The introduction of carbides such as Mo_xC, Mo being isoelectronic with W, or ZrC[219] would also be well within the remit of the topic. The doping of nitrides has also been observed to enhance chemical stability and electrocatalytic

activity towards ORR,[220,221] a similar approach to the carbides would be of great interest in promoting core stability and Pt activity.

Aside from developing the carbide materials themselves, further investigation of possible tie-layer and alloy overlayers would also prove instructive. Given the known activity and tunability of Pt containing alloys towards the ORR,[106,69] Co and Ni containing Pt alloy overlayers should be modelled and tested. Within this different stoichiometries and thicknesses would have to be investigated. The predicted migration of O towards oxophilic tie-metals also raises the question: what effect would oxidation have on the carbide or tie-layer and would this hamper or aid Pt adsorption and activity? The formation of oxide tie-layers or the oxidation of the top bilayer of carbide and subsequent Pt adsorption would provide insight again in the area of system stability and predicted activity losses.

Finally, the development of the various Pt clusters models and EMT simulation in the last results chapter have laid a foundation for further exploration of Pt cluster interactions with carbide surfaces. The geometry optimisation of larger Pt clusters using GPAW or the relaxation of hemispheres in contact with carbides would allow the accuracy of the numerical energy prediction and interaction models to be tested. The EMT model could also now be used to consider different interaction energies to mimic the different carbide surfaces or include multi-metal systems since other PGM and TM potentials are available.

8.3 Closing Remarks

In conclusion then, over the course of this research project a theoretical proof of concept for Pt/carbide core shell nanoparticles has been made. WC and SiC were predicted to allow full encapsulation by Pt, however the adsorption of Pt on to unfavoured carbide surfaces could be improved via the addition of metallic tie layers. Although Pt-like or weakened adsorption of O were found for several carbide surfaces, simulations suggest that 1ML Pt overlayers were unlikely to be contiguous on the carbide surface. Increasing the thickness of the Pt would increase the stability of the system but also resulted in the loss of the electronic effect of the underlying carbide.

In terms of our original targets, the reduction of Pt loading via the replacement of Pt bulk with carbide cores has been proven viable. Whilst the improvement of specific activity may not be

feasible given the required thickness of Pt needed to make the systems viable, the mass activity of the Pt may still be better than Pt/C_{black} given the greater availability of the Pt. Inclusion of extra metals in the overlayer however may provide another route to activity enhancement. Lastly, the stability of these systems still requires further study and collaboration with experimentalists will be essential in verify the findings of our interaction models.

Appendix A

The Kohn Sham method relies upon mapping a system of interacting electrons on to a system of non-interacting electrons with the same electron density. Using the non-interacting system allowed for the kinetic energy contributions and electrostatic contributions to be calculated accurately reducing the contribution covered by the approximate exchange correlation functional.

(A.1) $$F[\rho(\vec{r})] = T_s[\rho(\vec{r})] + J[\rho(\vec{r})] + E_{xc}[\rho(\vec{r})]$$

Where $T_s[\rho(\vec{r})]$is the kinetic energy of a non-interacting gas, $J[\rho(\vec{r})]$ are the classical electrostatic contributions and $Exc[\rho(\vec{r})]$ is the exchange correlation.

(A.2) $$E_{xc}[\rho(\vec{r})] = (T[\rho] - T_S[\rho]) + (E_{ee}[\rho] - J[\rho]) = T_{interact}[\rho] + E_{non-classical}[\rho]$$

Where $T_{interact}$ is the kinetic energy correction between the interacting and non-interacting systems and $E_{non\text{-}classical}$ the quantum mechanical electron interactions.

Appendix B

The following appendix describes the convergence approaches undertaken to establish our set up for the GPAW cluster calculation.

Initially, the grid spacing was tested on Pt bulk and 0.18 was selected, with literature attestation, to be a suitable spacing to produce converged energy values. Following this the Pt_{13} cluster was used in single point calculations to establish the size of unit cell required for no potential from the cluster to interact with the cell walls or other images of the system should periodic conditions be used. Verification of this was made via energy convergence and visualisation of the electron density information from the wavefunctions.

SI 1 Unit cell convergence tests highlighted an error with the assignment of grid spacing

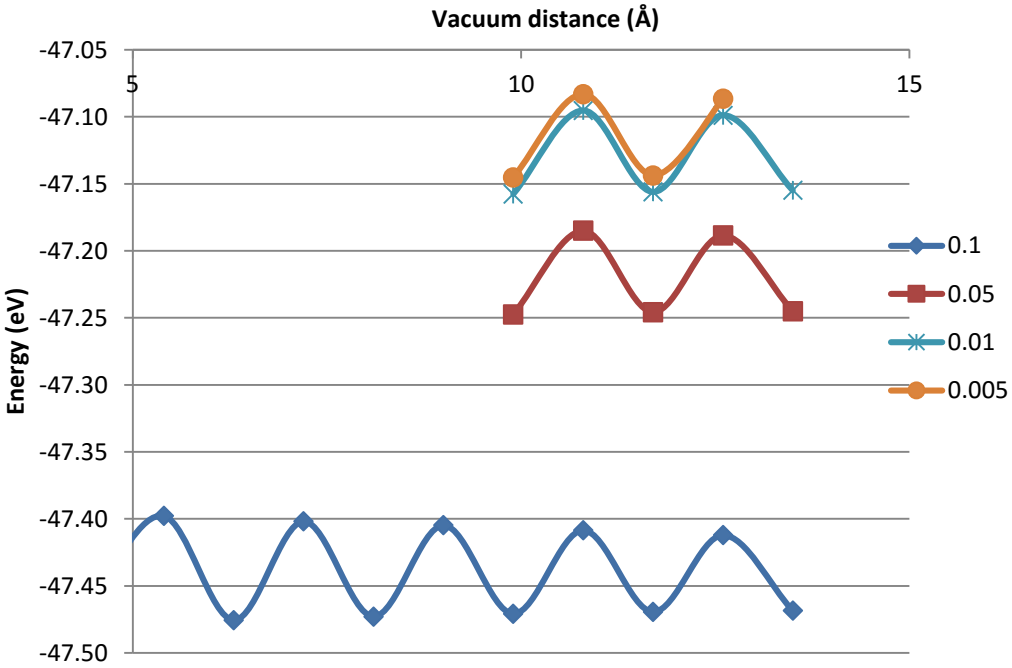

Upon setting the unit cell parameters to be the width of the cluster plus twice the vacuum distance values, oscillations in the energy results indicated a systematic problem, S1 1. In this case the unit cells were being treated with different grid spacing values due to the divisibility or otherwise of the unit cell parameters. In order to be able to use the 0.18 grid spacing, vacuum values were made divisible by 0.18. The convergence of the energy results with the trial of these vacuum values can be found in SI 2. The larger clusters were tested in this way using the LCAO mode only to save computational resources.

SI 2 Table showing FD cluster energies for N=13-55 at 0.01 and 0.1 smearing widths, green boxes indicate converged unit cell size choice.

Cluster	Cell Parameter (Å)				
	Width	14.4	18	21.6	25.2
13	0.01	-47.141	-47.145	-47.145	
	0.1	-47.455	-47.459	-47.459	
19	0.01		-75.967	-75.968	-75.968
	0.1		-76.303	-76.304	-76.303
43	0.01		-182.626	-182.635	-182.635
	0.1		-182.999	-183.009	-183.009
55	0.01		-243.774	-243.787	-243.787
	0.1		-244.228	-244.240	-244.240

In addition to this the smearing width for the clusters was also tested, two Fermi Dirac smearing widths, 0.01eV and 0.1eV were chosen to carry out the optimisation calculations however for the larger clusters the added computational expense of carrying out the 0.01eV calculations led to the 0.1eV values being used throughout the reported work.

SI 3 Computational usage for Pt_{13} optimisations with cell parameters

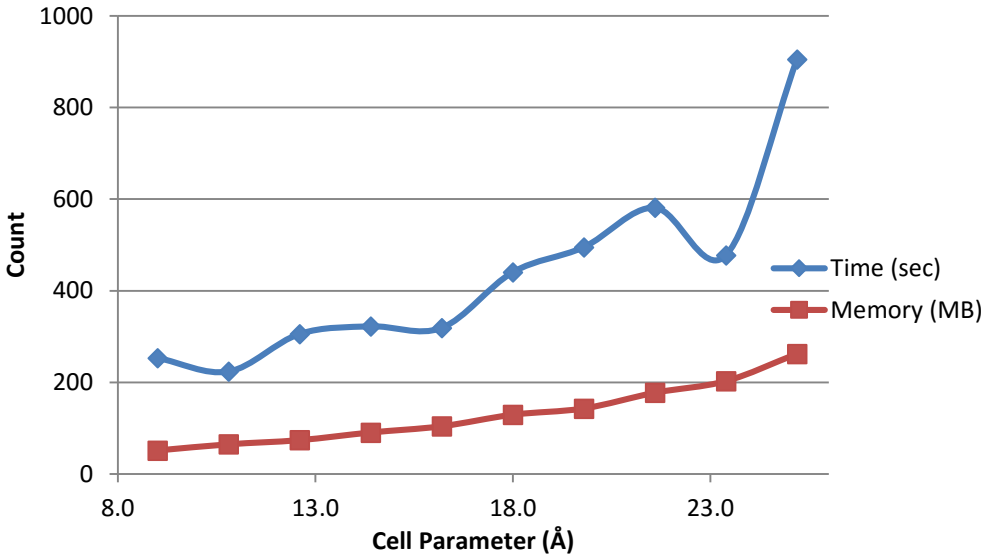

Bibliography

1. K. J. Chalvatzis and E. Hooper, *Renew. Sustain. Energy Rev.*, 2009, **13**, 2703–2709.
2. B. J. M. de Vries, D. P. van Vuuren, and M. M. Hoogwijk, *Energy Policy*, 2007, **35**, 2590–2610.
3. S. Dunn, *Int. J. Hydrogen Energy*, 2002, **27**, 235–264.
4. A. B. Stambouli and E. Traversa, 2002, **6**, 297–306.
5. J. Turner, *Science (80-.).*, 1999, **285**, 687–689.
6. *Fuel Cell Today*, 2011, 1–36.
7. European Commission, *Energy balance sheets 2011-2012*, Eurostat Statistical Books, 2014th edn., 2014.
8. M. Sturc, *Renewable energy Analysis of the latest data on energy from renewable sources*, Eurostat Statistical Books, 44/2012 edn., 2012.
9. *Energy consumption in the United Kingdom : 2011 Overall energy consumption in the UK since 1970 Overall energy consumption in primary terms*, 2011.
10. F. T. Wagner, B. Lakshmanan, and M. F. Mathias, *J. Phys. Chem. Lett.*, 2010, **1**, 2204–2219.
11. *The Department of Energy Hydrogen and Fuel Cells Program Plan*, 2011.
12. A.-C. Dupuis, *Prog. Mater. Sci.*, 2011, **56**, 289–327.
13. in *CRC Handbook of Chemistry and Physics*, Boca Raton, Florida, 84th edn., 2003, pp. 8–30.
14. M. K. Debe, *Nature*, 2012, **486**, 43–51.
15. J. K. Nørskov, J. Rossmeisl, a. Logadottir, L. Lindqvist, J. R. Kitchin, T. Bligaard, and H. Jónsson, *J. Phys. Chem. B*, 2004, **108**, 17886–17892.
16. R. Ouyang, J.-X. Liu, and W.-X. Li, *J. Am. Chem. Soc.*, 2013, **135**, 1760–71.
17. Y. Shao-Horn, W. C. Sheng, S. Chen, P. J. Ferreira, E. F. Holby, and D. Morgan, *Top. Catal.*, 2007, **46**, 285–305.
18. W. Schmittinger and A. Vahidi, *J. Power Sources*, 2008, **180**, 1–14.
19. D. Strmcnik, K. Kodama, D. van der Vliet, J. Greeley, V. Stamenkovic, and N. M. Markovic, *Nat. Chem.*, 2009, **1**, 466–72.
20. N. Zamel and X. Li, *Prog. Energy Combust. Sci.*, 2011, **37**, 292–329.
21. C. Song, *Catal. today*, 2002, **77**, 17–49.
22. S. J. Peighambardoust, S. Rowshanzamir, and M. Amjadi, *Review of the proton exchange membranes for fuel cell applications*, Elsevier Ltd, 2010, vol. 35.
23. L. Wang, B. L. Yi, H. M. Zhang, and D. M. Xing, *Electrochim. Acta*, 2007, **52**, 5479–5483.
24. *Fuel Cell Today*, 2013.
25. B. James and A. Spisak, *Rep. by Strateg. Anal. Inc., under …*, 2012, 1–62.
26. *Fuel Cell Technologies Office Multi-Year Research, Development and Demonstration Plan 3.4 Fuel Cells*, 2014.
27. A. Serov and C. Kwak, *Appl. Catal. B Environ.*, 2009, **90**, 313–320.
28. Z. Chen, D. Higgins, A. Yu, L. Zhang, and J. Zhang, *Energy Environ. Sci.*, 2011, **4**, 3167.
29. Y.-J. Wang, D. P. Wilkinson, and J. Zhang, *Chem. Rev.*, 2011, **111**, 7625–51.
30. W. Zhang, P. Sherrell, A. I. Minett, J. M. Razal, and J. Chen, *Energy Environ. Sci.*, 2010, **3**, 1286.
31. V. Stamenkovic, B. S. Mun, M. Arenz, K. J. J. Mayrhofer, C. A Lucas, G. Wang, P. N. Ross, and N. M. Markovic, *Nat. Mater.*, 2007, **6**, 241–7.
32. J. Greeley, I. E. L. Stephens, A. S. Bondarenko, T. P. Johansson, H. A. Hansen, T. F. Jaramillo, J. Rossmeisl, I. Chorkendorff, and J. K. Nørskov, *Nat. Chem.*, 2009, **1**, 552–6.
33. R. Jasinski, *Nature*, 1964, **201**, 1212.
34. R. Jasinski, *J. Electrochem. Soc.*, 1965, 526–528.
35. Z. Chen, D. Higgins, A. Yu, L. Zhang, and J. Zhang, *Energy Environ. Sci.*, 2011, **4**, 3167–3192.
36. H. Behret, H. Binder, and G. Sandstede, *Electrochem. Acta*, 1975, **20**, 111–117.

37. M. Lefèvre, E. Proietti, F. Jaouen, and J.-P. Dodelet, *Science*, 2009, **324**, 71–4.
38. H. A. Gasteiger, S. S. Kocha, B. Sompalli, and F. T. Wagner, *Appl. Catal. B Environ.*, 2005, **56**, 9–35.
39. H. Yano, J. Inukai, H. Uchida, M. Watanabe, P. K. Babu, T. Kobayashi, J. H. Chung, E. Oldfield, and A. Wieckowski, *Phys. Chem. Chem. Phys.*, 2006, **8**, 4932–9.
40. Z. Yang, S. Ball, D. Condit, and M. Gummalla, *J. Electrochem. Soc.*, 2011, **158**, B1439.
41. Y. Shao, J. Liu, Y. Wang, and Y. Lin, *J. Mater. Chem.*, 2009, **19**, 46.
42. Y. Einaga, J. S. Foord, and G. M. Swain, *MRS Bull.*, 2014, **39**, 525–532.
43. V. Tripković, F. Abild-Pedersen, F. Studt, I. Cerri, T. Nagami, T. Bligaard, and J. Rossmeisl, *ChemCatChem*, 2012, **4**, 228–235.
44. D. J. Ham and J. S. Lee, *Energies*, 2009, **2**, 873–899.
45. A. E. Fischer, M. a. Lowe, and G. M. Swain, *J. Electrochem. Soc.*, 2007, **154**, K61.
46. J. Wang and G. M. Swain, *J. Electrochem. Soc.*, 2003, **150**, E24.
47. Y. C. Kimmel, X. Xu, W. Yu, X. Yang, and J. G. Chen, *ACS Catal.*, 2014, **4**, 1558–1562.
48. T. G. Kelly and J. G. Chen, *Chem. Soc. Rev.*, 2012, **41**, 8021–34.
49. Y. Liu, T. G. Kelly, J. G. Chen, and W. E. Mustain, *ACS Catal.*, 2013, 11184–1194.
50. D.-J. Guo and H.-L. Li, *J. Power Sources*, 2006, **160**, 44–49.
51. S. Takenaka and M. Kishida, *J. Japan Pet. Inst.*, 2011, **54**, 80–8980.
52. Y. Shao, J. Sui, G. Yin, and Y. Gao, *Appl. Catal. B Environ.*, 2008, **79**, 89–99.
53. M. K. Debe, A. K. Schmoeckel, G. D. Vernstrom, and R. Atanasoski, *J. Power Sources*, 2006, **161**, 1002–1011.
54. A. Kongkanand, M. Dioguardi, C. Ji, and E. L. Thompson, *J. Electrochem. Soc.*, 2012, **159**, F405–F411.
55. M. Mavrikakis, B. Hammer, and J. K. Nørskov, *Phys. Rev. Lett.*, 1998, **81**, 2819–2822.
56. J. G. Chen, C. A. Menning, and M. B. Zellner, *Surf. Sci. Rep.*, 2008, **63**, 201–254.
57. B. Hammer and J. K. Nørskov, *Nature*, 1995, **376**, 238–240.
58. J. R. Kitchin, J. K. Nørskov, M. A. Barteau, and J. G. Chen, *Phys. Rev. Lett.*, 2004, **93**, 4–7.
59. J. Meier, J. Schiøtz, P. Liu, J. K. Nørskov, and U. Stimming, *Chem. Phys. Lett.*, 2004, **390**, 440–444.
60. P. Sabatier, *Berichte der Dtsch. Chem. Gesellschaft*, 1911, **44**, 1984.
61. J. Zhang, M. B. Vukmirovic, Y. Xu, M. Mavrikakis, and R. R. Adzic, *Angew. Chem. Int. Ed. Engl.*, 2005, **44**, 2132–5.
62. K. Sasaki, H. Naohara, Y. Cai, Y. M. Choi, P. Liu, M. B. Vukmirovic, J. X. Wang, and R. R. Adzic, *Angew. Chem. Int. Ed. Engl.*, 2010, **49**, 8602–7.
63. J. R. Kitchin, J. K. Nørskov, M. A. Barteau, and J. G. Chen, *J. Chem. Phys.*, 2004, **120**, 10240–6.
64. R. Ferrando, J. Jellinek, and R. L. Johnston, *Chem. Rev.*, 2008, **108**, 845–910.
65. S. Mukerjee, S. Srinivasan, M. P. Soriaga, and J. Mcbreen, *J. Electrochem. Soc.*, 1995, **142**, 1409–1422.
66. T. Toda, H. Igarashi, H. Uchida, and M. Watanabe, 1999, **146**, 3750–3756.
67. N. M. Markovic, T. J. Schmidt, V. Stamenkovic, and P. N. Ross, *Fuel Cells*, 2001, 105–116.
68. E. Antolini, J. R. C. Salgado, and E. R. Gonzalez, *J. Power Sources*, 2006, **160**, 957–968.
69. V. Stamenkovic, B. Fowler, B. S. Mun, G. Wang, P. N. Ross, C. a Lucas, and N. M. Markovic, *Science*, 2007, **315**, 493–7.
70. G. Jones, *Private communication*, 2012.
71. Y. Bing, H. Liu, L. Zhang, D. Ghosh, and J. Zhang, *Chem. Soc. Rev.*, 2010, **39**, 2184–202.
72. S. Koh and P. Strasser, *J. Am. Chem. Soc.*, 2007, **129**, 12624–5.
73. C. Wang, M. Chi, D. Li, D. Strmcnik, D. van der Vliet, G. Wang, V. Komanicky, K.-C. Chang, A. P. Paulikas, D. Tripkovic, J. Pearson, K. L. More, N. M. Markovic, and V. Stamenkovic, *J. Am. Chem. Soc.*, 2011, **133**, 14396–403.
74. G. Treglia, B. Legrande, and F. Ducastelle, *Europhys. Lett.*, 1988, **7**, 575–580.

75. L.-L. Wang and D. D. Johnson, *J. Am. Chem. Soc.*, 2009, **131**, 14023–9.
76. A. V Ruban, H. L. Skriver, and J. K. Nørskov, *Phys. Rev. B*, 1999, **59**, 990–1000.
77. G. Wang, M. Vanhove, P. Ross, and M. Baskes, *Prog. Surf. Sci.*, 2005, **79**, 28–45.
78. R. Ferrando, A. Fortunelli, and R. L. Johnston, *Phys. Chem. Chem. Phys.*, 2008, **10**, 640.
79. L. Li, A. H. Larsen, N. a. Romero, V. a. Morozov, C. Glinsvad, F. Abild-Pedersen, J. Greeley, K. W. Jacobsen, and J. K. Nørskov, *J. Phys. Chem. Lett.*, 2013, **4**, 222–226.
80. C. J. Pickard and R. J. Needs, *J. Phys. Condens. Matter*, 2011, **23**, 053201.
81. R. B. Levy and M. Boudart, *Science*, 1973, **181**, 547–9.
82. M. Nie, P. K. Shen, M. Wu, Z. Wei, and H. Meng, *J. Power Sources*, 2006, **162**, 173–176.
83. M. B. Zellner and J. G. Chen, *J. Electrochem. Soc.*, 2005, **152**, A1483.
84. C. Ma, T. Liu, and L. Chen, *Appl. Surf. Sci.*, 2010, **256**, 7400–7405.
85. M. Pourbaix, *Atlas of Electrochemical Equilibria*, Pergamon Press Ltd., 1966.
86. M. C. Weidman, D. V. Esposito, I. J. Hsu, and J. G. Chen, *J. Electrochem. Soc.*, 2010, **157**, F179.
87. M. C. Weidman, D. V. Esposito, Y.-C. Hsu, and J. G. Chen, *J. Power Sources*, 2012, **202**, 11–17.
88. H. Chhina, S. Campbell, and O. Kesler, *J. Power Sources*, 2007, **164**, 431–440.
89. D. V. Esposito and J. G. Chen, *Energy Environ. Sci.*, 2011, **4**, 3900–3912.
90. K. Lee, *Electrochim. Acta*, 2004, **49**, 3479–3485.
91. W. Zhu, A. Ignaszak, C. Song, R. Baker, R. Hui, J. Zhang, F. Nan, G. Botton, S. Ye, and S. Campbell, *Electrochim. Acta*, 2012, **61**, 198–206.
92. G. He, Z. Yan, X. Ma, H. Meng, P. K. Shen, and C. Wang, *Nanoscale*, 2011, **3**, 3578–82.
93. R. Ganesan and J. S. Lee, *Angew. Chem. Int. Ed. Engl.*, 2005, **44**, 6557–60.
94. I. J. Hsu, D. V. Esposito, E. G. Mahoney, A. Black, and J. G. Chen, *J. Power Sources*, 2011, **196**, 8307–8312.
95. D. V. Esposito, S. T. Hunt, A. L. Stottlemyer, K. D. Dobson, B. E. McCandless, R. W. Birkmire, and J. G. Chen, *Angew. Chem. Int. Ed. Engl.*, 2010, **49**, 9859–62.
96. I. J. Hsu, D. A. Hansgen, B. E. McCandless, B. G. Willis, and J. G. Chen, *J. Phys. Chem. C*, 2011, **115**, 3709–3715.
97. I. J. Hsu, Y. C. Kimmel, X. Jiang, B. G. Willis, and J. G. Chen, *Chem. Commun. (Camb).*, 2012, **48**, 1063–5.
98. Y. Kido, L. Yang, T. G. Kelly, S. a. Rykov, and J. G. Chen, *J. Catal.*, 2014, **312**, 216–220.
99. J. Greeley, J. K. Nørskov, and M. Mavrikakis, *Annu. Rev. Phys. Chem.*, 2002, **53**, 319–48.
100. P. Hohenberg and W. Kohn, *Phys. Rev.*, 1964, **136**, B864–B871.
101. W. Kohn and L. J. Sham, *Phys. Rev.*, 1965, **140**, A1133–A1138.
102. Z. Shi, J. Zhang, Z. Liu, H. Wang, and D. Wilkinson, *Electrochim. Acta*, 2006, **51**, 1905–1916.
103. C. J. Jacobsen, S. Dahl, B. S. Clausen, S. Bahn, a Logadottir, and J. K. Nørskov, *J. Am. Chem. Soc.*, 2001, **123**, 8404–5.
104. J. Greeley, T. F. Jaramillo, J. Bonde, I. Chorkendorff, and J. K. Nørskov, *Nat. Mater.*, 2006, **5**, 909–13.
105. J. Greeley and M. Mavrikakis, *Nat. Mater.*, 2004, **3**, 810–5.
106. J. Greeley and J. K. Nørskov, *J. Phys. Chem. C*, 2009, **113**, 4932–4939.
107. J. K. Nørskov, *J. Catal.*, 2002, **209**, 275–278.
108. J. Bronsted, *Chem Rev*, 1928, **5**, 231.
109. M. G. Evans and M. Polanyi, *Trans. Faraday Soc.*, 1938, **34**, 11.
110. J. K. Nørskov, F. Abild-Pedersen, F. Studt, and T. Bligaard, *Proc. Natl. Acad. Sci. U. S. A.*, 2011, **108**, 937–43.
111. J. K. Nørskov, T. Bligaard, J. Rossmeisl, and C. H. Christensen, *Nat. Chem.*, 2009, **1**, 37–46.
112. S. Goel and A. E. Masunov, *Int. J. Quantum Chem.*, 2011, **111**, 4276–4287.
113. A. Iwaszuk and M. Nolan, *J. Phys. Chem. C*, 2011, **115**, 12995–13007.

114. A. J. Cohen, P. Mori-Sánchez, and W. Yang, *Science*, 2008, **321**, 792–4.
115. J. R. Kitchin, J. K. Nørskov, M. A. Barteau, and J. G. Chen, *Catal. Today*, 2005, **105**, 66–73.
116. H. Toulhoat and P. Raybaud, *J. Catal.*, 2003, **216**, 63–72.
117. A. Vojvodic, C. Ruberto, and B. Lundqvist, *J. physics. Condens. matter*, 2010, **22**, 375504.
118. A. Vojvodic, A. Hellman, C. Ruberto, and B. Lundqvist, *Phys. Rev. Lett.*, 2009, **103**, 1–4.
119. W. Koch and M. C. Holthausen, *A Chemist's Guide to Density Functional Thoery: An Introduction and Practical Guide to DFT Calculations*, Wiley-VCH, Weinheim, 2000.
120. D. S. Sholl and J. A. Steckel, *Density Functional Theory A Practical Introduction*, Wiley, Hoboken, 2009.
121. M. C. Payne, M. C. Teter, D. C. Allan, T. A. Arias, and J. D. Joannopoulos, *Rev. Mod. Phys.*, 1992, **64**, 1045–97.
122. A. D. Becke, *J. Chem. Phys.*, 1992, **96**, 2155.
123. A. D. Becke, *J. Chem. Phys.*, 1993, **98**, 5648.
124. C. Lee, W. Yang, and R. Parr, *Phys. Rev. B*, 1988, **37**, 785–789.
125. A. Becke, *Phys. Rev. A*, 1988, **38**, 3098–3100.
126. J. Perdew, K. Burke, and M. Ernzerhof, *Phys. Rev. Lett.*, 1996, **77**, 3865–3868.
127. B. Hammer, L. B. Hansen, and J. K. Nørskov, *Phys. Rev. B*, 1999, **59**, 7413–7421.
128. V. Anisimov, J. Zaanen, and O. Andersen, *Phys. Rev. B*, 1991, **44**.
129. M. Segall, P. J. D. Lindan, M. Probert, C. Pickard, P. Hasnip, S. Clark, and M. C. Payne, *J. Phys. Condens. Matter*, 2002, **14**, 2717.
130. J. Mortensen, L. Hansen, and K. Jacobsen, *Phys. Rev. B*, 2005, **71**, 1–11.
131. H. Monkhorst and J. Pack, *Phys. Rev. B*, 1976, **13**, 5188–5192.
132. D. Vanderbilt, *Appl. Opt.*, 1990, **41**, 7892.
133. P. Blöchl, *Phys. Rev. B*, 1994, **50**, 17953–17979.
134. G. Kresse and D. Joubert, *Phys. Rev. B*, 1999, **59**, 1758–1775.
135. B. G. Pfrommer, M. Côté, S. G. Louie, and M. L. Cohen, *J. Comput. Phys.*, 1997, **131**, 233–240.
136. K. B. Wiberg and P. R. Rablen, *J. Comput. Chem.*, 1993, **14**, 1504–1518.
137. R. S. Mulliken, *J. Chem. Phys.*, 1955, **23**, 1833.
138. R. F. W. Bader and P. M. Beddall, *Chem. Phys. Lett.*, 1971, **8**, 29–36.
139. G. V Gibbs, D. F. Cox, T. D. Crawford, K. M. Rosso, N. L. Ross, and R. T. Downs, *J. Chem. Phys.*, 2006, **124**, 084704.
140. G. Jones, S. J. Jenkins, and D. A. King, *Surf. Sci.*, 2006, **600**, 224–228.
141. A. Morris and C. Pickard, *LINDOS version 1.3 User Manual*, UCL, London, 2011.
142. A. Vojvodic and C. Ruberto, *J. Phys. Condens. Matter*, 2010, **22**, 375501.
143. H. O. Pierson, *Handbook of Refractory Carbides and Nitrides*, Noyes Publishers, Westwood, New Jersey, 1996.
144. L. Johansson, *Surf. Sci. Rep.*, 1995, **21**, 177–250.
145. F. Viñes, C. Sousa, P. Liu, J. A. Rodriguez, and F. Illas, *J. Chem. Phys.*, 2005, **122**, 174709.
146. Y. Li, Y. Gao, B. Xiao, T. Min, Z. Fan, S. Ma, and L. Xu, *J. Alloys Compd.*, 2010, **502**, 28–37.
147. F. Bechstedt, P. Kackell, A. Zywietz, K. Karch, B. Adolph, K. Tenelsen, and J. Furthmuller, *Phys. Stat. Sol.*, 1997, **202**, 35–62.
148. L. S. Ramsdell, *Am. Minerol.*, 1947, **32**, 64.
149. A. L. H. Bennett, J. R. Cuthill, A. J. McAlister, N. E. Erickson, R. E. Watson, and S. Url, *Science (80-.).*, 1975, **187**, 858–859.
150. H. H. Hwu and J. G. Chen, *Chem. Rev.*, 2005, **105**, 185–212.
151. S. Bahn and K. W. Jacobsen, *Comput. Sience Eng.*, 2002, **4**, 56–66.
152. S. J. Clark, M. D. Segall, C. J. Pickard, P. J. Hasnip, M. I. J. Probert, K. Refson and M. C. Payne, *Zeitschrift für Kristallographie*, 2005, **220**, 567–570.
153. P. Pulay, *Chem. Phys. Lett.*, 1980, **73**, 393–398.
154. S. J. Jenkins, *Personal Communication*.

155. D. R. Lide, Ed., in *CRC Handbook of Chemistry and Physics*, CRC Press, Boca Raton, Florida, 84th edn., 2003, p. 76.
156. W. Lengauer, S. Binder, and K. Aigner, *J. Alloys Compd.*, 1995, **217**, 137–147.
157. L. Ramqvist, *Jernkontorets Ann.*, 1968, **152**, 465–475.
158. J. Leciejewicz, *Acta Crystallogr.*, 1961, **14**, 200–200.
159. Z. Li and R. Bradt, *J. Mater. Sci.*, 1986, **21**, 4366–4368.
160. E. Owen and E. Yates, *Philos. Mag. Ser. 7*, 1933, **15**, 472–488.
161. S. Bağcı, S. Duman, H. M. Tütüncü, and G. P. Srivastava, *Diam. Relat. Mater.*, 2009, **18**, 1057–1060.
162. L. Vitos, A. V Ruban, H. L. Skriver, and J. Kolla, *Surf. Sci.*, 1998, **411**, 186–202.
163. J. C. Slater, *J. Chem. Phys.*, 1964, **41**, 3199–3205.
164. W. Y. Ching, Y.-N. Xu, P. Rulis, and L. Ouyang, *Mater. Sci. Eng. A*, 2006, **422**, 147–156.
165. G. Zhao and D. Bagayoko, *New J. Phys.*, 2000, **2**, 16.1–16.12.
166. W. J. Choyke, D. R. Hamilton, and L. Patrick, *Phys. Rev.*, 1964, **133**, 465.
167. A. Seidl, A. Görling, P. Vogl, J. A. Majewski, and M. Levy, *Phys. Rev. B. Condens. Matter*, 1996, **53**, 3764–3774.
168. D. D. Vasić Anićijević, I. a. Pašti, and S. V. Mentus, *Int. J. Hydrogen Energy*, 2013, **38**, 5009–5018.
169. S. Zaima, Y. Shibata, H. Adachi, and C. Oshima, *Surf. Sci.*, 1985, **157**, 380–392.
170. D. J. Siegel, L. G. Hector, and J. B. Adams, *Surf. Sci.*, 2002, **498**, 21664–21671.
171. S. Ball, S. L. Burton, J. Fisher, R. O'Malley, B. Tessier, B. Theobald, D. Thompsett, W. P. Zhou, D. Su, and R. Adzic, *ECS Trans.*, 2009, **25**, 1023–1036.
172. M. P. Humbert, C. A. Menning, and J. G. Chen, *J. Catal.*, 2010, **271**, 132–139.
173. J. L. R. Yates, G. H. Spikes, and G. Jones, *Phys. Chem. Chem. Phys.*, 2015, **17**, 4250–4258.
174. D. V. Esposito, S. T. Hunt, Y. C. Kimmel, and J. G. Chen, *J. Am. Chem. Soc.*, 2012, **134**, 3025–3033.
175. D. D. Vasić Anićijević, V. M. Nikolić, M. P. Marčeta-Kaninski, and I. a. Pašti, *Int. J. Hydrogen Energy*, 2013, **38**, 16071–16079.
176. G. Wang, B. Huang, L. Xiao, Z. Ren, H. Chen, D. Wang, H. D. Abruña, J. Lu, and L. Zhuang, *J. Am. Chem. Soc.*, 2014, **136**, 9643–9.
177. E. van Steen, *Personal Communication*, 2014.
178. *http://www.sigmaaldrich.com/materials-science/material-science-products.html?TablePage=21092524*, 2015.
179. B. S. Lim, A. Rahtu, and R. G. Gordon, *Nat. Mater.*, 2003, **2**, 749–54.
180. M. Ritala, J. Hamalainen, and M. Leskela, *Chem. Mater.*, 2014, **26**, 786–801.
181. R. G. Parkhomenko, S. V. Trubin, A. E. Turgambaeva, and I. K. Igumenov, *J. Cryst. Growth*, 2015, **414**, 143–150.
182. S. Chen, H. A. Gasteiger, K. Hayakawa, T. Tada, and Y. Shao-Horn, *J. Electrochem. Soc.*, 2010, **157**, A82.
183. D. Wang, H. L. Xin, Y. Yu, H. Wang, E. Rus, D. A. Muller, and H. D. Abruña, 2010, 17664–17666.
184. P. Gouy-Pailler, *J. Vac. Sci. Technol. A Vacuum, Surfaces, Film.*, 1993, **11**, 96.
185. A. Smigelskas and E. Kirkendall, *Trans. AIME*, 1947, **171**, 130–142.
186. M. Lopez-Haro, L. Dubau, L. Guétaz, P. Bayle-Guillemaud, M. Chatenet, J. André, N. Caqué, E. Rossinot, and F. Maillard, *Appl. Catal. B Environ.*, 2014, **152-153**, 300–308.
187. J. X. Wang, C. Ma, Y. Choi, D. Su, Y. Zhu, P. Liu, R. Si, M. B. Vukmirovic, Y. Zhang, and R. R. Adzic, *J. Am. Chem. Soc.*, 2011, **133**, 13551–7.
188. K. N. Tu and U. Gösele, *Appl. Phys. Lett.*, 2005, **86**, 093111.
189. E. Clementi, D. L. Raimondi, and W. P. Reinhardt, *J. Chem. Phys.*, 1963, **38**, 2686.
190. E. Clementi, D. L. Raimondi, and W. P. Reinhardt, *J. Chem. Phys.*, 1967, **47**, 1300–1307.

191. N. N. Greenwood and A. Earnshaw, *Chemistry of the Elements*, Butterworth-Heinemann, Oxford, 2nd edn., 1997.
192. T. G. Kelly, A. L. Stottlemyer, H. Ren, and J. G. Chen, 2011, 6644–6650.
193. T. Li, P. A. J. Bagot, E. Christian, B. R. C. Theobald, J. D. B. Sharman, D. Ozkaya, M. P. Moody, S. C. E. Tsang, and G. D. W. Smith, *ACS Catal.*, 2014, **4**, 695–702.
194. T. Bligaard, J. K. Nørskov, S. Dahl, J. Matthiesen, C. H. Christensen, and J. Sehested, *J. Catal.*, 2004, **224**, 206–217.
195. F. Viñes, A. Vojvodic, F. Abild-Pedersen, and F. Illas, *J. Phys. Chem. C*, 2013, **117**, 4168–4171.
196. J. Rossmeisl, A. Logadottir, and J. K. Nørskov, *Chem. Phys.*, 2005, **319**, 178–184.
197. E. M. Fernández, P. G. Moses, A. Toftelund, H. A Hansen, J. I. Martínez, F. Abild-Pedersen, J. Kleis, B. Hinnemann, J. Rossmeisl, T. Bligaard, and J. K. Nørskov, *Angew. Chem. Int. Ed. Engl.*, 2008, **47**, 4683–6.
198. F. Abild-Pedersen, J. Greeley, F. Studt, J. Rossmeisl, T. Munter, P. Moses, E. Skúlason, T. Bligaard, and J. K. Nørskov, *Phys. Rev. Lett.*, 2007, **99**, 016105.
199. I. E. L. Stephens, A. S. Bondarenko, U. Grønbjerg, J. Rossmeisl, and I. Chorkendorff, *Energy Environ. Sci.*, 2012, **5**, 6744.
200. K. Raghavan, K. Foster, and M. Berkowitz, *Chem. Phys. Lett.*, 1991, **177**, 426–432.
201. A. Michaelides, V. Ranea, P. de Andres, and D. King, *Phys. Rev. Lett.*, 2003, **90**, 1–4.
202. A. Michaelides and P. Hu, *J. Chem. Phys.*, 2001, **114**, 513.
203. H. Ogasawara, B. Brena, D. Nordlund, M. Nyberg, A. Pelmenschikov, L. G. M. Pettersson, and A. Nilsson, *Phys. Rev. Lett.*, 2002, **89**, 276102.
204. Department of Energy and Office of Energy Efficiency and Renewable Energy, *Fuel Cell Technologies Office Multi-Year Research, Development and Demonstration Plan*, 2014.
205. Y. Shao, G. Yin, and Y. Gao, *J. Power Sources*, 2007, **171**, 558–566.
206. J. Greeley and J. K. Nørskov, *Electrochim. Acta*, 2007, **52**, 5829–5836.
207. P. Parthasarathy and A. V. Virkar, *J. Power Sources*, 2011, **196**, 9204–9212.
208. K. Jacobsen, J. Norskov, and M. Puska, *Phys. Rev. B*, 1987, **35**, 7423–7442.
209. J. Enkovaara, C. Rostgaard, J. J. Mortensen, J. Chen, M. Dułak, L. Ferrighi, J. Gavnholt, C. Glinsvad, V. Haikola, H. A. Hansen, H. H. Kristoffersen, M. Kuisma, A. H. Larsen, L. Lehtovaara, M. Ljungberg, O. Lopez-Acevedo, P. G. Moses, J. Ojanen, T. Olsen, V. Petzold, N. A. Romero, J. Stausholm-Møller, M. Strange, G. a Tritsaris, M. Vanin, M. Walter, B. Hammer, H. Häkkinen, G. K. H. Madsen, R. M. Nieminen, J. K. Nørskov, M. Puska, T. T. Rantala, J. Schiøtz, K. S. Thygesen, and K. W. Jacobsen, *J. Phys. Condens. Matter*, 2010, **22**, 253202.
210. C.-K. Skylaris, P. D. Haynes, A. A Mostofi, and M. C. Payne, *J. Chem. Phys.*, 2005, **122**, 84119.
211. Á. Ruiz-Serrano and C.-K. Skylaris, *J. Chem. Phys.*, 2013, **139**, 054107.
212. L. Xiao and L. Wang, *J. Phys. Chem. A*, 2004, **108**, 8605–8614.
213. A. Nie, J. Wu, C. Zhou, and S. Yao, *Int. J. Quantum Chem*, 2007, **107**, 219–224.
214. K. W. Jacobsen, P. Stoltze, and J. K. Nørskov, *Surf. Sci.*, 1996, **366**, 394–402.
215. P. Morse, *Phys. Rev.*, 1929, **34**, 57–64.
216. E. Bitzek, P. Koskinen, F. Gähler, M. Moseler, and P. Gumbsch, *Phys. Rev. Lett.*, 2006, **97**, 170201.
217. S. K. Gupta, B. M. Nappi, K. A. Gingerichs, K. A. Gingerich, R. D. Grigsby, and M. Trans, *Inorg. Chem.*, 1981, **471**, 966–969.
218. W. A. Harrison, *Solid State Theory*, Dover Publications, 1979.
219. N. Cheng, M. Norouzi Banis, J. Liu, A. Riese, S. Mu, R. Li, T.-K. Sham, and X. Sun, *Energy Environ. Sci.*, 2015, **8**, 1450–1455.
220. Z. Cui, R. Burns, and F. DiSalvo, *Chem. Mater.*, 2013, 3782–3784.

221. Y. Xiao, G. Zhan, Z. Fu, Z. Pan, C. Xiao, S. Wu, C. Chen, G. Hu, and Z. Wei, *J. Power Sources*, 2015, **284**, 296–304.